SOLUTION PROCESSING OF STRIPES, PATCHES AND DIGITAL PATTERNS USING A NOVEL SLOT DIE COATING-INSPIRED APPROACH

A Dissertation
Presented to
The Academic Faculty

by

Ara Parsekian

In Partial Fulfillment
of the Requirements for the Degree
Doctor of Philosophy in the
George W. Woodruff School of Mechanical Engineering

Georgia Institute of Technology
May 2020

SOLUTION PROCESSING OF STRIPES, PATCHES AND DIGITAL PATTERNS USING A NOVEL SLOT DIE COATING-INSPIRED APPROACH

Approved by:

Dr. Tequila A. L. Harris, Advisor
School of Mechanical Engineering
Georgia Institute of Technology

Dr. John R. Reynolds
School of Chemistry
Georgia Institute of Technology

Dr. Minami Yoda
School of Mechanical Engineering
Georgia Institute of Technology

Dr. Victor Breedveld
School of Chemical Engineering
Georgia Institute of Technology

Dr. Suresh K. Sitaraman
School of Mechanical Engineering
Georgia Institute of Technology

Date Approved: December 4, 2019

To my friends Andrey and Pushparghya

ACKNOWLEDGEMENTS

I would like to thank my advisor, Dr. Tequila Harris, for her guidance and support throughout the entirety of my Ph.D. career. I have been grateful to work under an advisor who has taken my best ideas seriously and has continually challenged me to produce my best work. I am grateful as well to my committee members Dr. Minami Yoda, Dr. Suresh Sitaraman, Dr. John Reynolds, and Dr. Victor Breedveld for their expert guidance in honing the focus of my thesis work, and special thanks to Dr. Sitaraman for generously making available his laboratory facilities.

I would like to thank Dr. Marc Smith for his thorough review and insightful commentary regarding the perturbation analysis contained in this thesis, in addition to his advice on articulating the value of the work. I would also like to thank the members of my laboratory group, particularly Tae-Joong Jeong and Peter Griffiths for providing helpful feedback, as well as the many undergraduate researchers who I have had the pleasure of mentoring during my Ph.D. career. I would like to thank the scientists and engineers at NovaCentrix for significant professional mentorship and for their early investment in the ideas presented here. Finally, I would like to thank my family, for their confidence in me and for their unceasing encouragement.

This work was supported by the National Science Foundation under Grant No. 1069138, CMMI MEP-1562255, and IGERT Grant No. 1069138.

TABLE OF CONTENTS

LIST OF TABLES

LIST OF FIGURES

LIST OF SYMBOLS AND ABBREVIATIONS

Roman Letters

A, B	Labels for fluid species comprising a two-fluid alternating-stripe pattern
Ca	Capillary number
$\boldsymbol{e}_x$, $\boldsymbol{e}_y$, $\boldsymbol{e}_z$	Unit vectors for a Cartesian coordinate system
$\boldsymbol{e}_r$, $\boldsymbol{e}_\theta$, $\boldsymbol{e}_z$	Unit vectors for a cylindrical polar coordinate system
G	Slot gap
G_e	Electrical conductance
H	Coating gap
H^*	Dimensionless Coating Gap
i,j	Indices for stripe interfaces in co-laminar flow of two materials through a converging rectangular slot
L_d, L_u	Length of downstream and upstream portions of slot die lip, respectively
ℓ_{start}, ℓ_{stop}	Length of leading-edge and trailing-edge taper defects, respectively, on an intermittent stripe pattern feature
m_{PVA}	Mass fraction of PVA in aqueous solution
M, N	Number of stripes of each material in a two-material alternating-stripe pattern
n	Index for series summations in mathematical derivations
p	Pressure
p_A, p_B, p_d	Reference pressure values for mathematical analysis of internal flow in a converging rectangular slot

$P1_i$, $P2_i$, $P2_i$, $P4_i$	Functions of cylindrical coordinates r, θ, and z used in analytical expressions for flow velocity field for co-laminar flow through a converging rectangular slot
Pe	Peclet number (mass transport)
Q	Volumetric flow rate
Q_A, Q_B	Volumetric flow rate for fluids A and B, respectively
$Q_{Ag\text{-}NP}$, $Q_{PEDOT:PSS}$, Q_{PVA}, Q_{PVP}	Volumetric flow rate of solutions of silver nanoparticle ink, PEDOT:PSS ink, aqueous PVA, and aqueous PVP, respectively
Q_{A+B}	Sum of Q_A and Q_B
Q_i	Volumetric flow-rate of multi-fluid co-laminar flow in the region bounded by interfaces indexed at $i\text{-}1$ and i, where i is an integer.
Q_*	Dimensionless volumetric flow rate
R	Electrical resistance
Re	Reynolds number
Re^*	Modified Reynolds number
r	Radial coordinate (cylindrical coordinate system)
r_d, r_u	Upstream and downstream r-axis boundaries for a converging rectangular slot
s	Center-to-center spacing of adjacent narrow stripes deposited by slot die
s_0	Center-to-center spacing of adjacent channels that compose a segmented slot geometry in a slot die coater
s_{inlet}	Center-to-center of inlet spacing for the internal cavity of an HSSC tool
$\boldsymbol{T}$	Stress tensor
$\boldsymbol{T}_A$, $\boldsymbol{T}_B$	Stress tensor for fluids A and B, respectively

t	Time
t_{dry}, t_{wet}	Dry film thickness and wet film thickness
t_{start}, t_{stop}	Time intervals required for full development and breakup of a coating bead following on-actuation and off-actuation of flow, respectively
U_{outlet}	Average flow velocity at slot die outlet
U_{web}	Substrate/webbing velocity
$\vec{U}$	Vector form of outer velocity
U_r, U_θ, U_z	Outer velocity components in the cylindrical coordinate system
$U_{r,0}$, $U_{\theta,0}$, $U_{z,0}$	$\mathcal{O}(1)$ outer velocity components in the cylindrical coordinate system
$U_{r,1}$, $U_{\theta,1}$, $U_{z,1}$	$\mathcal{O}(\alpha)$ outer velocity components in the cylindrical coordinate system
$\vec{u}$	Vector form of flow velocity
u_r, u_θ, u_z	Velocity components in the cylindrical coordinate system
$u_{r,0}$, $u_{\theta,0}$, $u_{z,0}$	$\mathcal{O}(1)$ composite velocity components in the cylindrical coordinate system
$u_{r,1}$, $u_{\theta,1}$, $u_{z,1}$	$\mathcal{O}(\alpha)$ composite velocity components in the cylindrical coordinate system
$\overrightarrow{UI}$	Flow velocity at internal fluid-fluid boundaries
$\vec{V}$	Vector form of right inner velocity
V_r, V_θ, V_z	Right inner velocity components in the cylindrical coordinate system
$V_{r,0}$, $V_{\theta,0}$, $V_{z,0}$	$\mathcal{O}(1)$ right inner velocity components in the cylindrical coordinate system
$V_{r,1}$, $V_{\theta,1}$, $V_{z,1}$	$\mathcal{O}(\alpha)$ right inner velocity components in the cylindrical coordinate system
$\overrightarrow{W}$	Vector form of left inner velocity
W_r, W_θ, W_z	Left inner velocity components in the cylindrical coordinate system
$W_{r,0}$, $W_{\theta,0}$, $W_{z,0}$	$\mathcal{O}(1)$ left inner velocity components in the cylindrical coordinate system

$W_{r,1}$, $W_{\theta,1}$, $W_{z,1}$	$\mathcal{O}(\alpha)$ left inner velocity components in the cylindrical coordinate system
w	Width of coated narrow stripe
w_0	Width of slot outlet or channel outlet
w_*	Dimensionless width of coated narrow stripe
w_{a*}, w_{r*}	Dimensionless width of a coated narrow stripe in advancing and receding states, respectively
w_d, w_u	Width of converging narrow slot at downstream and upstream boundaries, respectively
$w_{II\text{-}III}^*$	Dimensionless width of slot-coated narrow stripe at the point of transition between two regimes of contact bead confinement along the bottom of a slot die lip
x	Coordinate vertical to coating direction
y	Coordinate along width of slot die
z	Coordinate along coating direction
A_a, A_r, B_a, B_r, C_a, C_r, D_a, D_r	Empirical constants for model of slot die-coated narrow stripe width
A_0, B_0, C_0, D_0	Constant coefficients used in mathematical derivations of flow through a converging rectangular slot
$A_{n,1}$, $A_{n,2,}$ $B_{n,1}$, $B_{n,2}$, $B_{n,3}$,	Constant coefficients used in mathematical derivations of multi-fluid co-laminar flow through a converging rectangular slot, which are indexed by n in infinite series
AI_i, BI_i, $CI_{1,i}$, $CI_{2,i}$, $DI_{1,i}$, $DI_{2,i}$	Constant coefficients used in mathematical derivations of multi-fluid co-laminar flow through a converging rectangular slot, which are indexed by i and associated with specific fluid interfaces
$C_{n,1}$, $C_{n,2}$, $D_{n,1}$, $D_{n,2}$	Constant coefficients used in mathematical derivations of single-fluid flow through a converging rectangular slot, which are indexed by n in infinite series

E_n, F_n, H_n Constant coefficients used in mathematical derivations of both multi-fluid and single-fluid flow through a converging rectangular slot, which are indexed by n in infinite series

$A_{0,err}$, $C_{0,err}$ Correction factors to A_0 and C_0 based on enforcement of a flow-rate condition

Greek Letters

α Inverse of aspect ratio of rectangular cross-section

β Ratio between width reduction and distance along primary flow axis in a converging rectangular slot

γ Surface tension

δ_n Indexed constant coefficient that appear in infinite series in analytical model of flow through a converging rectangular slot

ε Offset between the center of rotation and geometric center for a webbing roller

ζ_i Intermediate coordinate associated with i-th fluid interface in two-fluid co-laminar flow through a converging rectangular channel

ζ_l Intermediate coordinate associated with left boundary of a converging rectangular slot

ζ_r Intermediate coordinate associated with right boundary of a converging rectangular slot

γ_{AB} Interfacial tension for two fluids A and B

$\gamma_{S\text{-}A}$, $\gamma_{S\text{-}B}$ Solid-liquid interfacial energy for fluids A and B, respectively

$\gamma_{G\text{-}S}$ Interfacial energy of a gas-solid interface

θ Circumferential coordinate (cylindrical coordinate system)

θ_A, θ_B Contact angles of fluids A and B, respectively

$\theta_{B,A}$ Contact angle of a droplet of fluid B with fluid A as the outer phase

θ_a, θ_r Advancing and receding contact angle, respectively

θ_H Convergence angle of a narrowing rectangular slot

θ_i θ-coordinate of the ith fluid interface of co-laminar flow of two fluids through a converging rectangular slot

θ_S θ-coordinate of a streamline of internal flow through a converging rectangular slot

μ Dynamic viscosity

μ_A, μ_B Dynamic viscosity of fluids *A* and *B*, respectively

μ_{A+B} Sum of μ_A and μ_B

μ_i Viscosity of multi-fluid co-laminar flow in the region bounded by interfaces indexed at *i-1* and *i*

ξ_i Inner coordinate associated with *i*-th fluid interface in two-fluid co-laminar flow through a converging rectangular channel

ξ_l Inner coordinate associated with the left boundary in a converging rectangular slot

ξ_r Inner coordinate associated with the right boundary in a converging rectangular slot

Π_a, Π_r Dimensionless Pi-groups used in empirical model of slot-coated narrow stripe width

ρ Density

σ Surface tension

τ_{rr}, $\tau_{r\theta}$, $\tau_{\theta r}$, $\tau_{\theta\theta}$, τ_{rz}, τ_{zr}, $\tau_{\theta z}$, $\tau_{z\theta}$, τ_{zz} Stress tensor components in a cylindrical coordinate system

σ_e Electrical conductivity

φ_A, φ_B Geometric angles in equilibrium wetting analysis of liquid-liquid gas contact line

χ_{PVA}	Volume fraction of PVA in mixture.
ψ	Function of α used in matching by intermediate variable

Abbreviations

Ag-NP	Silver nanoparticle
C/EOD	Coating/extrusion-on-demand
DC	Direct current
DLOR	Discrete localized outflow region
HDF	Hydrodynamic focusing
HSSC	Heterogeneous stripe slot coating
MIF	Multi-inlet flow
PEDOT:PSS	poly(3,4-ethylenedioxythiophene) polystyrene sulfonate
PAF	Pin-actuated flow
PDMS	polydimethylsiloxane
PET	polyethylene terephthalate
PMMA	polymethyl methacrylate
PVA	polyvinyl alcohol
PVP	polyvinyl pyrrolidone
VPO	Vacuum pump oil

SUMMARY

In recent decades, printing and coating techniques have received interest for manufacturing of low-cost wearable electronics, sensors, displays, photovoltaics, and energy storage devices. The functionality of these devices depends significantly on the print resolution, with typical feature sizes ranging from millimeters to microns. Although feature sizes across this range are technically feasible with established techniques, process scalability and wide-area patterning have presented persistent challenges. Thus, the commercial impact of various low-cost printed devices has been constrained significantly by manufacturing limitations. To address these limitations, this dissertation develops an approach based on slot die coating, which benefits from proven advantages for scalable wide-area deposition. Investigations of the fluid phenomena responsible for generating high-resolution patterns provide the fundamental understanding necessary to impart a sophisticated patterning capability to slot die coating. The resulting manufacturing techniques constitute a novel capability for generating micro-scale pattern features across a wide area, without costly pre-patterning or post-deposition subtractive steps.

Using experimental and analytical approaches, an understanding of processing limits in terms of pattern resolution and feature size is developed for novel slot die-inspired processes that enable patterning of a single liquid as well as multiple liquids deposited simultaneously. Regardless of the number of liquids deposited simultaneously, manipulation of the shape and volume of the liquid bridge constitutes one method for

process control over feature size. In this work, an empirical model has been developed that relates dynamic wetting and liquid bridge phenomena to pattern morphology. Additionally, when coating multiple liquids, wetting equilibrium of the heterogeneous liquid film and diffusion mixing must be considered. Therefore, this work also derives a set of analytical models for co-laminar flow inside the coating tool as a first approximation of the pattern feature size. The model finds good agreement with flow visualizations inside the physical coating tool. The experimental findings also show that hydrodynamic focusing can enable feature sizes that are orders of magnitude smaller than the state-of-the-art for the conventional slot die approach.

CHAPTER 1. INTRODUCTION AND BACKGROUND

1.1 Motivation

For applications spanning optoelectronics[1-10], sensors[11-18], computing[19-27], microfluidics[28-30], and energy conversion[31-34], printing and coating processes offer unique routes toward high-volume production and on-demand customizability. The prospect of functional devices manufactured using graphical printing techniques, in the same manner as newsprint or instant film, is a significant motivation driving research in device architecture and solution-processible materials[35-39]. However, in addition to more demanding patterning requirements, functional devices encompass a range of materials and functionality that are more diverse than traditional graphics. These application-derived demands continually push the boundaries of what existing printing techniques can realistically achieve. Furthermore, the capabilities of established manufacturing approaches must be considered in terms of per-unit cost and scalability, since these aspects are pivotal for the commercial viability and societal impact of a given application. In short, strong demand exists for improved manufacturing capabilities relevant to printed devices.

The research community of coatings and printing technologies has sought to address this demand through optimization of established processes, through improved fundamental understanding of the physical mechanisms that influences patterned deposition of structures and through the development of novel manufacturing techniques.

While the contributions of this thesis are most closely aligned with the latter, due consideration is also given to process optimization and fundamental physics where appropriate. The remainder of Chapter 1 is centered around current state-of-the-art in printed device manufacturing to a) provide an overview of established techniques for printed device manufacture, b) propose appropriate metrics for assessing process capability and c) compare those metrics across existing techniques.

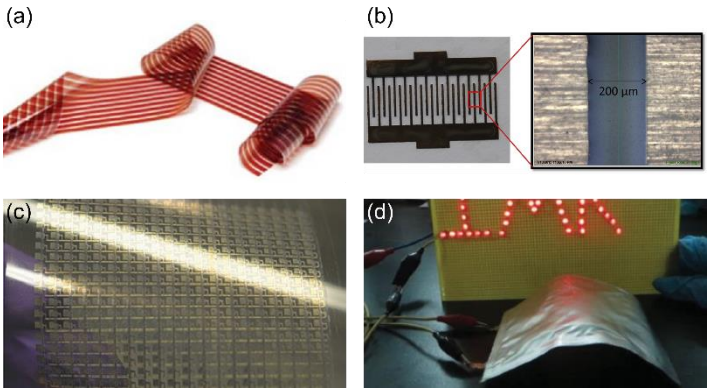

Figure 1.1 – Applications including (a) photovoltaics[5], (b) sensors[16], (c) thin film transistors[25], and (d) flexible batteries[34] can be manufactured from architectures incorporating continuous narrow stripes.

1.2 Roll-to-Roll (R2R) Manufacturing

1.2.1 Merits of R2R Processing

Liquid-phase film deposition techniques have long been recognized for their suitability for roll-to-roll (R2R) production to achieve significant economies of scale. R2R refers to a manufacturing operation of the type illustrated in Figure 1.2, where successive processing steps are carried out on a continuous length of substrate unwound from a roll at the start of the operation and re-wound at the end of the operation. Generally, R2R

manufacturing is associated with low material waste, high throughput, and wide-area deposition[35-40]. Printing and coating methods lend themselves to this approach because they can be carried out continuously, under atmospheric conditions, and near room temperature. Furthermore, these methods are well suited for deposition on flexible substrate, which makes them especially attractive for the burgeoning field of flexible electronics and wearables.

This manufacturing paradigm has been extended to an exceptionally broad range of functional materials, including conjugated polymers[41-44]; organic small molecules[45-48]; fullerenes[49-52]; carbon nanotubes[53-56]; graphene oxide [57-59]; metallic nanostructures[60-65]; ceramics[66-69]; metal oxides[70-72]; and perovskites[73-76]. Though representative, this list is not comprehensive. In fact, the difficulty in compiling a comprehensive account of all solution-processible materials that the current taxonomy of viable coating materials is subject to ongoing rapid innovation and is thus continuously changing and evolving.

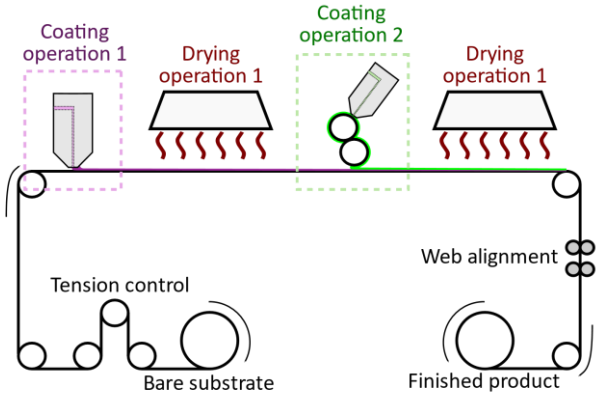

Figure 1.2 – Schematic illustration of a typical R2R manufacturing setup.

1.2.2 Overview of R2R Deposition Techniques

A visual summary of established techniques suitable for R2R deposition are shown in Figure 1.3(a). The first group in Figure 1.3(a) comprises pre-metered extrusion-derived techniques[77] such as slide coating, curtain coating[78], direct ink writing[79], and of note, slot die coating. The commonality between these four coating methods is continuous flow emanating from a narrow orifice, which is deposited onto a moving substrate through a steady liquid bridge. The first three techniques, which develop a parabolic 2D flow through a narrow slot, are economical for wide-area coverage in the absence of patterning. Slide and curtain coating are particularly suitable for deposition over raised features and uneven surfaces since these tools can be positioned high above the substrate. Slot die coating, where the coating tool is positioned close to the substrate, is optimal for extremely uniform films deposited at web speeds. In contrast to these three methods, direct ink writing deposits flow from a narrow microchannel or micro-pipet across a relatively narrow width. However, as with slot die, slide coating, and curtain coating, direct ink writing deposits fluid through a steady liquid bridge subject to continuous shear. This physical mode of deposition allows the four methods in Figure 1.3(a) to operate across a wide range of coating fluid viscosities.

A second group comprises spray coating[80, 81], screen printing[82, 83] and stencil printing[84, 85], shown in Figure 1.3(b). Spray coating and stencil printing rely on a physical mask to define the boundaries of a pattern, with coating fluid deposited as a physical vapor in spray coating and as a liquid or paste in stencil printing. Screen printing forces paste

through a permeable screen mesh whose primary function is to define a uniform film thickness across the entirety of the pattern. The presence of the mesh introduces a practical limitation on the feature size that can be printed, roughly corresponding to the diameter of the wire mesh that composes the screen[86]. Another important consideration for all three methods is the potential for pattern defects if the underside of the mask/screen/mesh becomes contaminated with coating fluid. Once contamination occurs, the resulting defect persists across runs until the underside of the mask/screen/mesh is cleaned, which limits the suitability of the methods for large-scale runs. While spray, stencil, and screen printing are most recognizable as a plate-to-plate operation, rotary incarnations of these approaches are available. For this reason, they can be considered R2R-compatible methods.

Gravure[87-89] and flexographic[90-92] printing, shown in Figure 1.3(c), transfer ink or coating fluid by physical contact from a pattern master roller to the substrate. The primary difference between the two methods is the type of pattern master used. In the case of flexography, this is a flexible relief plate adhered to a roller, which defines the areas where material should be transferred to the substrate. The pattern master in gravure coating is an engraved roller which defines a negative pattern image. Various intermediate components are also typically incorporated into the chain of ink transfers, such as anilox rollers to meter the area loading onto the pattern master or a doctor blade to remove excess ink from a roller.

The final group among established printing and coating approaches are the three droplet-based approaches shown in Figure 1.3(d). Inkjet[93-97] is the premier digital manufacturing technique for R2R manufacturing, delivering exceptional customizability through on-demand patterning. Most inkjet print heads can be categorized either continuous inkjet printing (CIJ) or as drop-on-demand (DoD)[95].In CIJ, droplets are formed by the Raleigh instability in a continuous liquid stream and deflected selectively by an electric potential into a reservoir. This approach has largely been superseded by DoD [96], wherein droplets are formed as needed by either piezoelectric actuation of the print head reservoir or thermally induced cavitation of the ink.

Aerosol[18, 98] and electrohydrodynamic jet (e-jet)[99-102] methods are conceptually similar to inkjet, with key differences in how coating fluid exits the print head. Aerosol jet printing incorporates a sheath gas to focus the liquid stream, which enables positioning of the print head far from the substrate surface. This technique is well-suited for deposition atop raised features and complex surfaces, although it is susceptible to splattering or overspray defects[98] due to the high velocity of fluid droplets impacting the substrate. E-jet uses an electric field to overcome surface tension of the ink and to form exceptionally small liquid droplets and filaments. The primary benefit of e-jet printing is significantly increased pattern resolution, at the cost of process complexity and reduced suitability for wide-area coverage.

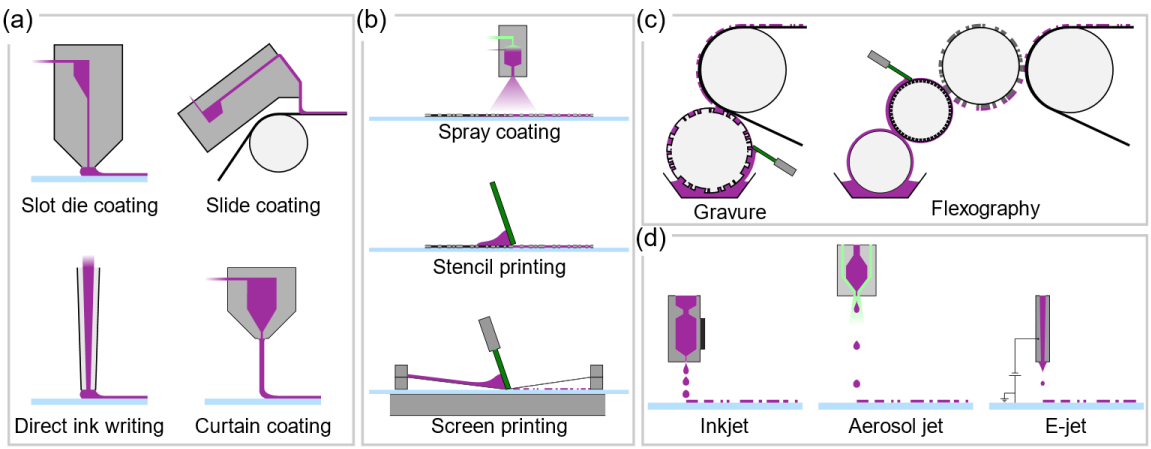

Figure 1.3 – Schematic illustrations of the various established printing and coating methods, which consist of (a) slot die coating, (b) curtain coating, (c) slide coating, (d) direct write, (e) stencil printing, (f) screen printing, (g) flexographic printing, (h) gravure printing, (i) inkjet printing, (j) aerosol jet printing, and (k) e-jet printing.

1.2.3 Slot Die Coating

Slot die coating is one of the most scalable and versatile established methods for wide-area coating. As illustrated in Figure 1.4, a slot die comprises a narrow slot expanding from a single inlet to a wide, thin outlet. Pre-metered coating flow through the slot die develops a uniform parabolic profile and is conveyed from tool to substrate through a steady liquid bridge. Deposition of a stratified film comprising multiple materials using this technique has been described in a number of previous studies[103-105]. Solutions, inks and slurries across a wide range of viscosities, both Newtonian and shear-dependent, are routinely processed by slot die coating within the ecosystem of printed devices[106-108]. Furthermore, the required tooling and process control is simple compared to other methods. In practice, slot die coating can be implemented with a specialty-cut shim(s) clamped between two die block halves. The parameters relevant to process control are volumetric

flow rate (Q), webbing velocity (U_{web}), and coating gap (H). The important geometrical parameters of the tool include the width of the slot (w_0), length of upstream and downstream portion of die lip (L_u and L_d, respectively), and slot gap (G), illustrated in Figure 1.4**.**

In its conventional form, slot die coating is suitable for uniform wide-area films and continuous stripes. Rather than patterning capabilities, the vast majority of research on the slot die coating process has focused on the onset of defects mediated by the coating bead, which is typically visualized as a coating window similar to that illustrated in Figure 1.4(b)[104, 109-111]. For interpretation of this process chart, it should be noted that both axes represent inputs to the process. Thus, the shaded region on the plot corresponds to combinations of independent variables, in this case volumetric flow rate (Q) and substrate velocity (U_{web}) that result in a defect-free wet film.

The boundaries of the shaded region correspond to the onset of various defects, and existing literature provides several useful models that describe the locations of these boundaries under representative conditions. For example, the visco-capillary model first proposed by Ruschak[112] describes three limiting conditions for stability of the upstream and downstream free surfaces of the coating bead, which reflect a balance between pressure, viscous forces, and interfacial forces. For a given slot die geometry and material system, there exists a mapping from Q to a critical value of U_{web} for each of the three stability conditions. The resulting coating window boundaries correspond to failure of the steady coating bead configuration, and the introduction of dripping, break lines, and air

entrainment defects[113] as indicated in Figure 1.4(b). It should be noted that the shape of the coating window varies widely across tool geometry, material system, and operating conditions. For example, Ding et al.[111] provide the three coating window shapes in Figure 1.4 (c) as illustrative examples of the coating window for slot die coating flows dominated by interfacial, viscous, and inertial forces, respectively. These coating windows correspond to the operating regimes originally described in experimental work by Chang et al.[107]

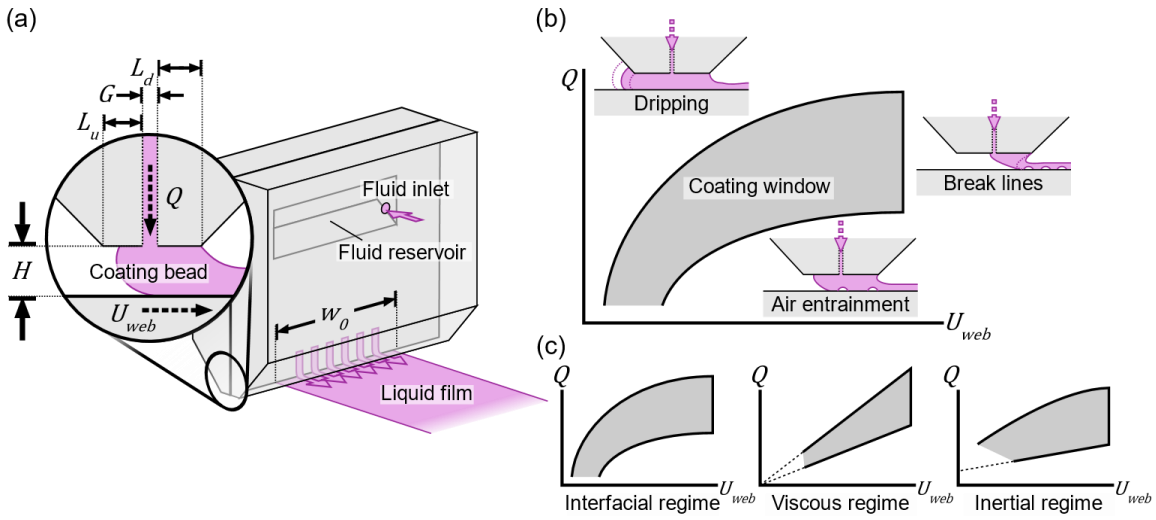

Figure 1.4 – (a) Geometry and process parameters of conventional slot die coating. (b) Defect onset in slot die coating described in terms of a viscocapillary coating window. (c) Representative coating window shapes for slot die processes across three operating regimes, adapted from [111].

1.3 State-of-the-Art for R2R Processing Capabilities

Surveys of established R2R deposition techniques[35-40, 56], can be used to evaluate process capability across several core areas related to patterning, materials, and scalability.

These three categories encompass the following essential questions for selection of the processing approach suitable for a given device:

1. Can the deposition technique process the material that composes the device?
2. Can the deposition technique deposit the requisite pattern features?
3. Is the deposition technique feasible for large-scale manufacturing, that can ultimately achieve a desired economy-of-scale?

While select techniques have exhibited superior performance in select aspects of each category, the challenge for large-scale manufacturing lies in achieving an affirmative answer for each of the three questions above. In many cases, no established method meets this standard, despite numerous published proofs-of-concept at the laboratory scale. The challenge for manufacturing, then, is to advance the state-of-the-art across multiple process performance metrics simultaneously. The remainder of this section provides a summary of each of the three categories – patterning capabilities, material selection, and scalability – reported in various studies within the past 10 years.

1.3.1 Feature Size Performance and Pattern Complexity

The pattern capability of R2R coating methods is summarized across several metrics in Table 1.1. Here, each method is described as suitable for arbitrary 2D patterns, limited to continuous stripes (1D), or unsuitable for patterning altogether (0D). Recent reviews of the state-of-the-art in R2R coating methods occasionally include an additional category for on-demand or digital patterning capabilities [37, 105], as exemplified by droplet-

based approaches as well as direct-ink writing[79, 114]. These methods offer the most direct and consolidated approach to pattern printing, with dramatic and well-established benefits to design optimization and customizability. The on-demand patterning capability of these methods is compared in Table 1.1 to the template requirements of the remaining methods. In this regard, the most demanding are those methods that provide no inherent patterning capability of their own, effectively requiring additional processing steps such as selective pre-treatment of the substrate[115-120] or subtractive techniques such as laser ablation[121-123] and localized dissolution[124]. For each of these methods, the pattern template requirements imply significant additional tooling and complexity for each additional pattern produced. The fabrication, cleaning, and re-use of pattern templates may be cost-prohibitive for some applications. Similarly, the need for tooling tailored to each individual pattern, and potentially optimized for specific coating materials, places a significant limitation on the customizability of these processes.

Resolution is frequently evaluated as the smallest feature size that can be deposited. The pattern feature of choice must be sufficiently simple for straightforward comparison. Printed lines are a popular choice for this purpose, although patches and dot arrays are also considered[98]. The resolution aspect of patterning is closely tied to the physical mechanism that mediates pattern formation. For direct ink writing, wherein the deposition mechanism is a liquid bridge that forms between the tool outlet and substrate, feature sizes approaching 10 μm are routinely possible provided only one liquid bridge is established at time and there is no coalescence of multiple liquid bridges.

Screen-printing, gravure, and flexography also involve deposition through liquid bridges, although they predominately involve stretching and separation of the liquid bridge whereas slot die coating involves continuous shear. At the extreme end of the resolution spectrum, aerosol, inkjet, and particularly e-jet printing have proven reliable for complex feature sizes smaller than 1 μm[125-127]. Since jet-based approaches deposit fluid through droplets and threads, rather than liquid bridges, the limiting phenomena for their feature size are the dynamics of droplet pinch-off, impact, and coalescence[102, 128-131]. Additionally, the potential for nozzle clogging due to spot curing and material build-up presents a practical limitation for droplet-based methods as well as spray coating. For inkjet, aerosol and e-jet, nozzle clogging effectively limits the minimum nozzle diameter that can be used dependably, and thus the minimum feature size that can be produced[93, 96].

Table 1.1 – Patterning capabilities compared across established coating and printing methods.

Method	Complexity [a]	Template	Resolution (μm)
Spray coating	0D	Mask/axillary process	N/A
Curtain coating	0D	Mask/axillary process	N/A
Slide coating	0D	Mask/axillary process	N/A
Slot die	**1D**	**Meniscus guides**	**1,000**[132-135]
Screen printing	2D	Mask	30-100[85, 125, 136-138]
Stencil printing	2D	Mask	5-30[84, 85]
Gravure	2D	Master	10-50[125, 139, 140]

Table 1.1 continued

Flexography	2D	Master	20-100[125, 141-144]
Direct ink writing	2D	None	10-1,000[125]
Inkjet	2D	None	10-50[67, 72, 95, 125, 145]
Aerosol	2D	None	10-50[72, 98, 146, 147]
E-jet printing	2D	None	0.5-2[72, 125, 148]

[a] Pattern complexity is categorized as none (0D), continuous stripes (1D), and arbitrary 2D regions (2D).

1.3.2 Material Requirements

The range of ink viscosity (μ) that can be processed constitutes one of the primary restrictions on material formulation for the various printing methods in Table 1.2. As with feature size, this constraint is closely tied to the physical mechanism that mediates pattern generation. In the case of droplet-based methods such as inkjet, the necessity of rapid periodic expulsion of ink from the print head and droplet pinch-off effectively limits ink viscosity to the range of 50 cP or lower [37, 125, 149]. This is a relatively restrictive range compared to other methods such as gravure printing and flexography, which are suitable for viscosities roughly as high as 1,000 cP[37, 125, 127]. At the medium-to-high range of viscosity, screen printing and stencil printing are suitable for pastes between 1,000 cP and 100,000 cP[37, 84, 125, 127], while slot die coating spans virtually the entire range of all other methods[37].

Wetting behavior is another important consideration for the various printing and coating techniques. This aspect of material selection encompasses surface tension (γ) of the coating fluid in the surrounding atmosphere, as well as advancing (θ_a) and receding contact angles (θ_r) on both substrate and coating tool surfaces. The primary restriction on these parameters is post-deposition stability of the wet film, which is simple to verify and largely independent of deposition method. On the other hand, the role of wetting is highly influential in process behavior. Furthermore, since surface tension and contact angle are sensitive to ambient conditions and potentially rate-dependent, extensive characterization efforts are required to understand and model this influence, as required for the slot die coating window discussed in Figure 1.4(b). On the other hand, a variety of workarounds are available to compensate for unfavorable wetting behavior in real-world manufacturing operations, such as spot-curing of a contact line in shear coating[150], substrate pre-treatments[71, 116, 118],or the application of a vacuum to position the upstream meniscus in slot die coating[151].

From an application standpoint, the considerations for viscosity and wetting constitute a process-imposed burden on the formulation of coating materials. The necessity of tuning and adjusting these properties for a given printing process diverts resources and expertise away from optimization for functional properties of the materials. The practical difficulties of material formulation will only continue to become more consequential as the range of available solution-processible materials continues to expand.

1.3.3 Operational Range and Scalability

The range of web speed (U_{web}) and wet film thickness (t_{wet}) achievable for a given manufacturing technique are the parameters most relevant to suitability for large-scale production. A comparison among the various methods in Table 1.2 shows excellent performance for slot die coating relative to the remaining methods, with significant restriction on throughput for screen and stencil printing, and on film thickness for gravure and flexography. Aerosol, inkjet and e-jet printing are the least impressive in this respect, largely constrained to web speeds below 10 m/min and thicknesses in the range of a few microns[37, 98, 125-127, 146]. Furthermore, it is also important to consider the width of coverage per tool pass for each of these methods. In this regard, droplet-based technologies are again the least impressive of the entire group. To achieve the feature size performance listed in Table 1.1 these techniques deposit across a correspondingly narrow width, which constrains their ability to deposit material across a wide area at high throughput. Other methods including screen and stencil printing, gravure and flexography, and slide, slot and curtain coating are all well-suited to single-pass deposition across the entire substrate width.

Table 1.2 – Process scalability and material requirements compared across established coating methods.

Method	Ink viscosity (cP)	Web speed (m/min)	Wet film thickness (μm)	Wide-area [a]
E-jet printing	1-10k[125]	<1[125]	0.001-0.1[125]	No
Aerosol	0.5-1,000[147]	<10[98, 127]	0.1-5[126, 146]	No
Inkjet	1-100[37, 125, 149]	<10[37, 98, 127]	0.1-5[125, 127]	No
Direct ink writing	<10-10,000[127]	<1[127]	5-100[125, 127]	No
Stencil printing	1,000-100,000[84, 127]	<10[127]	10-200[85, 127]	No
Screen printing	100-100,000[37, 125, 127]	50-150[37, 125, 127]	5-500[37, 125, 127]	Yes
Spray coating	10-1,000[37, 127]	<100[37, 127]	1-500[37, 127]	Yes
Gravure	<10-1,000[37, 125]	1-1,000[37, 125]	0.1-80[37, 125]	Yes
Flexography	<10-1,000[37, 127]	1-1,000[37, 125, 127]	0.5-200[37, 125, 127]	Yes
Curtain coating	<10-10,000[37]	10-1,000[37]	5-500[37]	Yes
Slide coating	<10-1,000[37]	1-1,000[37]	25-250[37]	Yes
Slot die (stripes)	**10-100,000**[37]	**1-1,000**[37]	**10-250**[37]	**Yes**

[a] Wide-area coating refers to single-pass coverage across a width several times greater than the average pattern feature size.

Comparing this assessment of scalability to the summary of feature size in Table 1.1, it is evident that a significant trade-off exists between throughput and pattern complexity. The core issue is that the precision and the coverage area of a given deposition technique are inherently challenging to reconcile. Reducing the minimum line width of a

print head, for example, implies a proportional reduction in the completion time for the overall pattern. This is true to some degree for each of the methods listed in Table 1.2. To address this fundamental conflict, the development of novel pattern coating techniques is required.

1.3.4 Emerging Slot Die Coating-Inspired Techniques

One strategy for advancing the state-of-the-art in R2R print manufacturing is to combine the inherent advantages of the aforementioned techniques with some additional innovative capability. Slot die, which offers an excellent outlook for scalability, is an appealing archetype on which to incorporate innovation. Several notable research efforts during the past two decades have endeavored to graft a complex additive-only patterning mechanism onto the traditional incarnation of slot die coating. The earliest of these involved the incorporation of a segmented internal slot geometry[152-154] to produce narrow continuous stripes. Subsequently, mechanisms for stop-start actuation of flow have been used to achieve quadrilateral patches[103, 133, 155, 156], and the curvature and width of slot-coated stripes have been manipulated by translating the coating tool and varying process inputs Q and U_{web} during process operation[154, 157].

Throughout these efforts, feature size performance has persisted as a practical challenge for slot die coating-inspired approaches. For slot die coating, the mechanism mediating pattern generation and thus resolution performance is the coating bead that forms between the tool outlet and substrate. In practice, the potential for translation of the

dynamic contact line and subsequent coalescence of adjacent coating beads makes it difficult to achieve features smaller than 1 mm[132-135]. Recent efforts have achieved stripes as narrow as 168 μm using a shim and meniscus guide with 150 μm-wide micro-tips[158, 159]. However, the potential for unwanted coalescence of adjacent coating beads has persisted as a practical restriction on feature size, by virtue of the trade-off between patterning resolution and process yield. Considering the variety of devices that can be fabricated as micro-stripe architectures, the 1 mm feature size limitation is consequential. The impact of a slot die coating-inspired approach for patterned coating depends strongly on the development of new strategies for overcoming this limitation.

1.4 Thesis Scope

1.4.1 Research Objectives and Key Questions

The **objective** of this work is to achieve printed features smaller than 50 μm using a slot die coating approach that integrates internal flow as a pattern-generating mechanism. This objective will be achieved through the design, characterization, modeling, and validation of **novel slot die coating-inspired techniques that advance the state-of-the-art** in deposition of high-resolution patterns across a wide area. The manufacturing techniques discussed in this thesis achieve a balance across three key aspects of process performance:

1. Pattern complexity and/or minimum feature size,
2. Restrictions and considerations for material formulation imposed by the processing method, and
3. Throughput and width coverage per coating tool pass.

In addressing these points, the discussions and analyses contained in this thesis specifically consider extensibility of the process across materials and pattern structures, consolidation of discrete processing steps, and requirements for process modeling and control. The following ***key questions*** are addressed through these research tasks:

1. What are the **physical mechanisms** that mediate pattern generation?
2. What **limits on pattern capability** are implied by the physical mechanisms identified above?
3. How do **process inputs and material properties** couple to pattern output?
4. What additional considerations for **material formulation** are imposed by the process?
5. Does the manufacturing approach offer a favorable balance of **novel capabilities** against added complexity and challenges?

The questions above have been selected on the basis of information most urgently needed to motivate continued development of these techniques beyond the present dissertation. For similar reasons, the work of this dissertation comprises demonstrations

with functional materials that are widely known and used within the printed device research community.

The ***impact*** of this work is to advance the suitability of print-based manufacturing for wide-area deposition at high resolution. Continued development and advancement of the slot die coating-inspired methods presented here will be facilitated based on the content of the chapters that follow. In addition, the operating principles, design guidelines, and process analyses presented here are designed to be readily extensible to future research efforts.

1.4.2 Organization of Thesis

The remainder of this thesis is organized as follows:

- **Chapter 2** provides a conceptual overview for two slot die coating-inspired techniques that provide an advantage to pattern capability over the conventional approach.
    - Coating/extrusion-on-demand (C/EOD) addresses the complexity of the coated pattern.
    - Heterogeneous stripe slot coating (HSSC) advances the allowable feature size and the number of materials that can be simultaneously coated across-web of the method.
- **Chapter 3** considers the process capability of C/EOD.
    - The coating bead is classified as a liquid bridge that mediates pattern output.

    - Wetting phenomena integral to the steady-state behavior of the coating bead are described.
    - An empirical model is developed to describe process control in C/EOD under steady-state conditions.
    - Complex patterning performance of C/EOD is discussed in the context of transient coating bead behavior.
- **Chapter 4** explores the fundamental principles of operation for HSSC implemented with a segmented slot geometry
    - Material formulation requirements for HSSC are developed on the basis of wetting and spreading of co-deposited fluids, with both analytical and experimental validation.
    - Electrically conductive polymer stripes are deposited with HSSC, with characterization of the resulting film structure and functional performance.
    - Process control over pattern morphology and film thickness is compared to C/EOD and conventional slot die coating of narrow stripes.
- **Chapter 5** describes the fluid mechanics of internal flow of a single fluid through an HSSC tool with a converging slot geometry.
    - The present work is compared to previous modeling efforts for similar microchannel and micro-slot geometries.

- A perturbation analysis is developed which characterizes the magnitude and range of influence for boundary layers that develop along the side-channels of the converging slot.

- **Chapter 6** describes the fluid mechanics of hydrodynamic focusing of two fluids in an HSSC tool, with experimental demonstration of the resulting feature size performance.
  - The perturbation analysis from the single-fluid case is extended to co-laminar flow of two fluids to generate an alternating-stripe pattern. This provides a predictive capability for patterned outflow from the HSSC tool.
  - Internal flow through a converging HSSC slot is investigated using aqueous polymer solutions across a range of viscosity. Experimental measurements of pattern morphology are compared to the model results across various slot geometry and flow rates.
  - Metallic nanoparticle inks are deposited on a commercial pilot-scale R2R system, with concurrent demonstrations of process scale-up and significant feature size performance improvement.
- **Chapter 7** summarizes the key findings of this dissertation in context of the objectives and fundamental questions.
- **Chapter 8** summarizes the key contributions and this work and provides recommendations for future study.

CHAPTER 2. PROCESS AND EXPERIMENTAL FACILITY

2.1 Introduction

The first section of this chapter describes two novel slot die-inspired patterning techniques used to achieve the objectives of the present dissertation. These techniques are the coating/extrusion-on-demand (C/EOD) approach, which deposits complex patterns from a single coating material, and heterogeneous stripe slot coating (HSSC), which deposits continuous narrow stripes alternating between multiple materials. The discussion that follows develops the tooling and operating principles for two implementations of each method, each with distinct features and advantages. The facility used for experimental demonstration and characterization of these techniques are subsequently described in Section 2.3. Finally, the coating materials selected for experimental investigations in Chapters 3-6 of this thesis are described in Section 2.4. Explanations are given for the relevance of the selected materials to the fields of coatings research and printed devices in Section 2.4.1. Physical properties of the coating materials that are relevant to the coating process are provided in Section 2.4.2 alongside explanation of the procedures for their characterization.

2.2 Novel Slot Die Coating-Inspired Patterning Strategies

As previously described, slot die coating is traditionally conducted using a single fluid that flows between two parallel plates offset by a shim, with limited patterning capability. Taking inspiration from this traditional approach, an innovative set of slot die-

inspired techniques that allow for implementing various patterns, flow behaviors and/or coating multiple fluids is discussed here. Figure 2.1 provides an overview of these patterning strategies. The process classification tree extends only as far as the scope of the present work, including C/EOD using both multi-inlet flow (MIF) and pin-actuated flow (PAF) control and HSSC with and without hydrodynamic focusing of the patterned coating flow. Other slot-die inspired patterning mechanisms are possible, and a few have been reported in recent works by other authors[157, 158]. Details for the approaches of interests in this work, as shown in Figure 2.1, are provided in the sub-sections that follow.

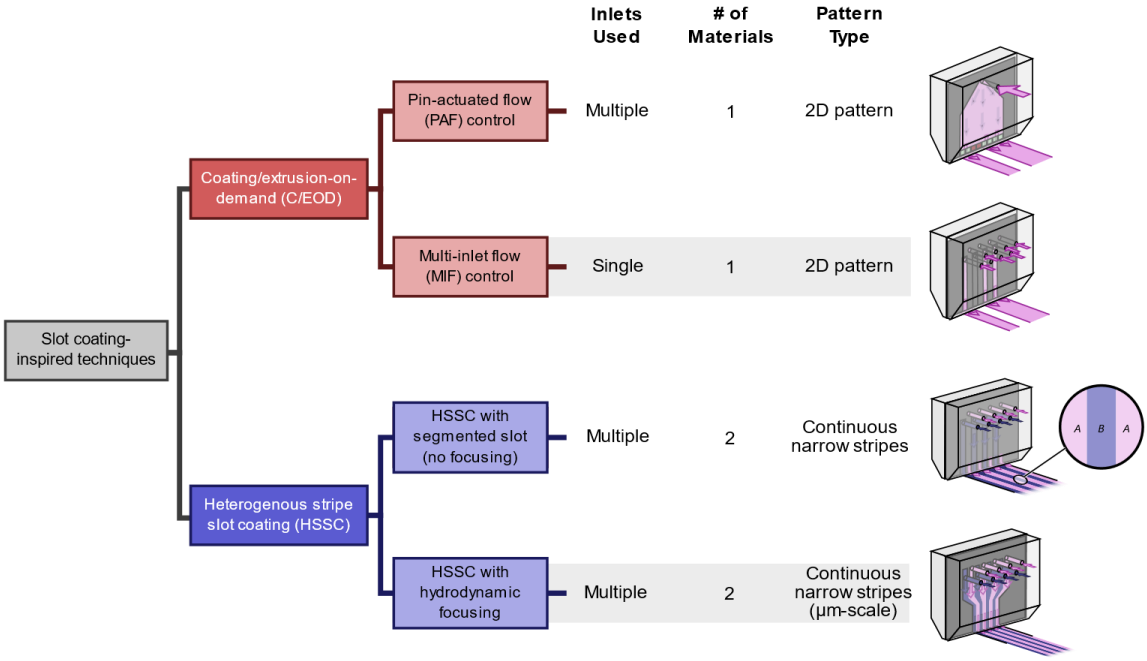

Figure 2.1 – Classification tree of slot die coating-inspired patterning strategies used in this work, with the required hardware for each strategy tabulated to the right.

2.2.1 Coating/Extrusion-on-Demand (C/EOD) Approach

The coating/extrusion-on-demand (C/EOD) method of patterned slot die coating, illustrated in Figure 2.2, is a general-purpose approach for deposition of arbitrary two-dimensional patterns. Here, a single fluid is selectively transferred to the substrate through a series of discrete localized outflow regions (DLORs). As illustrated in Figure 2.2(a), the flow rate and actuation timing of each DLOR generates the desired outflow. Two implementations of the requisite on/off flow control are considered multi-inlet flow (MIF) and pin-actuated flow (PAF) control. The PAF control scheme, illustrated in Figure 2.2(b), utilizes one wide slot in conjunction with additional external hardware (e.g., pins and actuators) that implement a variable tool outlet geometry. The additional hardware consists of an array of individually actuated pins located along the base of one die half, on the side immediately upstream from the deposition region. The MIF control scheme, illustrated in Figure 2.2(c), features a segmented shim, which defines flow channels leading to DLORs. For MIF, coating fluid enters the tool through up to eight separate inlets and is deposited through one or more coating beads that form between the tool outlet and substrate. Both the number of coating beads and the number of fluid inlets required are variable and depend on the shim configuration in use. Whereas the additional tooling required for PAF control must be designed to fit within a small physical space near the coating tool outlet, MIF control can be decoupled from the coating tool entirely.

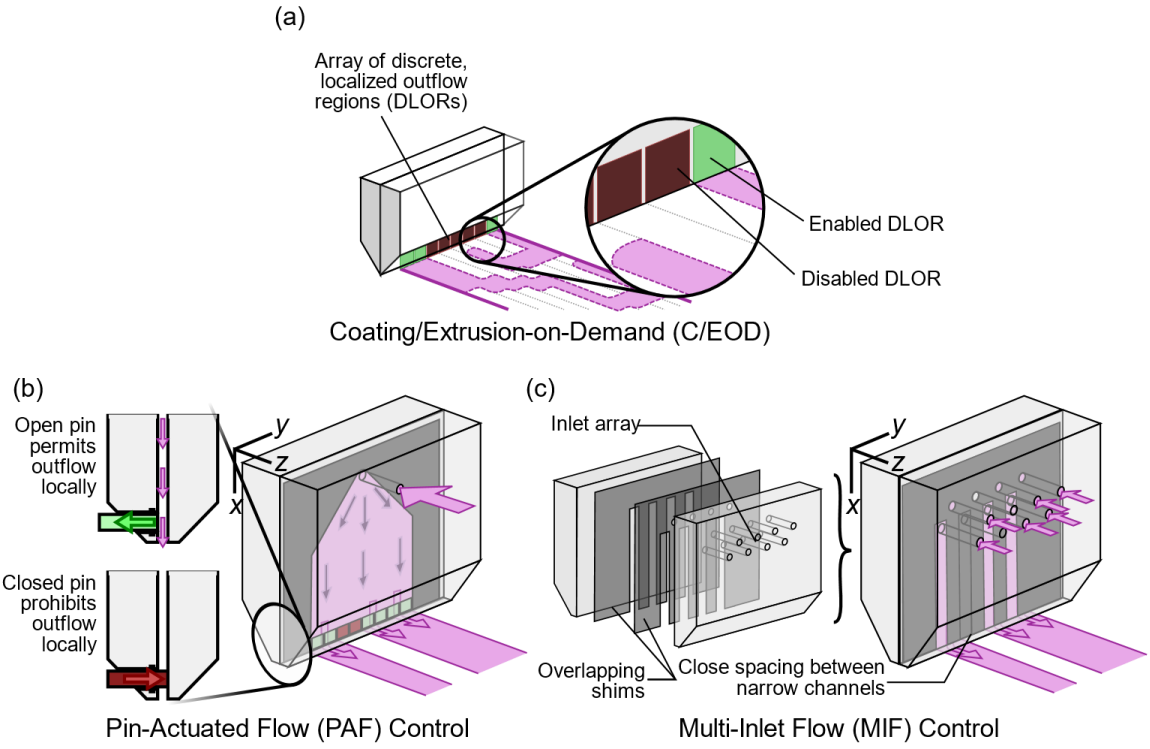

Figure 2.2 – (a) In C/EOD coating, flow is permitted at enabled DLORs (light squares) and prohibited at disabled DLORs (dark squares) in sequence to produce arbitrary 2D patterns. (b) The PAF control scheme and (c) MIF control schemes illustrated.

2.2.2 Heterogeneous Stripe Slot Coating (HSSC)

The segmented shim configuration introduced in Figure 2.2(b) can also be used for co-deposition of multiple coating materials as continuous alternating stripes. For simplification, only two materials are considered in this work. As illustrated schematically in Figure 2.3(a), a heterogeneous alternating-stripe pattern is produced when two liquid phases are fed into alternating inlets of the HSSC tool, under the same principles previously mentioned. Figure 2.3(b) shows deposition flow viewed from beneath the coating tool as horizontally stratified narrow stripes.

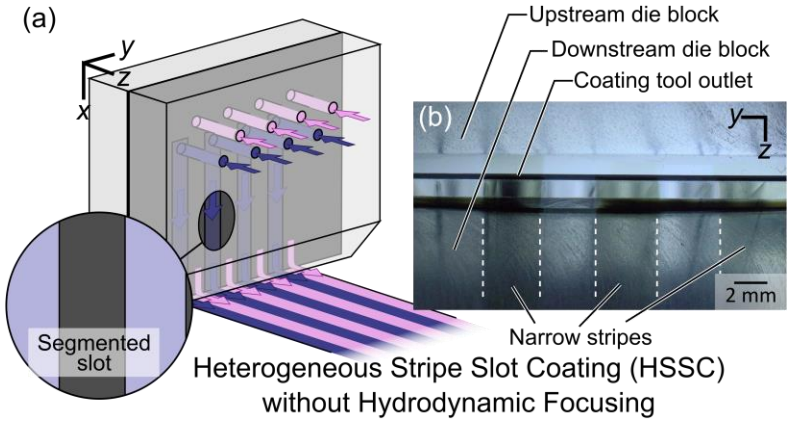

Figure 2.3 – (a) HSSC tool configuration and (b) the resulting heterogeneous stripe pattern comprising two or more materials. Stripe boundaries are highlighted by dashed lines.

Co-deposition of two coating fluids to form an alternating stripe pattern can be combined with hydrodynamic focusing, a phenomenon routinely exploited in microfluidic applications[160-164], to achieve significantly smaller feature sizes. Similar converging features have also been described in patent literature for extrusion of viscous slurries[165]. Here, flow within the coating tool is co-laminar rather than physically segmented, as illustrated in Figure 2.4. The internal cavity comprises an array of inlet channels leading to one wide slot, followed by a contraction in slot width that produces a proportional narrowing of each stripe region. The inset in Figure 2.4 shows the shape of the internal cavity of the coating tool, which narrows from an initial upstream width (w_u) to a final downstream width (w_d) immediately preceding outflow. The hydrodynamic focusing mechanism enables the deposition of pattern features orders of magnitudes smaller than the width of the coating tool cavity. This offers a potentially significant improvement over previous tool designs[37, 152], where the minimum achievable center-to-center distance of the

narrow stripe pattern is limited by the precision of coating tool during fabrication and assembly.

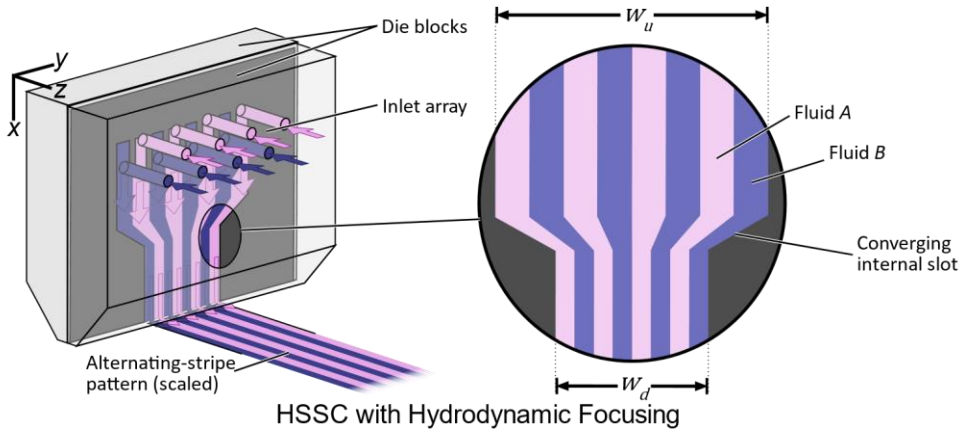

Figure 2.4 – The HSSC tool configured to generate a scaled alternating-stripe pattern with interaction between the coating fluids within the tool.

2.3 Roll-to-Roll Imaging System (R2RIS)

Observation of the pattern coating process is conducted on the custom roll-to-roll imaging system (R2RIS) illustrated schematically in Figure 2.5. Several configurations of coating tools, fluid inputs, and imaging hardware are used to accommodate the scale and location of fluid phenomena. Flow rate is controlled by up to two Chemyx Fusion 200 syringe pumps shown in Figure 2.5(b), or pressurized reservoir, shown in Figure 2.5(c). For simultaneous coating of multiple liquids, a manifold with separate distribution chambers for each fluid species, illustrated in Figure 2.5(d), is incorporated into the feed line. The HSSC tool, in particular, can be oriented flat on its side as shown in Figure 2.5(e) for observation of internal flow or upright as shown in Figure 2.5(f) for observation of the liquid bridge and film pattern immediately downstream from the coating tool outlet, as

done with the C/EOD coating tools. The transparent platen is constructed from a plate of cast borosilicate glass. A digital camera (Thorlabs DCC324) and 25 mm fixed-focal length lens (Edmond Optics 59-871) are used for wide-area image acquisition at a resolution of 1280-by-1024 pixels, with a pixel width of 21.6 μm.

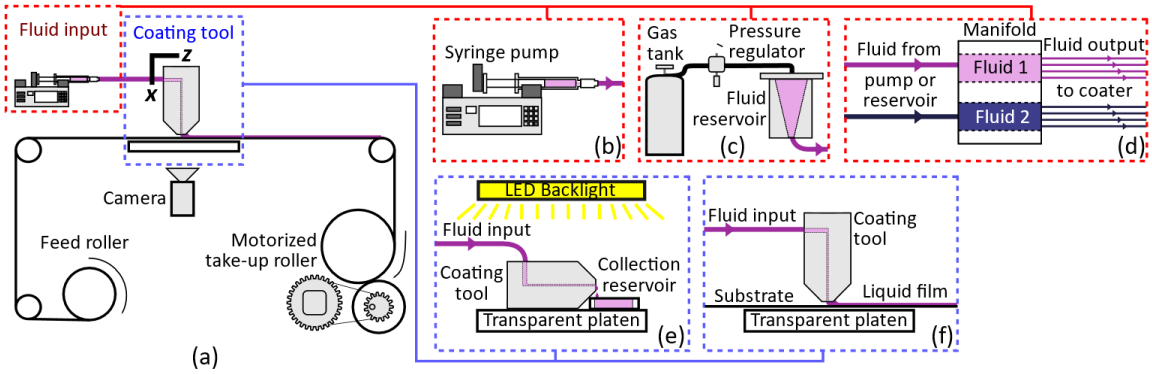

Figure 2.5 – (a) The RFIS configured for imaging of a film pattern during processing. (b)-(d) Configurations for of flow rate control. (e)-(f) Possible orientations of the C/EOD and HSSC tools.

The physical apparatus of the R2RIS is shown in Figure 2.6. In-process image acquisition is carried out using a custom LabView program, which automatically logs relevant process parameters such as flow rate (Q), substrate velocity (U_{web}), and coating gap (H) for each collected image. The user interface for the data acquisition program is shown in Figure 2.6(b). Additionally, pattern feature measurements are carried out using the MATLAB image processing toolbox to minimize human error. An example of imaging output from the R2RIS is shown in Figure 2.6(c).

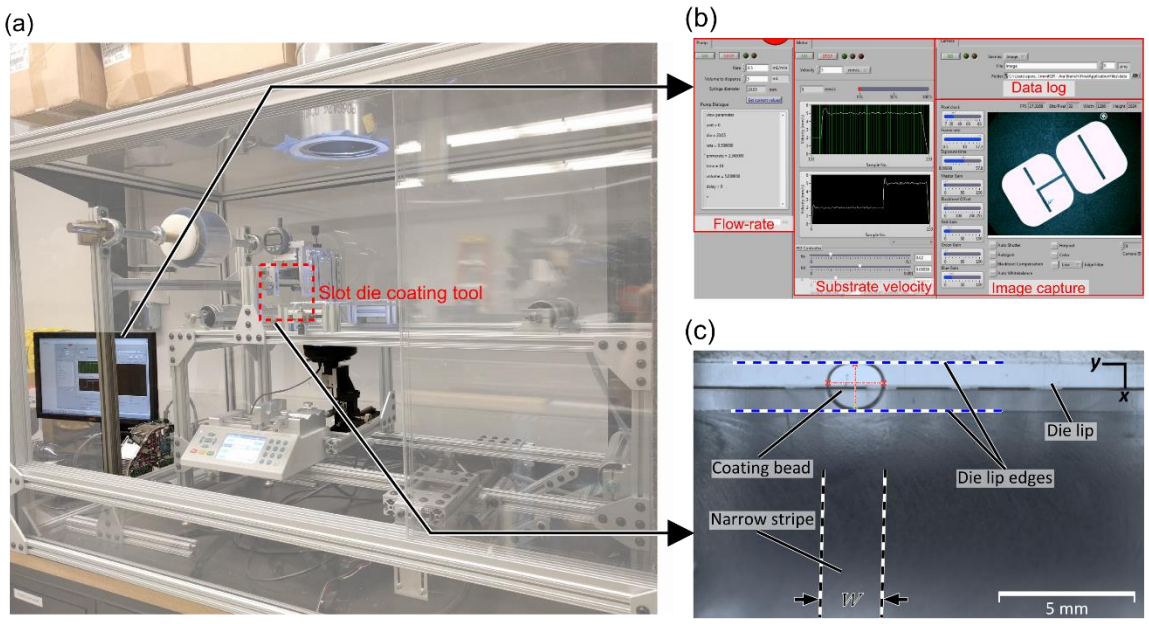

Figure 2.6 – (a) An image of the R2RIS physical apparatus, (b) graphical user interface for the image acquisition and data logging, and (c) example of image output overlaid with annotations to highlight the geometry of the slot die hardware and coating bead.

2.4 Materials

2.4.1 Materials Selection

Aqueous polyvinyl alcohol (PVA), Mowiol® 4-88 purchased from Sigma Aldrich Corp. is used as a model material for the majority of experimental process characterizations. PVA is a safe and widely available polymer that permits a range of coating viscosities across various concentrations. In this work, aqueous PVA solutions are prepared by continuous stirring for 30 minutes at 60°C in deionized water.

Several functional materials are also considered in this work. Poly(3,4-ethylenedioxythiophene):polystyrene sulfonate (PEDOT-PSS), Clevios ™ PH-1000,

purchased from Heraeus GmbH in 1.0-1.3 wt.% aqueous dispersion, and Metalon® JS-A102A, a 40 wt.% aqueous silver nanoparticle (Ag-NP) ink provided by NCC Nano, LLC (dba NovaCentrix), are the conductive inks selected for demonstrations of functional materials. PEDOT:PSS and Ag-NP are both widely used and representative of commercially available functional materials used in flexible and organic electronic devices, among others. As they appear in this work, both functional inks are co-deposited with a support material, either aqueous PVA or a proprietary aqueous polyvinylpyrrolidone (PVP) prepared in 30 wt.% solution with added surfactant provided by NovaCentrix.

Additional materials are considered within the scope of Section 4.2.2.1, which discusses the role of interfacial tension on post-deposition pattern stability. These materials are PVA prepared in 24 wt.% aqueous solution, glycerol purchased from Sigma Aldrich Corp. and prepared in 95 wt.% solution, polydimethylsiloxane (PDMS), Dow Corning 200® fluid purchased from Sigma-Aldrich Co., and vacuum pump oil (VPO), L340 purchased from Virginia KMP Corporation.

Polyethelene terephthalate (PET) film with a nominal thickness of 100 µm, ES301400 purchased from Goodfellow Cambridge Ltd., is used as the substrate for majority of the deposition studies in this thesis. In other sections, Ag-NP ink and PVP solution are co-deposited on silica-coated PET substrate to prevent post-deposition dewetting of the substrate. The slot die coating tools used in experiments are all fabricated

out of polymethyl methacrylate (PMMA), cast acrylic plate purchased from McMaster-Carr Supply Co.

2.4.2 Material Properties

Viscosity and density at 25 °C for the materials previously described are organized in Table 2.1. References are provided where physical properties have been obtained from existing literature. Viscosity (μ) of aqueous PEDOT:PSS is measured with a Cannon-Fenske viscometer tube, and all remaining viscosity values not taken from literature are obtained using an Anton-Paar Physica MCR-301 rheometer with a 50 mm parallel plate diameter and 0.1 mm plate gap. Aqueous PVA solutions have been shown in previous work[166] to exhibit approximately constant viscosity at shear rates of 10 s^{-1} and below, while for the remaining coating materials, shear rate independence below 100 s^{-1} are confirmed by experimental measurements.

Table 2.1 **– Viscosity and density of select coating materials at 25 °C. Uncertainty bounds, where provided, represent the full range of collected data.**

Material	**μ (cP)**	**ρ (g cm^{-3})**
PVA, 10 wt.%	26[167]	1.02[167]
PVA, 15 wt.%	109[167]	1.04[167]
PVA, 20 wt.%	392[167]	1.05[167]
PEDOT:PSS, 1.0-1.3 wt.%	29	1.01

Table 2.1 **continued**

PVP, 30 wt.% + surfactant [a]	75 ± 1.7	1.03
Ag-NP ink, 40 wt.% [a]	11 ± 0.7	1.6

Advancing contact angle (θ_a), receding contact angle (θ_r) and surface tension (γ) are measured using a model 500-U1 Ramé-Hart goniometer at 25 °C and 46-52% relative humidity. These wetting properties are organized in Table 2.2 for the same coating materials that appear in Table **2.1**. It should be noted that since these experiments are not conducted in a saturated atmosphere, evaporation effects may be significant. Thus, these contact angles and surface tension measurements are not necessarily reflective of inherent wetting properties of the fluid-solid system isolated from evaporation, but rather observed behavior for the same ambient conditions under which the coating experiments are conducted. For surface tension measurements of single fluids, the pendant drop method is used with disposable polytetrafluoroethylene (PTFE) syringe tips as the solid phase. Contact angles are measured using the sessile drop method described in previous literature[168-170]. Here, θ_a is measured following incremental addition of fluid to the sessile drop through an embedded syringe as the contact line of the droplet advances. Subsequently, fluid is removed from the droplet through the syringe until the contact line begins to recede, and θ_r is measured following incremental volume removal. The total period is 30 s for each measurement of θ_a and θ_r, and fluid addition and removal are carried

out at a rate of 0.166 μL/s. Contact angle characterizations are carried out both on PMMA, the slot die material, and on PET film. For the PVP and Ag-NP solutions, contact angle measurements are made on silica-coated PET substrate. For all other coating solutions, plain untreated PET is used.

For cases of apparent contact line pinning, such that no measurable receding movement of the contact line occurs, θ_r is recorded as 0 in Table 2.2. This follows the convention used in previous wetting studies[171-174] where complete pinning denotes the case where the contact line remains pinned even as θ_r reduces to zero. It should be noted that by this definition, $\theta_r = 0$ implies that dewetting does not occur since the contact line does not recede. Examining the recorded contact angle values organized in Table 2.2, the apparent pinning of receding contact lines for most materials is notable. Similar results have previously been reported for aqueous PVP and various surfactant solutions on both PMMA and PET[175], and for aqueous PVA on hydrophilic substrates[64]. Pinning of the receding contact line was also verified for 10 wt.% PVA solution on PET substrate in saturated atmosphere by repeating the contact angle measurement in an enclosed Ramé-Hart environmental chamber.

Ag-NP ink droplets on silica-coated PET film exhibit apparent pinning alternating with abrupt slippage for the advancing contact line, as well as apparent pinning of the receding contact line. This behavior is consistent with wetting transitions described in previous work for highly texturized hydrophilic surfaces[176-178]. These previous studies have

shown that sufficiently large contact angle hysteresis prevents dewetting even though advancing contact angles may be large or even in excess of 90°. Effectively, the propensity of both advancing and receding contact lines to become pinned facilitates the stability of printed Ag-NP pattern features on the silica-coated PET surface.

Table 2.2 – Wetting properties of select coating materials at 25 °C and 48 ±2% relative humidity. Uncertainty bounds, where provided, represent the full range of collected data.

Material	ρ	θ on PET		θ on PMMA	
	(g cm^{-3})	θ_a (°)	θ_r (°) [d]	θ_a (°)	θ_r (°) [d]
PVA, 10 wt.%	1.02[167]	56 ± 1.2 [b]	0 [b]	59 ± 2.7	0
PVA, 15 wt.%	1.04[167]	58 ± 2.2 [b]	0 [b]	62 ± 2.4	0
PVA, 20 wt.%	1.05[167]	60 ± 1.3 [b]	0 [b]	65 ± 1.8	0
PEDOT:PSS, 1.0-1.3 wt.%	1.01	81.4 ± 0.6 [b]	41.9 ± 4.4 [b]	--	--
PVP, 30 wt.% + surfactant [a]	1.03	30.8 ± 8.1 [c]	0 [c]	56 ± 5.4	0
Ag-NP ink, 40 wt.% [a]	1.6	99.2 ± 7.4 [c]	0 [c]	59 ± 2.7	39 ± 4.3

[a] Proprietary formulation provided by NovaCentrix.
[b] Contact angle measurements on plain untreated PET.
[c] Contact angle measurements on proprietary silica-coated PET provided by NovaCentrix.
[d] A value of 0 for θ_r denotes apparent pinning of the receding contact line on the solid phase.

The results of interfacial tension measurements conducted for pairs of liquids that appear in Section 4.2.2.1 are organized in Table 2.3. Here, the liquid-liquid interfacial

tension (γ_{AB}) is presented alongside surface tension of materials *A* (γ_A) and *B* (γ_B). Measurements are conducted using the pendant drop method, with the outer liquid phase contained in a Ramé-Hart quartz cell for γ_{AB} and ambient atmosphere at 25 °C and 46-52% relative humidity used as the outer phase for γ_A and γ_B.

Table 2.3 – Interfacial tension measurements of several pairs of fluids at 25 °C. Uncertainty bounds, where provided, represent the full range of collected data.

Material A	Material B	γ_A (mN m^{-1})	γ_B (mN m^{-1})	γ_{AB} (mN m^{-1})
PVA, 24 wt.%	PDMS	41.2 ± 0.2	20.3 ± 2.5	5.3 ± 0.7
PVA, 24 wt.%	VPO	41.2 ± 0.2	31.4 ± 0.9	8.2 ± 0.5
Glycerol, 95 wt.%	VPO	63.5 ± 1.0	31.4 ± 0.9	9.1 ± 0.9

Based on the measured properties summarized in Table 2.2, it is evident that the selected materials will generally wet the selected substrates and not undergo dewetting once deposited. The sole possible exception to this is the PEDOT:PSS ink, which appears in experimental investigations in Section 4.5.2, and is discussed further in terms of wetting behavior in Section 4.5.3. The interfacial measurements in Table 2.3 for three representative pairs of immiscible liquids show significantly lower interfacial tension at the surface of liquid-liquid contact ($\boldsymbol{\gamma_{AB}}$) compared to the surface tension of either fluid ($\boldsymbol{\gamma_A}$, $\boldsymbol{\gamma_B}$). The significance of this point in the context of slot die coating-inspired patterning techniques is discussed in Section 4.2.2.1.

2.5 Conclusions

This chapter has provided a conceptual overview of new slot die coating-inspired techniques to deposit patterned coatings. Two implementations have been provided for C/EOD, which enables deposition of complex patterns across a wide area. The pin-actuated flow (PAF) control implementation relies on physical hardware near the coating tool outlet, while multi-inlet flow (MIF) control relies on multiple inlets with flow actuation de-coupled from the coating tool entirely. The HSSC approach, which produces continuous narrow stripes, has also been introduced for two separate embodiments. One implementation of HSSC relies on a segmented slot geometry similar to C/EOD with MIF control. The second implementation relies on co-laminar flow of two materials, such that the entire pattern can be scaled to achieve printed feature sizes smaller than the overall width of the internal slot die channel.

Coating materials have been selected for the experimental evaluation of C/EOD and HSSC in subsequent chapters. Two nonhazardous polymers, PVA and PVP, can be prepared in aqueous solution across a range of viscosity in order to probe the behavior the slot die coating-inspired techniques. Additionally, commercially available conductive inks based on PEDOT:PSS and silver nanoparticles have been selected on the basis of their relevance to printed device manufacturing. Substrate materials have been selected for each of these materials to ensure that dewetting of patterned wet films will not occur following deposition. Experimental investigations in the chapters that follow are designed to

incorporate the material systems discussed above to evaluate the process capability of C/EOD and HSSC.

CHAPTER 3. LIQUID BRIDGE-MEDIATED PATTERNING CAPABILITIES OF COATING/EXTRUSION-ON-DEMAND (C/EOD)

3.1 Introduction

This chapter considers the patterning capabilities of coating/extrusion-on-demand (C/EOD) in the context of wetting and spreading behavior at the coating tool outlet. Here, the wet film is deposited through a liquid bridge that forms between the coating tool outlet and the substrate, known colloquially as the coating bead. Flow through the liquid bridge is the physical mechanism that mediates between process inputs and pattern output for C/EOD, as in conventional slot die coating across a wide area. The experimental efforts in this chapter place special emphasis on steady state configurations of the coating bead, which correspond to deposition of continuous narrow stripes as a representative pattern feature. The coupling between process inputs and stripe width provides an assessment of the achievable pattern resolution as well as its sensitivity parameters that dictate process behavior.

The first section of this chapter identifies the basic features of the coating beads in C/EOD with comparison to conventional slot die coating. Relevant observations from recent fundamental studies of liquid bridge phenomena are used to develop a preliminary understanding of the coating bead geometry. Next, in Section 3.3, spreading and

confinement of the narrow coating bead along the underside of the C/EOD tool is discussed. In-process imaging of flow emanating from a slot die configured for narrow stripe coating are used to illustrate the relevance of these behaviors to the output from the C/EOD tool, as described in Section 3.3.2. In Section 3.3.3, these observations are used to inform an empirical mapping between steady state process inputs and the resulting narrow stripe width, which addresses simple but consequential shortcomings in previous studies on similar coating phenomena.

Finally, complex patterning capabilities of C/EOD are considered in Section 3.4 with respect to localized flow actuation and non-steady coating bead phenomena. First, periodic breakup of the coating bead resulting in intermittent stripe features are considered in the context of C/EOD patterning. For this discussion, the two flow actuation schemes illustrated in Figure 2.2(b) and (c) are evaluated experimentally for a model coating fluid in Section 3.4.2. Next, the interaction of two adjacent coating beads is demonstrated and discussed in Section 3.4.3. Whereas this phenomenon has been rightfully treated as a pattern defect for deposition of continuous stripes[158], the discussion here also considers it as a potential patterning mechanism when using C/EOD. Finally, a brief explanation of observed processing defects in C/EOD is provided in Section 3.5.

3.2 Background on Narrow Coating Beads

3.2.1 Comparison to Slot Coating across Wide Area

In conventional sot die coating, the coating bead is sufficiently wide to be treated as a two-dimensional steady structure[104, 109-112] as illustrated in Figure 3.1(a). The only parameter of interest related to the geometry of the wet film is its average wet thickness (t_{wet}), which is easily determined by continuity as follows:

$$t_{wet} = \frac{Q}{U_{web}w} \tag{3.1}$$

In this case, flow rate (Q) and substrate speed (U_{web}) are controlled directly, and the width of the coated region (w) is known from the width of the slot (w_0). This assumption is valid if Q and U_{web} are within the coating window introduced in Section 1.2.3 and illustrated in Figure 3.1(b). Lateral spreading of the coating bead beyond the width of the outlet denotes the dripping boundary at the top of the coating window, while air entrainment and break line defects develop at the remaining coating window boundaries, when the substrate speed is excessively high compared to the flow rate. The rightmost boundary of the coating window is also referred to as the low-flow limit, since it corresponds to the minimum wet film thickness that can be achieved without the introduction of defects into the wet film[111].

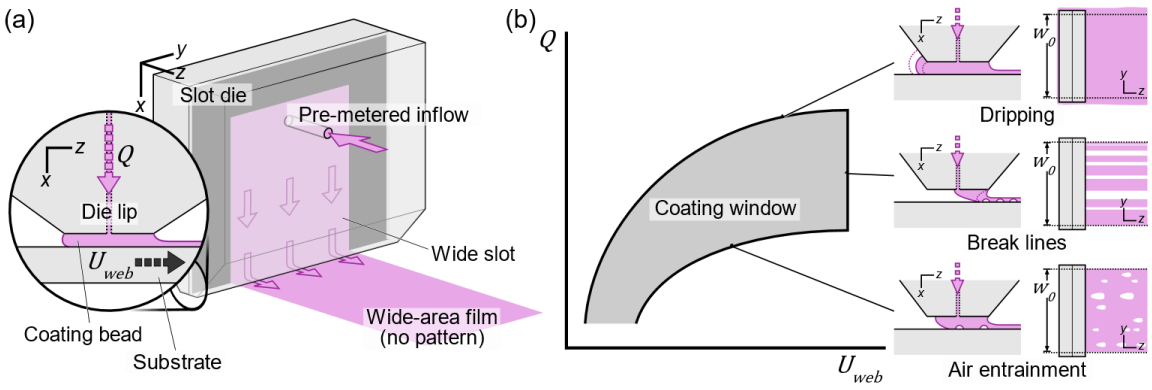

Figure 3.1 – (a) Isometric view of the a slot die coater configured for deposition of a single wide region. (b) Illustrations of defects at coating window boundaries for a conventional slot die process.

For small feature sizes and complex patterns fabricated using C/EOD, the coating beads required are significantly more narrow (2 mm or less) than in the case of conventional slot die coating (typically in excess of 50 mm), as illustrated in Figure 3.2(a). This has several implications. First, the narrow coating bead cannot be treated as two-dimensional. The lateral edges of the narrow coating bead are influential across a significant portion of the domain of interest, whereas for conventional slot die coating, the majority of the coating bead is sufficiently far from the edges to ignore their effect. Because the width of the liquid bridge (along the *y*-axis) is comparable to its length (along the *z*-axis), spreading of the coating bead along the surface of the die lip occurs in significant measure along both axes. Figure 3.2(b) illustrates how this corresponds to operation outside of the conventional slot die coating window. Denoting w_0 as the fixed outlet width, changes in flow rate and substrate velocity will have a significant impact on *w*, the width of each of the coated stripes. At the dripping boundary, the coating bead expands outward along the

y-axis and produces a stripe whose width exceeds w_0, due to the influx of extra fluid at higher flow rates. However, the coating bead remains stable. This phenomenon is similar to what is observed for conventional slot die coating, except that the extra fluid has space to spread beneath the die. Thus, this coating process is limited by coalescence of adjacent stripes rather than the traditional dripping defect[135, 154]. Similarly, beyond the conventional air entrainment boundary, extrusion flow from a sufficiently narrow slot produces a liquid bridge that is stable yet more narrow than w_0[154]. In these cases, the low-flow limit of the process corresponds to complete separation of the liquid bridge.

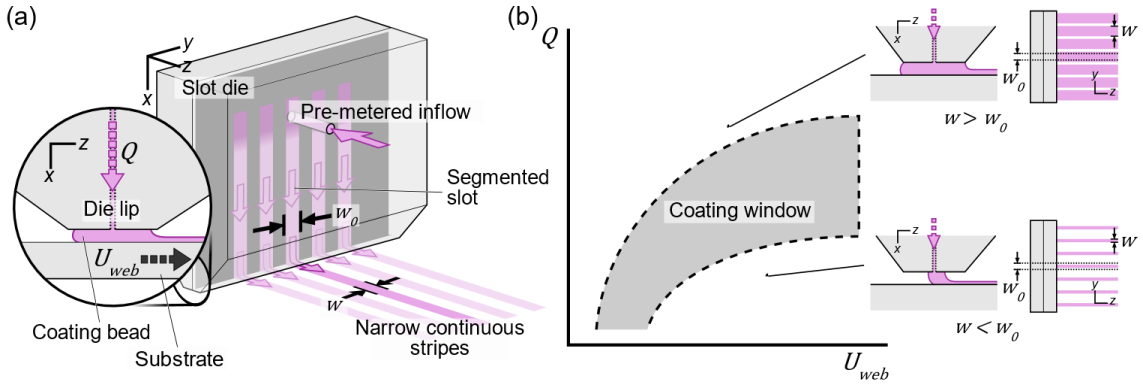

Figure 3.2 – (a) Isometric view of the slot die coater configured for deposition of multiple narrow stripes. (b) Illustrations of stable narrow stripes emanating from the slot die beyond the conventional coating window boundaries.

To develop a description of the C/EOD process, it is important to recognize that the coating window does not retain the same meaning as for conventional slot die coating of wide regions. As other authors have demonstrated previously for slot die coating of narrow regions[154], w varies continuously across a range of Q, U_{web}, and coating gap (H). Furthermore, since the width of the narrow coated region cannot be assumed from the outlet

width, w and t are co-dependent and functions of the process inputs. Thus, the need arises for a means to predict w as a function of parameters Q, U_{web}, and H as well as coating tool geometry and material properties.

3.2.2 Comparison to Fundamental Research on Liquid Bridges

The narrow coating bead in C/EOD is characterized by a continuous volume flux at the slot die outlet and downstream boundary, shearing translation of the substrate, and confinement along the sharp geometric features of the coating tool surface. These aspects have been considered previously in the context of 2D coating flows that emulate the region in the vicinity of a slot die lip[109, 112, 179, 180]. However, since the narrow stripes that occur in C/EOD cannot be approximated as 2D phenomena, it is helpful to refer to fundamental studies on liquid bridges. Although this body of literature focuses primarily on fixed-volume cases under extension and compression, they do address complex capillary confinement[181], shearing and rotation[182-184], and translation of unpinned contact lines[185-188] as isolated phenomena. These studies have also considered curvature of the liquid bridge surface[189-191] and conditions for its stability and breakup[192-194].

Many of these liquid bridge phenomena are conceptually similar to the behaviors of narrow slot coated stripes described in Section 3.2.1. Investigations on the evolution of unpinned contact lines frequently denote a contact radius[185, 195], such as that illustrated in Figure 3.3(a), at the interface between the capillary bridge and a solid surface. This geometric feature is comparable to the width of a narrow coating bead in C/EOD, and its

dependence on the separation distance between parallel plates that bound a liquid bridge is roughly analogous to the relationship between *w* and *H* in C/EOD. This relationship is illustrated in Figure 3.3(b) and (c), based on recent work by Chen, Amirfazli, and Tang[187] on the effect of contact angle hysteresis on the evolution of unpinned contact lines and eventual fluid transfer. Here, a capillary bridge is established upon contact between a pinned droplet and a bottom plate, and subsequently subjected to compression followed by extension or retraction of the top plate until breakup. The breakup event that occurs between Figure 3.3(b4) and Figure 3.3(b5) is comparable to separation of the narrow coating bead at the low-flow limit, and the contact radius at breakup is analogous to the minimum feature size achievable by C/EOD.

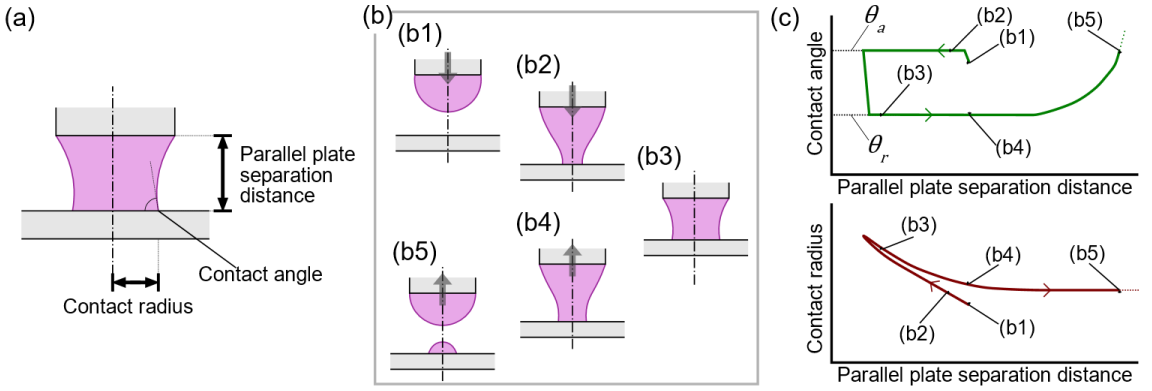

Figure 3.3 – (a) Geometry of a fixed-volume axisymmetric liquid bridge subject to stretching and compression, with pinned contact lines at the top solid surface. (b) Evolution of the capillary bridge shown in (a) due to compression as a top plate moves closer to a bottom plate before recessing. (b1) Stable pinned bead, (b2) initial contact of fluid with bottom plate followed by (b3) stretching of liquid bead followed by (b4) retraction of the liquid bead until (b5) breakup. (c) Contact angle and contact radius as a function of parallel plate separation distance for the flow behavior illustrated in (b), assuming nonzero contact angle hysteresis, based on work by Chen, Amirfazli, and Tang[186-188].

It should be noted that there have been several recent publications by Dodds, Carvalho and Kumar[182, 183, 196] that describe coating processes in terms of liquid bridge phenomena, with significant attention to 3D confinement effects along trapezoidal cavities and movement of unpinned contact lines. However, these efforts have been oriented towards transfer processes such as flexography and gravure printing. Thus, these studies have focused on the volume transfer ratio achieved by breakup of the liquid bridge under stretching, and have considered evolution of a fixed volume rather than continuous deposition through a standing capillary bridge. The significance of these efforts to the present problem is a recognition within the research community that liquid bridge behaviors are useful and appropriate for describing fluid transfer in patterned coating. Therefore, the discussions throughout the remainder of this chapter will also adopt terminology derived from liquid bridge research in the examination of narrow coating beads in C/EOD.

3.2.3 Previous Empirical Modeling Efforts for Narrow Stripe Coating

The literature outlined above has highlighted dynamic wetting, spreading, and confinement of contact lines on a 3D liquid bridge as the physical coupling between process inputs and stripe width in slot die coating of narrow stripes. The fluid properties related to these behaviors include the coating fluid viscosity (μ), surface tension (γ), and advancing (θ_a) and receding contact angles (θ_r) on both the tool surface and substrate. These properties are sensitive to ambient conditions and potentially rate dependent. Thus, it must be appreciated that any analytical or numerical model will depend on substantial

material characterization. Furthermore, application of those properties to a physical experimental setup also presents a substantial challenge.

For these reasons, it has proven most realistic in recent studies to explore process behavior through empirical correlations. The most recent and comprehensive of these efforts was conducted by Lin et al., who observed that stripe width correlates positively with Q and negatively with U_{web} and H[154]. The relationship between w, Q, and U_{web} discussed by Lin et al. reflects the coupling between stripe width and the size of the coating bead, which increases in tandem with the amount of fluid deposited per unit length of substrate. Additionally, the relationship between w and H observed by Lin et al. is conceptually similar to the relationship between contact radius and separation distance for a capillary bridge located between two plates[186, 188]. Despite the intuitive explanations for correlations between individual parameters, however, a practical approach for characterizing the combined influence of process parameters Q, U_{web}, and H is not as straightforward. Lin et al. ultimately relied on a set of dimensionless groups, which could account for majority of the variation in the data, on the basis of goodness-of-fit. The same approach is adopted in this work.

3.3 Empirical Process Model for Steady-State Stripe Width

The section that follows describes the development of a model to predict the widths of narrow stripes deposited by a slot die coater. Here, the coating flow is the same as for a slot die configured with a segmented internal channel[152-154]. The relevance of this scenario

to C/EOD is the assessment it provides for feature size and the sensitivity of pattern output to inputs such as volumetric flow rate (Q), substrate velocity (U_{web}), and coating gap (H). While the empirical modeling approach adopted here is similar to that of previous work[154], it extends this work by incorporating knowledge of observed spreading behavior described in Section 3.3.2. Consequentially, the model that follows is able to address a simple but consequential shortcoming in the previous approach.

3.3.1 Experimental Procedure

3.3.1.1 Materials

Polyvinyl alcohol (PVA), Mowiol® 4-88 from Sigma Aldrich Corp. prepared in 10 wt.% and 15 wt.% aqueous solutions, was used as the coating material for the experiments in this investigation. The physical properties of these materials are listed in Table 2.2.

3.3.1.2 Methods

All experimental investigations discussed in this chapter were carried out on the roll-to-roll imaging system (R2RIS) introduced in Section 2.3, using a slot die coating tool configured for C/EOD pattern deposition. The fixed geometric parameters of the tool were the same across experiments, with a coating gap (G) of 76.2 µm, an outlet width (w_0) of 1.4 mm for each discrete localized outflow region (DLOR), an upstream die lip dimension (L_u) of 1.2 mm, and a downstream die lip dimension (L_d) of 1.1 mm. Flow rate (Q) was controlled by a syringe pump and substrate velocity (U_{web}) was regulated by custom-built

PID controller integrated into the R2RIS apparatus. Measurements of stripe width (w) were carried out using the MATLAB image processing toolbox in order to reduce user error in edge location and transcription of data. For each recorded image, the coating bead was qualified as either advancing or receding, and either pinned, unpinned, or partially pinned at the die lip edge.

3.3.2 Observed Spreading and Pinning Behaviors

Process imaging across various conditions reveal two key aspects of the narrow coating bead behavior, which are illustrated in Figure 3.4 and Figure 3.5. First, spreading of the coating bead along the underside of the coating tool is effectively confined along the z-axis by the coating tool geometry, and is permitted to spread freely along the *y-axis*. Thus, a range of stripe widths are possible across various Q, U_{web}, and H even though the width of the tool outlet is fixed. This gives rise to the three confinement regimes pictured in Figure 3.4, for a deposition process with 10 wt.% PVA. For regimes I and II, the shape of the contact line appears nearly circular, while the coating bead is distorted significantly by the slot die geometry when pinned to both edges in regime III. This difference in the shape of the contact line for regime III versus regimes I and II encompasses a corresponding difference in the geometrical relationship between coating bead volume and stripe width. It follows that any correlations between stripe width and process inputs will experience a transition at the onset of confinement at both upstream and downstream edges of the slot die lip.

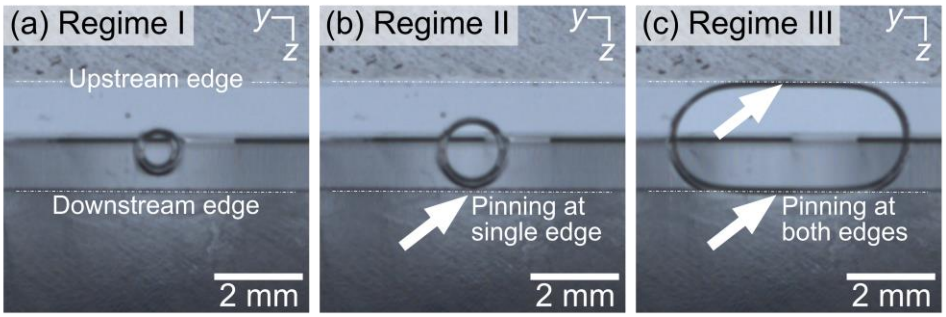

Figure 3.4 – Three regimes of coating bead contact line confinement along the upstream and downstream edges of the slot die lip. These comprise (a) no confinement, (b) confinement along one die lip edge, and (c) confinement along both die lip edges. The regimes in (a), (b), and (c) are denoted as I, II, and III, respectively Adapted with permission from [198].

Experimental observations also show that the shape of the steady-state coating bead, and thus the width of the resulting stripe, depends on its most recent previous state. In other words, a range of steady, stable coating bead shapes are attainable under the same Q, U_{web}, and H based on whether the coating bead has most recently increased or decreased, in order to stabilize at its present geometric configuration. This is illustrated by the two experimental curves in Figure 3.5. The only difference in process conditions across the two sub-plots is the change in substrate velocity from each measurement to the next, i.e., in Figure 3.5(a) it is decreasing and in Figure 3.5(b) it is increasing. In Figure 3.5(a), where the size of the coating bead decreases across the curve, the observed stripe width is consistently larger than in Figure 3.5(b), where the size of the coating bead increases across the curve. It must be stressed that these measurements represent steady-state conditions. Following a change in velocity along the curves in Figure 3.5(a) and (b), coating bead width is allowed to stabilize prior to recording of each data point. Additionally, it may be

noted that the data in Figure 3.5(a) were collected after the data in Figure 3.5(b), during the same run. As substrate velocity is increased far beyond the final data point to the far right of Figure 3.5(b), the coating bead eventually separates from the substrate. Prior to analysis of the advancing coating bead width, the substrate velocity must be lowered slightly, such that a steady coating bead is can be re-established, and subsequently lowered again, such that the coating bead width begins to advance, before recording the first data point along the curve in Figure 3.5(a).

The physical mechanism that causes this behavior is not yet well understood and warrants future exploration. However, based on this work, it is believed that the physical phenomenon of contact angle hysteresis, which is rather substantial for the PVA solutions used here, permits a range of stable geometric configurations for the steady narrow stripe. However, these investigations neither confirm nor exclude this possibility. Rather, the observed behavior is treated pragmatically and interpreted only in the context of the empirical process model.

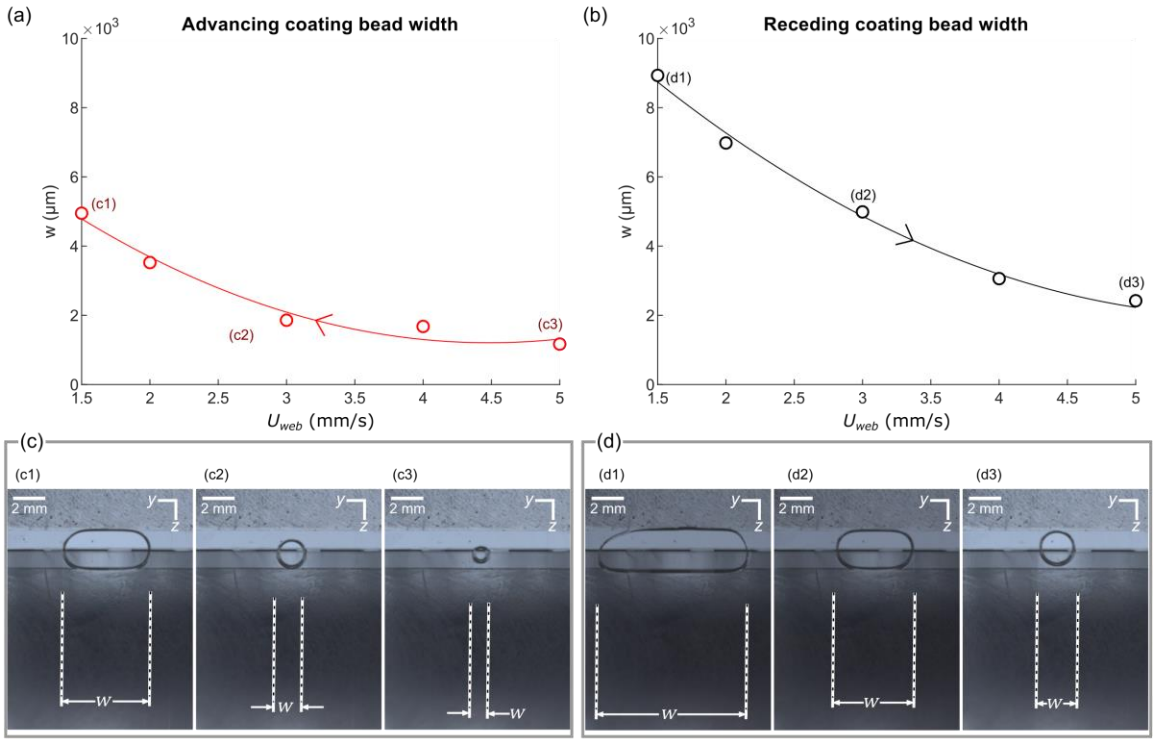

Figure 3.5 – Effect of coating velocity (U_{web}) on steady-state stripe width for a flow rate (Q) of 0.835 µL/s and coating gap (H) of 500 µm. The arrows along each curve indicate the direction of time for each experiment, such that the coating bead size is decreasing in (a) and increasing in (b). Inset images depict the coating bead and coated stripe viewed from below using the R2RIS. Images in (c) and (d) correspond to the charts in (a) and (b), respectively.

3.3.3 Empirical Modeling Approach

3.3.3.1 Dimensionless Groups

Previous studies on slot die coating of narrow stripes[154, 197] suggest the following dimensionless groups to guide the empirical model formulation:

$$H^* \equiv H/(L_u + L_d + G) \tag{3.2a}$$

$$Ca \equiv \mu U_{web}/\sigma \tag{3.2b}$$

$$Re \equiv \rho U_{outlet}^2/(\mu U_{web}/H) \tag{3.2c}$$

$$w^* \equiv w/w_0 \tag{3.2d}$$

H^* is a dimensionless length which expresses the ratio between the coating gap and die lip length, Ca is the capillary number, which expresses the ratio of viscous to interfacial forces, and Re is a modified form of the Reynolds number, which expresses the ratio of inertial forces at the die outlet to viscous shear forces between the slot die and the moving substrate, and w^* is a dimensionless stripe width which expresses output pattern morphology as a multiple of the slot outlet width, w_0. $U_{outlet} \equiv Q/(w_0 G)$, the average flow velocity at the slot die outlet is taken as the velocity scale for inertial forces, while U_{web} is the velocity scale used for viscous forces.

3.3.3.2 Assumptions and Model Form

Based on the observations of coating bead spreading and confinement from Section 3.3.2, the empirical model must consider two values for stripe width, one where the steady-state coating bead has increased in volume from a previous state, and one where the bead volume as decreased from a previous state. In dimensionless form, these two widths are denoted as w_a^* and w_r^*, respectively, with the subscript denoting whether the contact line beneath the coating tool has advanced or receded to stabilize at a given state. Furthermore,

the confinement regimes illustrated in Figure 3.4 must be reflected in the model. This is accomplished by assuming one set of correlations across the range of w^* that results in confinement at both edges of the slot die lip and a separate set of correlations across the remaining range of w^*. The critical coating bead width, which corresponds to the boundary between confinement regimes II and III is denoted as $w_{II\text{-}III}$.

It is also assumed, based on previous work, that a dimensionless group can be constructed from a linear combination of parameters in Eqns. (3.2a)-(3.2c) to explain the majority of the variation in w across various Q, U_{web}, and H. The dimensionless groups for w_a^* and w_r^* are denoted as Π_a and Π_r, respectively. Each of these is constructed on the basis of goodness-of-fit across experimental data for a given coating material and tool geometry.

Finally, the correlations between Π_a and w_a^*, and between Π_r, and w_r^*, are assumed to be logarithmic. This choice also has been made on the basis of goodness-of-fit for available data. While it would be equally possible to use a polynomial correlation, the logarithmic fit is guaranteed to impose no upper bound on the stripe width, which is not true for a polynomial curve fit. This reflects the fact that the width of the coating tool is large compared to the width of the coated stripe, and that the model does not assume physical bounds on the y-axis dimension of the coating bead. Together the assumptions outlined above can be summarized as follows:

1. Width of the coating tool is large compared to the width of the coating bead, such that the stripe width is unbounded by geometry.
2. Stripe width follows from the width of the narrow coating bead.
3. The coating process produces stable outflow outside the boundaries of a conventional coating window, as discussed in Section 3.2.1.
4. The shape of the coating bead is influenced by parameters that describe viscous and capillary forces (Q, U_{web}, and H), based on the discussion from Section 3.2.2.
5. Empirical correlations are constructed on the basis of goodness-of-fit across dimensionless groups identified in previous work, based on the discussion from 3.2.3.

The mathematical form of the correlations between process parameters and stripe width, with the assumptions above, are as follows:

$$w_a^* = \mathrm{A_a} \ln(\Pi_\mathrm{a}) + \mathrm{B_a} \quad \text{for } 0 < w_a^* \leq w_{II\text{-}III}^* \quad (3.3a)$$

$$w_a^* = \mathrm{C_a} \ln(\Pi_\mathrm{a}) + \mathrm{D_a} \quad \text{for } w_a^* > w_{II\text{-}III}^* \quad (3.3b)$$

$$w_\mathrm{r}^* = \mathrm{A_r} \ln(\Pi_\mathrm{r}) + \mathrm{B_r} \quad \text{for } 0 < w_r^* \leq w_{II\text{-}III}^* \quad (3.3c)$$

$$w_\mathrm{r}^* = \mathrm{C_r} \ln(\Pi_\mathrm{r}) + \mathrm{D_r} \quad \text{for } w_r^* > w_{II\text{-}III}^* \quad (3.3d)$$

where $w_{II\text{-}III}$* is the dimensionless stripe width coinciding with the transition between confinement regimes II and III; A_a, B_a, C_a, D_a, A_r, B_r, C_r and D_r are empirical constants. Assuming that w_a* and w_r* are continuous along Π_a and Π_r, respectively, Eqns. (3.3a)-(3.3d) amount to a piecewise continuous model with a break point located at $w_{II\text{-}III}$*:

$$A_a \ln(\Pi_a) + B_a = C_a \ln(\Pi_a) + D_a \qquad \text{for } w_a^* = w_{II\text{-}III}^* \qquad (3.4a)$$

$$A_r \ln(\Pi_r) + B_r = C_r \ln(\Pi_r) + D_r \qquad \text{for } w_r^* = w_{II\text{-}III}^* \qquad (3.4b)$$

3.3.3.3 Empirical Modeling Procedure

For a specific combination of coating fluid, substrate, and coating tool geometry, the empirical model is derived by the following three-step process:

1. Narrow stripe width (w) is sampled across a range of process parameters (Q, U_{web}, H). Each sample point is associated with either advancing or receding coating bead width, based on the history of the sample run (*e.g.* increasing U_{web} from its previous value implies advancing bead width, and *vice versa*).

2. Regression analysis is used to construct a piecewise model of the form described by Eqns. (3.3a)-(3.3d).

    a. Since $w_{II\text{-}III}$* is not known explicitly, $w_{II\text{-}III}^* \approx (L_u + L_d + G)/w_0$ is used as an initial estimate.

b. Data is binned into two subsets based on measurements of w^*. One bin contains data where $0 < w^* \leq w_{II\text{-}III}^*$, and one bin contains data where $w^* > w_{II\text{-}III}^*$.

3. Binning and regression analysis are updated in order to ensure that the transition between liquid bridge confinement regimes is reflected appropriately, while maintaining continuity of the piecewise model.

    a. Uncertainty analysis is performed on model components B_a, B_r, D_a and D_r to construct bounds for each piecewise model segment.

    b. The uncertainty level where the bounds for the two model segments intersect at $w_{II\text{-}III}^*$ is determined.

    c. The binning process is repeated about $\Pi_a(w_{II\text{-}III}^*)$ and $\Pi_r(w_{II\text{-}III}^*)$.

    d. Regression analysis and determination of $w^*_{II\text{-}III}$ are repeated using the updated binning scheme.

    e. Regression analysis is repeated a final time, with the additional constraint imposed by Eqns. (3.4a)-(3.4b).

3.3.4 Model Demonstration

3.3.4.1 Dimensional Analysis

For 10 wt.% and 15 wt.% PVA, linear combinations of H^*, Ca, and Re can be constructed that relate pattern morphology to process parameters Q, U_{web}, and H along a unified trend. These dimensionless groups are selected on the basis of goodness-of-fit, as discussed in in Appendix A1, and found to be the following:

$$\Pi_a \equiv Re^{0.5} Ca^{-1} H^{*-2} \qquad \text{for } w^* = w_a^* \tag{3.5a}$$

$$\Pi_r \equiv Re^{0.5} Ca^{-3} H^{*-3} \qquad \text{for } w^* = w_r^* \tag{3.5b}$$

The effect of this dimensional scaling for 10 wt.% PVA across various Q, U_{web}, and H is illustrated in Figure 3.6. Correlations are apparent across Q, in Figure 3.6 (a) and (b), with H and U_{web} held constant. These trends capture the increase in stripe width that emerges as Q increases in order to accommodate the increased rate of fluid transfer through the liquid bridge. The dimensional scaling from Eqns. (3.5a) and (3.5b) produces the unified trends shown in Figure 3.6(c) and (d), respectively. Here, the influence of the slot die geometry and the relative importance of interfacial forces are captured by H^* and Ca, respectively. Flow rate is implicit in Re, which represents the importance of inertial force in the coating bead relative to viscous shear in the deposition region.

As expected from the spreading and confinement effects observed in Section 3.3.2, the trends in Figure 3.6(c) and (d) exhibit apparent breakpoints corresponding to confinement regimes II and III. Trend features corresponding to the transition regimes I and II are not easily identifiable, which likely reflects the type of influence that each confinement regime exerts on the liquid bridge. Specifically, whereas the primary effect of regime II is to confine the location of the liquid bridge, regime III results in a significant distortion of the coating bead shape. To accommodate these observations, the linear regression fit results in Figure 3.6(c) and (d) have been performed separately for measurements exhibiting regime III confinement and the remaining measurements. Comparing results across confinement regimes, it is noteworthy that regime III exhibits a high degree of process sensitivity relative to regimes I and II. With respect to coating tool geometry, the implication is that it should be possible to achieve a greater range of stripe widths for a given film thickness at the cost of process robustness, by reducing the slot die lip dimensions L_u and L_d. In addition, it can be observed that process sensitivity is at its minimum value near the smallest feature size produced.

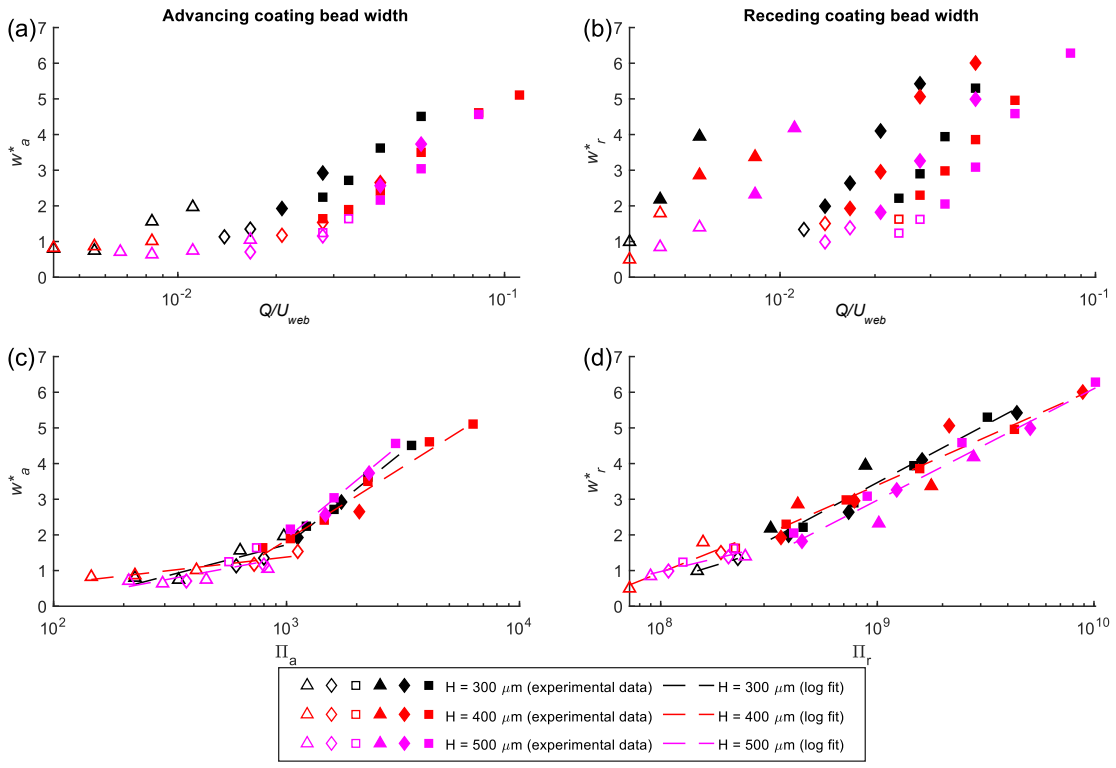

Figure 3.6 – Results for 10% wt. PVA collected under (a) advancing and (b) receding contact line configurations. Unfilled markers (Δ, ◊, □) denote pinning regimes I and II and filled markers (▲, ♦, ■) denote pinning regime III. Flow rate is 0.017 μL/s for triangles (Δ, ▲), 0.083 μL/s for diamonds (◊, ♦), and 0.167 μL/s, for squares (□, ■). Coating gap is denoted by color as indicated in the legend. Adapted with permission from [198].

To assess the consistency of results produced by this approach, the regression slope coefficients, A_a, C_a, A_r and C_r in Eqns. (3.3a)-(3.3d) are plotted across several data subsets for both 10 wt.% and 15% wt.% PVA in Figure 3.7. The error bars denote a 95% confidence interval for each constant, assuming a normal sampling distribution. The model parameters are consistent within these bounds for each case considered, although the confidence interval is rather large, particularly for the higher viscosity formulation and lower values of *H*. The uncertainty in the model fit is most likely a consequence of transient fluctuations

in Q or U_{web} introduced by the physical hardware of the R2RIS, such as the substrate motor and PID controller, the stepper motor that drives the syringe pump, as well as vibration from electromechanical components on the system. Due to the range of coating bead widths that will remain stable under the same steady-state conditions, the disruption of stripe width due to these transient effects can be expected to persist as long as process inputs are held constant.

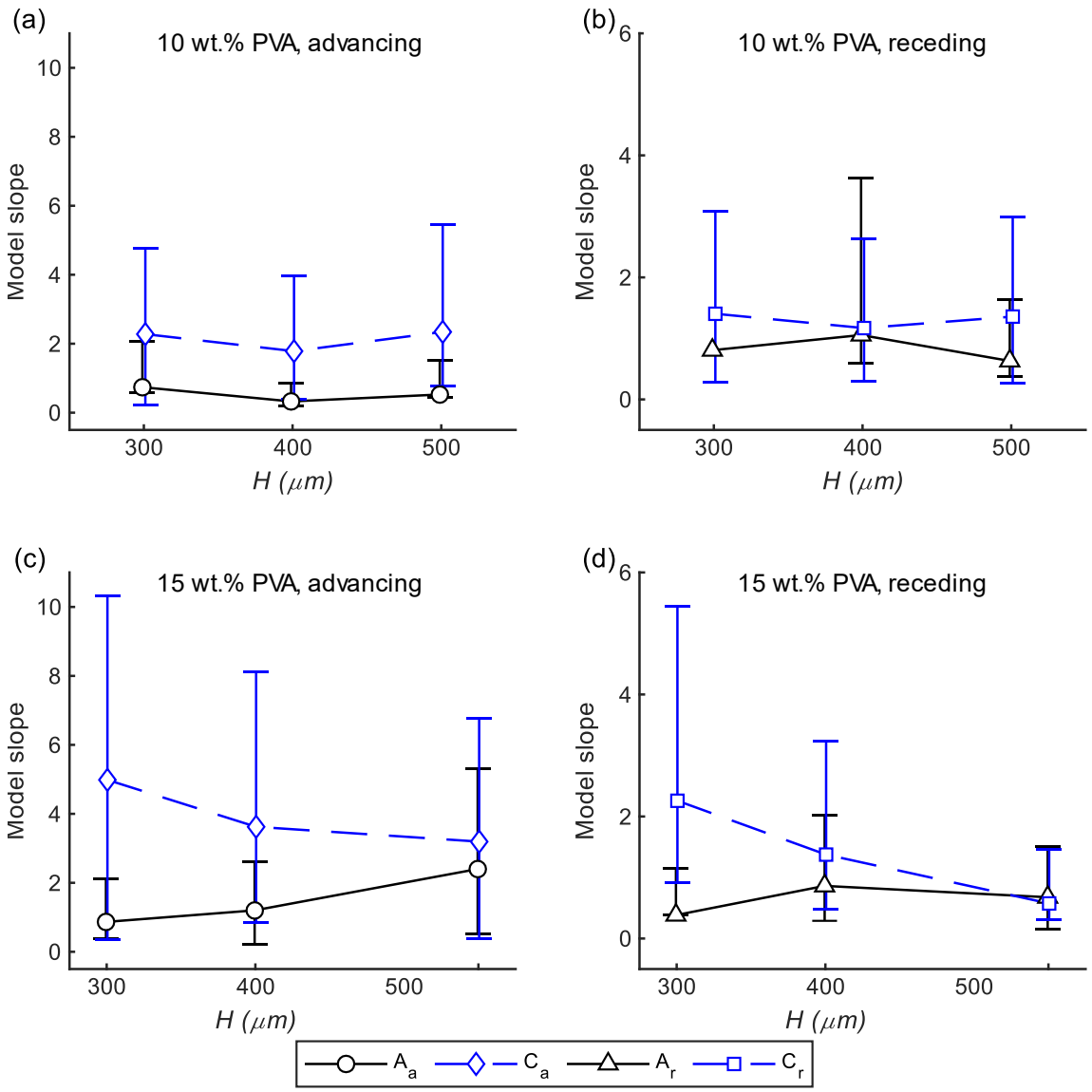

Figure 3.7 – Model uncertainty for (a) advancing coating bead width with 10 wt.% PVA, (b) receding coating bead width with 10 wt.% PVA, (b) advancing coating bead width with 15 wt.% PVA, and (a) receding coating bead width with 15 wt.% PVA. Adapted with permission from [198].

3.3.4.2 Piecewise Logarithmic Correlations

Empirical process modeling results for 10 wt.% PVA are shown in Figure 3.8, in relationship to intermediate steps in the development of the final piecewise correlations that describe the output stripe width from the process. Plotted against the dimensionless groups from Equations. (3.5a) and (3.5b), coating bead width decreases in an apparent logarithmic fashion, with a transition point corresponding to the boundary between confinement regimes II and III, as shown in Figure 3.8(a) and (c). The empirical fits constructed for each permutation of confinement regime and advancing/receding coating bead geometry with the transition between confinement regimes II and III indicated as a breakpoint in the empirical model are shown in Figure 3.8(b) and (d).

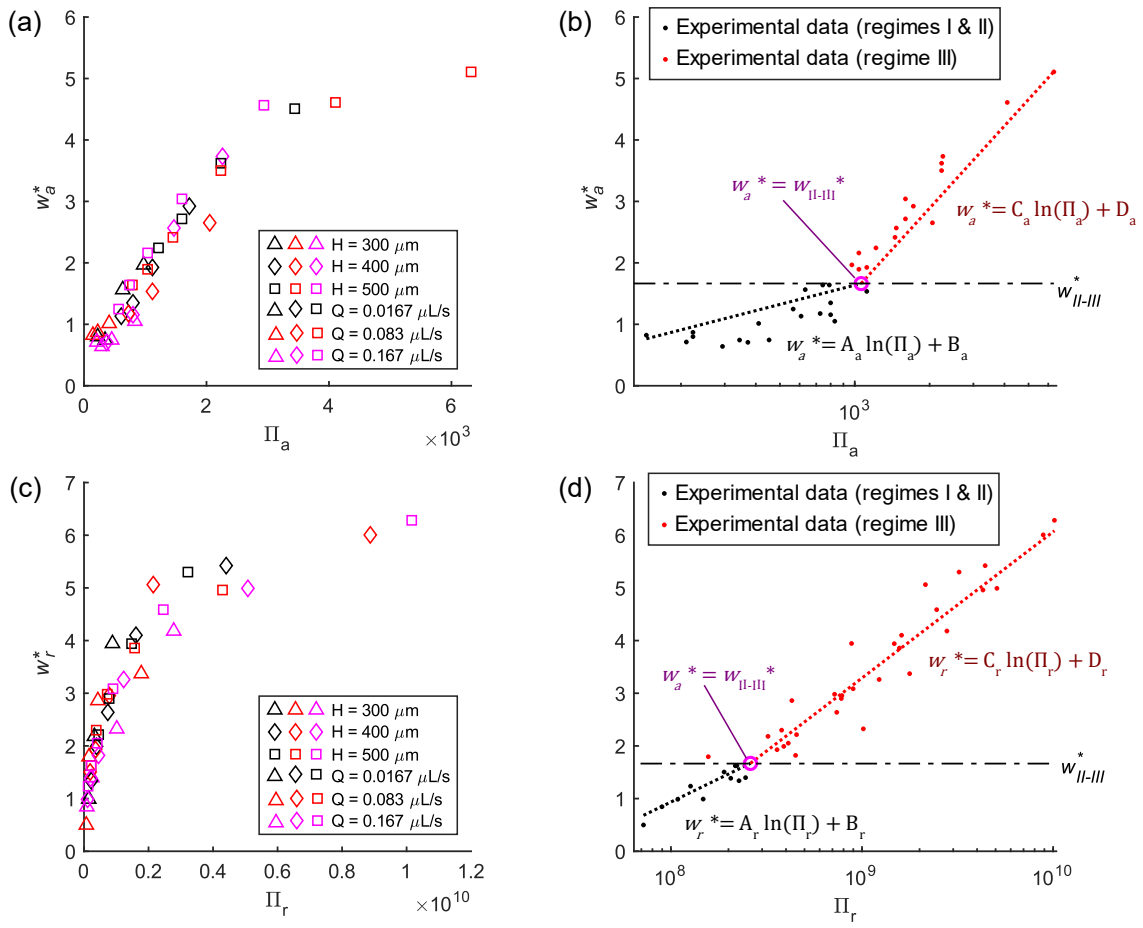

Figure 3.8 – Dimensional scaling and resulting empirical correlations for (a-b) advancing coating bead width and (c-d) receding coating bead width for slot die coating of 10 wt.% PVA in narrow stripes. Adapted with permission from [198].

In a physical sense, the empirical model provides a range of achievable widths (w) for each specific combination of Q, U_{web}, and H. The piecewise curve fits for w_a^* and w_r^* constitute a stripe width minimum and maximum, respectively. Interestingly, since the models for w_a^* and w_r^* each depend on a different dimensionless group, it follows that process parameters can be chosen to produce a range of w_a^* when w_r^* is held constant, and *vice versa*. This underscores the high degree of variability in stripe width exhibited by the

slot die coating process. By incorporating basic knowledge about the wetting behavior into the process model, it is possible to account for this variability as a physical and repeatable consequence of process conditions.

3.4 Complex Patterning

While the process model developed in Section 3.3 addresses one important aspect of feature size for coating/extrusion-on-demand (C/EOD), transient flow effects such as those illustrated in Figure 3.9 must be considered in order to develop a more comprehensive model. Dynamic manipulations of the liquid bridge are inherent to the digital patterning functionality that C/EOD is designed to provide. The task of modeling transient liquid bridge phenomena with asymmetric dynamic contact lines, under complex confinement effects and shearing boundary conditions, presents a significant challenge. Considering the current state of progress on liquid bridges and narrow coating flows discussed in Section 3.2.2, this challenge is likely to span multiple future investigations. At present, it is reasonable for this work to classify some common dynamic phenomena at the coating bead with respect to the patterning capabilities of C/EOD. In this section, two such behaviors are discussed. On-off flow actuation, illustrated in Figure 3.9(a), produces an intermittent stripe pattern with tapering defects at the leading and trailing edges of each stripe, denoted as ℓ_{start} and ℓ_{stop}, respectively. This effect is discussed in Section 3.4.2, with comparison across pin-actuated flow (PAF) and multi-inlet flow (MIF) control for C/EOD. Subsequently, coalescence between adjacent coating beads, illustrated in Figure 3.9(b), is

considered in Section 3.4. This behavior is discussed both in terms of potential defects in Section 3.4.3.1 as well as possibilities for pattern control in Section 3.4.3.2.

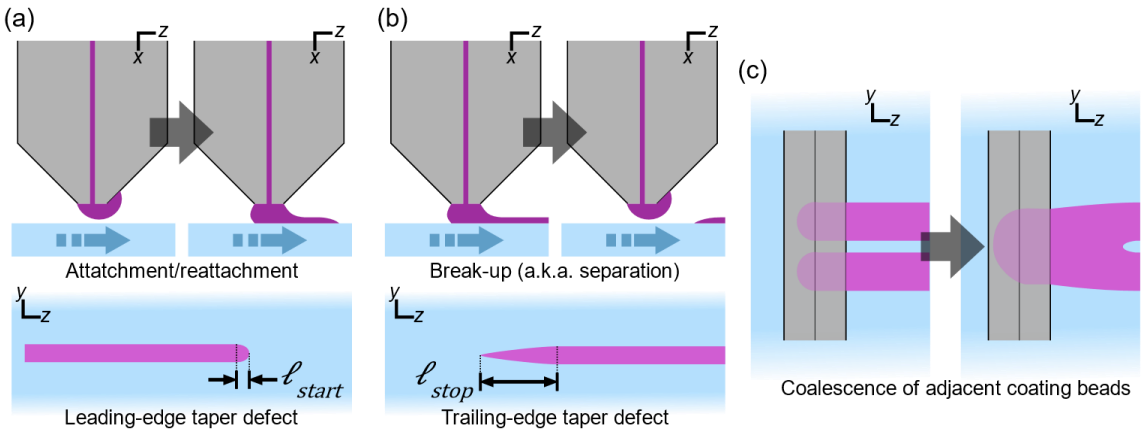

Figure 3.9 – Transient behaviors of a narrow coating bead that produce complex pattern features include (a) breakup, (b) attachment/re-attachment, and (c) coalescence of adjacent coating beads.

3.4.1 Experimental Procedure

3.4.1.1 Materials

Polyvinyl alcohol (PVA), Mowiol® 4-88 from Sigma Aldrich Corp., prepared in 15 wt.% and 20 wt.% aqueous solutions were used as the coating materials for majority of the experimental work in this section. Poly(3,4-ethylenedioxythiophene):polystyrene sulfonate (PEDOT-PSS) ink doped with 6% ethylene glycol and 1% Triton X-100 was used for the visualizations of coating bead interactions discussed in Section 3.4. This formulation was chosen as a representative example of a functional material used routinely to manufacture printed electronic devices[43, 199]. The purpose of surfactant in the PEDOT:PSS ink formulation is to prevent dewetting of the ink after deposition. The

surfactant reduces the surface tension (σ) of the ink to 32 mN m^{-1} and the contact angles to θ_a = 17° and $\theta_r \approx 0°$ on both untreated PET and PMMA. As with the remaining wetting properties reported in Section 2.4.2, these values represent observed behavior at 25°C and 48 ±2% relative humidity, the ambient conditions of coating processes imaged on the R2RIS on a time scale of 60 s.

3.4.1.2 Methods

All experimental investigations discussed in this section were carried out on the roll-to-roll imaging system (R2RIS) introduced in Section 2.3, using a slot die coating tool configured for C/EOD pattern deposition. The fixed geometric parameters of the tool were the same as for experiments from in Section 3.3. However, flow rate was regulated by a pressurized reservoir rather than a syringe pump, and calculated from surface profile measurements of dry films obtained using a Dektak 6M contact profilometer. For given surface profile measurement of dry film thickness (t_{dry}) along the *y*-axis across the width (*w*) of a coated stripe, flow-rate (*Q*) is given by the following expression:

$$Q = \frac{\rho_{PVA}/\rho_{solution}}{m_{PVA}} \cdot v \int_0^w t_{dry}(y)dy \tag{3.6}$$

In Equation (3.6), m_{PVA} is the mass fraction of PVA in the aqueous solution, ρ_{PVA} = 1.245 g/mL is the density of dry polyvinyl alcohol[167], and $\rho_{solution}$ is the density of the coated aqueous polyvinyl alcohol solution. For observations on liquid bridge breakup and

reformation, in Section 3.4.2, time intervals required for full development of the coating bead and for complete flow cutoff were recorded as t_{start} and t_{stop}, respectively.

3.4.2 On/off Flow Actuation

Several experimental studies on slot die coating with narrow stripes have examined the response of the coating bead to intermittent flow start-up and shut-off[154, 200, 201]. These efforts have indicated the presence of tapering defects in the resulting printed feature. These defects represent a transition between steady flow states, and a time delay between flow actuation and the resulting pattern features that are introduced. For leading edge defects, the transition between flow states comprises formation and stabilization of the narrow coating bead. For trailing-edge defects, the transition entails separation of the liquid bridge.

The severity of these defects for C/EOD coating is compared for PAF control and MIF control in Figure 3.10 for 15 wt.% PVA. These are presented in terms of dimensionless flow rate, Q^*, which is defined as follows:

$$Q^* \equiv \frac{Q/U_{web}}{Gw_0} \tag{3.7}$$

This quantity represents fluid volume per unit width of substrate scaled to the fixed outlet area of each discrete localized actuation region (DLOR) on the C/EOD tool. The flow

response is related to the resulting pattern through the length of tapering defects, ℓ_{start} and ℓ_{stop} which are defined according to Eqns. (3.8a) and (3.8b) below:

$$\ell_{start} = t_{start} U_{web} \tag{3.8a}$$

$$\ell_{stop} = t_{stop} U_{web} \tag{3.8b}$$

With PAF control, the coating bead is fully established within 19 ±3.5 mm for a Q^* range of 1.98 to 3.86 and bead establishment is relatively insensitive to changes in coating gap (H), as shown in Figure 3.10(a). There is also a slight trend towards a longer leading-edge taper defect with increasing Q^*, which is significantly more pronounced with MIF control. While the coating bead with MIF control is fully established within 15 mm at around a Q^* of 0.20, this length increases to 55 mm at a Q^* value of 0.98. Sensitivity of ℓ_{start} to H is also greater for MIF control, with the variation in ℓ_{start} increasing with larger values of Q^*.

Examining the results for trailing-edge defects, ℓ_{stop} is generally more severe and more sensitive to Q^* than ℓ_{start}. With PAF control, response length gradually increases from 24 mm or less to 30 ± 1.5 mm across the range of Q^* considered. For MIF control, these same trends in off-actuation response are more pronounced. The smallest trailing-edge defect observed is 28.9 mm at $Q^* = 0.20$, while at $Q^* = 0.98$, ℓ_{stop} ranges from 326 to 697 mm. This represents an order-of-magnitude increase in trailing taper, with significantly greater variation at each value of Q^* than observed for PAF control. Repeated breakup and

reforming of the coating bead, as observed previously for narrow stripe coating from a conventional slot die[154], is observed to contribute significantly to the increase for MIF control.

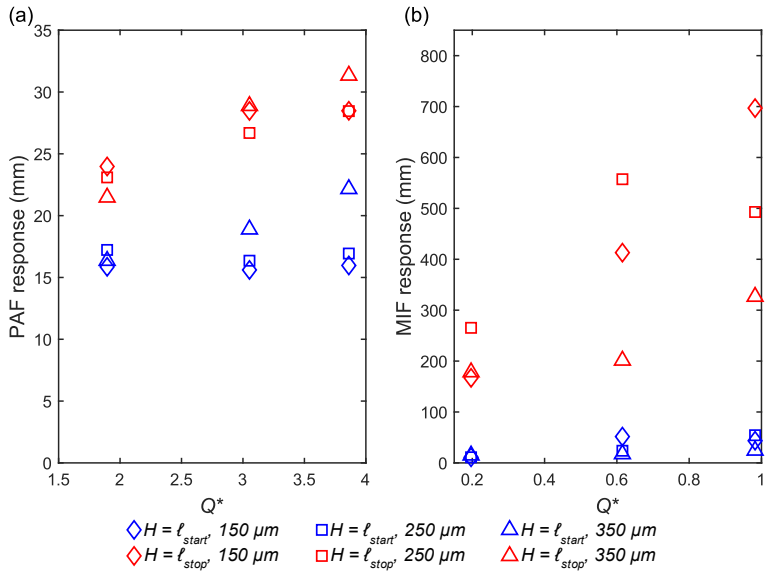

Figure 3.10 – Length of tapered pattern defects in intermittent 15 wt.% PVA stripes. The length of defects produced for off-on actuation (ℓ_{start}) and on-off actuation (ℓ_{stop}) is plotted against dimensionless flow rate (Q^*) for both (a) PAF control and (b) MIF control. Adapted with permission from [197].

The results presented in Figure 3.10 suggest an advantage in patterning control offered by the PAF control scheme over MIF control. It is important to qualify, however, that these results depend strongly on the particular tooling design used to implement both flow control strategies. A key difference between PAF and MIF as implemented here relates to the residual fluid that remains within the coating tool cavity after off-actuation of flow rate. PAF control ensures that this residual fluid is physically separate from the coating bead following off-actuation, while MIF control does not. For C/EOD with MIF

control, this residual fluid is permitted to flow into the coating bead even after off-actuation of flow, while PAF control effectively limits the available volume to replenish the coating bead after off-actuation. Thus, flow response for MIF control is generally slower and less consistent, with a larger spread in data across various values of H. While leading and trailing taper lengths are similar for PAF control, ℓ_{stop} is roughly an order of magnitude greater than ℓ_{start} with MIF control.

3.4.3 Coating Bead Interactions

3.4.3.1 Coalescence

The interaction of adjacent coating beads in C/EOD coating gives rise to several distinct bead shapes, which are shown for 20 wt.% PVA in Figure 3.11. In cases where coated stripe width (w) exceeds the outlet width (w_0) for two adjacent stripes, coalescence of the coating beads for each stripe occurs. In most cases involving liquid bridge coalescence across adjacent discrete localized outflow regions (DLORs), outflow is centered midway between the two DLORs, as pictured in Figure 3.11(a). At smaller values of Q^*, near the low-flow limit, outflow from adjacent DLORs remains distinct, as shown in Figure 3.11(b). Comparing these two examples with the case in Figure 3.11(c) illustrates the role of H with respect to this coating bead behavior. Since coating gap is correlated inversely with contact line radius of the liquid bridge, decreasing H corresponds to spreading of both adjacent liquid bridges and facilitates the onset of their coalescence. Broadly, coalescence will be facilitated by other factors that promote spreading along the

die lip, as well. For this reason, the onset of coalescence is achieved more readily for surfactant-doped PEDOT:PSS ink than for surfactant-free 20 wt.% PVA.

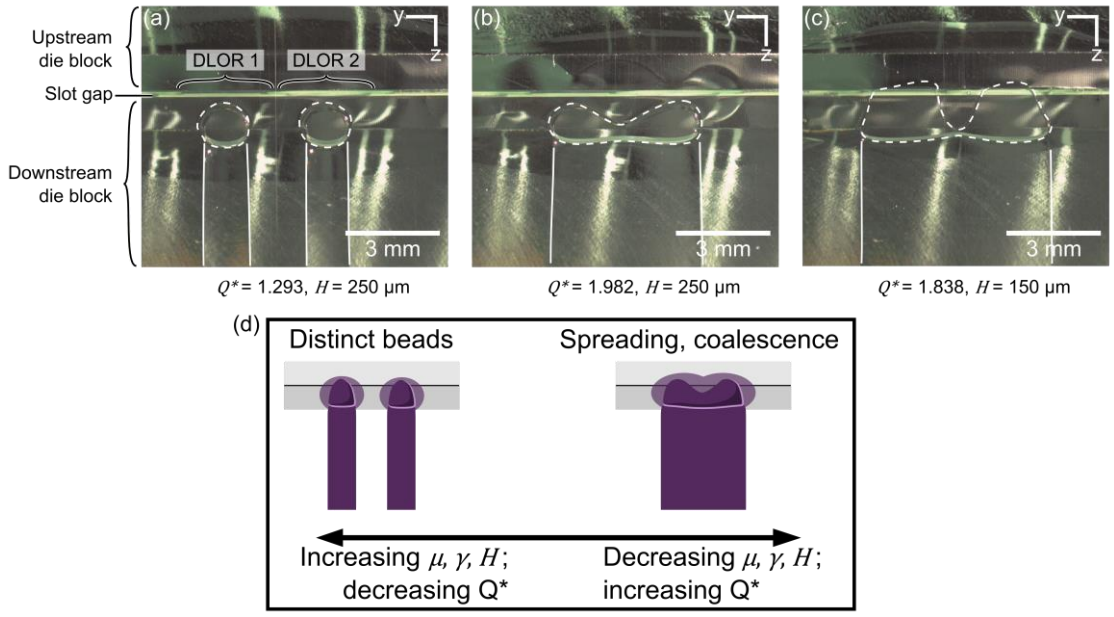

Figure 3.11 – Interactions between adjacent coating beads emanating from the slot die coating tool configured with MIF control include (a) two distinct coating beads formed along adjacent DLORs, (b) coalescence of coating beads, with the resulting stripe located between DLORs, due to increased flow rate, and (c) further increased stripe width due to decreased *H*. Lines have been superimposed over images in (a)-(c) to identify the extruded pattern (solid) and coating bead contact line (dashed). (d) A schematic illustration of the general trends observed between process inputs and coating bead coalescence. Adapted with permission from [197].

3.4.3.2 Outflow Relocation

As an example of patterning functionality provided by C/EOD that cannot be achieved with conventional slot die coating, a diagonal stair step pattern is demonstrated. The target pattern comprises discrete overlapping stripe segments and requires asynchronous multi-DLOR actuation. As illustrated in Figure 3.12, the pattern is deposited

by successive on-off-on (startup-cutoff) actuation of adjacent DLORs, proceeding across the width of the coating tool.

Microscope images of the coating bead during pattern deposition with 15 wt.% PVA are provided for two cases. In Figure 3.12(a), at H = 250 μm, the widths of coating beads emanating from adjacent DLORs are sufficiently wide to enable the desired coalescence. By contrast, with H = 350 μm as shown in Figure 3.12(b), coalescence does not occur. One major difference in flow behavior across these two examples is the time required for the cessation of fluid deposition at a particular location. For the case in Figure 3.12(a), the flow response is comparatively rapid because the coalesced coating bead is able to translate from the inactive DLOR toward the active DLOR. In the case without coalescence, however, flow ceases only following separation of the liquid bridge, which is prolonged by the availability of residual fluid inside the coating tool cavity as discussed in Section 3.4.2. A comparison between the resulting pattern features is given in Figure 3.12 (c) and (d). Here, highly tapered trailing edge pattern defects are present only in the case without coalescence. These results suggest that bead coalescence can, in some cases, be leveraged as a means to redirect and position flow across adjacent DLORs deliberately.

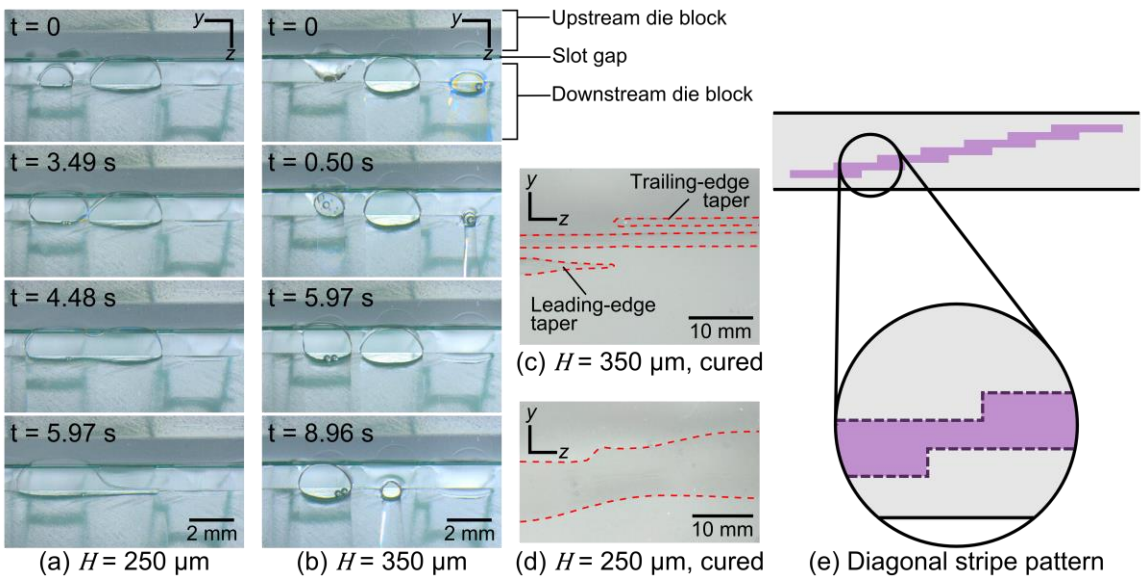

Figure 3.12 – 15 vol% PVA deposited by C/EOD at (a) 250 µm, with coalescence of adjacent coating beads and (b) at 350 µm, where coalescence does not occur. The resulting diagonal pattern feature (c) without coalescence and (d) with coalescence, where darker regions indicate coated substrate, dashed lines have been added to help identify the pattern boundary. (e) A conceptual schematic of the target pattern feature, a diagonal stair-step stripe. Adapted with permission from [197].

3.5 Miscellaneous Defects

Deposition coating across multiple fluid stripes in the manner required for the C/EOD process permits several phenomena that are undesirable from the standpoint of patterning. First, unwanted coalescence of adjacent coating beads, as illustrated in Figure 3.13(a) for deposition of surfactant-doped PEDOT:PSS is difficult to rectify without flow cessation through the corresponding DLORs. This has been noted previously as a critical pattern defect for high-resolution deposition using more conventional versions of slot die coating[158]. Conversely, unwanted separation of liquid bridges from the substrate surface, as illustrated in Figure 3.13(b), constitutes another unwanted defect. It is critical to note

that both defects scale with the addition of more DLORs as required for increasingly complex patterns. Furthermore periodic flow disturbances, vibrations, and similar effects might exacerbate instability phenomena, which can contribute to the issue.

In addition to unwanted bridge coalescence and separation, air inclusions and surfactant bubble buildup, illustrated in Figure 3.13(c) and (d) respectively, facilitated by the on-off actuation inherent to the C/EOD process. While this same issue can also occur with conventional slot die coating, the steady characteristic of that approach helps to mitigate the danger considerably. Since the addition of surfactant exacerbates these issues associated with C/EOD for PEDOT:PSS, it is reasonable to expect similar issues with other surfactant-doped solutions unless preventative measures are made with respect to coating tool design.

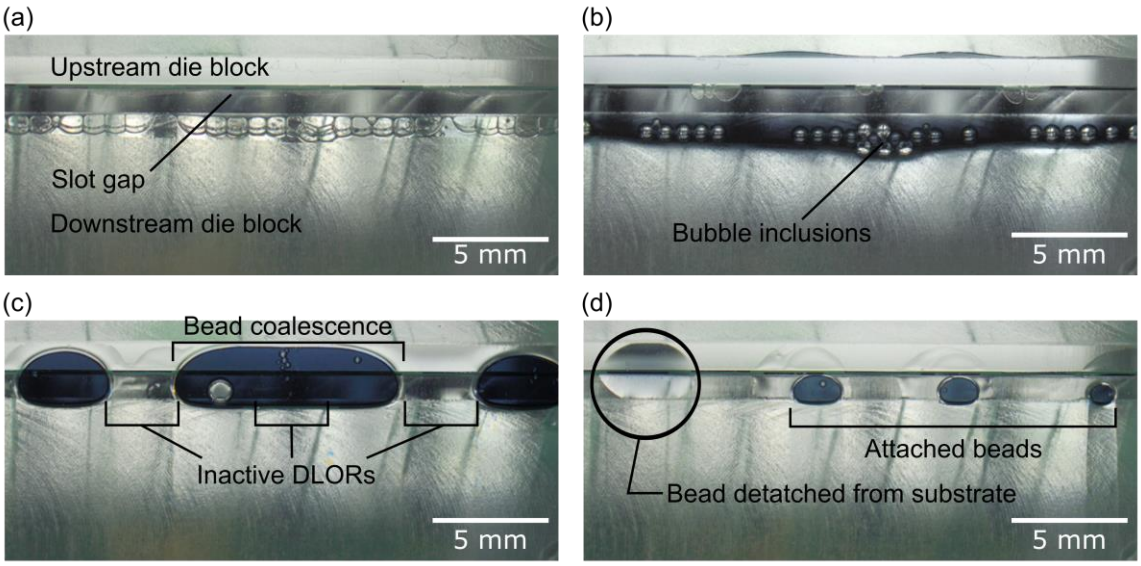

Figure 3.13 – A variety of flow effects for PEDOT:PSS during on/off flow illustrating a) surfactant-induced material buildup, b) bubble inclusions expelled from the die cavity, (c) unwanted lateral spreading and bubble generation, and (d) localized coating bead detachment from the substrate. Adapted with permission from [197].

3.6 Conclusions

This chapter has investigated the complex patterning capabilities of C/EOD by examining spreading, confinement, development and breakup of narrow coating beads. The continuous deposition of narrow stripes under steady-state conditions has first been explored as a basic measure of feature size. Process visualizations made possible by the R2RIS have aided identification of lateral spreading along the bottom of the coating tool, which permits a range of possible stripe widths at a given set of processing conditions. To account for the effect, an empirical process model has been developed and demonstrated, based on recent literature in addition to this work. The empirical correlations describe two possible values for *w*, based on whether the coating bead has reached steady state by

increasing or decreasing in size relative to changing U_{web}. By considering both values, the model is able to account for a key source of variation in the coupling between parameters Q, U_{web}, H, and stripe width. It is also of practical importance that the empirical modeling approach is suitable for application to other material systems even when knowledge of their physical properties is limited.

Dynamic behaviors of narrow liquid bridges have also been considered in the context of complex patterning capabilities offered by the C/EOD approach. In-process imaging of narrow coating beads has helped to illustrate how the coating bead volume mediates flow actuation and pattern deposition. Selective deposition requiring flow startup and cutoff events necessitates attachment, development and separation of the liquid bridge. Coalescence of liquid bridges across neighboring outlet regions has been found to offer an intriguing means of repositioning flow emanating from the coating tool, although coalescence corresponds to an undesired pattern defect in conventional slot die coating. These dynamic liquid bridge behaviors are particularly dependent on the coating tool design, and thus there are opportunities to conduct future investigations on the manipulation of liquid bridges relative to the C/EOD tool design.

The discussions of this chapter have benefitted from an observation that C/EOD encompasses recognizable aspects of traditional coating flow, in addition to behaviors associated with capillary bridges. It is evident from Section 3.3 that process control over coating bead size is dictated by the balance of flow rate substrate velocity. From Section

3.4, it is clear that adjacent coating beads coalesce due to spreading, as well as beads that remain uncoalesced, can be produced by the same coating tool. Furthermore, the experimental results in Section 3.4.2 suggest that a key physical limitation on feature size for C/EOD, breakup of the coating bead, occurs outside of the traditional slot die coating window and approximately corresponds to the physical length scale of capillary bridges.

The remaining chapters consider strategies to achieve feature sizes smaller than the coating bead width by building upon the MIF approach. In these efforts, the multiple-inlet slot die design is reapplied towards patterning of the coating flow composition. The resulting heterogeneous coating bead is subject to the same phenomena investigated in this chapter, in addition to aspects of heterogeneous flow that enable new possibilities for pattern generation.

CHAPTER 4. HETEROGENEOUS STRIPE SLOT COATING (HSSC)

4.1 Introduction

In this chapter, a novel approach coined heterogeneous stripe slot coating (HSSC) is introduced, which builds upon the coating/extrusion-on-demand (C/EOD) with a multi-inlet flow (MIF) tool. The conceptual design of HSSC is oriented towards several perceived benefits to process control and pattern resolution performance. These benefits are demonstrated experimentally throughout the remainder of this dissertation with several material systems. Section 4.3 introduces the fundamental principles of operation for the HSSC approach, and establishes guidelines for material selection based on the role of interfacial and wetting properties. This section investigates the role of a surface tension mismatch between two fluids co-deposited in an alternating-stripe pattern, supported by results for representative pairs of fluid materials.

In Section 4.4, HSSC is demonstrated for aqueous dispersions of poly(3,4-ethylenedioxythiophene) (PEDOT): polystyrene sulfonate (PSS), a widely used transparent hole injection[83, 132, 202-204] and electrochromic layer material[44, 205-207]. These demonstrations serve to demonstrate the utility of HSSC with functional materials well-known in the field of printed electronic devices. To evaluate the role of the coating process on device

functionality, the direct current (DC) electrical performance of thermally annealed films is also characterized and compared to the cross-section structure of the patterned films.

Finally, in Section 4.5, process control over the size of deposited stripe features is compared to the liquid bridge-driven patterning approach used for C/EOD as well as conventional stripe coating. The capability of HSSC to deposit aqueous PEDOT:PSS ink as-received is compared to the prevailing approach in recent literature, wherein wetting-enhancing dopants are used to ensure stability of the wet film after deposition[92, 105, 132, 158, 197]. These investigations highlight the advantages provided by HSSC for well-controlled deposition of stripe-patterned films, with material systems that are challenging to process using C/EOD and conventional slot die coating.

4.2 Experimental Procedures

4.2.1 Materials

PEDOT:PSS, Clevios ™ PH-1000 colloid ink purchased from Heraeus GmbH, was used for HSSC deposition of conductive stripe-patterned films. PEDOT:PSS ink was filtered prior to deposition but otherwise used as received. The secondary material used during deposition of continuous stripe features was PVA, Mowiol® 4-88 from Sigma Aldrich, prepared in 10 wt.% and 15 wt.% aqueous solutions by continuous stirring for 30 minutes at 60°C. For visualization of spreading behavior in the heterogeneous coating bead, 15 wt.% PVA was co-deposited with a second 15 wt.% PVA formulation with < 2% added food dye. For fabrication of conductive stripe structures, PEDOT:PSS ink was co-

deposited with 10 wt.% PVA. This pairing was selected because the viscosities of the PEDOT:PSS ink and 10 wt.% PVA solutions are nearly matched, at 29 cP and 26 cP[167], respectively. Heterogeneous films were deposited on flexible PET film, ES301400 purchased from Goodfellow Cambridge Ltd.

Additional fluids were used in demonstrations of wetting and spreading behavior in Section 4.3. These include PVA prepared in 24 wt.%, glycerol purchased from Sigma Aldrich Corp. prepared in 95 wt.% aqueous solution, polydimethylsiloxane (PDMS), Dow Corning 200® fluid purchased from Sigma-Aldrich, and vacuum pump oil (VPO), L340 purchased from Virginia KMP Corp.

4.2.2 Methods

4.2.2.1 Syringe Dispensing of Immiscible Fluids

For demonstrations of wetting behavior of immiscible fluids, an initial fluid phase, either polyvinyl alcohol (PVA) prepared in 24 wt.% aqueous solution or glycerol prepared in 95 wt.% solution, was deposited by a syringe dispenser on PET substrate in narrow stripes. Subsequently, a second fluid phase, either PDMS or VPO, was deposited to form an alternating-stripe pattern. Profile views of the equilibrium structure of these alternating-stripe heterogeneous films were obtained using a model 500-U1 Ramé-Hart goniometer.

4.2.2.2 HSSC Tool Geometry and Apparatus

The tooling required for HSSC without hydrodynamic focusing is illustrated in Figure 4.1(a). Both the geometry of the coating tool and the relevant process parameters are similar to C/EOD with MIF control illustrated in Figure 2.2(c). A fixed slot gap (G) of 76 μm, upstream slot die lip dimension (L_u) of 1.2 mm, and downstream slot die lip dimension (L_e) of 1.1 mm were used for all deposition trials. For co-deposition of aqueous PEDOT:PSS ink and aqueous PVA, an outlet width (w_0) of 0.94 mm and center-to-center outlet spacing (s_0) of 2.9 mm were used. For co-deposition of two aqueous PVA solutions, w_0 and s_0 were 1.4 mm and 4.0 mm, respectively. For HSSC deposition experiments, the stationary coating tool was positioned above a moving substrate on the roll-to-roll imaging system (R2RIS) and supported by a vacuum platen with a transparent borosilicate window for viewing deposition flow, as illustrated in Figure 4.1(b). The manifold configuration first introduced in Figure 2.5(d) and reproduced in Figure 4.1(b) was used distribute metered flow among the multiple inlets. Following deposition, stripe width (w) and center-to-center spacing (s) were measured using the MATLAB image processing toolbox.

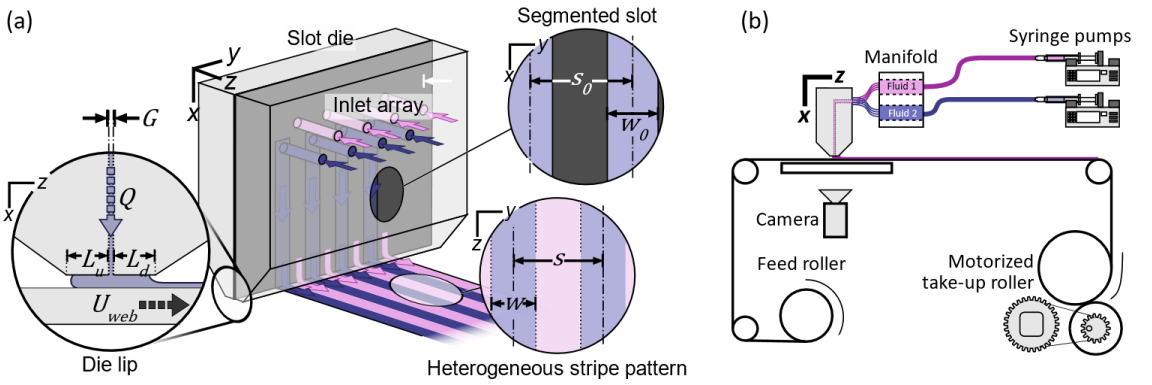

Figure 4.1 – (a) Schematic illustration of a multi-outlet slot die tool configured for heterogeneous stripe slot coating (HSSC). In addition to the coating parameters of conventional slot die coating, HSSC comprises a segmented internal slot with fixed width (w_0) and center-to-center spacing (s_0) of a series of outlets. The deposited pattern comprises continuous stripes of width *w* and center-to-center spacing *s*. (b) Roll-to-roll imaging system (R2RIS) configured with an HSSC tool.

4.2.2.3 Pattern Deposition with HSSC

Alternating narrow stripes of PVA and PEDOT:PSS were deposited using HSSC without hydrodynamic focusing as illustrated in Figure 4.3. As a basis for comparison with the conventional slot die approach, PVA was also deposited in homogeneous narrow stripes. Continuous-stripe films were deposited for various substrate velocity (U_{web}), total flow rate, (Q), flow rate-per-stripe ratio between fluid species ($Q_{PEDOT:PSS}/Q_{PVA}$), and coating gap (H) between the tool and substrate. Following deposition, oven drying and thermal annealing was carried out at 130°C for 30 minutes, following similar annealing procedures used in previous works[43, 91, 132, 202] with the expectation of improved electrical conductivity[208-210].

4.2.2.4 Optical Microscopy of Dry Films

Thermally cured and annealed PEDOT:PSS stripes were imaged using a Leica DVM6 confocal optical microscope. Both top-down and cross-section images were captured. The cross-sections were prepared in cast acrylic mold compound, Castamount purchased from Pace Technologies, and mechanically faced with an end mill.

4.2.2.5 Electrical Characterizations

DC electrical resistance was measured using a Keithley 2401 source-meter and a 4-contact probe. The electrical contacts were line structures constructed from polished copper, with 2.31 mm center-to-center spacing and 25.5 μm width. For conductivity measurements, the PEDOT:PSS stripe films were lifted from the PET substrate using scotch tape, in order to expose a pristine surface for contact with the copper line probes. Electrical conductivity was calculated from the resistance measured across the inner two line probes, which have an effective spacing of a 2.29 mm. The thicknesses of individual samples were measured directly from optical microscopy of prepared cross-sections.

4.3 Role of Interfacial Tension in Post-Deposition Stability

In all previous discussions and demonstrations of heterogeneous stripe slot coating, mixing across interfaces between fluid materials has been assumed to be negligibly small. The resulting alternating-stripe structures have been treated as immiscible in the sense that the time scale of diffusion transport is large compared to the time scales for advection and

post-deposition film curing. The previous discussions have also assumed that the interfacial tension associated with the fluid phases is zero, as might be expected for two solutions of the same polymer at different concentrations. Here, wetting equilibrium of the deposited alternating-stripe film is briefly considered for a case that does not make these assumptions. For brevity, fluid materials that exhibit a sharp interface with nonzero tension – for example, oil and water – will be referred to as immiscible for the purposes of this section. Assuming all other fluid domains, including deposition flow through the heterogeneous liquid bridge, permit deposition of the desired continuous-stripe pattern, the post-deposition heterogeneous film is subject to the wetting regime illustrated in Figure 4.2. Here, Young's equation for wetting and spreading is used to construct a macro-scale view of the equilibrium state[211].

Figure 4.2(a) illustrates the case where the two immiscible fluids do not interact. This corresponds to successive deposition of two fluid species, each by successive process steps. Static equilibrium of the resulting heterogeneous structure is given by the following:

$$\gamma_{G,S} = \gamma_{S,A} + \gamma_A \cos(\theta_A) \tag{4.1a}$$

$$\gamma_{G,S} = \gamma_{S,B} + \gamma_B \cos(\theta_B) \tag{4.1b}$$

Above, $\gamma_{G,S}$ is the gas-solid interfacial energy, γ_A and γ_B are surface tension values, and *A* and *B* subscripts denote liquid species. In Figure 4.2(a), the liquid-solid interfacial energies

for both fluids *A* and *B* are assumed to be similar in magnitude ($\gamma_{S\text{-}A} \approx \gamma_{S\text{-}B}$), and the surface tension of *B* is assumed to be greater than that of *A* ($\gamma_A < \gamma_B$).

By comparison, the case where liquids *A* and *B* are allowed to interact includes a liquid-liquid interface, a liquid-liquid-gas contact line, and a liquid-liquid-solid contact line as illustrated in Figure 4.2(b). At the liquid-liquid-solid contact line, static equilibrium is given by:

$$0 = \gamma_{S,B} - \gamma_{S,A} + \gamma_{AB}\cos\left(\theta_{B,A}\right) \tag{4.2}$$

Where γ_{AB} is the liquid-liquid interfacial energy, $\gamma_{S,A}$ and $\gamma_{S,B}$ are liquid-solid interfacial energies, and $\theta_{B,A}$ is the contact angle of fluid species *B* with *A* as the outer phase. To preclude any Rayleigh-Taylor instabilities, it is also assumed that the density of *B* is greater than the density of *A*

For most immiscible fluids at room temperature, the liquid-liquid interfacial tension can be assumed to be significantly smaller than the surface tension of either fluid *A* or fluid *B* ($\gamma_{AB} \ll \gamma_A$, $\gamma_{AB} \ll \gamma_B$). Comparing the liquid-liquid-solid contact line in Figure 4.2(b) with the scenario in Figure 4.2(a), the contact angle of liquid phase *B* must adjust to a significantly smaller value than the case illustrated in Figure 4.2(a). Since the liquid regions are finite in volume, this corresponds to spreading of *B* into *A* along the substrate.

Similarly, at the liquid-liquid-gas contact line, static equilibrium is given by Young's equation as:

$$0 = \gamma_{AB} - \gamma_A \cos(\varphi_A) + \gamma_B \cos(\varphi_B) \tag{4.3a}$$

$$0 = \gamma_A \sin(\varphi_A) - \gamma_B \sin(\varphi_A) \tag{4.3b}$$

Where φ_A and φ_B denote contact angles at the liquid-liquid-gas contact. Here, the small value of γ_{AB} relative to either surface tension produces a significant difference in contact angles for the two fluid species, corresponding to a preferential wetting of *A* along the surface of *B*. Together, the behaviors of both contact lines implied by Equations (4.2) and (4.3) produce the shallow sawtooth-like structure illustrated in Figure 4.2. Thus, the equilibrium analysis describes a spreading mechanism driven by the interface between two immiscible liquid phases in HSSC.

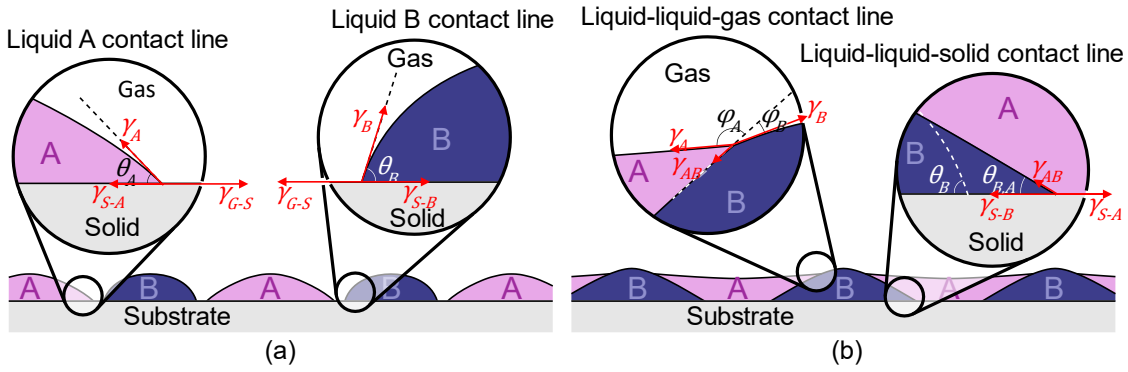

Figure 4.2 – Schematic of macro-scale wetting equilibrium of alternating stripes of two immiscible materials, for the scenarios where (a) the liquid phases interact to form a liquid-liquid interface and (b) where the liquid phases remain separate. Surface tension of liquid phases *A* and *B* are denoted as γ_A and γ_B, respectively, and γ_{AB} is the interfacial tension between *A* and *B*. The surface energy of the substrate in atmosphere, in liquid A, and in liquid B, are denoted as $\gamma_{G\text{-}S}$, $\gamma_{S\text{-}A}$, and $\gamma_{S\text{-}B}$, respectively. Adapted with permission from [212].

The wetting regime described by Young's equations is demonstrated with several immiscible fluid pairs in Figure 4.3. In the context of HSSC, this wetting regime has a significant and detrimental effect, as illustrated in Figure 4.3(g). Co-deposition of 24 wt.% PVA and PDMS has been carried out to generate the continuous-stripe pattern pictured, with less than 1 wt.% dye added to the PVA for the purpose of visualization. While relatively narrow stripes of each material are deposited through single-material liquid bridges, the onset of fluid-fluid interaction near the center of the pattern, as shown in Figure 4.3(g) corresponds to abrupt and significant spreading of the stripes. This is due to preferential spreading of the second fluid along the surface of the first fluid, which follows from Equation (4.3) provided that there is a significant difference between the geometric angles φ_A and φ_B. This condition is achieved for each of the three fluid pairs in Figure 4.3

since the interfacial tension is roughly an order of magnitude lower than the surface tension for either fluid. Specifically, the interfacial tension between PVA and PDMS, PVA and VPO, and glycerol and VPO are 5.3, 8.2, and 9.1 mN m^{-1}, respectively, at 25°C. By comparison, the surface tension of 24 wt.% PVA, 95 wt.% glycerol, PDMS, and VPO are 41, 64, 20, and 31 mN m^{-1}, respectively, at 25°C and 48 ± 2% relative humidity.

The formation of the immiscible fluid-fluid interface corresponds to a transition between wetting equilibrium states that is not conducive to high-resolution pattern features. It should be noted that the wetting properties of the fluid pairs discussed above encompass a representative range for coating fluids at ambient conditions. Therefore, it is reasonable to expect this behavior for other co-deposited fluids that form a liquid interface with nonzero interfacial tension. Considering the effect of this negative phenomenon on the HSSC process, only miscible fluids are considered for the remainder of the experimental work.

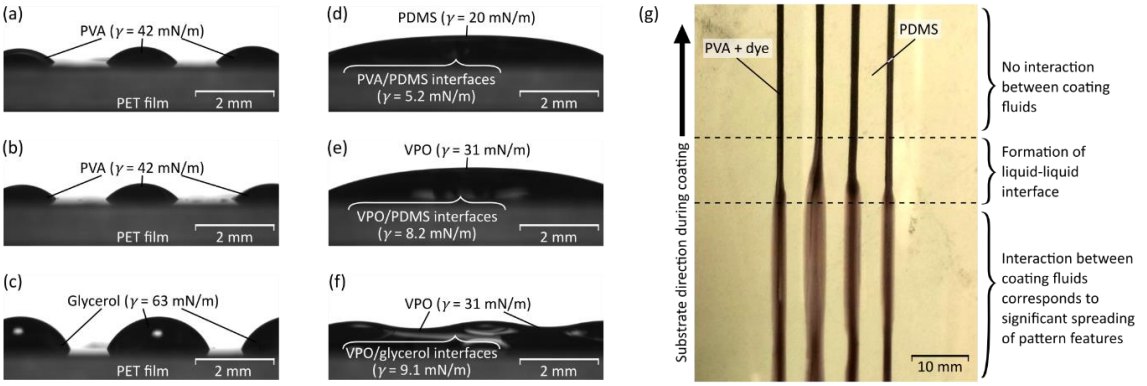

Figure 4.3 – Wetting behavior of heterogeneous narrow stripe films structures comprising two immiscible liquids. Profile views of the film structure for three immiscible fluid pairs (a-c) with only the denser of the two fluid species deposited in narrow stripes, and (d-f) after deposition of the second fluid species. (g) Onset of severe spreading in a PVA-PDMS narrow stripe pattern due to formation of the liquid-liquid interface. Reproduced with permission from [212].

4.4 Heterogeneous Stripe Slot Coating of PEDOT:PSS

4.4.1 Pattern Morphology

Microscopy images of individual stripes, shown in Figure 4.4(a) and (b), exhibit gradated regions roughly 200-300 μm across and the images constitute the majority of total stripe width (*w*). Microscopy images of composite PEDOT:PSS-PVA stripes deposited with HSSC, shown in Figure 4.4(a) and (b), exhibit gradated regions roughly 200-300 μm across, and constituting the majority of total stripe width. Since the composition of the mixture does not appear to vary across the film thickness at the resolution available in the cross-sectional microscopy images in Figure 4.4(a2) and Figure 4.4(b2), the available data suggests that these gradated regions represent an interphase, and comprise a blend of PEDOT:PSS and PVA. Regions of concentrated PEDOT:PSS are apparent along the

centerlines of stripes and at the lateral edges of the entire film, especially at higher PEDOT:PSS loading.

Using the HSSC approach, it is primarily the volume loading ratio between the two coating fluids ($Q_{PEDOT:PSS}/Q_{PVA}$) that determines the feature size, rather than Q, U_{web}, and H as with conventional slot die coating of narrow stripes. Examining w and center-to-center spacing (s) as functions of $Q_{PEDOT:PSS}/Q_{PVA}$ in Figure 4.4(c), stripe width appears to exhibit higher process sensitivity than s, which is largely determined by outlet spacing of the coating tool (w_0). The slight decrease in s with increasing $Q_{PEDOT:PSS}/Q_{PVA}$ appears to originate from a redistribution of conductive ink toward the lateral edges of the film, which can be observed in Figure 4.4(a) and (b). Similarly, w is sensitive to $Q_{PEDOT:PSS}/Q_{PVA}$, but not directly proportional. The film samples in Figure 4.4 (a) and (b), for example, correspond to only a 5% increase in stripe width resulting from a 100% increase in PEDOT:PSS loading. In fact, the major difference between pattern morphology in the two samples is not overall stripe width, but concentration of PEDOT:PSS along the centerline of the stripe. This suggests that for the materials and coating conditions considered here, stripe width is defined largely by the passive mixing processes that produce the gradated interphase region. The segmented slot geometry of the HSSC tool precludes mixing upstream from the slot outlet, it follows that these processes occur either within the coating bead or after deposition and prior to thermal curing.

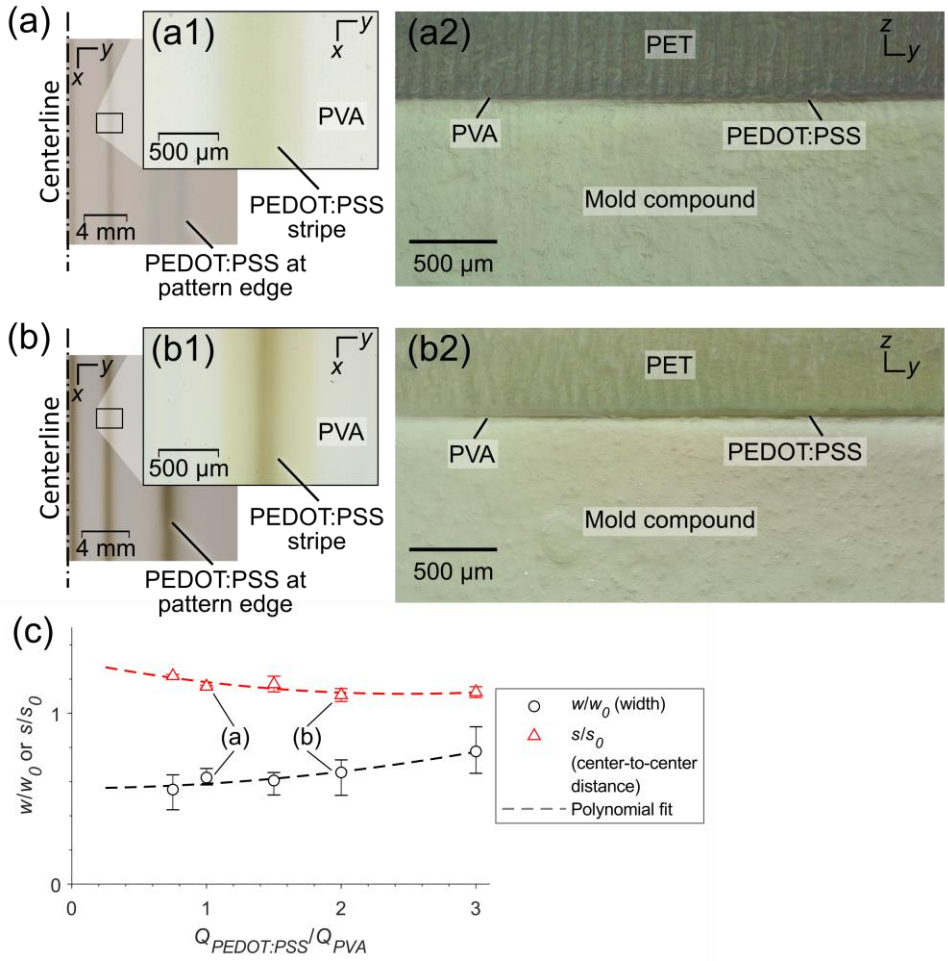

Figure 4.4 – Optical microscopy of dry films for (a) $Q_{PEDOT:PSS}/Q_{PVA}$ = 1.0 and (b) $Q_{PEDOT:PSS}/Q_{PVA}$ = 2.0, with redistribution of PEDOT:PSS to the lateral edges of the pattern indicated. Individual stripes from (a) and (b) are shown from top in (a1) and (b1), respectively. Cross-sectional images of PEDOT:PSS-PVA interphase regions from (a) and (ba) are shown in (a2) and (b2), respectively. (c) Pattern feature size as a function of $Q_{PEDOT:PSS}/Q_{PVA}$, with process conditions corresponding (a) and (b) indicated. Here, w and s are normalized to outlet dimensions w_0 = 0.94 mm and s_0 = 2.9 mm, respectively, while $Q_{PEDOT:PSS}$ and Q_{PVA} represent the flow rate-per-stripe for corresponding fluid species. Adapted with permission from [212].

4.4.2 Electrical Performance

Electrical conductivity (σ_e) of films after thermal is illustrated in Figure 4.5 across a range of feature sizes. For comparison, un-doped PEDOT:PSS exhibits electrical conductivity that ranges from 10^{-2} to 10^{0} S cm^{-1} as reported in previous literature [43, 204, 208, 213, 214]. In Figure 4.5(a), the correlation between σ_e and $Q_{PEDOT:PSS}/Q_{PVA}$ appears roughly linear for $Q_{PEDOT:PSS}/Q_{PVA} < 1.5$, and begins to level off toward 1.5 S cm^{-1} for $Q_{PEDOT:PSS}/Q_{PVA} > 1.5$. The observed conductivity is likely tied to the concentration of PEDOT:PSS across the overall width of the stripe, while the diminishing correlation at higher values of $Q_{PEDOT:PSS}/Q_{PVA}$ can be explained by the observed redistribution of PEDOT:PSS to the pattern edges. The range of σ measured at each $Q_{PEDOT:PSS}/Q_{PVA}$ value is largely attributable to an unequal distribution of PEDOT:PSS across individual stripes. Although the total value of $Q_{PEDOT:PSS}$ is pre-metered, the flow rate delivered to individual stripes is subject to the geometry of the manifold and flexible tubing upstream from the coating tool inlets, as well as possible transient wetting and mixing effects at the liquid bridge and motor vibration throughout the experimental apparatus.

Electrical conductance (G) as a function of the cross-sectional area of individual stripes ($w \cdot t_{dry}$) is shown in Figure 4.5(b). The correlation between G and $w \cdot t_{dry}$ is roughly linear across the range of feature sizes produced. For stripes with large $w \cdot t_{dry}$, the PVA-free portion of the stripe is also large, which implies comparatively high conductance. Furthermore, extrapolation of the linear trend predicts $G = 0$ around $w \cdot t_{wet} = 1{,}900$ μm^2. For film thicknesses in the range of 5-10 μm, this corresponds to stripe widths of 190-380

μm. Notably, this length scale corresponds roughly to that of the PEDOT:PSS-PVA interfaces shown in Figure 4.5(a) and Figure 4.5(b). In summary, these observations indicate that the limiting feature size of roughly 400 μm, below which electrical conductance drops to zero, reflects the importance of the PEDOT:PSS-depleted interphase region discussed in Section 4.4.1, relative to the total width of the stripe.

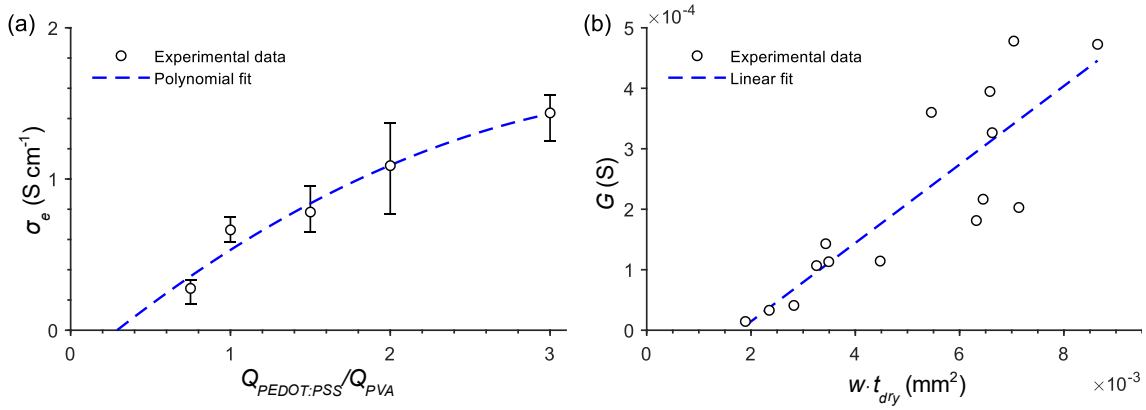

Figure 4.5 – (a) Electrical conductivity (σ_e) as a function of $Q_{PEDOT:PSS}/Q_{PVA}$ for various samples. Error bars indicate the full range of variation for a given flow rate ratio. (b) Electrical conductance (G) as a function of apparent cross-sectional area (wt_{dry}) for individual printed stripes. Adapted with permission from [212].

4.5 Feature Size Control with HSSC

4.5.1 Deposition of Aqueous PVA

Deposition of 15 wt.% PVA in narrow stripes illustrated in Figure 4.6 both for the HSSC approach illustrated in Figure 4.1(a) and the narrow stripe coating approach introduced in Figure 3.2(a) for C/EOD and conventional stripe coating. The narrow coating bead structure in Figure 4.6(a) shows a strong dependency on both coating gap (H) and

flow rate (Q). The mapping between these two process inputs and stripe width (w) is shown in Figure 4.6(b). Q and H are plotted in dimensionless forms, Q^* and H^*, respectively, as follows:

$$Q^* \equiv \frac{Q/U_{web}}{Gw_0} \tag{4.4a}$$

$$H^* \equiv H/(L_u + L_d + G) \tag{4.4b}$$

As expected from previous studies[154, 197] as well as the investigations in Chapter 3, the mapping in Figure 4.6(b) reflects complex spreading and confinement behavior along the bottom of the coating tool. The coating bead structure for HSSC is different in two respects. Co-deposition of a second 15 wt.% solution with <2% added dye results in the heterogeneous coating flow shown in Figure 4.6(c). For HSSC, the pattern is defined by fluid-fluid interfaces rather than the edges of the wetted area. Furthermore, the coating bead for HSSC is wide compared to the case in Figure 4.6(a).

Based on these key aspects of the HSSC coating bead structure, the process behavior of HSSC is very different than for conventional narrow stripe slot coating or C/EOD. As shown in Figure 4.6(d), the pattern output from HSSC is relatively insensitive to both H and Q, in contrast to the trends in Figure 4.6(c). The average w slightly exceeds w_0 for the runs considered here, and the overall variation in stripe width is more pronounced at lower values of H and the higher Q value. The reason for this is that while heterogeneous

stripes towards the center of the outlet region are of relatively stable width, the width of the entire flow is still subject to the spreading effects present in Figure 4.6(a). In contrast to C/EOD, however, spreading of the overall pattern in HSSC primarily affects only the outermost stripes, where the edges of the coating are influential. Toward the center of the coating bead, flow is approximately two-dimensional, and undistorted by the pattern edges. Thus, the resulting pattern is largely preserved from outflow at the die orifice. This outflow is patterned by the segmented shim geometry illustrated in Figure 4.1(b), rather than the traditional process inputs which determine wet film thickness. The significance of this result to the processing approach is that HSSC provides a means to de-couple the width and spacing of stripes from conventional slot die process parameters, Q, U_{web}, and H.

In summary, while the same principles of spreading behavior apply to both HSSC and C/EOD, HSSC provides an additional mechanism, the heterogeneity of the coating flow, to generate the pattern. This has been demonstrated here for a relatively forgiving case of two coating materials with nearly identical properties. However, it is also important to consider a case where the two coating materials have significantly different wetting properties, which is discussed in the section that follows.

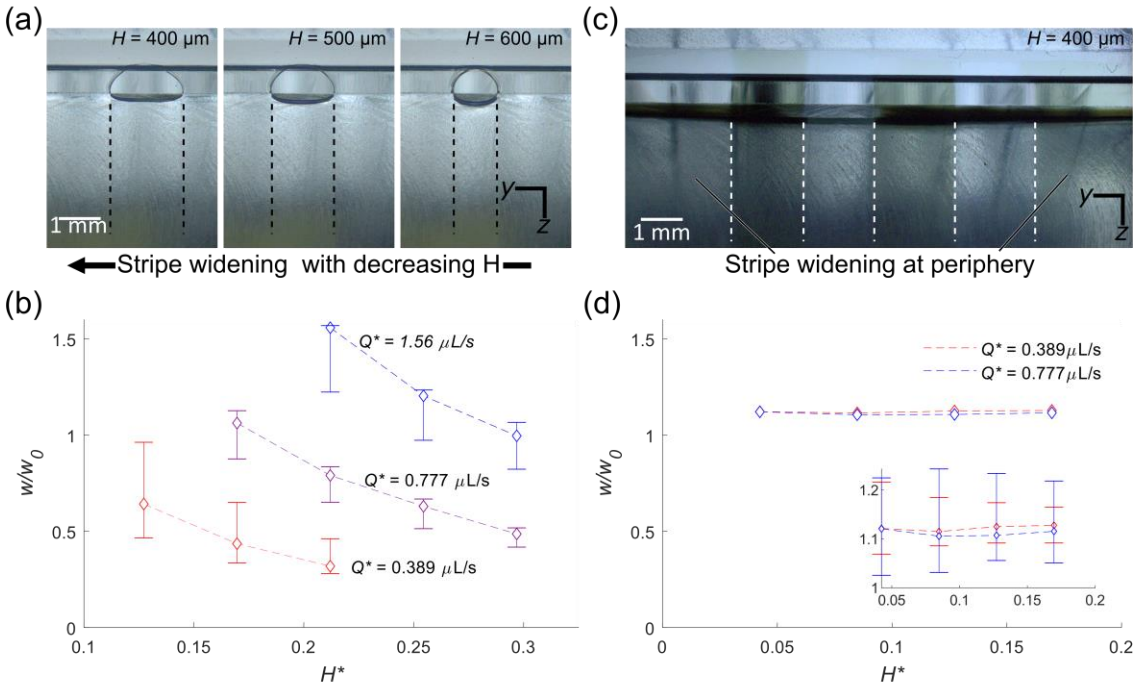

Figure 4.6 – (a) Spreading behavior of a 15 wt.% PVA narrow coating bead resulting in a range of stable coated stripe widths. (b) A heterogeneous wide coating bead comprising regions of 15 wt.% PVA (light) and 15 wt.% PVA with <2% added. (c) Width of the stripe produced by the coating flow in (a) across various Q^* and H^* for fixed U_{web} = 10 mm/s. (d) Stripe widths produced by the HSSC process depicted in (b) for U_{web} = 5 mm/s and various Q^* and H^*. Stripe width is normalized to w_0 = 4.0 mm in both (c) and (d).

4.5.2 Co-deposition of Aqueous PEDOT:PSS and PVA

Pattern morphology as a function of process conditions for heterogeneous PEDOT:PSS/PVA films, compared against conventional slot die-deposited narrow 10 wt.% PVA stripes, is shown in Figure 4.7. The metric of interest for this investigation is stripe width (w) normalized against the outlet width (w_0), as in Section 4.5.1. The rate of coating fluid deposition, Q, and coating gap, H, are again represented in dimensionless form according to Equations (4.4a) and (4.4b). As expected, w/w_0 is strongly influenced by

both process inputs for conventional coating of 10 wt.% PVA in narrow single-fluid stripes, as shown in Figure 4.7(a). Whereas the trendlines in Figure 4.6(b) are plotted across H^*, the trendlines in Figure 4.7(a) are plotted across Q^*. However, both charts illustrate that stripe width depends significantly on Q, U_{web}, and H for C/EOD and conventional narrow stripe slot coating of a single material. This dependence necessitates significant process characterization in order to achieve a desired stripe width and average wet film thickness (t_{wet}) reliably.

By contrast, the HSSC process illustrated in Figure 4.7(b) produces a relatively constant pattern morphology over a range of Q^* and H^*. This aspect of process control mirrors the results in Figure 4.6(d) for deposition of 15 wt.% PVA. The capability of HSSC to deposit a pattern morphology that remains constant across conventional process inputs for slot die coating is a key advantage for the approach. The results in Figure 4.7(b) confirm that this advantage is transferable to a material system with widespread use in printed electronics. The PEDOT:PSS/PVA material system also represents a case where the wetting properties of the two fluids differ significantly. These wetting properties are worthy of a closer look, which is provided in Section 4.5.3.

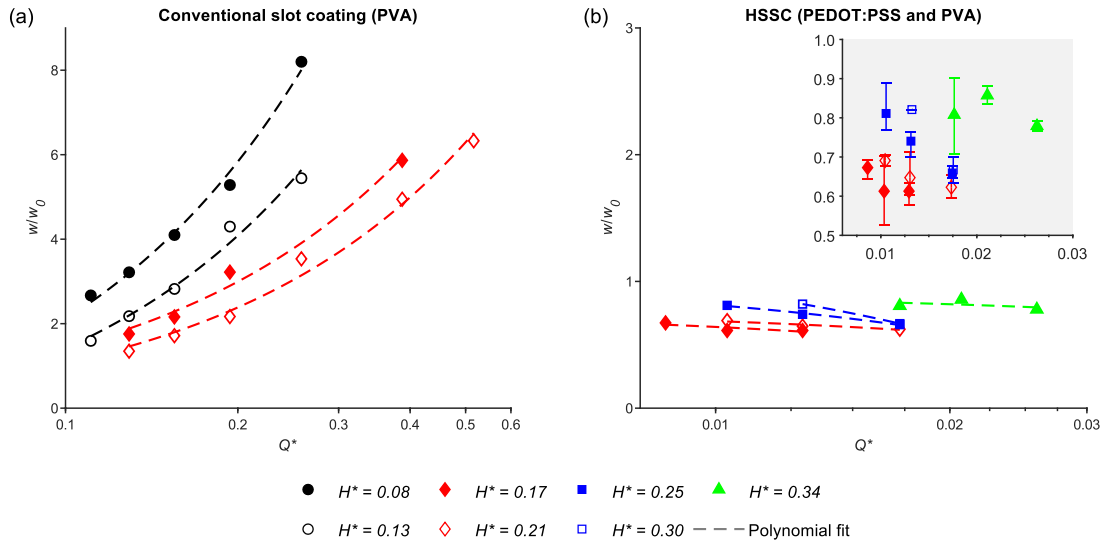

Figure 4.7 – Pattern morphology of the wet film measured in-process across a range of *Q and *H** for (a) the conventional stripe slot coating approach and (b) the heterogeneous stripe slot coating approach. Outlet width w_0 is set to 1.4 mm and 0.94 mm in (a) and (b), respectively. Adapted with permission from [212].**

4.5.3 Mitigation of Dewetting

For processing of PEDOT:PSS inks on plastic substrates, surfactants or other additives for prevention of post-deposition dewetting have so far been treated as mandatory in relevant literature[203, 204, 215]. However, the results presented in Section 4.4 have demonstrated that this material formulation requirement can be forgone by co-depositing a support material, PVA in this case, which permits mixing with the PEDOT:PSS ink at a sufficiently slow rate to develop and maintain the printed pattern after deposition. To further investigate the this favorable wetting behavior, Figure 4.8 presents measurements of contact angles on PET substrate for various mixtures of PEDOT:PSS ink and 10 wt.% PVA under ambient conditions, 25°C and 48 ±2% relative humidity.

In Figure 4.8(a), pinning of the contact line is observed for every mixture considered, even with as little as 0.5 wt.% PVA added. Furthermore, the majority of variation in advancing contact angle falls within the narrow range of $0 \leq \chi_{PVA} < 0.1$, where χ_{PVA} is the volume fraction of 10 wt.% PVA in the aqueous PVA-PEDOT:PSS mixture. These results suggest the PVA itself acts to enhance wetting of the heterogeneous films, and thus, that the PVA-derived wettability enhancement is present at the heterogeneous liquid phase boundaries. Additionally, it is worth noting the alternating-stripe patterns remain stable even in cases with high PEDOT:PSS volume loading, which contain significant regions of PVA-free wet film. It may be the case that the PVA acts as a structural scaffold for the PEDOT:PSS stripes as well as a wettability enhancer, which further contributes to the excellent post-deposition stability of the deposited stripe pattern.

The significance of these results is related to the constraints on wetting properties that routinely necessitate material formulation requirements for conventional printing methods. Effectively, the burden of satisfying the manufacturing process-imposed wettability requirement can be transferred from the functional ink to a non-functional support material.

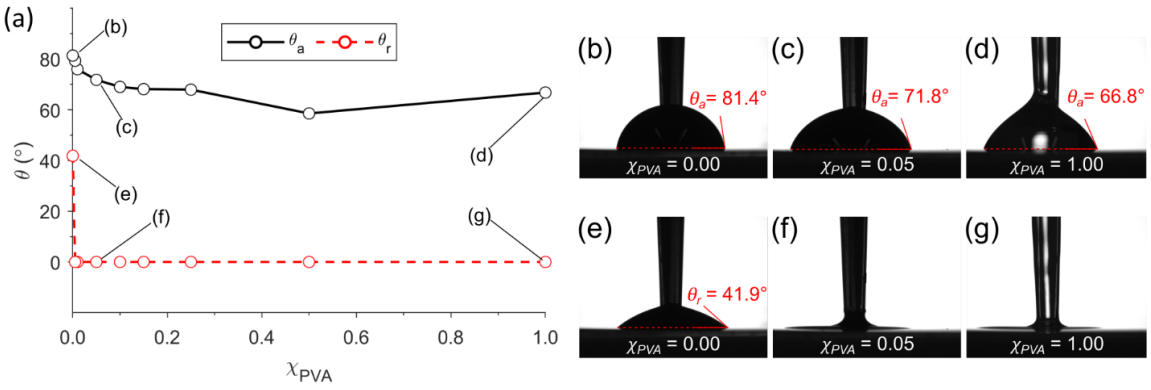

Figure 4.8 – (a) Advancing and receding contact angles of PEDOT:PSS/PVA mixtures ranging from various volume fraction of PVA (χ_{PVA}), where χ_{PVA} = 0 denotes as-received PEDOT:PSS solution and χ_{PVA} = 1 denotes 10 wt.% aqueous PVA. Where pinning of the contact line is observed, θ_r is recorded as 0. For χ_{PVA} = 1, χ_{PVA} = 0.05, and χ_{PVA} = 0, advancing contact angle images are shown in (b-d), and receding contact angles are shown in (e-g). Adapted with permission from [212].

4.6 Conclusions

In this chapter, continuous stripe features have been deposited using the slot die coating-inspired HSSC approach for a representative functional material, PEDOT:PSS. Conductive stripe features produced using the narrow stripe slot coating technique range from 400 to 850 µm in width, with electrical performance that compares favorably with published characterizations of PEDOT:PSS prior to standard acid post-treatments[43, 204, 208, 213, 214]. The observed correlations between stripe width and conductance, in conjunction with visualizations of the PEDOT:PSS-PVA interface region, suggest that the conductive portion of each stripe is concentrated near its centerline. Additionally, for the conditions used in this study, the majority of added PEDOT:PSS loading appears to result in further concentration of this region, rather than to expanding the total width of the stripe.

Analysis of wetting equilibrium of the heterogeneous film has highlighted the role of fluid-fluid interfacial tension in promoting unwanted spreading after deposition. This necessitates the selection of miscible fluid materials for stable pattern deposition using HSSC. Within this constraint, however, HSSC has been shown to perform well with materials that are challenging to deposit using conventional coating techniques. The co-deposited secondary material that is inherent to HSSC offers a unique means to prevent dewetting. Effectively, the HSSC approach allows a functional material to be formulated on the basis of requirements other than processing, and thus provides for increased flexibility in material selection. Furthermore, advantages to process control over pattern morphology have also been demonstrated relative to conventional slot die coating. Stripe width has been successfully de-coupled from Q, U_{web} and H, the traditional process parameters that determine the total film thickness. This aspect of HSSC dramatically reduces the burden of process modeling that would otherwise be necessary to map process inputs to a desired pattern morphology.

CHAPTER 5. PERTURBATION ANALYSIS OF SINGLE-FLUID INTERNAL FLOW FOR HSSC WITH HYDRODYNAMIC FOCUSING

5.1 Introduction

Based on the experimental work conducted in Chapters 3 and 4, it is evident that there is a need to be able to predict pattern outflow from the HSSC tool. In this chapter, internal flow of a single fluid through the HSSC coating tool is analyzed using perturbation theory, a mathematical approach that facilitates physical interpretation of interrelated phenomena as discrete contributions from specific parameters. The key benefit of this approach for the present problem is the rich physical intuition it affords[216, 217]. In typical cases, this interpretation can be carried out to a significant extent on the final mathematical expressions, prior to case studies and visualized correlations. Perturbation theory also excels at valuating the accuracy gained by successive refinements to the solution before they are performed. Each successive iteration produces a correction phrased in terms of some small parameter with physical significance to the problem. The result of the first iteration, referred to as the leading-order solution, often reproduces the same final result as a judiciously simplified version of the problem. Effectively, the impact of this simplification on the accuracy of the solution is borne out by a comparison between leading-order terms and the remainder of the perturbation solution. Furthermore, this aspect

of perturbation theory tends to provide a quantifiable measure of assurance for a given result. Since the accuracy valuation is phrased in terms of parameters that govern the problem, it is straightforward to predict the circumstances under which a perturbation model will be appropriate, and those under which it will not, to a high degree of granularity.

In terms of the present application, perturbation theory offers a means to discern and justify simple correlations that predict HSSC feature size. These correlations are simply the leading-order terms in the asymptotic expansions produced by perturbation techniques. Higher-order terms produced by this approach are useful not only to refine the accuracy of the model, but to also describe in quantitative terms where simplified scaling may be sufficient. Additionally, perturbation theory facilitates interpretation of correlations between influential parameters and specific characteristics of the flow. This point helps ensure that this analysis provides fundamental insights that can be repurposed to other tool designs and even other applications.

5.2 Previous Modeling Efforts

The internal geometry of the HSSC tool is a planar slot converging at a moderate-to-abrupt ratio along the primary flow axis. While this geometry is novel in the context of slot die coating, similar internal flow geometries appear across a range of microfluidic areas spanning medicine, chemical synthesis, cell biology, and materials characterization[218-221]. The ubiquity of planar microfluidic platforms among these applications, due in large part to the ease of fabrication afforded by parallel-plate

architectures[222], has helped generate interest in modeling flow through planar channels of varying widths at low Reynolds number.

Balsa[223] conducted some of the pioneering work in this field, relating the streamwise vorticity of Hele-Shaw flow around an obstructing body to the curvature of the obstruction. The work by Balsa recognized the limitations of conventional Hele-Shaw theory[224] with respect to the boundary layers that form at sidewalls. Lauga et al. later considered a channel cross-section with gradually varying width and gradual curvature[225]. The work by Lauga et al. was concerned with the three-dimensionality of the flow in a slowly varying planar channel, and demonstrated analytically the existence of secondary flow in all cases where channel cross-section is not constant. This principle has been noted elsewhere and frequently exploited as a mechanism for laminar microchannel mixing[226-230]. Both works presented a perturbation analysis formulated about a small geometric parameter, similar to the analysis presented in this chapter.

Numerical and empirical modeling efforts have also been carried out on moderately varying slots and channels. An approximate model for microchannels with arbitrary cross-sections was developed by Akbari et al., based on dimensional analysis that accounted for inertial and frictional effects[231]. Duryodhan et al. produced empirical correlations based on experimental and computational results for planar microchannels that converge or diverge at a constant angle[232-234]. More recently, Tao et al.[235] and Goli et al.[236] extended these efforts to coupled converging-diverging and diverging-converging microchannel

geometries. These previous modeling efforts in relationship to the current work are summarized in Table 5.1.

Table 5.1 – Summary of previous modeling work for single-fluid flow through planar microchannels.

Authors	Assumptions [a]	Geometry [b]	Model type	Output	Validation
Balsa[223]	Stokes flow	Hele-Shaw flow with obstruction	Analytical (perturbation)	3D flow field	None
Lauga et al.[225]		Gradually varying width or curvature	Analytical (perturbation)	3D flow field	None
Akbari et al.[231]	Laminar and turbulent (k-epsilon model)	Gradually varying cross-section of arbitrary shape	Empirical	Channel flow resistance	Experimental; existing simplified models
Duryodhan et al.[232-234]		Diverging or converging width	Empirical & numerical (ANSYS Fluent)	Channel flow resistance	Experimental
Tao et al.[235]		Converging-diverging features	Empirical & numerical (ANSYS Fluent)	Channel flow resistance	Experimental
Goli et al.[236]		Gradual diverging-converging feature	Empirical & numerical (ANSYS Fluent)	Channel flow resistance	Experimental
Present study		Converging width, at arbitrary convergence angle	Analytical (perturbation)	3D flow field	None

[a] Except where stated otherwise, all models assume laminar, incompressible flow of Newtonian fluids and proceed from Navier-Stokes equations.

[b] Except where stated otherwise, geometry comprises a rectangular cross-section of constant height.

While the insights gained from these studies are valuable and relevant to the present problem, they are limited in two key respects. First, the perturbation analyses by Balsa[223] and Lauga et al.[225] proceed from the assumption that channel cross-section varies

gradually, and even among the various numerical studies in Table 5.1, 12° is the greatest convergence angle considered[233]. For HSSC, where it is of practical importance to minimize the total pressure drop and length along the converging slot feature, it is necessary to also consider moderate and even abrupt reductions in channel width. Furthermore, the various numerical and empirical studies in Table 5.1 focus primarily on pressure drop[232-234, 236], flow resistance[235, 236], and diodicity[233-235] of the microchannel geometry. However, passive mixing may be exhibited in HSSC, therefore, it is also important to develop an understanding of the sidewall boundary layers in the converging slot. Thus, the contribution of this work beyond previous efforts is the 3D flow field solution for a converging slot with large convergence angles.

5.3 Three-Dimensional Geometry

The HSSC tool incorporating co-laminar flow and hydrodynamic focusing of two materials is illustrated schematically in Figure 5.1(a). The key feature of this tool is the converging section of the rectangular slot. For the mathematical analysis, a portion of this converging section is designated as the domain of interest. The width of the slot is $2w_u$ at its inflow boundary of the domain, and $2w_d$ at the outflow boundary. Where β represents the change in slot half-width along the y-axis, per unit distance along the x-axis, the width of the slot at an arbitrary location along the x-axis is given by $w_{slot}(x) = 2w_u - 2\beta x$. It should be noted that since there is flexibility in the selection of the domain of interest, the values w_d and w_u can be a range of possible values for a given internal slot geometry, as

illustrated in Figure 5.1(b) and Figure 5.1(c), respectively. Specifically, w_d and w_u may be chosen anywhere along the converging region of the coating tool. The analysis that follows hereafter proceeds after the selection of a domain of interest, such that the definitions of w_u and w_d are fixed, unless otherwise noted.

The three-dimensional (3D) geometry of the converging portion of the slot is illustrated in Figure 5.1(d). The slot has a thickness of $2G$ along the z-axis, which is equal to the coating gap of the HSSC tool. Analysis of the flow field, in this domain, can be carried out most conveniently using a polar cylindrical coordinate system with the origin located at $(x, y, z) = (\beta^{-1}w_u, 0,0)$. The location of this origin corresponds to the hypothetical point at which the channel width narrows to zero, beyond the domain of interest. This choice of origin for the cylindrical coordinate system is convenient because allows the lateral boundaries of the channel to be described by a constant value, θ_H. Another subtle benefit is that ensures that the no-flux and no-slip boundary conditions at the wall are each enforced for separate velocity components.

In the cylindrical coordinate system, the walls of the channel are located at $z = \pm G$ and $\theta = \pm\theta_H$, where $\theta_H \equiv -\operatorname{atan}(\beta)$, as illustrated in Figure 5.1(e). The inflow boundary is located at $r = r_u$, where $r_u \equiv \beta^{-1}w_u$ and the domain of interest extends as far as $r \geq r_d$, where $r_d \equiv \beta^{-1}w_d$. Thus, r_u and r_d constitute two reference points around which the mathematical analysis will be constructed, and w_u and w_d are the channel widths at those

reference points. The conversion between Cartesian and cylindrical coordinate systems illustrated in Figure 5.1(e) is given by the following:

$$r = \sqrt{(x - x_O)^2 + (y - y_O)^2} = \beta^{-1}\sqrt{w_{slot}(x)^2 + \beta^2 y^2} \tag{5.1a}$$

$$\theta = \text{atan}\left(\frac{-(y - y_0)}{-(x - x_0)}\right) = -\,\text{atan}\left(\frac{\beta y}{w_{slot}(x)}\right) \tag{5.1b}$$

$$z = z \tag{5.1c}$$

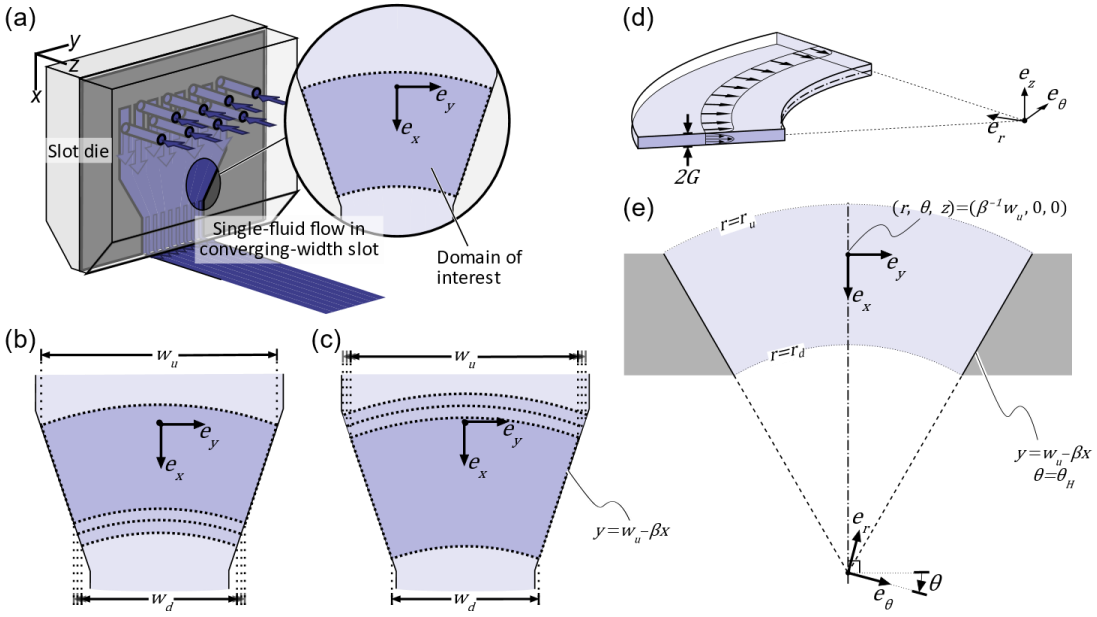

Figure 5.1 – (a) Geometry of an HSSC tool with a converging-width slot, configured for flow of only one coating material, with a domain of interest selected for the mathematical analysis. (b) Geometry of the converging portion of the HSSC internal slot. The velocity field at $\theta = 0$ and $z = 0$ is represented by arrows projected onto the top and front channel boundaries, respectively. (c) Top-down view of the microfluidic slot denoting the locations of r-axis and θ-axis boundaries. Unit vectors for(r, θ, z) and (x, y, z) coordinates are denoted as (e_r, e_θ, e_z) and (e_x, e_y, e_z), respectively.

5.4 Governing Equations and Boundary Conditions

The analysis here assumes incompressible, steady flow and $Re \ll 1$. Additionally, the velocity field is assumed to be independent of the pressure profiles far upstream from $r = r_u$ and far downstream from $r = r_d$. The viscosity of the fluid, μ, is assumed to be Newtonian, within the range of shear rate achieved during HSSC processing. With these assumptions, the governing equations for continuity and momentum are, respectively:

$$\nabla \cdot \vec{u} = 0 \qquad \text{(Continuity)} \qquad (5.2a)$$

$$0 = -\nabla p + \mu \nabla^2 \vec{u} \qquad \text{(Momentum)} \qquad (5.2b)$$

where $\vec{u}$ denotes the vector representation of the velocity field, and p is the scalar pressure field. In the cylindrical coordinate system, the governing equations are given by:

$$\frac{1}{r}\frac{\partial}{\partial r}(ru_r) + \frac{1}{r}\frac{\partial}{\partial \theta}(u_\theta) + \frac{\partial}{\partial z}(u_z) = 0 \qquad \text{(Continuity)} \qquad (5.3a)$$

$$\frac{\partial p}{\partial r} = \mu\left[\frac{1}{r}\frac{\partial}{\partial r}\left(r\frac{\partial u_r}{\partial r}\right) + \frac{1}{r^2}\frac{\partial^2 u_r}{\partial \theta^2} + \frac{\partial^2 u_r}{\partial z^2} - \frac{u_r}{r^2} - \frac{2}{r^2}\frac{\partial u_\theta}{\partial \theta}\right] \qquad (r\text{-momentum}) \qquad (5.3b)$$

$$\frac{1}{r}\frac{\partial p}{\partial \theta} = \mu\left[\frac{1}{r}\frac{\partial}{\partial r}\left(r\frac{\partial u_\theta}{\partial r}\right) + \frac{1}{r^2}\frac{\partial^2 u_\theta}{\partial \theta^2} + \frac{\partial^2 u_\theta}{\partial z^2} - \frac{u_\theta}{r^2} + \frac{2}{r^2}\frac{\partial u_r}{\partial \theta}\right] \qquad (\theta\text{-momentum}) \qquad (5.3c)$$

$$\frac{\partial p}{\partial z} = \mu\left[\frac{1}{r}\frac{\partial}{\partial r}\left(r\frac{\partial u_z}{\partial r}\right) + \frac{1}{r^2}\frac{\partial^2 u_z}{\partial \theta^2} + \frac{\partial^2 u_z}{\partial z^2}\right] \qquad (z\text{-momentum}) \qquad (5.3d)$$

where u_r, u_θ, and u_z are the velocity components along $\boldsymbol{e_r}$, $\boldsymbol{e_\theta}$, and $\boldsymbol{e_z}$, respectively. Asymptotic approximations of the velocity and pressure fields are developed around the small parameter α, which is the ratio between the slot gap and the slot width at the outflow boundary:

$$\alpha \equiv \frac{G}{w_d} \qquad (5.4)$$

Physically, α represents the inverse of the aspect ratio of the channel at its greatest value within the domain of interest. Assuming that $\alpha \ll 1$ implies that z-axis dimension of the slot is narrow relative to its width along the y-axis. To represent Equations (5.3a)- (5.3d) in dimensionless form, the following scaling is used:

$$(r, z) = (w_d\hat{r}, G\hat{z}) = G(\alpha^{-1}\hat{r}, \hat{z}) \qquad (5.5a)$$

$$\theta = \hat{\theta} \qquad (5.5b)$$

$$(u_r, u_\theta, u_z) = \left(\frac{Q}{w_d G}\hat{u}_r, \frac{Q}{w_d G}\hat{u}_\theta, \frac{Q}{w_d^2}\hat{u}_z\right) = \left(\frac{\alpha Q}{G^2}\right)(\hat{u}_r, \hat{u}_\theta, \alpha\hat{u}_z) \qquad (5.5c)$$

$$p = \left(\frac{\mu Q}{G^3}\right)\hat{p} \qquad (5.5d)$$

Based on Equations (5.5a)- (5.5d) above, G, $\alpha Q/G^2$, and $\mu Q/G^3$ are, respectively, the length scale, velocity scale, and pressure scale for this geometry, where Q is the total volumetric flow rate through the channel. In the dimensionless polar cylindrical coordinate system, the channel walls are located at $\hat{z} = \pm 1$ and $\hat{\theta} = \pm\theta_H$. The domain of interest extends from the inflow boundary at $\hat{r} = w_d^{-1} r_u$ to $\hat{r} = w_d^{-1} r_d$, or equivalently, from $\hat{r} = (r_u/r_d)\csc(\theta_H)$ to $\hat{r} = \csc(\theta_H)$. The channel is assumed to reduce at a moderately large rate along the primary flow axis, such that $\theta_H < \frac{\pi}{2}$and $\hat{r} > 1$. For reference, these scales apply to the Cartesian coordinate system as follows:

$$(x, y, z) = (w_d\hat{x}, w_d\hat{y}, G\hat{z}) = w_d(\hat{x}, \hat{y}, \alpha\hat{z}) \tag{5.6a}$$

$$(u, v, w) = \left(\frac{\alpha Q}{G^2}\right)(\alpha^{-1}\hat{u}, \alpha^{-1}\hat{v}, \hat{w}) \tag{5.6b}$$

The dimensionless governing equations are then given by Equations (5.7a)-(5.7d) below, with hats on the dimensionless variables dropped hereafter for the sake of brevity:

$$\frac{1}{r}\frac{\partial}{\partial r}(ru_r) + \frac{1}{r}\frac{\partial}{\partial \theta}(u_\theta) + \frac{\partial}{\partial z}(u_z) = 0 \tag{5.7a}$$

$$\frac{\partial p}{\partial r} = \alpha^2\frac{1}{r}\frac{\partial}{\partial r}\left(r\frac{\partial u_r}{\partial r}\right) + \alpha^2\frac{1}{r^2}\frac{\partial^2 u_r}{\partial \theta^2} + \frac{\partial^2 u_r}{\partial z^2} - \alpha^2\frac{u_r}{r^2} - \alpha^2\frac{2}{r^2}\frac{\partial u_\theta}{\partial \theta} \tag{5.7b}$$

$$\frac{1}{r}\frac{\partial p}{\partial \theta} = \alpha^2\frac{1}{r}\frac{\partial}{\partial r}\left(r\frac{\partial u_\theta}{\partial r}\right) + \alpha^2\frac{1}{r^2}\frac{\partial^2 u_\theta}{\partial \theta^2} + \frac{\partial^2 u_\theta}{\partial z^2} - \alpha^2\frac{u_\theta}{r^2} + \alpha^2\frac{2}{r^2}\frac{\partial u_r}{\partial \theta} \tag{5.7c}$$

$$\frac{\partial p}{\partial z} = \alpha^4 \frac{1}{r}\frac{\partial}{\partial r}\left(r\frac{\partial u_z}{\partial r}\right) + \alpha^4 \frac{1}{r^2}\frac{\partial^2 u_z}{\partial \theta^2} + \alpha^2 \frac{\partial^2 u_z}{\partial z^2} \tag{5.7d}$$

The velocity field governed by the equations above is subject to the following boundary conditions:

$$u_r = u_z = 0 \text{ at } \theta = \theta_H \quad \text{(No-slip, } \theta\text{-axis boundary)} \tag{5.8a}$$

$$u_\theta = 0 \text{ at } \theta = \theta_H \quad \text{(No-flux, } \theta\text{-axis boundary)} \tag{5.8b}$$

$$u_r = u_\theta = 0 \text{ at } z = 1 \quad \text{(No-slip, } z\text{-axis boundary)} \tag{5.8c}$$

$$u_z = 0 \text{ at } z = 1 \quad \text{(No-flux, } z\text{-axis boundary)} \tag{5.8d}$$

$$\frac{\partial u_r}{\partial \theta} = u_\theta = \frac{\partial u_z}{\partial \theta} = 0 \text{ at } \theta = 0 \quad \text{(Symmetry about } \theta = 0\text{)} \tag{5.8e}$$

$$\frac{\partial u_r}{\partial z} = \frac{\partial u_\theta}{\partial \hat{z}} = u_z = 0 \text{ at } z = 0 \quad \text{(Symmetry about } z = 0\text{)} \tag{5.8f}$$

The velocity field is also subject to a flow rate condition:

$$-1 = \int_{-1}^{1} \int_{-\theta_H}^{\theta_H} u_r \, r d\theta dz \qquad \text{(Flow rate condition)} \tag{5.8g}$$

Finally, the following condition is used to derive the pressure field relative to a point in the channel beyond the outflow boundary:

$$p = p_d \text{ at } (r, \theta, z) = (r_d, 0, 0) \qquad \text{(Reference pressure)} \tag{5.8h}$$

Setting $\alpha = 0$ reduces the order of Equations (5.7a)-(5.7d) such that θ-axis boundary conditions cannot all be satisfied simultaneously. Therefore, this analysis seeks a composite expansion incorporating inner velocity fields $\vec{V} \equiv (V_r, V_\theta, V_z)$ and $\overrightarrow{W} \equiv (W_r, W_\theta, W_z)$, which are valid near $\theta = \theta_H$ and $\theta = -\theta_H$, respectively, and an outer velocity field $\vec{U} \equiv (U_r, U_\theta, U_z)$, which is valid far from the θ-axis boundaries. In physical terms, $\vec{V}$ and $\overrightarrow{W}$ represent the boundary layers of the flow at the sidewalls of the channel. $\vec{U}$, which represents outer flow beyond the influence of these boundary layers, is nevertheless subject to a squeezing effect due to decreasing channel width.

5.5 Outer Solution

For the outer velocity solution, an asymptotic expansion of the following form is assumed:

$$(U_r, U_\theta, U_z, p) = \left(U_{r,0}, U_{\theta,0}\,, U_{z,0}, p_0\right) + \alpha\left(U_{r,1}, U_{\theta,1}\,, U_{z,1}, p_1\right) + \mathcal{O}(\alpha^2) \tag{5.9}$$

The term $\mathcal{O}(\alpha^2)$ in Equation (5.9) denotes terms that are of order α^2. Similarly, $\mathcal{O}(1)$ and $\mathcal{O}(\alpha)$ are used hereafter to refer to terms of order 1 (leading order) and order α, respectively. Substituting $(u_r, u_\theta, u_z, p) = (U_r, U_\theta, U_z, p)$ in Equations (5.7a)-(5.7d) and setting $\alpha = 0$ yields the leading-order $\mathcal{O}(1)$ governing equations for the outer velocity:

$$\frac{1}{r}\frac{\partial}{\partial r}\left(rU_{r,0}\right) + \frac{1}{r}\frac{\partial}{\partial \theta}\left(U_{\theta,0}\right) + \frac{\partial}{\partial z}\left(U_{z,0}\right) = 0 \tag{5.10a}$$

$$\frac{\partial p_0}{\partial r} = \frac{\partial^2 U_{r,0}}{\partial z^2} \tag{5.10b}$$

$$\frac{1}{r}\frac{\partial p_0}{\partial \theta} = \frac{\partial^2 U_{\theta,0}}{\partial z^2} \tag{5.10c}$$

$$\frac{\partial p_0}{\partial z} = 0 \tag{5.10d}$$

These are subject to the following boundary conditions:

$$U_{r,0} = U_{\theta,0} = 0 \text{ at } z = 1 \quad \text{(No-slip, z-axis boundary)} \tag{5.11a}$$

$$U_{z,0} = 0 \text{ at } z = 1 \quad \text{(No-flux, z-axis boundary)} \tag{5.11b}$$

$$\frac{\partial U_{r,0}}{\partial \theta} = U_{\theta,0} = \frac{\partial U_{z,0}}{\partial \theta} = 0 \text{ at } \theta = 0 \quad \text{(Symmetry about } \theta = 0\text{)} \tag{5.11c}$$

$$\frac{\partial U_{\theta,0}}{\partial z} = \frac{\partial U_{r,0}}{\partial z} = U_{z,0} = 0 \text{ at } z = 0 \quad \text{(Symmetry about } z = 0\text{)} \tag{5.11d}$$

$$p_0 = p_d \text{ at } (r, \theta, z) = (r_d, 0, 0) \quad \text{(Reference pressure)} \tag{5.11e}$$

Similarly, the $\mathcal{O}(\alpha)$ correction in the outer region is governed by the following:

$$\frac{1}{r}\frac{\partial}{\partial r}\left(rU_{r,1}\right) + \frac{1}{r}\frac{\partial}{\partial \theta}\left(U_{\theta,1}\right) + \frac{\partial}{\partial z}\left(U_{z,1}\right) = 0 \tag{5.12a}$$

$$\frac{\partial p_1}{\partial r} = \frac{\partial^2 U_{r,1}}{\partial z^2} \tag{5.12b}$$

$$\frac{1}{r}\frac{\partial p_1}{\partial \theta} = \frac{\partial^2 U_{\theta,1}}{\partial z^2} \tag{5.12c}$$

$$\frac{\partial p_1}{\partial z} = 0 \tag{5.12d}$$

The $\mathcal{O}(\alpha)$ governing equations are subject to the following boundary conditions:

$$U_{r,1} = U_{\theta,1} = 0 \text{ at } z = 1 \quad \text{(No-slip, z-axis boundary)} \tag{5.13a}$$

$$U_{z,1} = 0 \text{ at } z = 1 \quad \text{(No-flux, z-axis boundary)} \tag{5.13b}$$

$$\frac{\partial U_{r,1}}{\partial \theta} = U_{\theta,1} = \frac{\partial U_{z,1}}{\partial \theta} = 0 \text{ at } \theta = 0 \quad \text{(Symmetry about } \theta = 0\text{)} \tag{5.13c}$$

$$\frac{\partial U_{\theta,1}}{\partial z} = \frac{\partial U_{r,1}}{\partial z} = U_{z,1} = 0 \text{ at } z = 0 \quad \text{(Symmetry about } z = 0\text{)} \tag{5.13d}$$

$$p_0 = 0 \text{ at } (r, \theta, z) = (r_d, 0, 0) \quad \text{(Reference pressure)} \tag{5.13e}$$

The following form of the $\mathcal{O}(1)$ pressure field and its $\mathcal{O}(\alpha)$ correction can be found to satisfy the governing equations and boundary conditions given above:

$$p_0 - p_d = C_0 \ln\left(\frac{r}{r_d}\right) + \sum_{n=1}^{\infty}\left(-C_{n,1}r^{-n} + C_{n,2}r^{n}\right)\cos(n\theta) - \sum_{n=1}^{\infty}\left(-C_{n,1}{r_d}^{-n} + C_{n,2}{r_d}^{n}\right) \tag{5.14a}$$

$$p_1 = D_0 \ln\left(\frac{r}{r_d}\right) + \sum_{n=1}^{\infty}\left(-D_{n,1}r^{-n} + D_{n,2}r^{n}\right)\cos(n\theta) - \sum_{n=1}^{\infty}\left(-D_{n,1}{r_d}^{-n} + D_{n,2}{r_d}^{n}\right) \tag{5.14b}$$

where C_0, $C_{n,1}$, $C_{n,2}$, D_0, $D_{n,1}$, and $D_{n,2}$ are constants that will be determined based on boundary conditions and by matching with the inner solution. Taking partial derivatives of Equations (5.14a) and (5.14b) gives the following form of the velocity field:

$$U_{r,0} = -\frac{1}{r}\left\{C_0 + \sum_{n=1}^{\infty} n\left(C_{n,1}r^{-n} + C_{n,2}r^{n}\right)\cos(n\theta)\right\}\left(\frac{1-z^2}{2}\right) \tag{5.15a}$$

$$U_{\theta,0} = \frac{1}{r}\left\{\sum_{n=1}^{\infty} n\left(-C_{n,1}r^{-n} + C_{n,2}r^{n}\right)\sin(n\theta)\right\}\left(\frac{1-z^2}{2}\right) \tag{5.15b}$$

$$U_{z,0} = 0 \tag{5.15c}$$

$$U_{r,1} = -\frac{1}{r}\left\{D_0 + \sum_{n=1}^{\infty} n\left(D_{n,1}r^{-n} + D_{n,2}r^{n}\right)\cos(n\theta)\right\}\left(\frac{1-z^2}{2}\right) \tag{5.16a}$$

$$U_{\theta,1} = \frac{1}{r}\left\{\sum_{n=1}^{\infty} n\left(-D_{n,1}r^{-n} + D_{n,2}r^{n}\right)\sin(n\theta)\right\}\left(\frac{1-z^2}{2}\right) \tag{5.16b}$$

$$U_{z,1} = 0 \tag{5.16c}$$

Intermediate steps for the derivation of these solutions are provided in Appendix B1.

5.6 Inner Solutions

To study the velocity field near $\theta = \theta_H$, the scaled inner variable $\xi_r \equiv \frac{\theta-\theta_H}{\alpha}$ is introduced, and an asymptotic expansion of the velocity field of the following form is assumed:

$$(V_r, V_\theta, V_z, p) = \left(V_{r,0}, V_{\theta,0}, V_{z,0}, p_0\right) + \alpha\left(V_{r,1}, V_{\theta,1}, V_{z,1}, p_1\right) + \mathcal{O}(\alpha^2) \tag{5.17}$$

where $\mathcal{O}(\alpha^2)$ denotes terms on the order of α^2 or smaller. The leading-order $\mathcal{O}(1)$ terms of Equations (5.7a)- (5.7d) are expressed in terms inner coordinate as follows:

$$\frac{1}{r}\frac{\partial}{\partial \xi_r}\left(V_{\theta,0}\right) = 0 \tag{5.18a}$$

$$\frac{\partial p_0}{\partial r} = \frac{1}{r^2}\frac{\partial^2 V_{r,0}}{\partial {\xi_r}^2} + \frac{\partial^2 V_{r,0}}{\partial z^2} \tag{5.18b}$$

$$\frac{1}{r}\frac{\partial p_0}{\partial \xi_r} = 0 \tag{5.18c}$$

$$\frac{\partial p_0}{\partial z} = 0 \tag{5.18d}$$

Equations (5.18a)- (5.18d) are subject to the following boundary conditions:

$$V_{r,0} = 0 \text{ at } \xi_r = 0 \quad \text{(No-slip, } \theta\text{-axis boundary)} \tag{5.19a}$$

$$V_{\theta,0} = 0 \text{ at } \xi_r = 0 \quad \text{(No-flux, } \theta\text{-axis boundary)} \tag{5.19b}$$

$$V_{r,0} = V_{\theta,0} = 0 \text{ at } z = 1 \quad \text{(No-slip, } z\text{-axis boundary)} \tag{5.19c}$$

$$\frac{\partial V_{r,0}}{\partial z} = \frac{\partial V_{\theta,0}}{\partial z} = 0 \text{ at } z = 0 \quad \text{(Symmetry about } z = 0\text{)} \tag{5.19d}$$

Above, Equation (5.18c) implies that the pressure field is inherited from the outer region. Thus, the same pressure field expansion has been used for the governing equations in both outer and inner regions. Pressure gradients can be obtained from the outer solution and substituted into the $\mathcal{O}(1)$ governing equations. Substitution into Equation (5.18c), gives the following:

$$\frac{\partial p_0}{\partial \xi_r} = \frac{\partial \theta}{\partial \xi_r}\frac{\partial p_0}{\partial \theta}\bigg|_{\theta=\theta_H} = \alpha \frac{\partial p_0}{\partial \theta}\bigg|_{\theta=\theta_H} = -\alpha \sum_{n=1}^{\infty} n\left(-C_{n,1} r^{-n} + C_{n,2} r^{n}\right) \sin(n\theta_H) \tag{5.20}$$

$$= 0$$

Since the $\sin(n\theta_H)$ terms above are nonzero for all $n \neq \pi/\theta_h$, $C_{n,1}$ and $C_{n,2}$ must be zero for all $n \neq \pi/\theta_h$ as well. Otherwise, the θ-component of pressure gradient will be nonzero and a function of r at the channel walls at $\theta = \pm\theta_H$. Among special cases where $n\theta_H = \pi$, only the when $\theta_H = \pi$ and $n = 1$ is matching permitted with the form of the outer velocity determined in Equation (5.15a)and (5.15b). However, since $\theta_H < \pi/2$, this case case is not physically achievable. Effectively, $C_{n,1} = C_{n,2} = 0$ for all n, and it can be inferred that $\frac{\partial p_0}{\partial r}\Big|_{\theta=\theta_H} = \frac{C_0}{r}$. Substituting this result directly into Equation (5.18b) gives the following:

$$\frac{C_0}{r} = \frac{1}{r^2}\frac{\partial^2 V_{r,0}}{\partial {\xi_r}^2} + \frac{\partial^2 V_{r,0}}{\partial z^2} \tag{5.21}$$

Taking a separation of variables approach, the following form of $V_{r,0}$ is found to satisfy Equation (5.21) and boundary conditions (5.19a)-(5.19d):

$$V_{r,0} = \frac{C_0}{r}\sum_{n=1}^{\infty} E_n \exp\{\delta_n r \xi_r\} \cos(\delta_n z) - \frac{C_0}{r}\left(\frac{1 - z^2}{2}\right) \tag{5.22}$$

where $\delta_n \equiv \frac{2n-1}{2}\pi$ and $E_n = 2\frac{(-1)^{n-1}}{(\delta_n)^3}$. Additional details for the derivation of this solution are given in Appendix B2.

At this point in the analysis, an expression for the inner z-velocity has not yet been found, since the appropriate governing equations come from the $\mathcal{O}(\alpha)$ correction. The governing equations for the $\mathcal{O}(\alpha)$ correction are as follows:

$$\frac{1}{r}\frac{\partial}{\partial r}\left(rV_{r,0}\right) + \frac{1}{r}\frac{\partial}{\partial \xi_r}\left(V_{\theta,1}\right) + \frac{\partial}{\partial z}\left(V_{z,0}\right) = 0 \tag{5.23a}$$

$$\frac{\partial p_1}{\partial r} = \frac{1}{r^2}\frac{\partial^2 V_{r,1}}{\partial {\xi_r}^2} + \frac{\partial^2 V_{r,1}}{\partial z^2} - \frac{2}{r^2}\frac{\partial V_{\theta,0}}{\partial \xi_r} \tag{5.23b}$$

$$\frac{1}{r}\frac{\partial p_1}{\partial \xi_r} = \frac{1}{r^2}\frac{\partial^2 V_{\theta,0}}{\partial {\xi_r}^2} + \frac{\partial^2 V_{\theta,0}}{\partial z^2} \tag{5.23c}$$

$$\frac{\partial p_1}{\partial z} = 0 \tag{5.23d}$$

The $O(\alpha)$ correction to $\vec{V}$ is subject to the additional boundary conditions:

$$V_{r,1} = V_{z,1} = 0 \text{ at } \xi_r = 0 \qquad \text{(No-slip, } \theta\text{-axis boundary)} \tag{5.24a}$$

$$V_{\theta,1} = 0 \text{ at } \xi_r = 0 \qquad \text{(No-flux, } \theta\text{-axis boundary)} \qquad (5.24b)$$

$$V_{r,1} = V_{\theta,1} = 0 \text{ at } z = 1 \qquad \text{(No-slip, } z\text{-axis boundary)} \qquad (5.24c)$$

$$V_{z,0} = 0 \text{ at } z = 1 \qquad \text{(No-flux, } z\text{-axis boundary)} \qquad (5.24d)$$

$$\frac{\partial V_{r,1}}{\partial z} = \frac{\partial V_{\theta,1}}{\partial z} = V_{z,0} = 0 \text{ at } z = 0 \qquad \text{(Symmetry about } z = 0) \qquad (5.24e)$$

Using the same approach as with the $\mathcal{O}(1)$ inner radial velocity, the following form of $V_{r,1}$ is determined:

$$V_{r,1} = \left(\left.\frac{\partial p_1}{\partial r}\right|_{\theta=\theta_H}\right)\left\{\sum_{n=1}^{\infty} E_n \exp\{\delta_n r \xi_r\}\cos(\delta_n z) - \left(\frac{1-z^2}{2}\right)\right\} \qquad (5.25)$$

The above form of $V_{r,1}$ satisfies Equation (5.23a), as well as appropriate boundary conditions, and permits matching in the intermediate region. Here, $\left.\frac{\partial p_1}{\partial r}\right|_{\theta=\theta_H}$ is found by integrating Equation (5.16a). The expression for $\left.\frac{\partial p_1}{\partial r}\right|_{\theta=\theta_H}$ includes constant coefficients D_0, $D_{n,1}$ and $D_{n,2}$ which must be determined either from boundary conditions for the remaining velocity components, or through matching with the outer solution.

Using the procedure detailed in Appendices B3 and B4, the following solutions for velocity components $V_{\theta,1}$ and $V_{z,0}$ are determined:

$$V_{\theta,1} = -\frac{C_0}{r^2}\sum_{n=1}^{\infty}\frac{6}{\delta_n^5}\left[(\delta_n r\xi_r - 1)\exp\{\delta_n r\xi_r\} + 1\right]\left(\frac{1-z^2}{2}\right) \tag{5.26a}$$

$$V_{z,0} = -\frac{C_0}{r^2}\sum_{n=1}^{\infty}\delta_n r\xi_r \exp\{\delta_n r\xi_r\}\left[\frac{E_n}{\delta_n}\sin(\delta_n z) - \frac{6}{\delta_n^4}\left(\frac{3z - z^3}{6}\right)\right] \tag{5.26b}$$

It should be noted that $V_{z,1}$ does not appear in the $\mathcal{O}(\alpha)$ equations, suggesting that $V_{z,1}$ is smaller than $\mathcal{O}(\alpha)$. If the analysis is extended to higher-order corrections, it will be found that the $\mathcal{O}(\alpha^2)$ equations are required to determine $V_{z,1}$.

The inner velocity field near the boundary at $\theta = -\theta_H$ to $\mathcal{O}(\alpha)$ can be inferred by symmetry. For $\overrightarrow{W}$, a second inner variable is defined as $\xi_l \equiv \frac{\theta+\theta_H}{\alpha}$ and, again, an asymptotic expansion of the velocity field of the following form is assumed:

$$(W_r, W_\theta, W_z, p) = \left(W_{r,0}, W_{\theta,0}, W_{z,0}, p_0\right) + \alpha\left(W_{r,1}, W_{\theta,1}, W_{z,1}, p_1\right) + \mathcal{O}(\alpha^2) \tag{5.27}$$

The governing equations for asymptotic terms of $\overrightarrow{W}$ are analogous to (5.18a)- (5.18d) and (5.23a)-(5.18d), and the applicable boundary conditions are analogous to (5.19a)- (5.19d) and (5.24a)- (5.24d). Here, however, matching requires that $\xi_l \geq 0$, as opposed to $\xi_r \leq 0$ for $\vec{V}$. The $\mathcal{O}(1)$ components of $\overrightarrow{W}$ can be expressed as follows:

$$W_{r,0} = \frac{C_0}{r}\sum_{n=1}^{\infty} E_n \exp\{-\delta_n r\xi_l\}\cos(\delta_n z) - \frac{C_0}{r}\left(\frac{1-z^2}{2}\right) \tag{5.28a}$$

$$W_{\theta,0} = 0 \tag{5.28b}$$

The $\mathcal{O}(\alpha)$ correction terms for $\overrightarrow{W}$ are as follows:

$$W_{r,1} = \left(\frac{\partial p_1}{\partial r}\Big|_{\theta=-\theta_H}\right)\left\{\sum_{n=1}^{\infty} E_n \exp\{-\delta_n r\xi_l\}\cos(\delta_n z) - \left(\frac{1-z^2}{2}\right)\right\} \tag{5.29a}$$

$$W_{\theta,1} = -\frac{C_0}{r^2}\sum_{n=1}^{\infty}\frac{6}{\delta_n^5}[(\delta_n r\xi_l + 1)\exp\{-\delta_n r\xi_l\} - 1]\left(\frac{1-z^2}{2}\right) \tag{5.29b}$$

$$W_{z,0} = \frac{C_0}{r^2}\sum_{n=1}^{\infty}\delta_n r\xi_l \exp\{-\delta_n r\xi_l\}\left[\frac{E_n}{\delta_n}\sin(\delta_n z) - \frac{6}{\delta_n^4}\left(\frac{3z-z^3}{6}\right)\right] \tag{5.29c}$$

5.7 Composite Solution

To construct a composite solution, matching between the outer solutions and each of the inner solutions is required. Matching between $\vec{U}$ and $\vec{V}$ is carried out first by means of an intermediate variable $\zeta_r \equiv (\theta - \theta_r)/\psi(\alpha)$, where $\lim_{\alpha\to 0}\big(\psi(\alpha)\big) = 0$ and $\lim_{\alpha\to 0}(\alpha/\psi(\alpha)) = 0$. Matching by intermediate variable is carried out by ensuring that the following is satisfied:

$$\lim_{\alpha\to 0}\left\{\vec{U}(\theta = \psi(\alpha)\zeta_r + \theta_H)\right\} = \lim_{\alpha\to 0}\left\{\vec{V}(\xi_r = \alpha^{-1}\psi(\alpha)\zeta_r)\right\} \tag{5.30}$$

Intermediate steps for the matching procedure are provided in Appendix B5. In summary, matching shows that for $V_{\theta,1}$ and $U_{\theta,1}$to satisfy Equation (5.30), $D_{n,1} = 0$ for all $n \neq 1$, and that $D_{n,2} = 0$ for all n. Furthermore, it can be shown that $D_{1,1} = \frac{C_0}{\sin(\theta_H)}\sum_{n=1}^{\infty}\frac{6}{\delta_n^5}$. The constant coefficients C_0 and D_0, which remain unknown following the matching procedure, must be determined based on the flow rate condition. Matching of $\vec{U}$ and $\overrightarrow{W}$ by the intermediate variable $\zeta_l \equiv (\theta + \theta_r)/\psi(\alpha)$ can be carried out with the same results.

Next, the redundant contributions from the inner and outer velocity components, conventionally referred to as the overlap, must be subtracted from the superposition of the inner and outer flow fields. The overlap between $\vec{U}$ and $\vec{V}$ is defined as $\lim_{\alpha\to 0}\left\{\vec{U}(\theta = \psi(\alpha)\zeta_r - \theta_H)\right\} = \lim_{\alpha\to 0}\left\{\vec{V}(\xi_r = \alpha^{-1}\psi(\alpha)\zeta_r)\right\}$ and the overlap between $\vec{U}$ and $\overrightarrow{W}$ is $\lim_{\alpha\to 0}\left\{\vec{U}(\theta = \psi(\alpha)\zeta_r - \theta_H)\right\} = \lim_{\alpha\to 0}\left\{\overrightarrow{W}(\xi_l = \alpha^{-1}\psi(\alpha)\zeta_l)\right\}$. Intermediate steps of this procedure, as well as subsequent collections of terms, are provided in Appendix B6. The composite solutions can then be expressed in terms of outer coordinates as follows:

$$u_r = \left(\frac{C_0}{r} + \alpha\frac{D_0}{r}\right)\left\{2\sum_{n=1}^{\infty} E_n \exp\left\{-\delta_n r\frac{\theta_H}{\alpha}\right\}\cosh\left\{\delta_n r\frac{\theta}{\alpha}\right\}\cos(\delta_n z)\right.$$
$$\left. - \left(\frac{1-z^2}{2}\right)\right\} + \left(\alpha\frac{C_0}{r^2}\cot(\theta_H)\sum_{n=1}^{\infty}\frac{6}{\delta_n^5}\right)$$
$$\cdot\left\{2\sum_{n=1}^{\infty} E_n \exp\left\{-\delta_n r\frac{\theta_H}{\alpha}\right\}\cosh\left\{\delta_n r\frac{\theta}{\alpha}\right\}\cos(\delta_n z)\right.$$
$$\left. - \left(\frac{\cos(\theta)}{\cos(\theta_H)}\right)\left(\frac{1-z^2}{2}\right)\right\} + \mathcal{O}(\alpha^2) \tag{5.31a}$$

$$u_\theta = -\left(\alpha\frac{C_0}{r^2}\right)\sum_{n=1}^{\infty}\frac{6}{\delta_n^5}\left\{\frac{\sin(\theta)}{\sin(\theta_H)}\right.$$
$$+ 2\exp\left\{-\delta_n\frac{r\theta_H}{\alpha}\right\}\left[\left(\delta_n\frac{r\theta}{\alpha}\right)\cosh\left\{\delta_n\frac{r\theta}{\alpha}\right\}\right. \tag{5.31b}$$
$$\left.\left. - \left(1+\delta_n\frac{r\theta_H}{\alpha}\right)\sinh\left\{\delta_n\frac{r\theta}{\alpha}\right\}\right]\right\}\left(\frac{1-z^2}{2}\right) + \mathcal{O}(\alpha^2)$$

$$u_z = 2\frac{C_0}{r^2}\sum_{n=1}^{\infty}\left(\delta_n\frac{r\theta_H}{\alpha}\right)\exp\left\{-\delta_n\frac{r\theta_H}{\alpha}\right\}\left[\cosh\left\{\delta_n\frac{r\theta}{\alpha}\right\}\right.$$
$$\left. - \frac{\theta}{\theta_H}\sinh\left\{\delta_n\frac{r\theta}{\alpha}\right\}\right]\left[\frac{E_n}{\delta_n}\sin(\delta_n z) - \frac{6}{\delta_n^4}\left(\frac{3z-z^3}{6}\right)\right] + \mathcal{O}(\alpha^2) \tag{5.31c}$$

where $\delta_n \equiv \frac{2n-1}{2}\pi$ and $E_n = 2\frac{(-1)^{n-1}}{(\delta_n)^3}$.

Finally, the flow rate condition from Equation (5.8g) must be applied to determine the constant coefficients C_0 and D_0. To leading order, the flow rate condition can be expressed as follows:

$$-1 = \int_{-1}^{1}\int_{-\theta_H}^{\theta_H} u_r \, r d\theta dz = 4\int_{0}^{1}\int_{0}^{\theta_H} \left(u_{r,0} + \alpha u_{r,1}\right) r d\theta dz + \mathcal{O}(\alpha^2) \tag{5.32}$$

Intermediate steps for the evaluation of this integral are available in Appendix B7, which gives the following definitions for C_0 and D_0:

$$C_0 = \frac{4}{3\theta_H}\left(1 - C_{0,err}\right)^{-1} \tag{5.33a}$$

$$C_0 + \alpha D_0 = \frac{4}{3\theta_H} \tag{5.33b}$$

In Equation (5.33a) above, $C_{0,err} \equiv \frac{\alpha}{r}\cot(\theta_H)\left(\sum_{n=1}^{\infty}\frac{6}{{\delta_n}^5}\right)$ denotes an order $\mathcal{O}(\alpha/r)$ fractional error for C_0, which is plotted against various α, r, and θ_H in Figure 5.2. The linear relationship between $C_{0,err}$ and α/r reflects the influence of boundary layers at $\theta = \pm\theta_H$. It is this aspect of the that necessitates a correction to the composite expansions of pressure and velocity, in order to ensure continuity. However, it is important to note that the flow rate contribution resulting from this correction factor is of order $\mathcal{O}(\alpha^2)$, as discussed in Appendix B7, and corresponds to higher-order terms in the asymptotic expansions. Thus, $C_{0,err}$ provides an indication of the significance of those higher-order terms relative to the terms that appear in Equations (5.31a)-(5.31c). It is also helpful to

remark on the physical meaning of α/r in the context of the HSSC tool geometry. This quantity corresponds to the dimensional form of the r-coordinate, which depends only on the convergence angle of the channel. Thus, the accuracy of the flow-rate condition is independent of G. The relationship between $C_{0,err}$ and α in Figure 5.2(b) is merely a consequence of the flexibility in selecting the domain of influence and defining the length scale w_d as discussed in Section 5.3.

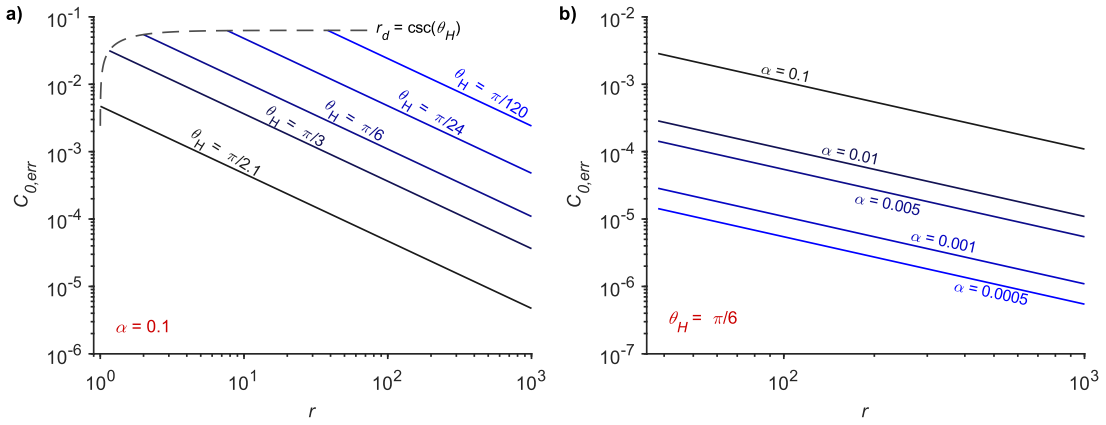

Figure 5.2 – $C_{o,err}$ plotted as a function of r for various (a) channel convergence angle (θ_H) and (b) inverse aspect ratio (α) values. At the outflow boundary, r_d is bounded by $\csc(\theta_H)$, as indicated by the dashed line in (a).

Finally, after substituting the definitions for constant coefficients C_0 and D_0 from Equations (5.33a) and (5.33b) into Equations (5.31a)-(5.31c), the $\mathcal{O}(\alpha)$ expansion for the velocity field can be expressed as follows:

$$u_r$$

$$= \frac{4}{3r\theta_H}\left\{2\sum_{n=1}^{\infty} E_n \exp\left\{-\delta_n r\frac{\theta_H}{\alpha}\right\}\cosh\left\{\delta_n r\frac{\theta}{\alpha}\right\}\cos(\delta_n z) - \left(\frac{1-z^2}{2}\right)\right\}$$

$$+\frac{4}{3r\theta_H}\left(\frac{\alpha}{r}\cot(\theta_H)\sum_{n=1}^{\infty}\frac{6}{\delta_n^5}\right)\left\{2\sum_{n=1}^{\infty} E_n \exp\left\{-\delta_n r\frac{\theta_H}{\alpha}\right\}\cosh\left\{\delta_n r\frac{\theta}{\alpha}\right\}\cos(\delta_n z)\right. \tag{5.34a}$$

$$\left.-\left(\frac{\cos(\theta)}{\cos(\theta_H)}\right)\left(\frac{1-z^2}{2}\right)\right\}\left(1-C_{0,err}\right)^{-1} + \mathcal{O}(\alpha^2)$$

$$u_\theta = -\frac{4}{3r\theta_H}\left(\frac{\alpha}{r}\right)\sum_{n=1}^{\infty}\frac{6}{\delta_n^5}\left\{\frac{\sin(\theta)}{\sin(\theta_H)}\right.$$

$$-2\exp\left\{-\delta_n\frac{r\theta_H}{\alpha}\right\}\left[\left(\delta_n\frac{r\theta}{\alpha}\right)\cosh\left\{\delta_n\frac{r\theta}{\alpha}\right\}\right. \tag{5.34b}$$

$$\left.\left.-\left(1+\delta_n\frac{r\theta_H}{\alpha}\right)\sinh\left\{\delta_n\frac{r\theta}{\alpha}\right\}\right]\right\}\left(\frac{1-z^2}{2}\right)\left(1-C_{0,err}\right)^{-1}$$

$$+\mathcal{O}(\alpha^2)$$

$$u_z = \frac{4}{3r\theta_H}\left(\frac{2}{r}\right)\sum_{n=1}^{\infty}\left(\delta_n\frac{r\theta_H}{\alpha}\right)\exp\left\{-\delta_n\frac{r\theta_H}{\alpha}\right\}\left[\cosh\left\{\delta_n\frac{r\theta}{\alpha}\right\}\right.$$

$$\left.-\frac{\theta}{\theta_H}\sinh\left\{\delta_n\frac{r\theta}{\alpha}\right\}\right]\left[\frac{E_n}{\delta_n}\sin(\delta_n z) - \frac{6}{\delta_n^4}\left(\frac{3z-z^3}{6}\right)\right]\left(1\right. \tag{5.34c}$$

$$\left.-C_{0,err}\right)^{-1} + \mathcal{O}(\alpha^2)$$

Where $\delta_n \equiv \frac{2n-1}{2}\pi$, $E_n = 2\frac{(-1)^{n-1}}{(\delta_n)^3}$, $C_{0,err} \equiv \frac{\alpha}{r}\cot(\theta_H)\left(\sum_{n=1}^{\infty}\frac{6}{{\delta_n}^5}\right)$, and $\left(\sum_{n=1}^{\infty}\frac{6}{\delta_n^5}\right) \approx$ 0.6302.

5.8 Flow Field Visualizations

The order $\mathcal{O}(\alpha)$ velocity field exhibits two secondary flow effects due to the convergence of the narrow channel. The first effect proceeds from the conformance of the flow field to the channel boundaries at $\theta = \pm\theta_H$, which implies a θ-axis velocity component roughly equal to $u_r \sin(\theta)$. The second effect is the boundary layer that develops near the channel sidewalls due to the no-slip boundary condition. To distinguish between these effects, and in order to illustrate their relative significance with respect to the geometry of the channel, velocity contours are presented in Figure 5.3 for three representative cases. A case where (α/r) is small and the entire velocity field is dominated by its leading-order behavior in the outer region is illustrated in Figure 5.3(a). In Figure 5.3(b) and (c), (α/r) is an order of magnitude larger, and thus the influence of boundary layers at $\theta = \pm\theta_H$ are significantly greater. The distinction between Figure 5.3(b) and (c) is the convergence angle of the channel, θ_H.

First, it is helpful to consider the magnitude of the velocity field along each axis. In Figure 5.3(a), the case with α = 0.05 and $r = 10\csc(\theta_H)$ exhibits an r-velocity profile that is largely parabolic along z and unchanging along θ. Since (α/r) is small, the leading-order outer velocity field is dominant, and the shapes of streamlines correspond to Stokes

flow. By contrast, the r-velocity components in Figure 5.3(b) and (c), where α = 0.05 and $r = \csc(\theta_H)$, are influenced significantly by boundary layers in proximity of the channel wall at $\theta = \pm\theta_H$. Comparing the results in Figure 5.3(a) with the other two cases, it is clear that the magnitude of the flow velocity and the size of the boundary layers relative to the total cross-sectional area both correlate with decreasing r. While the scaling of u_r with r^{-1} follows predictably from continuity, the scaling of secondary flow components along θ and z is more interesting. Relative to the Figure 5.3(a) case, the secondary flow magnitude in Figure 5.3(b) and (c) exhibits an increase of two orders-of-magnitude due to an order-of-magnitude decrease in r. Careful examination of Equations (5.34b) and (5.34c) reveals that these velocity components are roughly proportional to $(\alpha/r)\exp\{-r/\alpha\}$. Thus, a simple exponential scaling provides only a partial understanding of this flow behavior, although it may be adequate for some limited range of (α/r).

Next, the shape of the velocity contours can be compared across u_r, u_θ, and u_z to delineate between the two secondary flow effects described above: conformance to channel geometry and boundary layer development at $\theta = \pm\theta_H$. The three cases in Figure 5.3 exhibit nonzero u_z only in proximity to the lateral channel boundaries, whereas u_θ is roughly proportional to $u_r \sin(\theta)$ throughout the entire domain. Thus, it is reasonable to interpret u_θ as the combination of both flow effects, whereas u_z represents boundary layer flow in isolation. This interpretation is further supported by comparison between the cases represented in Figure 5.3(b), where $\theta_H = \pi/6$, and in Figure 5.3(c), where $\theta_H = 16$. Here,

the θ-velocity magnitude differs significantly between the two cases whereas u_z is virtually unchanged. This underscores the idea that nonzero z-velocity corresponds to a flow effect confined to the inner regions near the lateral channel boundaries. Additionally, comparing Figure 5.3(a) with the other two cases, the θ-velocity contours can be seen to detach from the lateral channel walls as secondary flows induced by the boundary layer become more pronounced. In physical terms, this observed effect in u_θ with decreasing (α/r) represents the no-slip condition at channel boundaries becoming significant over a larger fraction of the channel relative to the squeezing effect due to channel convergence.

Previous analytical treatments of similar geometries[223, 225] in the Cartesian coordinate system have demonstrated qualitatively similar velocity fields for secondary flow components. However, the results of these efforts do not distinguish boundary layer effects due no-slip at the lateral boundaries from squeezing effects from the varying cross-section. By contrast, the result of this perturbation analysis in Equations (5.34a)-(5.34c) lends itself naturally to such a distinction.

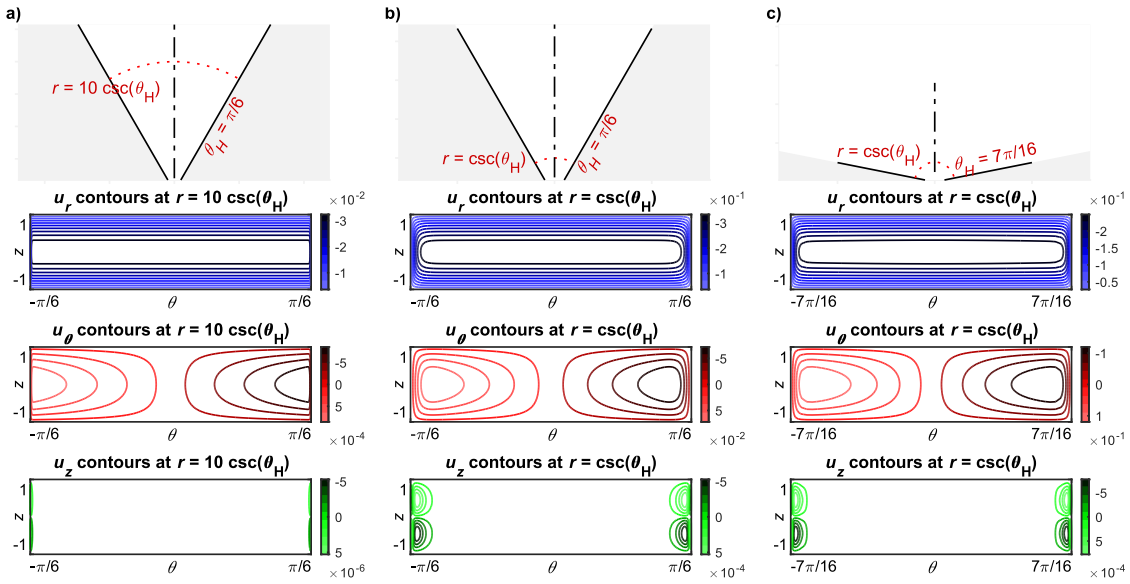

Figure 5.3 – Velocity field contours of the 3D order $O(\alpha)$ flow field for three representative cases: $(\alpha/r)\sim10^{-3}$ and $\theta_H = \pi/6$ (a); $(\alpha/r)\sim10^{-2}$ and $\theta_H = \pi/6$ (b); and $(\alpha/r)\sim10^{-2}$ and $\theta_H = 7\pi/16$ (c). For all three cases, $\alpha = 0.05$, and r is given in multiples of $\csc(\theta_H)$, its minimum possible value.

In the context of flow patterning applications, these results elucidate the domain of influence for secondary flow conducive to circulation mixing. They provide a detailed estimate for the portion of the channel cross-section where boundary layer effects may be neglected. It is this circulation mixing, and thus the boundary layer domain at the channel sidewalls, where unwanted distortion of patterned flow is significant. For the remainder of the domain, the observed secondary velocity component along θ reflects flow conformal to the channel geometry, which produces a desirable scaling effect across the entire patterned flow. In this region, it is of practical convenience to adopt a simplified velocity field model. The ability to determine this model easily with physical significance readily attributable to each constituent term is a core strength of the perturbation analysis approach.

In the case of the present analysis, it is the outer solution from Equations (5.15) and (5.16) that may be adopted as a simplified velocity field. Substituting the definitions for C_0 and D_0 determined in Section 5.7, these outer solutions can be expressed as follows:

$$U_r = -\frac{4}{3r\theta_H}\left[1 + \frac{\alpha}{r}\left(\frac{\cos(\theta)}{\sin(\theta_H)}\right)\sum_{n=1}^{\infty}\frac{6}{\delta_n^5}\left(1 - C_{0,err}\right)^{-1}\right]\left(\frac{1-z^2}{2}\right) + \mathcal{O}(\alpha^2) \qquad (5.35a)$$

$$U_\theta = -\frac{4}{3r\theta_H}\left[\frac{\alpha}{r}\left(\frac{\sin(\theta)}{\sin(\theta_H)}\right)\sum_{n=1}^{\infty}\frac{6}{\delta_n^5}\left(1 - C_{0,err}\right)^{-1}\right]\left(\frac{1-z^2}{2}\right) + \mathcal{O}(\alpha^2) \qquad (5.35b)$$

$$U_z = \mathcal{O}(\alpha^2) \qquad (5.35c)$$

where $\delta_n \equiv \frac{2n-1}{2}\pi$, $C_{0,err} \equiv \frac{\alpha}{r}\cot(\theta_H)\left(\sum_{n=1}^{\infty}\frac{6}{{\delta_n}^5}\right)$, and $\left(\sum_{n=1}^{\infty}\frac{6}{\delta_n^5}\right) \approx 0.6302$.

These expressions are simple enough to examine and interpret piece by piece. The term $(4/3r\theta_H)$ reflects the overall scaling of both r-velocity and θ-velocity with channel cross-section; the term $(1-z^2)$ conveys the parabolic aspect of the velocity profile along z; the $\cos(\theta)$ and $\sin(\theta)$ terms in U_r and U_θ, respectively, constitute an additional order $\mathcal{O}(\alpha/r)$ component that varies across a given channel cross-section; and the $\mathcal{O}(\alpha^2)$ term, as before, conveys the understanding that this approximation neglects terms that are of order $\mathcal{O}(\alpha^2)$ and smaller.

Compared to the full composite expansion in Equations (5.34a)-(5.34c), Equations (5.35a)-(5.35c) constitute a much simpler and distinguishable scaling relationship between

flow velocity and channel geometry. The simplified expansion is useful in regions sufficiently far from the lateral channel walls that boundary layer effects can be neglected. To quantify what precisely is meant by "sufficiently far", it is helpful to compare the full composite expansion with the inner velocity near $\theta = \pm\theta_H$, given by:

$$V_r + W_r = \frac{8}{3r\theta_H}\left\{1 + \frac{\alpha}{r}\cot(\theta_H)\sum_{n=1}^{\infty}\frac{6}{\delta_n^5}\left(1 - C_{0,err}\right)^{-1}\right\} \cdot\left\{\sum_{n=1}^{\infty} E_n \exp\left\{-\delta_n\frac{r\theta_H}{\alpha}\right\}\cosh\left\{\delta_n\frac{r\theta}{\alpha}\right\}\cos(\delta_n z) - \left(\frac{1-z^2}{2}\right)\right\} + \mathcal{O}(\alpha^2) \tag{5.36a}$$

$$V_\theta + W_\theta = -\frac{4}{3r\theta_H}\left(\frac{\alpha}{r}\right)\sum_{n=1}^{\infty}\frac{6}{\delta_n^5}\exp\left\{-\delta_n\frac{r\theta_H}{\alpha}\right\}\left\{2\left(\delta_n\frac{r\theta}{\alpha}\right)\cosh\left\{\delta_n\frac{r\theta}{\alpha}\right\} - 2\left(1 + \delta_n\frac{r\theta_H}{\alpha}\right)\sinh\left(\delta_n\frac{r\theta}{\alpha}\right)\right\}\left(1 - C_{0,err}\right)^{-1}\left(\frac{1-z^2}{2}\right) + \mathcal{O}(\alpha^2) \tag{5.36b}$$

$$V_z + W_z = \frac{4}{3r\theta_H}\left(\frac{2}{r}\right)\sum_{n=1}^{\infty}\left(\delta_n\frac{r\theta_H}{\alpha}\right)\exp\left\{-\delta_n\frac{r\theta_H}{\alpha}\right\}\left[\cosh\left\{\delta_n\frac{r\theta}{\alpha}\right\} - \frac{\theta}{\theta_H}\sinh\left\{\delta_n\frac{r\theta}{\alpha}\right\}\right]\left[\frac{E_n}{\delta_n}\sin(\delta_n z) - \frac{6}{\delta_n^4}\left(\frac{3z - z^3}{6}\right)\right]\left(1 - C_{0,err}\right)^{-1} + \mathcal{O}(\alpha^2) \tag{5.36c}$$

where $\delta_n \equiv \frac{2n-1}{2}\pi$, $E_n = 2\frac{(-1)^{n-1}}{(\delta_n)^3}$, $C_{0,err} \equiv \frac{\alpha}{r}\cot(\theta_H)\left(\sum_{n=1}^{\infty}\frac{6}{{\delta_n}^5}\right)$, and $\left(\sum_{n=1}^{\infty}\frac{6}{\delta_n^5}\right) \approx 0.6302$. The infinite summation terms included in this series can easily be computed numerically and truncated to reasonable accuracy after only a few iterations. Subsequently, quantifying the domain of influence for boundary layers at arbitrary r and θ_H is straightforward by simply comparing results from Equations (5.34a)-(5.34c) to results from Equations (5.36a)-(5.36c). The ease of such a comparison also speaks to the strengths of the perturbation methods approach.

The simplified scaling in terms of the maximum velocity components at $z = 0$ for various α and θ_H is illustrated in Figure 5.4, with comparison to both the full composite expansion and inner velocity components, near $\theta = \theta_H$. Notably, these relationships are invariant of fluid properties such as viscosity (μ) and density (ρ), based on the forms of the governing equations in Equation (5.7). For the matched composite expansion, the velocity field experiences a transition between two regimes – one dominated by the inner expansion, and the other by the outer expansion – at some intermediate region. Figure 5.4 also provides a helpful visualization of the results between $\vec{U}$ and $\vec{V}$ from the matching procedure discussed Section 5.7 since it represents the composite expansion alongside the matched inner an outer expansions within the intermediate region where matching occurs.

The three cases represented in Figure 5.4(a)-(c) reflect many of the same insights regarding velocity magnitude, secondary flow, and boundary layer phenomena previously discussed for Figure 5.3. In Figure 5.4(a), where (α/r) is comparatively small, the radial

velocity is greater than other components by roughly two orders of magnitude, and secondary flow due to the θ-axis boundary can be neglected for $\xi_r < -10^{-1}$. For the remaining two cases, however, both the severity and the domain of influence for secondary flow are greater by an order of magnitude. Along the z-axis, boundary layer-induced secondary flow dissipates to zero in the outer region, but the θ-component of velocity is nonzero and proportional to $\sin(\theta)$ even in regions far from the channel boundaries.

Comparing the case in Figure 5.4(c), which describes a geometry approaching a sudden contraction, to the case in Figure 5.4(b), where the change in width is significantly more gradual, the differences for all three velocity components are relatively minor. Although the analytical model appears at first glance to perform reasonably well for both cases, a measure of skepticism is appropriate here. Specifically, the assumption of fully developed flow may not be realistic or justifiable, for cases where θ_H is large. While it may be reasonable to expect fully developed flow for moderate θ_H, for practical cases where $\theta_H \to \pi/2$, as the outflow boundary becomes zero, i.e., at increasingly large r, the pressure field will becomes more influential. Thus, in a physical microfluidic slot, changes in channel width approaching an abrupt contraction will invalidate the assumptions used for this work unless purposeful precautions are taken to match the pressure profile, as the outflow boundary becomes zero, with the profile predicted by this model.

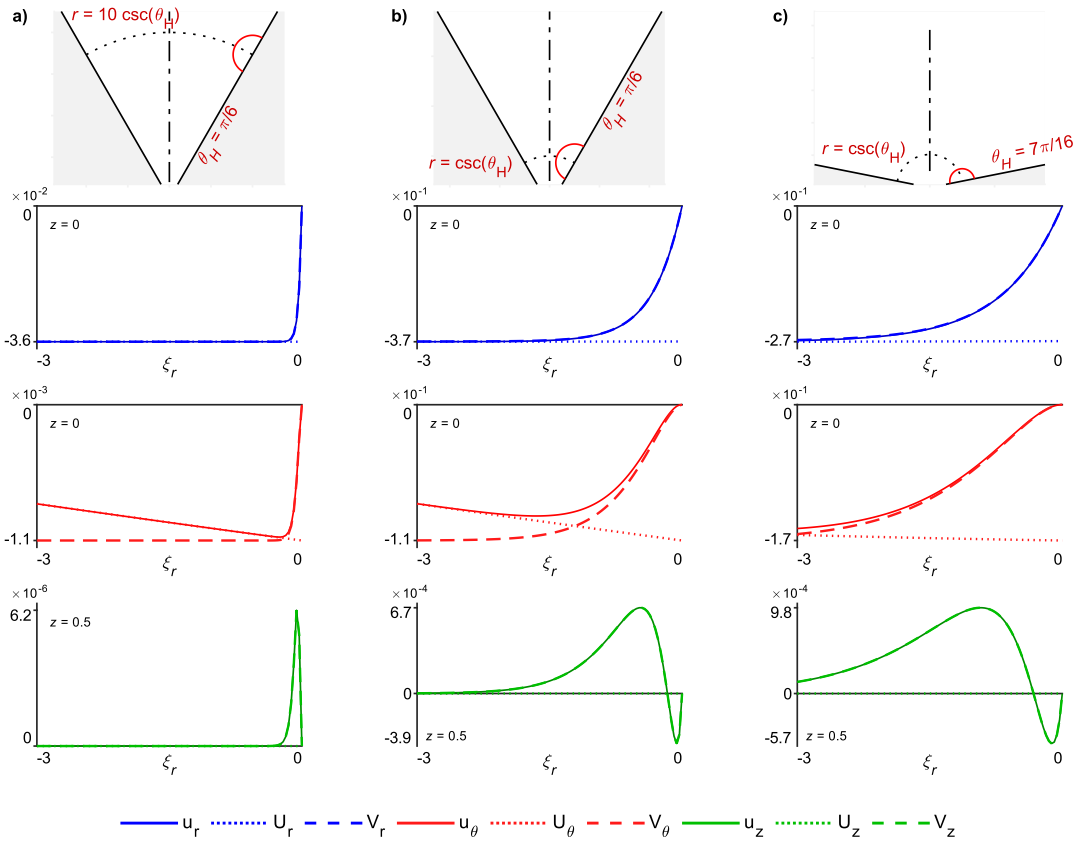

Figure 5.4 – Visualizations of the 3D velocity field in the intermediate region for (a) $(\alpha/r)\sim10^{-3}$ and $\theta_H = \pi/6$, (b) $(\alpha/r)\sim10^{-2}$ and $\theta_H = \pi/6$, and (c) $(\alpha/r)\sim10^{-2}$ and $\theta_H = 7\pi/16$. For all three cases, $\alpha = 0.05$ and r is given in multiples of $csc(\theta_H)$, its minimum possible value.

5.9 Conclusions

The work in this chapter contributes a fundamental understanding of internal flow effects that facilitate and limit feature size for heterogeneous stripe slot coating (HSSC). Most significantly, the analysis successfully distinguishes between two secondary flows in the contracting planar slot. These flows comprise a squeezing effect due to conformance of the flow to the channel geometry, in addition to a boundary layer that develops at each

sidewall of the channel due to no-slip at those boundaries. In the context of HSSC, the first of these is responsible for pattern scaling and thus feature size improvement, while the second of these is responsible for circulation mixing that reduces feature size performance. Thus, the distinction is of practical importance for the determination and improvement of minimum feature size.

The perturbation approximation produced by this work also provides a foundation for a subsequent analysis that considers multiple liquid phases. For HSSC, where co-laminar flow of two materials constitutes an alternating-stripe pattern, this is the physical scenario of interest addressed in the next chapter. The analysis here also provides several simple relations between geometric parameters and flow characteristics that remain valid even in cases where channel width converges rapidly. With cautious optimism, it may be possible to extend these insights to future work in other applications that incorporate microchannels with moderately varying cross-sections.

CHAPTER 6. PERTURBATION ANALYSIS OF MULTI-FLUID INTERNAL FLOW FOR HSSC WITH HYDRODYNAMIC FOCUSING

6.1 Introduction

In this chapter, a perturbation analysis of internal flow within the heterogeneous stripe slot coating (HSSC) tool is described. The modeling efforts of this chapter consider a portion of the tool cavity with a converging width, wherein co-laminar flow of two materials develops a series of hydrodynamically focused continuous stripes. These efforts pursue a means to predict individual stripe widths at the coating tool outlet as a function of slot geometry, flow velocity, and material properties. As in Chapter 5, perturbation theory is used as the mathematical approach for this problem on the basis of the physical interpretation and intuition it provides. This approach excels at bridging the gap between high accuracy and coarse estimation with fundamental understanding.

In this case, the narrowing of an arbitrary number of stripes through internal geometry of the HSSC tool is considered. Background related to other modeling approaches from relevant past work is discussed in Section 6.2, and compared to the combination of assumptions considered by this work for the first time. The extended perturbation model is developed in Sections 6.3-6.7, leading to an analytical model for the shape of stripe patterns subject to hydrodynamic focusing within an HSSC tool.

In Section 6.9, experimental validation of the model results and assumptions is presented for the internal flow domain. Visualizations of co-laminar flow inside a transparent HSSC coating tool compare observed modes of mixing with those assumed by the analytical model in Chapter 6. Furthermore, the leading-order predictions of stripe interfaces from Chapter 6 are compared to experimental results with aqueous polyvinyl alcohol (PVA) solutions across various concentrations.

In Section 6.10, HSSC deposition and hydrodynamic focusing of narrow stripe structures is demonstrated with a commercial silver nanoparticle (Ag-NP) ink on a commercial pilot-scale roll-to-roll (R2R) system. This investigation constitutes a practical demonstration of hydrodynamically focused HSSC with a widely available functional material. The work in this section compares predictions from the perturbation analysis, which considers only the internal flow domain, with the final morphology of a printed film, which is influenced also by the coating flow domain and post-deposition curing phenomena. Additionally, capabilities for process control over pattern morphology, as well as the overall feature size performance of the HSSC deposition technique, are compared to the state-of-the art in conventional slot die coating.

6.2 Previous Modeling Efforts

With respect to coating and printing applications, co-deposition of two fluid materials through a focusing geometric feature constitutes a key innovation for the HSSC method. Perhaps the closest analogue among established printing techniques is found in

aerosol jet printing, which uses a sheath gas to focus a stream of fluid droplets oriented towards the substrate[18, 98]. Thus, the internal flow analysis required for the present work is informed primarily by existing literature in microfluidics, wherein co-laminar flow through planar geometries of varying cross-section is routinely encountered[218-221].

In the microfluidic regime, flow is non-turbulent, and the dominant mechanisms for mixing are diffusion and advection of fluid-fluid boundaries. Considerable research efforts have been devoted to maximizing the rate of microfluidic mixing, which constitutes a central engineering challenge for many applications[226-230]. In other cases, including the present work, slow passive mixing is a desirable characteristic of the flow, since it allows a fluid interface or interphase to be established, preserved, and manipulated[164, 237-242]. Special attention has been paid to core-annular flows and hydrodynamic focusing (HDF), wherein one fluid species is confined to a narrow portion of a channel cross section by virtue of a viscosity or flow rate mismatch[160-164]. These phenomena have been combined to fabricate polymeric tube structures[239] and microfibers[242], measure viscosity[243, 244] and chemical gradients[241], and to aid in biological cell analysis[240]. Additionally, HDF has been studied in conjunction with instability phenomena such as droplet formation[245, 246] and viscous buckling[247-249] to produce more complex microstructures. For HSSC, HDF can be considered the physical mechanism by which an alternating-stripe pattern, once established, is scaled to achieve feature sizes many times smaller than the minimum width of the channel.

Several previous modeling efforts have considered fully developed sheath flow in straight rectangular channels. Stiles and Fletcher described the location of an immiscible interface as a function of flow rate and viscosity ratio[250]. Sheath flow of two immiscible materials was later modeled by Tripathi et al., with ample discussion on the influence of viscosity ratio as well as channel aspect ratio[251]. Sheath flow with significant diffusion across the liquid-liquid interface was studied empirically by Cubaud and Mason[163], and analytically by Wu and Nguyen with the simplifying assumption of a uniform average velocity[162]. More recently, the problem was revisited by Sadeghi without the uniform-velocity assumption, who modeled the concentration field for fully-developed 2D sheath flow at moderate-to-large Peclet number (*Pe*)[252]. A comparison between existing modeling efforts and the modeling approach used in this work is organized in Table 6.1.

Table 6.1 – Summary of previous modeling efforts for two-fluid co-laminar flow through planar microchannels.

Authors	Assumptions [a]	No. of Interfaces	Model type	Validation
Stiles and Fletcher[250]	Immiscible fluids	1	Analytical	Numerical (CFX)
Wu and Nguyen[162]	Diffusion neglected along one axis; uniform velocity	2	Analytical	Numerical (custom)
Cubaud and Mason[163]		2	Empirical	Simplified analytical relation

Table 6.1 continued

Tripathi, Chakravarthy, and Agrawal[251]	Immiscible fluids	2	Analytical	Experiment
Sadeghi[252]	Diffusion neglected for derivation of velocity field	2	Analytical	Comparison of limiting cases
Present study	Diffusion neglected for derivation of velocity field	Arbitrary	Analytical	Experiment

[a] Except where stated otherwise, all models assume laminar, incompressible flow of Newtonian fluids, and analysis proceeds from convection-diffusion and Navier-Stokes equations; all models consider flow through a straight rectangular microchannel.

In summary, the existing literature provides extensive coverage of stripe-patterned sheath flow through straight rectangular channels, with considerable attention paid to diffusion transport coupled with convection transport at significantly different time scales. What existing literature does not provide is a model for the large-scale shape of the fluid boundaries in moderate-to-abrupt channel width reductions. The studies in Table 6.1 are also limited in scope to two fluid interfaces or fewer, in stratified or sheath flow configurations. Therefore, the analysis that follows addresses two points that benefit process modeling of HSSC. The theoretical approach considers a nonzero convergence angle for planar channel width, as well as the existence of an arbitrary number of fluid boundaries that do not mix.

6.3 3D Geometry and Governing Equations

The case where flow through the geometry first considered in Section 5.3 comprises N stripes of material *A*, alternating with N stripes of material *B*, can now be considered. This is illustrated schematically for $N = 4$ in Figure 6.1. With the introduction of the second fluid phase, the analysis here makes two additional assumptions. First, the rate of diffusive cross-mixing between the two fluids is treated as negligible compared to the mass transport by convection. Second, the pressure drop across fluid-fluid interfaces is taken to be zero. These assumptions are equivalent to a scenario where the Peclet number (*Pe*) is sufficiently large to treat two liquid species as immiscible, though it would be physically possible to produce a stable mixture comprising both. Hence, the fluid boundaries will not mix due to the large *Pe.* Two polymeric solutions of sufficiently high molecular weight, and which share a common solvent, are one example of a material system that can achieve this. The flow rate is the same across individual stripes for each fluid material, such that a volume flux of $\frac{1}{N}Q_A$ passes through stripes comprising fluid *A*, and a volume flux of $\frac{1}{N}Q_B$ passes through stripes comprising fluid *B*. Flow is assumed to be fully-developed, in the sense that the velocity field is not influenced by pressure conditions at $r \gg r_u$ or $r \ll r_d$. At $r = r_u$, the boundaries between adjacent stripes are located at some $\theta = \theta_2, \dots, \theta_{2N}$, which remain to be be determined. The boundaries of the channel are located, as before, at $\theta = \theta_1 = -\theta_H$ and $\theta = \theta_{2N+1} = \theta_H$. Mixing between the two fluids is assumed to be small, such that the gradation between *A* and *B* at interfaces is neglected for the purpose of

determining the velocity field. Q_A and Q_B, the total flow rate for fluid species *A* and *B*, respectively, are not assumed to be equal. Similarly, the respective viscosities of each, μ_A and μ_B, are not assumed to be equal.

It should be noted that while the analysis that follows assumes an even number of stripes, it is also possible to consider an odd number of stripes, where M stripes of material *A*, each with a volume flux of $\frac{1}{M}Q_A$ alternate with $M-1$ stripes of material *B*, each with a volume flux of $\frac{1}{M-1}Q_B$. The mathematical steps required for a case with $2M-1$ stripes are identical to a case with $2N$ stripes, aside from this difference in the flow rate condition. Therefore, the analysis that follows provides intermediate steps for the case of an even number of stripes. Where appropriate, alternate forms of derived solutions are expressed for an odd number of stripes for the sake of completeness.

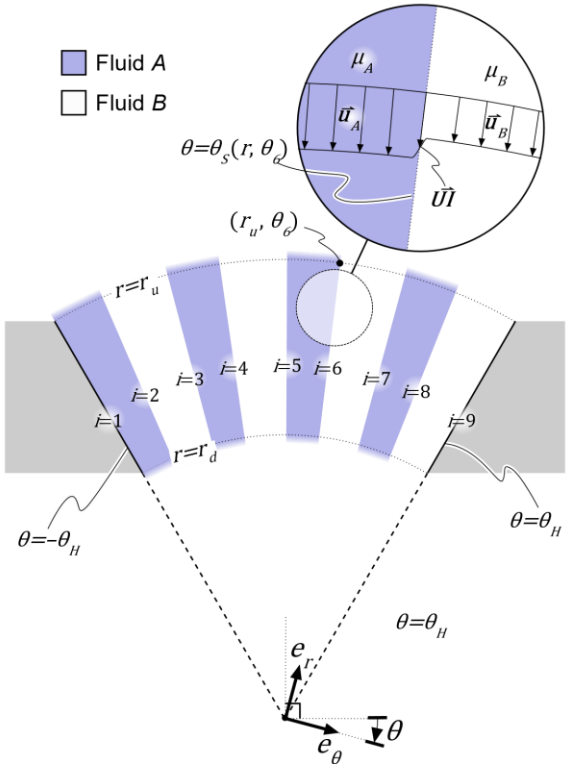

Figure 6.1 – Geometry of two-material flow through the microfluidic slot, shown from the top down for an example with eight regions alternating between two fluids. Fluid species *A* and *B* are denoted by color, as shown. Interfaces between fluid regions are numbered from $i = 2$ through $i = 8$, whereas boundaries indexed at $i = 1$ and $i = 9$ are the left and right channel boundaries, respectively. The inset view denotes the location of stripe interface 6 and visualizes the associated flow velocity at some $-1 < z < 1$. UI is the flow velocity at stripe interfaces.

To proceed with the formulation of this problem, the governing equations must be adjusted to account for the differences in flow rate and viscosity between fluids *A* and *B*. First, the total flow rate for both materials, denoted as $Q_{A+B} \equiv Q_A + Q_B$, is used in place of Q in Equations (5.5a)-(5.5d) in Section 5.4. Additionally, the sum of viscosities μ_A and μ_B, $\mu_{A+B} \equiv \mu_A + \mu_B$ is used in place of μ. Thus, the pressure and velocity scales can be

defined as $(\mu_{A+B}Q_{A+B})/G^3$ and $(\alpha Q_{A+B})/G^2$, respectively. The dimensionless coordinates are unchanged from Equations (5.5a)-(5.5d). Using these scales, the dimensionless governing equations for material *A* are as follows:

$$\frac{1}{r}\frac{\partial}{\partial r}(ru_{rA}) + \frac{1}{r}\frac{\partial}{\partial \theta}(u_{\theta A}) + \frac{\partial}{\partial z}(u_{zA}) = 0 \tag{6.1a}$$

$$\left(\frac{\mu_{A+B}}{\mu_A}\right)\frac{\partial p_A}{\partial r} = \alpha^2\frac{1}{r}\frac{\partial}{\partial r}\left(r\frac{\partial u_{rA}}{\partial r}\right) + \alpha^2\frac{1}{r^2}\frac{\partial^2 u_{rA}}{\partial \theta^2} + \frac{\partial^2 u_{rA}}{\partial z^2} - \alpha^2\frac{u_{rA}}{r^2} - \alpha^2\frac{2}{r^2}\frac{\partial u_{\theta A}}{\partial \theta} \tag{6.1b}$$

$$\left(\frac{\mu_{A+B}}{\mu_A}\right)\frac{\partial p_A}{\partial \theta} = \alpha^2\frac{1}{r}\frac{\partial}{\partial r}\left(r\frac{\partial u_{\theta A}}{\partial r}\right) + \alpha^2\frac{1}{r^2}\frac{\partial^2 u_{\theta A}}{\partial \theta^2} + \frac{\partial^2 u_{\theta A}}{\partial z^2} - \alpha^2\frac{u_{\theta A}}{r^2} + \alpha^2\frac{2}{r^2}\frac{\partial u_{rA}}{\partial \theta} \tag{6.1c}$$

$$\left(\frac{\mu_{A+B}}{\mu_A}\right)\frac{\partial p_A}{\partial z} = \alpha^4\frac{1}{r}\frac{\partial}{\partial r}\left(r\frac{\partial u_{zA}}{\partial r}\right) + \alpha^4\frac{1}{r^2}\frac{\partial^2 u_{zA}}{\partial \theta^2} + \alpha^2\frac{\partial^2 u_{zA}}{\partial z^2} \tag{6.1d}$$

Next, the dimensionless governing equations for material *B* are as follows:

$$\frac{1}{r}\frac{\partial}{\partial r}(ru_{rB}) + \frac{1}{r}\frac{\partial}{\partial \theta}(u_{\theta B}) + \frac{\partial}{\partial z}(u_{zB}) = 0 \tag{6.2a}$$

$$\left(\frac{\mu_{A+B}}{\mu_B}\right)\frac{\partial p_B}{\partial r} = \alpha^2\frac{1}{r}\frac{\partial}{\partial r}\left(r\frac{\partial u_{rB}}{\partial r}\right) + \alpha^2\frac{1}{r^2}\frac{\partial^2 u_{rB}}{\partial \theta^2} + \frac{\partial^2 u_{rB}}{\partial z^2} - \alpha^2\frac{u_{rB}}{r^2} - \alpha^2\frac{2}{r^2}\frac{\partial u_{\theta B}}{\partial \theta} \tag{6.2b}$$

$$\left(\frac{\mu_{A+B}}{\mu_B}\right)\frac{\partial p_B}{\partial \theta} = \alpha^2\frac{1}{r}\frac{\partial}{\partial r}\left(r\frac{\partial u_{\theta B}}{\partial r}\right) + \alpha^2\frac{1}{r^2}\frac{\partial^2 u_{\theta B}}{\partial \theta^2} + \frac{\partial^2 u_{\theta B}}{\partial z^2} - \alpha^2\frac{u_{\theta B}}{r^2} + \alpha^2\frac{2}{r^2}\frac{\partial u_{rB}}{\partial \theta} \tag{6.2c}$$

$$\left(\frac{\mu_{A+B}}{\mu_B}\right)\frac{\partial p_B}{\partial z} = \alpha^4\frac{1}{r}\frac{\partial}{\partial r}\left(r\frac{\partial u_{zB}}{\partial r}\right) + \alpha^4\frac{1}{r^2}\frac{\partial^2 u_{zB}}{\partial \theta^2} + \alpha^2\frac{\partial^2 u_{zB}}{\partial z^2} \tag{6.2d}$$

The forms of these equations are unchanged from Equations (5.7a)-(5.7d), other than the replacement of (u_r, u_θ, u_z) with $\left(\frac{\mu_A}{\mu_{A+B}}\right)(u_{rA}, u_{\theta A}, u_{zA})$ and p with p_A in Equations (6.1a)-(6.1d), and (u_r, u_θ, u_z) with $\left(\frac{\mu_B}{\mu_{A+B}}\right)(u_{rB}, u_{\theta B}, u_{zB})$ and p with p_A in Equations (6.2a)-(6.2d).

6.4 Boundary Conditions

The boundary conditions for the two-fluid case are also similar to those for flow of a single fluid:

$$u_{rA} = u_{zA} = 0 \text{ at } \theta = \theta_1 \quad \text{(No-slip, } \theta\text{-axis left boundary, fluid } A\text{)} \tag{6.3a}$$

$$u_{rB} = u_{zB} = 0 \text{ at } \theta = \theta_{2N} \quad \text{(No-slip, } \theta\text{-axis right boundary, fluid } B\text{)} \tag{6.3b}$$

$$u_{\theta A} = 0 \text{ at } \theta = \theta_1 = -\theta_H \qquad \text{(No-flux, } \theta\text{-axis left boundary, fluid } A\text{)} \qquad (6.3c)$$

$$u_{\theta B} = 0 \text{ at } \theta = \theta_9 = \theta_H \qquad \text{(No-flux, } \theta\text{-axis right boundary, fluid } B\text{)} \qquad (6.3d)$$

$$u_{rA} = u_{rB} = u_{\theta A} = u_{\theta B} = 0 \text{ at } z = 1 \qquad \text{(No-slip, } z\text{-axis boundary)} \qquad (6.3e)$$

$$u_{zA} = u_{zB} = 0 \text{ at } z = 1 \qquad \text{(No-flux, } z\text{-axis boundary)} \qquad (6.3f)$$

$$\frac{\partial u_{rA}}{\partial z} = \frac{\partial u_{\theta A}}{\partial \hat{z}} = u_{zA} = 0 \text{ at } z = 0 \qquad \text{(Symmetry about } z = 0\text{, fluid } A\text{)} \qquad (6.3g)$$

$$\frac{\partial u_{rB}}{\partial z} = \frac{\partial u_{\theta B}}{\partial \hat{z}} = u_{zB} = 0 \text{ at } z = 0 \qquad \text{(Symmetry about } z = 0\text{, fluid } B\text{)} \qquad (6.3h)$$

$$p_A = p_B = p_d \text{ at } (r, \theta, z) = (r_d, 0, 0) \qquad \text{(Reference pressure)} \qquad (6.3i)$$

In addition to those given above, additional boundary conditions are required for the interfaces between fluids *A* and *B*. In order to phrase these boundary conditions in a convenient form, however, insights from the single-fluid case will be exploited to infer the shapes of the fluid interfaces.

First, it can be recognized that in the single material velocity field, the shapes of streamlines are insensitive to viscosity to order $\mathcal{O}(\alpha)$. Second, for regions sufficiently far from the channel boundaries, the shapes of streamlines are also insensitive to z. To show that the shapes of streamlines are insensitive to z, one may consider a streamline, *S*, passing through the point $(r, \theta, z) = (r_u, \theta_i, z_j)$. The shape of the streamline is given by the following:

$$\frac{r\partial\theta}{\partial r} = \frac{u_\theta(r,\theta,z)}{u_r(r,\theta,z)} \tag{6.4a}$$

$$\frac{\partial z}{\partial r} = \frac{u_z(r,\theta,z)}{u_r(r,\theta,z)} \tag{6.4b}$$

Thus, $\frac{\partial\theta}{\partial r}$ is a function of r and θ only, and $\frac{\partial z}{\partial r} = 0$.

Substituting the outer velocity field expansion from Equations (6.4a)-(6.4c) provides the shape of a streamline in the form of the following initial value problem:

$$\begin{aligned}\frac{\partial}{\partial r}\{\theta_S(r)\} &= \frac{\frac{\alpha}{r}\left(\sum_{n=1}^{\infty}\frac{6}{\delta_n^5}\right)\frac{\sin(\theta)}{\sin(\theta_H)}}{1+\frac{\alpha}{r}\left(\sum_{n=1}^{\infty}\frac{6}{\delta_n^5}\right)\frac{\cos(\theta)}{\sin(\theta_H)} - C_{0,err}} \\ &= \frac{\frac{\alpha}{r}\left(\sum_{n=1}^{\infty}\frac{6}{\delta_n^5}\right)\frac{\sin(\theta)}{\sin(\theta_H)}}{1+\frac{\alpha}{r}\left(\sum_{n=1}^{\infty}\frac{6}{\delta_n^5}\right)\frac{\cos(\theta)-\cos(\theta_H)}{\sin(\theta_H)}}\end{aligned} \tag{6.5a}$$

$$\theta_S(r_u) = \theta_i \tag{6.5b}$$

where $i = 1 \ldots 2N + 1$ is the integer index for stripe boundaries, including left and right sidewalls at $i = 1$ and $i = 2N + 1$, respectively. The θ-coordinates of streamlines passing through $\theta_2, \ldots, \theta_{2N}$ at the inflow boundary are denoted as $\theta_S(r, \theta_2), \ldots, \theta_S(r, \theta_{2N})$. These can be determined by solving Equation (6.5a) for $\theta_S(r_u) = \theta_2, \ldots, \theta_S(r_u) = \theta_{2N}$. Using this notation, the flow rate conditions for individual stripes can now be formulated as follows:

$$\frac{1}{N}\frac{Q_A}{Q_{A+B}} = \int_{-1}^{1}\int_{\theta_S(r,\theta_{2n-1})}^{\theta_S(r,\theta_{2n})} u_{rA}\, r d\theta dz\,, n = 1, \ldots, N \qquad \text{(Flow rate condition for fluid A)} \tag{6.6a}$$

$$\frac{1}{N}\frac{Q_B}{Q_{A+B}} = \int_{-1}^{1}\int_{\theta_S(r,\theta_{2n})}^{\theta_S(r,\theta_{2n+1})} u_{rB}\, r d\theta dz\,, n = 1, \ldots, N \qquad \text{(Flow rate condition for fluid B)} \tag{6.6b}$$

The flow velocity components at a stripe interface passing through $(r, \theta) = (r_u, \theta_i)$ are denoted as $\overrightarrow{UI}(r, \theta_n, z) \equiv \vec{u}(r, \theta_S(r, \theta_i), z)$, as illustrated in Figure 6.1, where $\vec{u}_A \equiv (u_{rA}, u_{\theta A}, u_{zA})$ and $\vec{u}_B \equiv (u_{rB}, u_{\theta B}, u_{zB})$. The kinematic boundary condition at fluid interfaces can now be formulated as follows:

$$\vec{u}_A = \vec{u}_B = \overrightarrow{UI}(r, \theta_i, z) \text{ at } \theta_S(r, \theta_i) \qquad \text{for } i = 2, \ldots, 2N \qquad \text{(Continuous velocity at interfaces)} \tag{6.6c}$$

Here, the pressure drop across fluid boundaries is assumed to be zero. Furthermore, mechanical stress must be continuous across fluid boundaries. These points will be enforced with the following boundary conditions:

$$\boldsymbol{T}_A = \boldsymbol{T}_B \text{ at } \theta_S(r, \theta_i) \quad \text{for } i = 2, \dots, 2N \qquad \text{(Continuous stress at interfaces)} \tag{6.6d}$$

where $\boldsymbol{T}_A$ and $\boldsymbol{T}_B$ are the dimensionless stress tensors of fluids *A* and *B*, defined in cylindrical coordinates by:

$$\begin{aligned} \boldsymbol{T} &\equiv \begin{bmatrix} \tau_{rr} & \tau_{r\theta} & \tau_{rz} \\ \tau_{\theta r} & \tau_{\theta\theta} & \tau_{\theta z} \\ \tau_{zr} & \tau_{z\theta} & \tau_{zz} \end{bmatrix} \\ &\equiv -\alpha \begin{bmatrix} p & 0 & 0 \\ 0 & p & 0 \\ 0 & 0 & p \end{bmatrix} \\ &+ \left(\frac{\mu}{\mu_{A+B}}\right) \begin{bmatrix} 2\alpha \dfrac{\partial u_r}{\partial r} & \alpha\left[r\dfrac{\partial}{\partial r}\left(\dfrac{u_\theta}{r}\right) + \dfrac{1}{r}\dfrac{\partial u_r}{\partial \theta}\right] & \left(\dfrac{\partial u_r}{\partial z} + \alpha\dfrac{\partial u_z}{\partial r}\right) \\ \alpha\left[r\dfrac{\partial}{\partial r}\left(\dfrac{u_\theta}{r}\right) + \dfrac{1}{r}\dfrac{\partial u_r}{\partial \theta}\right] & 2\alpha\left(\dfrac{1}{r}\dfrac{\partial u_\theta}{\partial \theta} + \dfrac{u_r}{r}\right) & \left(\dfrac{\partial u_\theta}{\partial z} + \alpha\dfrac{1}{r}\dfrac{\partial u_z}{\partial \theta}\right) \\ \left(\dfrac{\partial u_r}{\partial z} + \alpha\dfrac{\partial u_z}{\partial r}\right) & \left(\dfrac{\partial u_\theta}{\partial z} + \alpha\dfrac{1}{r}\dfrac{\partial u_z}{\partial \theta}\right) & 2\dfrac{\partial u_z}{\partial z} \end{bmatrix} \end{aligned} \tag{6.7}$$

It should be noted that the locations of the fluid interfaces are still unknown at this stage. The determination of these interfaces constitutes a central difficulty for the problem under consideration in this chapter. This task will be addressed in Sections 6.7 and 6.8,

following the development of the $\mathcal{O}(\alpha)$ approximations of $(u_{rA}, u_{\theta A}, u_{zA})$ and $(u_{rB}, u_{\theta B}, u_{zB})$.

6.5 Outer Solutions

Composite velocity fields are sought for fluids *A* and *B*, denoted as $\vec{u}_A \equiv (u_{rA}, u_{\theta A}, u_{zA})$ and $\vec{u}_B \equiv (u_{rB}, u_{\theta B}, u_{zB})$, respectively. These velocity fields comprise an inner velocity valid near the boundaries of each stripe, as well as an outer velocity valid throughout the regions far from these boundaries. Hereafter, the velocity in the outer regions is denoted as $\vec{U}_i \equiv (U_{ri}, U_{\theta i}, U_{zi})$ for the region bounded by $\theta_S(r, \theta_{i+1})$ on the right and $\theta_S(r, \theta_i)$ on the left. The viscosity within this region is denoted as μ_i, such that $\mu_i = \mu_A$ for odd values of i and $\mu_i = \mu_B$ for even values of i. As with the single-fluid case, a first-order expansion about α is assumed for both velocity and pressure, as follows:

$$(U_{ri}, U_{\theta i}, U_{zi}) = \left(U_{ri,0}, U_{\theta i,0}, U_{zi,0}\right) + \alpha\left(U_{ri,1}, U_{\theta i,1}, U_{zi,1}\right) + \mathcal{O}(\alpha^2) \tag{6.8a}$$

$$p_i = p_{i,0} + \alpha p_{i,1} + \mathcal{O}(\alpha^2) \tag{6.8b}$$

Substituting $\mu_A(u_{rA}, u_{\theta A}, u_{zA}, p_A) = \mu_i(U_{ri}, U_{\theta i}, U_{zi}, p_i)$ for odd i in Equations (6.1a)-(6.1d), and $\mu_B(u_{rB}, u_{\theta B}, u_{zB}, p_B) = \mu_i(U_{ri}, U_{\theta i}, U_{zi}, p_i)$ for even i in Equations (6.2a)-(6.2d), then setting $\alpha = 0$, yields the leading-order $\mathcal{O}(1)$ governing equations for the outer regions:

$$\frac{1}{r}\frac{\partial}{\partial r}\left(rU_{ri,0}\right)+\frac{1}{r}\frac{\partial}{\partial \theta}\left(U_{\theta i,0}\right)+\frac{\partial}{\partial z}\left(U_{zi,0}\right)=0 \tag{6.9a}$$

$$\left(\frac{\mu_{A+B}}{\mu_i}\right)\frac{\partial p_{i,0}}{\partial r}=\frac{\partial^2 U_{ri,0}}{\partial z^2} \tag{6.9b}$$

$$\left(\frac{\mu_{A+B}}{\mu_i}\right)\frac{1}{r}\frac{\partial p_{i,0}}{\partial \theta}=\frac{\partial^2 U_{\theta i,0}}{\partial z^2} \tag{6.9c}$$

$$\frac{\partial p_{i,0}}{\partial z}=0 \tag{6.9d}$$

Equations (6.9a)- (6.9d) above are subject to the following boundary conditions:

$$U_{ri}=U_{\theta i}=0 \quad \text{(No-slip, } z\text{-axis boundary)} \tag{6.10a}$$

$$U_{zi}=0 \text{ at } z=1 \quad \text{(No-flux, } z\text{-axis boundary)} \tag{6.10b}$$

$$\frac{\partial U_{ri}}{\partial z}=\frac{\partial U_{\theta i}}{\partial \hat{z}}=U_{zi}=0 \text{ at } z=0 \quad \text{(Symmetry about } z=0\text{)} \tag{6.10c}$$

$$p_{i0}=p_d \text{ at } (r,\theta,z)=(r_d,0,0) \quad \text{(Reference pressure condition)} \tag{6.10d}$$

The same steps can be re-used from Section 5.5 to arrive at the Laplace equation in polar coordinates as the governing equation for pressure, which permits solutions of the following form:

$$p_{i,0} - p_d = A_{0,i} \ln\left(\frac{r}{r_d}\right) + \sum_{n=1}^{\infty}\left(-A_{n,1,i} r^{-n} + A_{n,2,i} r^{n}\right)\left[\cos(n\theta) + A_{n,3,i} \sin(n\theta)\right] - \sum_{n=1}^{\infty}\left(-A_{n,1,i} {r_d}^{-n} + A_{n,2,i} {r_d}^{n}\right) \tag{6.11a}$$

where $A_{0,i}, A_{n,1,i}$, $A_{n,2,i}$, and $A_{n,3,i}$ are constants that must be determined based on boundary conditions and by matching with the inner velocity field near the channel boundaries and fluid interfaces. The presence of $A_{n,3,i}$, in Equation (6.11a), which has no analog in Equation (5.14a) from the single-fluid case, reflects the lack of an assumed symmetry condition about $\theta = 0$.

The $\mathcal{O}(\alpha)$ governing equations for the outer region can be obtained by the same steps, and yield the same general form for the pressure field correction:

$$p_{i,1} = B_{0,i} \ln\left(\frac{r}{r_d}\right) + \sum_{n=1}^{\infty}\left(-B_{n,1,i} r^{-n} + B_{n,2,i} r^{n}\right)\left[\cos(n\theta) + B_{n,3,i}\sin(n\theta)\right] - \sum_{n=1}^{\infty}\left(-B_{n,1,i} {r_d}^{-n} + B_{n,2,i} {r_d}^{n}\right) \tag{6.11b}$$

In addition, the constant coefficients $B_{0,i}$, $B_{n,1,i}$, $B_{n,2,i}$, and $B_{n,3,i}$ must be determined based on boundary conditions and by matching with the inner velocity fields. As with the single-fluid case, the outer velocity components are parabolic with respect to z and can be expressed in terms of the pressure gradient as follows:

$$U_{ri} = -\left(\frac{\mu_{A+B}}{\mu_i}\right)\left(\frac{1-z^2}{2}\right)\frac{\partial}{\partial r}(p_0 + \alpha p_1) + \mathcal{O}(\alpha^2) \tag{6.12a}$$

$$U_{\theta i} = -\left(\frac{\mu_{A+B}}{\mu_i}\right)\left(\frac{1-z^2}{2r}\right)\frac{\partial}{\partial \theta}(p_0 + \alpha p_1) + \mathcal{O}(\alpha^2) \tag{6.12b}$$

$$U_{zi} \sim \mathcal{O}(\alpha^2) \tag{6.12b}$$

6.6 Inner Solutions

For a fluid interface located at $\theta_S(r, \theta_i)$, for some $2 \leq i \leq 2N$, the inner velocity is denoted as $\vec{V}_i \equiv (V_{ri}, V_{\theta i}, V_{zi})$ for the fluid species to the left of the interface, and $\vec{W}_i \equiv (W_{ri}, W_{\theta i}, W_{zi})$ for the fluid species to the right. It should be noted that $\vec{W}_1$ and $\vec{V}_{2N+1}$ correspond to the inner velocities near $\theta = -\theta_H$ and $\theta = \theta_H$, respectively, and require

separate θ-axis boundary conditions. Both inner velocities are expanded asymptotically about α, as follows:

$$(V_{ri}, V_{\theta i}, V_{zi}) = (V_{ri,0}, V_{\theta i,0}, V_{zi,0}) + \alpha(V_{ri,1}, V_{\theta i,1}, V_{zi,1}) + \mathcal{O}(\alpha^2) \tag{6.13a}$$

$$(W_{ri}, W_{\theta i}, W_{zi}) = (W_{ri,0}, W_{\theta i,0}, W_{zi,0}) + \alpha(W_{ri,1}, W_{\theta i,1}, W_{zi,1}) + \mathcal{O}(\alpha^2) \tag{6.13b}$$

Next, a scaled coordinate associated with the boundary, $\xi_i \equiv \frac{\theta - \theta_S(r,\theta_i)}{\alpha}$ is introduced. The leading-order $\mathcal{O}(1)$ terms of Equations (6.1a)-(6.1d) and (6.2a)-(6.2d) are expressed in terms of the inner coordinate as follows:

$$\frac{1}{r}\frac{\partial}{\partial \xi_i}(V_{\theta i,0}) = 0 \tag{6.14a}$$

$$\frac{1}{r}\frac{\partial}{\partial \xi_i}(W_{\theta i,0}) = 0 \tag{6.14b}$$

$$\left(\frac{\mu_{A+B}}{\mu_{(i-1)}}\right)\frac{\partial p_{(i-1),0}}{\partial r} = \frac{1}{r^2}\frac{\partial^2 V_{ri,0}}{\partial {\xi_i}^2} + \frac{\partial^2 V_{ri,0}}{\partial z^2} \tag{6.14c}$$

$$\left(\frac{\mu_{A+B}}{\mu_i}\right)\frac{\partial p_{i,0}}{\partial r} = \frac{1}{r^2}\frac{\partial^2 W_{ri,0}}{\partial {\xi_i}^2} + \frac{\partial^2 W_{ri,0}}{\partial z^2} \tag{6.14d}$$

$$\frac{1}{r}\frac{\partial p_{(i-1),0}}{\partial \xi_i} = 0 \tag{6.14e}$$

$$\frac{1}{r}\frac{\partial p_{i,0}}{\partial \xi_i} = 0 \tag{6.14f}$$

$$\frac{\partial p_{(i-1),0}}{\partial z} = 0 \tag{6.14g}$$

$$\frac{\partial p_{i,0}}{\partial z} = 0 \tag{6.14h}$$

Above, μ_i denotes the viscosity of the fluid species to the left of the interface at $\theta_S(r, \theta_i)$. Thus, for even-numbered boundaries, $\mu_{i-1} = \mu_A$ and $\mu_i = \mu_B$, and *vice versa* for odd-numbered boundaries. For $2 \leq i \leq 2N$, Equations (6.14a)-(6.14h) are subject to the following boundary conditions:

$$V_{ri,0} = V_{\theta i,0} = W_{ri,0} = W_{\theta i,0} = 0 \text{ at } z = 1 \quad \text{(No-slip, } z\text{-axis boundary)} \tag{6.15a}$$

$$\frac{\partial V_{ri,0}}{\partial z} = \frac{\partial V_{\theta i,0}}{\partial z} = \frac{\partial W_{ri,0}}{\partial z} = \frac{\partial W_{\theta i,0}}{\partial z} = 0 \text{ at } z = 1 \quad \text{(Symmetry about } z = 0\text{)} \tag{6.15b}$$

$$\vec{V}_{i,0} = \vec{W}_{i,0} = \vec{UI}(r, \theta_i, z) \text{ at } \xi_i = 0 \quad \text{(Continuous velocity across fluid interfaces)} \tag{6.15c}$$

The stress condition at $\xi_i = 0$ can be re-written in terms of the $\mathcal{O}(1)$ components of the stress tensor, as follows:

$$\left(\frac{\mu_{(i-1)}}{\mu_{A+B}}\right)\left(\frac{1}{r}\frac{\partial V_{\theta(i-1),0}}{\partial \xi_i} + \frac{\partial V_{z(i-1),0}}{\partial z}\right) = \left(\frac{\mu_i}{\mu_{A+B}}\right)\left(\frac{1}{r}\frac{\partial W_{\theta i,0}}{\partial \xi_i} + \frac{\partial W_{zi,0}}{\partial z}\right) \quad \text{(Normal stress at fluid interfaces)} \quad (6.15e)$$

$$\text{at } \xi_i = 0 \text{ for } i = 2, \dots, 2N$$

$$\left(\frac{\mu_{(i-1)}}{\mu_{A+B}}\right)\left(\frac{1}{r}\frac{\partial V_{r(i-1),0}}{\partial \xi_i}\right) = \left(\frac{\mu_i}{\mu_{A+B}}\right)\left(\frac{1}{r}\frac{\partial W_{ri,0}}{\partial \xi_i}\right);$$

$$\left(\frac{\mu_{(i-1)}}{\mu_{A+B}}\right)\left(\frac{\partial V_{\theta(i-1),0}}{\partial z} + \frac{1}{r}\frac{\partial V_{z(i-1),0}}{\partial \xi_i}\right) = \left(\frac{\mu_i}{\mu_{A+B}}\right)\left(\frac{\partial W_{\theta i,0}}{\partial z} + \frac{1}{r}\frac{\partial W_{zi,0}}{\partial \xi_i}\right) \quad \text{(Shear stress at fluid interfaces)} \quad (6.15f)$$

$$\text{at } \xi_i = 0 \text{ for } i = 2, \dots, 2N$$

At the boundaries of the channel, the velocity and shear conditions at $\xi_i = 0$ can be replaced by no-slip and no-flux conditions as follows:

$$V_{ri,0} = 0 \text{ at } \xi_i = 0 \text{ for } i = 2N + 1 \quad \text{(No-slip at } \theta\text{-axis right boundary)} \quad (6.16a)$$

$$V_{\theta i,0} = 0 \text{ at } \xi_i = 0 \text{ for } i = 2N + 1 \quad \text{(No-flux at } \theta\text{-axis right boundary)} \quad (6.16b)$$

$$W_{ri,0} = 0 \text{ at } \xi_i = 0 \text{ for } i = 1 \quad \text{(No-slip at } \theta\text{-axis left boundary)} \quad (6.16c)$$

$$W_{\theta i,0} = 0 \text{ at } \xi_i = 0 \text{ for } i = 1 \qquad \begin{matrix}\text{(No-flux at } \theta\text{-axis} \\ \text{left boundary)}\end{matrix} \tag{6.16d}$$

Equations (6.14e) and (6.14f) imply that the pressure field from the outer regions is impressed upon the regions near channel boundaries. Since the pressure drop across fluid interfaces is zero, both fluids A and B are described by the same pressure field. Furthermore, Equations (6.14a) and (6.14b) imply that θ-component of the inner velocity is inherited from the outer regions, and continuous across boundaries. Examining the form of the leading-order pressure field from Equation (6.11a) the constant coefficients $A_{n,1,i}$, $A_{n,2,i}$, and $A_{n,3,i}$ must all be zero in order to satisfy the no-flux boundary conditions at $\theta = -\theta_H$ and $\theta = \theta_H$. Thus, the leading-order pressure field can be simplified considerably, and takes the same form from the single-fluid case:

$$p_{i,0} - p_d = A_0 \ln\left(\frac{r}{r_d}\right) \tag{6.17}$$

For two fluids, a single constant, A_0, has been used in place of $A_{0,i}$, since the pressure field is the same for both fluid materials.

With this pressure field, $V_{\theta i,0}$ and $W_{\theta i,0}$ are both zero for all i, and the r-components of the outer velocities to the left and right of the interface are given by $U_{r(i-1),1} = -\left(\frac{\mu_{A+B}}{\mu_{(i-1)}}\right)\frac{A_0}{r}\left(\frac{1-z^2}{2}\right)$ and $U_{ri,1} = -\left(\frac{\mu_{A+B}}{\mu_i}\right)\frac{A_0}{r}\left(\frac{1-z^2}{2}\right)$, respectively. Since the leading-order

velocity profile is proportional to $\frac{1-z^2}{2r}$ on either side of the interface, intuition suggests that the velocity profile at the interface itself may be proportional to $\frac{1-z^2}{2r}$, as well. This requires solutions to Equations (6.14c) and (6.14d) that also satisfy $V_{ri,0} = W_{ri,0} = -\frac{AI_i}{r}\left(\frac{1-z^2}{2}\right)$ at $\xi_i = 0$, where AI_i is a constant coefficient associated with the interface at $\theta_S(r, \theta_i)$. These solutions can easily be adapted from the form of the leading-order radial velocity for the single-fluid case given by Equation (5.22):

$$V_{ri,0} = \left(\frac{\mu_{A+B}}{\mu_{(i-1)}}\right)\frac{A_0}{r}\left\{\sum_{n=1}^{\infty} E_n \exp\{\delta_n r \xi_i\}\cos(\delta_n z) - \left(\frac{1-z^2}{2}\right)\right\} - \frac{AI_i}{r}\sum_{n=1}^{\infty} E_n \exp\{\delta_n r \xi_i\}\cos(\delta_n z) \tag{6.18a}$$

$$W_{ri,0} = \left(\frac{\mu_{A+B}}{\mu_i}\right)\frac{A_0}{r}\left\{\sum_{n=1}^{\infty} E_n \exp\{-\delta_n r \xi_i\}\cos(\delta_n z) - \left(\frac{1-z^2}{2}\right)\right\} - \frac{AI_i}{r}\sum_{n=1}^{\infty} E_n \exp\{-\delta_n r \xi_i\}\cos(\delta_n z) \tag{6.18b}$$

where $E_n = 2\frac{(-1)^{n-1}}{(\delta_n)^3}$ and $\delta_n \equiv \frac{(2n-1)}{2}\pi$ retain their definitions from 0. For $2 \le i \le 2N$, AI_i will be determined by enforcing the stress condition at the interface. For the special cases of $i = 1$ and $i = 2N + 1$, the velocity profiles satisfying no-slip at $\xi_i = 0$ require $AI_1 = AI_{(2N+1)} = 0$:

$$V_{r(2N+1),0} = \left(\frac{\mu_{A+B}}{\mu_B}\right)\frac{A_0}{r}\left\{\sum_{n=1}^{\infty} E_n \exp\{\delta_n r\xi_i\}\cos(\delta_n z) - \left(\frac{1-z^2}{2}\right)\right\} \tag{6.19a}$$

$$W_{r1,0} = \left(\frac{\mu_{A+B}}{\mu_A}\right)\frac{A_0}{r}\left\{\sum_{n=1}^{\infty} E_n \exp\{-\delta_n r\xi_i\}\cos(\delta_n z) - \left(\frac{1-z^2}{2}\right)\right\} \tag{6.19b}$$

The analysis now proceeds to the $\mathcal{O}(\alpha)$ governing equations. Noting that $V_{\theta i,0} = W_{\theta i,0} = 0$, the $\mathcal{O}(\alpha)$ terms from Equations (6.1a)-(6.1d) and (6.2a)-(6.2d) are expressed in terms of the inner coordinate as follows:

$$\frac{1}{r}\frac{\partial}{\partial r}\left(rV_{ri,0}\right) + \frac{1}{r}\frac{\partial}{\partial \xi_i}\left(V_{\theta i,1}\right) + \frac{\partial}{\partial z}\left(V_{zi,0}\right) = 0 \tag{6.20a}$$

$$\frac{1}{r}\frac{\partial}{\partial r}\left(rW_{ri,0}\right) + \frac{1}{r}\frac{\partial}{\partial \xi_i}\left(W_{\theta i,1}\right) + \frac{\partial}{\partial z}\left(W_{zi,0}\right) = 0 \tag{6.20b}$$

$$\left(\frac{\mu_{A+B}}{\mu_{(i-1)}}\right)\frac{\partial p_1}{\partial r} = \frac{1}{r^2}\frac{\partial^2 V_{ri,1}}{\partial {\xi_i}^2} + \frac{\partial^2 V_{ri,1}}{\partial z^2} \tag{6.20c}$$

$$\left(\frac{\mu_{A+B}}{\mu_i}\right)\frac{\partial p_1}{\partial r} = \frac{1}{r^2}\frac{\partial^2 W_{ri,1}}{\partial {\xi_i}^2} + \frac{\partial^2 W_{ri,1}}{\partial z^2} \tag{6.20d}$$

$$\frac{1}{r}\frac{\partial p_{(i-1),1}}{\partial \xi_i} = 0 \tag{6.20e}$$

$$\frac{1}{r}\frac{\partial p_{i,1}}{\partial \xi_i} = 0 \tag{6.20f}$$

$$\frac{\partial p_{(i-1),1}}{\partial z} = 0 \tag{6.20g}$$

$$\frac{\partial p_{i,1}}{\partial z} = 0 \tag{6.20h}$$

The flow described by Equations (6.20a)-(6.20h) are subject to the following additional boundary conditions:

$$V_{ri,1} = V_{\theta i,1} = W_{ri,1} = W_{\theta i,1} = 0 \text{ at } z = 1 \quad \text{(No-slip, } z\text{-axis boundary)} \tag{6.21a}$$

$$V_{zi,0} = W_{zi,0} = 0 \text{ at } z = 1 \quad \text{(No-flux, } z\text{-axis boundary)} \tag{6.21b}$$

$$\frac{\partial V_{ri,1}}{\partial z} = \frac{\partial V_{\theta i,1}}{\partial z} = V_{zi,0} = \frac{\partial W_{ri,1}}{\partial z} = \frac{\partial W_{\theta i,1}}{\partial z} = W_{zi,0} = 0 \text{ at } z = 1 \quad \text{(Symmetry about } z = 0\text{)} \tag{6.21c}$$

$$\vec{V}_{i,1} = \vec{W}_{i,1} = \overrightarrow{UI}(r, \theta_i, z) \text{ at } \xi_i = 0 \quad \text{(Continuous velocity across fluid interfaces)} \tag{6.21d}$$

The stress condition at $\xi_i = 0$ can be rewritten in terms of the $\mathcal{O}(\alpha)$ components of the stress tensor, as follows:

$$3p_{(i-1)} - 2\left(\frac{\mu_{(i-1)}}{\mu_{A+B}}\right)\left(\frac{\partial V_{r(i-1),0}}{\partial r} + \frac{1}{r}\frac{\partial V_{\theta(i-1),1}}{\partial \xi_i} + \frac{V_{r(i-1),0}}{r} + \frac{\partial V_{z(i-1),1}}{\partial z}\right)$$

$$= 3p_i - 2\left(\frac{\mu_i}{\mu_{A+B}}\right)\left(\frac{\partial W_{ri,0}}{\partial r} + \frac{1}{r}\frac{\partial W_{\theta i,1}}{\partial \xi_i} + \frac{W_{ri,0}}{r} + \frac{\partial W_{zi,1}}{\partial z}\right)$$

(Normal stress at fluid interfaces) (6.21e)

at $\xi_i = 0$ for $i = 2, \ldots, 2N$

$$\left(\frac{\mu_{(i-1)}}{\mu_{A+B}}\right)\left(r\frac{\partial}{\partial r}\left(\frac{V_{\theta(i-1),0}}{r}\right) + \frac{1}{r}\frac{\partial V_{r(i-1),1}}{\partial \xi_i}\right) = \left(\frac{\mu_i}{\mu_{A+B}}\right)\left(r\frac{\partial}{\partial r}\left(\frac{W_{\theta i,0}}{r}\right) + \frac{1}{r}\frac{\partial W_{ri,1}}{\partial \xi_i}\right);$$

$$\left(\frac{\mu_{(i-1)}}{\mu_{A+B}}\right)\left(\frac{\partial V_{\theta(i-1),1}}{\partial z} + \frac{1}{r}\frac{\partial V_{z(i-1),1}}{\partial \xi_i}\right) = \left(\frac{\mu_i}{\mu_{A+B}}\right)\left(\frac{\partial W_{\theta i,1}}{\partial z} + \frac{1}{r}\frac{\partial W_{zi,1}}{\partial \xi_i}\right)$$

(Shear stress at fluid interfaces) (6.21f)

at $\xi_i = 0$ for $i = 2, \ldots, 2N$

At the boundaries of the channel, the velocity and shear conditions at $\xi_i = 0$ can be replaced by no-slip and no-flux conditions as follows:

$$V_{ri,1} = V_{zi,0} = 0 \text{ at } \xi_i = 0 \text{ for } i = 2N + 1$$

(No-slip at θ-axis right boundary) (6.22a)

$$V_{\theta i,1} = 0 \text{ at } \xi_i = 0 \text{ for } i = 2N + 1 \quad \text{(No-flux at } \theta\text{-axis right boundary)} \tag{6.22b}$$

$$W_{ri,1} = W_{zi,0} = 0 \text{ at } \xi_i = 0 \text{ for } i = 1 \quad \text{(No-slip at } \theta\text{-axis left boundary)} \tag{6.22c}$$

$$W_{\theta i,1} = 0 \text{ at } \xi_i = 0 \text{ for } i = 1 \quad \text{(No-flux at } \theta\text{-axis left boundary)} \tag{6.22d}$$

Equations (6.20e) and (6.20f) imply that to $\mathcal{O}(\alpha)$, the pressure from the outer regions is again imposed on the adjacent inner regions. Thus, again, the $\mathcal{O}(\alpha)$ pressure correction is the same for both fluid materials, and $\frac{\partial p_1}{\partial r}$ in Equations (6.20c) and (6.20d) can be obtained from its value in the outer regions near the boundary at $\theta_S(r, \theta_i)$. Hereafter, the $\mathcal{O}(\alpha)$ pressure correction can be rewritten as follows:

$$\begin{aligned} p_1 = B_0 \ln\left(\frac{r}{r_d}\right) + \sum_{n=1}^{\infty} \left(-B_{n,1} r^{-n} + B_{n,2} r^n\right) \cos(n\theta) \\ - \sum_{n=1}^{\infty} \left(-B_{n,1} {r_d}^{-n} + B_{n,2} {r_d}^n\right) \end{aligned} \tag{6.23}$$

Above, the constants $B_{0,i}$, $B_{n,1,i}$, and $B_{n,2,i}$ have been replaced by B_0, $B_{n,1}$, and $B_{n,2}$, respectively. The final i subscript is superfluous, since these constants are consistent across

flow regions containing different materials. Furthermore, symmetry about $\theta = 0$ can now be invoked to show that $B_{n,3,i} = 0$ for all n.

As with $V_{ri,0}$ and $W_{ri,0}$ solutions for $V_{ri,1}$ and $W_{ri,1}$ can be adapted from the single-fluid case result in Equation (5.25). This gives the following expressions:

$$V_{ri,1} = \left(\frac{\mu_{A+B}}{\mu_{(i-1)}}\right)\left(\left.\frac{\partial p_{i,1}}{\partial r}\right|_{\theta=\theta_S(r,\theta_i)}\right)\left\{\sum_{n=1}^{\infty} E_n \exp\{\delta_n r\xi_i\}\cos(\delta_n z) - \left(\frac{1-z^2}{2}\right)\right\} - BI_i(r)\sum_{n=1}^{\infty} E_n \exp\{\delta_n r\xi_i\}\cos(\delta_n z) \tag{6.24a}$$

$$W_{ri,1} = \left(\frac{\mu_{A+B}}{\mu_i}\right)\left(\left.\frac{\partial p_{i,1}}{\partial r}\right|_{\theta=\theta_S(r,\theta_i)}\right)\left\{\sum_{n=1}^{\infty} E_n \exp\{-\delta_n r\xi_i\}\cos(\delta_n z) - \left(\frac{1-z^2}{2}\right)\right\} - BI_i(r)\sum_{n=1}^{\infty} E_n \exp\{-\delta_n r\xi_i\}\cos(\delta_n z) \tag{6.24b}$$

were $BI_i(r)$ are coefficient functions of r that must be determined for $2 \le i \le 2N$ by enforcing continuous shear across fluid boundaries. For the special cases of $i = 1$ and $i = 2N + 1$, the velocity profiles satisfying no-slip at $\xi_i = 0$ require $BI_1(r) = BI_{(2N+1)}(r) = 0$:

$$V_{r(2N+1),0} = \left(\frac{\mu_{A+B}}{\mu_B}\right)\left(\left.\frac{\partial p_{i,1}}{\partial r}\right|_{\theta=-\theta_H}\right)\left\{\sum_{n=1}^{\infty} E_n \exp\{\delta_n r\xi_i\}\cos(\delta_n z) - \left(\frac{1-z^2}{2}\right)\right\} \tag{6.25a}$$

$$W_{r1,0} = \left(\frac{\mu_{A+B}}{\mu_A}\right)\left(\left.\frac{\partial p_{i,1}}{\partial r}\right|_{\theta=\theta_H}\right)\left\{\sum_{n=1}^{\infty} E_n \exp\{-\delta_n r\xi_i\}\cos(\delta_n z) - \left(\frac{1-z^2}{2}\right)\right\} \qquad (6.25b)$$

The remaining velocity components can also be adapted from the single-fluid case. Substituting the partial derivatives of $V_{ri,0}$ and $W_{ri,0}$ into Equations (6.20a) and (6.20b), the same steps outlined in Section 5.6 for $V_{\theta,1}$ and $V_{z,0}$ are followed again to arrive at the velocity components for the two-fluid case:

$$V_{\theta i,1} = -\frac{A_0}{r^2} CI_{1,i} \sum_{n=1}^{\infty} \frac{6}{\delta_n^5}\left[(\delta_n r\xi_i - 1)\exp\{\delta_n r\xi_i\} + DI_{1,i}\right]\left(\frac{1-z^2}{2}\right) \qquad (6.26a)$$

$$V_{zi,0} = -\frac{A_0}{r^2} CI_{1,i} \sum_{n=1}^{\infty} \delta_n r\xi_i \exp\{\delta_n r\xi_i\}\left[\frac{E_n}{\delta_n}\sin(\delta_n z) - \frac{6}{\delta_n^4}\left(\frac{3z-z^3}{6}\right)\right] \qquad (6.26b)$$

$$W_{\theta i,1} = -\frac{A_0}{r^2} CI_{2,i} \sum_{n=1}^{\infty} \frac{6}{\delta_n^5}\left[(\delta_n r\xi_i + 1)\exp\{-\delta_n r\xi_i\} - DI_{2,i}\right]\left(\frac{1-z^2}{2}\right) \qquad (6.26c)$$

$$W_{zi,0} = \frac{A_0}{r^2} CI_{2,i} \sum_{n=1}^{\infty} \delta_n r\xi_i \exp\{-\delta_n r\xi_i\}\left[\frac{E_n}{\delta_n}\sin(\delta_n z) - \frac{6}{\delta_n^4}\left(\frac{3z-z^3}{6}\right)\right] \qquad (6.26d)$$

$BI_{1,i}$ and $CI_{1,i}$ in Equation (6.26a) and $BI_{2,i}$and $CI_{2,i}$ in Equation (6.26b) above are constant coefficients. Enforcing continuous velocity across interior fluid interfaces and matching

with the outer θ-component of velocity, $U_{\theta,1}$, these coefficients can be determined to be $DI_{1,i} = \frac{\mu_{A+B}}{\mu_i}$, $DI_{2,i} = \frac{\mu_{A+B}}{\mu_{(i-1)}}$, $CI_{1,i} = \left(\frac{\mu_i}{\mu_{(i-1)}}\right)\frac{\sin(\theta_S(r,\theta_i))}{\sin(\theta_H)}$, and $CI_{2,i} = -\left(\frac{\mu_{(i-1)}}{\mu_i}\right)\frac{\sin(\theta_S(r,\theta_i))}{\sin(\theta_H)}$ for $2 \leq i \leq 2N$. At the wall boundaries of the channel, these constants become $CI_{2,1} = \frac{\mu_{A+B}}{\mu_A}$, $CI_{1,2N+1} = \frac{\mu_{A+B}}{\mu_B}$, and $DI_{1,2N+1} = DI_{2,1} = 1$. Intermediate steps in the determination of these constants are provided in Appendix C1.

It is convenient to enforce the continuous shear conditions at fluid interfaces here, before the matching procedure. Detailed steps and intermediate calculations for the mathematical models summarized here are available in Appendix C2. Enforcing continuity of normal stress across interfaces simply verifies that the pressure drop across interfaces is zero. However, the off-diagonal stress components involving θ, $\tau_{r\theta}$ and $\tau_{\theta z}$, provide expressions for the velocity at interfaces in terms of the outer pressure gradients. Evaluating these shear components at $\xi_i = 0$ and equating the resulting $\mathcal{O}(1)$ terms for $\vec{V}$ and $\overrightarrow{W}$ yields the following expression for AI_i:

$$AI_i = A_0 \qquad \text{for } 2 \leq i \leq 2N \quad (6.27a)$$

$$AI_1 = AI_{(2N+1)} = 0 \quad (6.27b)$$

Similarly, the $\mathcal{O}(\alpha)$ components of the shear stress can be equated to relate the $\mathcal{O}(\alpha)$ corrections to interfacial flow velocity and pressure gradient:

$$BI_i(r) = \left(\frac{\partial p_{i,1}}{\partial r}\right)_{\theta=\theta_S(r,\theta_i)} \tag{6.27c}$$

$$BI_1 = BI_{(2N+1)} = 0 \tag{6.27d}$$

6.7 Composite Solutions

Matching between the outer and inner solutions can be carried out by means of intermediate variables $\zeta_i \equiv \big(\theta - \theta_S(r,\theta_i)\big)/\psi(\alpha)$, where $\lim_{\alpha\to 0}\big(\psi(\alpha)\big) = 0$ and $\lim_{\alpha\to 0}(\alpha/\psi(\alpha)) = 0$. For all $2 \le i \le 2N$, the following must be satisfied:

$$\lim_{\alpha\to 0}\big\{\vec{U}_{(i-1)}\big(\theta = \psi(\alpha)\zeta_i + \theta_S(r,\theta_i)\big)\big\} = \lim_{\alpha\to 0}\big\{\vec{V}_i(\xi_i = \alpha^{-1}\psi(\alpha)\zeta_i)\big\} \tag{6.28a}$$

$$\lim_{\alpha\to 0}\big\{\vec{U}_i\big(\theta = \psi(\alpha)\zeta_i + \theta_S(r,\theta_i)\big)\big\} = \lim_{\alpha\to 0}\big\{\vec{W}_i(\xi_i = \alpha^{-1}\psi(\alpha)\zeta_i)\big\} \tag{6.28b}$$

The steps for matching are analogous to the single-fluid case, as detailed in Appendix B5. Since $\vec{U}_i = \vec{U}_{i+2}$, $\vec{V}_i = V_{i+2}$, and $\vec{W}_i = \vec{W}_{i+2}$ for $1 \le i \le 2N-2$, this matching process need not be carried out separately for each component at each interface. Rather, it is sufficient to first match between $\vec{U}_{(2N+1)}$ and $\vec{V}_{(2N+1)}$ near the right channel boundary and between $\vec{U}_1$ and $\vec{W}_1$ at the left channel boundary. It can be shown that matching is automatically satisfied at all fluid interfaces at the interior of the flow for the r-components and z-componens of the velocity field. Subsequently, the constants $CI_{1,i}$, $CI_{2,i}$, $DI_{1,i}$ and

$DI_{2,i}$ that appear in Equations (6.26a) and (6.26c) can be determined by matching with the outer solution, and by enforcing velocity boundary conditions at fluid boundaries.

First, matching between $U_{\theta(2N+1),1}$ and $V_{\theta(2N+1),1}$ near the right channel boundary requires $B_{n,2} = 0$ for all n and $B_{n,1} = 0$ for all $n \neq 1$, where $B_{n,1}$ and $B_{n,2}$ were previously defined in Equation (6.23). Of the remaining nonzero constants in Equation (6.11), $B_{1,1}$ is found to be $\frac{A_0}{\sin(\theta_H)} \sum_{n=1}^{\infty} \frac{6}{\delta_n^5}$. Matching between $U_{\theta 1,1}$ and $W_{\theta 1,1}$ near the left channel boundary yields the same results. The two constants A_0 and B_0 that appear in the expression for r-components of the velocity must be determined by enforcing the flow rate conditions for the flow field. This produces the following definitions for A_0 and $A_0 + \alpha B_0$:

$$A_0 + \alpha B_0 = \frac{3}{4\theta_H} \left(\frac{\mu_A Q_A + \mu_B Q_B}{\mu_{A+B} Q_{A+B}} \right) \tag{6.29a}$$

$$A_0 = \frac{3(2N+1)}{8\theta_H} \left(\frac{\mu_A Q_A + \mu_B Q_B}{\mu_{A+B} Q_{A+B}} \right) \{1 - A_{0,err}\}^{-1} \tag{6.29b}$$

where $A_{0,err} \equiv \left(\frac{\alpha}{r}\right) \left(\sum_{n=1}^{\infty} \frac{6}{\delta_n^5} \right) \sum_{i=1}^{2N+1} \frac{\cos(\theta_i)}{2\sin(\theta_H)}$ constitutes an order $\mathcal{O}(\alpha/r)$ fractional error to A_0 corresponding to flow rate contributions from higher-order terms in the asymptotic expansion. Intermediate steps for the application of the flow rate condition are provided in Appendix C3.

Matching among inner expansions $V_{\theta i,1}$and $W_{\theta i,1}$ and the outer expansion $U_{\theta i,1}$ at interior fluid boundaries yields the following definitions for the constants $CI_{1,i}$ and $CI_{2,i}$:

$$CI_{1,i} = \left(\frac{\mu_{(i-1)}}{\mu_i}\right)\frac{\sin\left(\theta_S(r,\theta_i)\right)}{DI_{1,i}\sin(\theta_H)}, 2 \le i \le 2N \tag{6.30a}$$

$$CI_{2,i} = -\left(\frac{\mu_i}{\mu_{(i-1)}}\right)\frac{\sin\left(\theta_S(r,\theta_i)\right)}{DI_{2,i}\sin(\theta_H)}, 2 \le i \le 2N \tag{6.30b}$$

For the remaining boundaries at $i = 1$ and $i = 2N + 1$ the no-flux condition gives $CI_{1,2N+1} = CI_{2,1} = 1$. Definitions for $DI_{1,i}$ and $DI_{2,i}$ can be determined numerically following the procedure detailed in Appendix C1.

The overlap between $\vec{U}_{(i-1)}$ and $\vec{V}_i$ and the overlap between $\vec{U}_i$ and $\vec{W}_i$, denoted as OR_i and OL_i, respectively, are defined as follows:

$$OR_i = \lim_{\alpha\to 0}\left\{\vec{U}_{(i-1)}\left(\theta = \psi(\alpha)\zeta_i - \theta_S(r,\theta_i)\right)\right\} = \lim_{\alpha\to 0}\left\{\vec{V}_i(\xi_i = \alpha^{-1}\psi(\alpha)\zeta_i)\right\} \tag{6.31a}$$

$$OL_i = \lim_{\alpha\to 0}\left\{\vec{U}_i\left(\theta = \psi(\alpha)\zeta_i - \theta_S(r,\theta_i)\right)\right\} = \lim_{\alpha\to 0}\left\{\vec{W}_i(\xi_i = \alpha^{-1}\psi(\alpha)\zeta_i)\right\} \tag{6.31b}$$

Intermediate steps and calculations in the subtraction of overlap to construct the composite velocity field are provided in Appendix C4. The composite solutions can then be expressed as follows:

$$u_{ri,0} + \alpha u_{ri,1} = \left(\frac{A_0}{r} + \alpha\frac{B_0}{r}\right)\left[P1_i(r,\theta,z) - \left(\frac{\mu_{A+B}}{\mu_i}\right)\left(\frac{1-z^2}{2}\right)\right] + \left(\frac{\alpha}{r}\right)\left(\frac{A_0}{r}\sum_{n=1}^{\infty}\frac{6}{\delta_n^5}\right)\left[P2_i(r,\theta,z) - \left(\frac{\mu_{A+B}}{\mu_i}\right)\frac{\cos(\theta)}{\sin(\theta_H)}\left(\frac{1-z^2}{2}\right)\right] \tag{6.32a}$$

$$u_{\theta i,0} + \alpha u_{\theta i,1} = u_{\theta i} = \alpha\frac{A_0}{r^2}\left\{P3_1(r,\theta,z) - \left(\frac{\mu_{A+B}}{\mu_i}\right)\frac{\sin(\theta)}{\sin(\theta_H)}\sum_{n=1}^{\infty}\frac{6}{\delta_n^5}\right\}\left(\frac{1-z^2}{2}\right) \tag{6.32b}$$

$$u_{zi,0} = -\frac{A_0}{r^2}P4_i(r,\theta,z) \tag{6.32c}$$

The contributions of channel boundaries and fluid interfaces are relegated to functions $P1_i$, $P2_i$, $P3_i$ and $P4_i$, which are defined in terms of r, z, and inner variables $\xi_i \equiv \frac{\theta-\theta_S(r,\theta_i)}{\alpha}$ as:

$$P1_i(r,\theta,z) = \left(\frac{\mu_{(i-1)}}{\mu_i}\right)\sum_{n=1}^{\infty}E_n\left(\exp\{-\delta_n r\xi_i\} + \exp\{\delta_n r\xi_{(i+1)}\}\right)\cos(\delta_n z) \tag{6.33a}$$

$$\text{for } 2 \le \text{i} \le 2\text{N} - 1$$

$$P1_1(r,\theta,z) = \left(\frac{\mu_{A+B}}{\mu_A}\right)\sum_{n=1}^{\infty}E_n\exp\{-\delta_n r\xi_1\}\cos(\delta_n z) + \left(\frac{\mu_B}{\mu_A}\right)\sum_{n=1}^{\infty}E_n\exp\{\delta_n r\xi_2\}\cos(\delta_n z) \tag{6.33b}$$

$$P1_{2N}(r,\theta,z) = \left(\frac{\mu_A}{\mu_B}\right)\sum_{n=1}^{\infty}E_n\exp\{\delta_n r\xi_{(2N+1)}\}\cos(\delta_n z) + \left(\frac{\mu_{A+B}}{\mu_B}\right)\sum_{n=1}^{\infty}E_n\exp\{-\delta_n r\xi_{2N}\}\cos(\delta_n z) \tag{6.33c}$$

$$P2_i(r,\theta,z) = \left(\frac{\mu_{(i-1)}}{\mu_i}\right)\sum_{n=1}^{\infty} E_n \left[\frac{\cos\left(\theta_S(r,\theta_i)\right)}{\sin(\theta_H)}\exp\{-\delta_n r\xi_i\} + \frac{\cos\left(\theta_S(r,\theta_{i+1})\right)}{\sin(\theta_H)}\exp\{\delta_n r\xi_{i+1}\}\right]\cos(\delta_n z) \tag{6.33d}$$

for $2 \le i \le 2\mathrm{N}-1$

$$P2_1(r,\theta,z) = \left(\frac{\mu_{A+B}}{\mu_A}\right)\sum_{n=1}^{\infty} E_n \cot(\theta_H)\exp\{-\delta_n r\xi_1\}\cos(\delta_n z) + \left(\frac{\mu_B}{\mu_A}\right)\sum_{n=1}^{\infty} E_n \frac{\cos\left(\theta_S(r,\theta_2)\right)}{\sin(\theta_H)}\exp\{\delta_n r\xi_2\}\cos(\delta_n z) \tag{6.33e}$$

$$P2_{(2N)}(r,\theta,z) = \left(\frac{\mu_A}{\mu_B}\right)\sum_{n=1}^{\infty} E_n \frac{\cos\left(\theta_S(r,\theta_{2N})\right)}{\sin(\theta_H)}\exp\{-\delta_n r\xi_N\}\cos(\delta_n z) + \left(\frac{\mu_{A+B}}{\mu_B}\right)\sum_{n=1}^{\infty} E_n \cot(\theta_H)\exp\{\delta_n r\xi_{(2N+1)}\}\cos(\delta_n z) \tag{6.33f}$$

$$P3_i(r,\theta,z) = \left(\frac{\mu_{(i-1)}}{\mu_i}\right)\sum_{n=1}^{\infty}\frac{6}{\delta_n^5}\left[\frac{\sin\left(\theta_S(r,\theta_i)\right)}{DI_{2,i}\sin(\theta_H)}(\delta_n r\xi_i + 1)\exp\{-\delta_n r\xi_i\} - \frac{\sin\left(\theta_S(r,\theta_{(i+1)})\right)}{DI_{1,(i+1)}\sin(\theta_H)}\left(\delta_n r\xi_{(i+1)} - 1\right)\exp\{\delta_n r\xi_{(i+1)}\}\right] \tag{6.33g}$$

for $2 \le i \le 2\mathrm{N}-1$

$$P3_1(r,\theta,z)=\sum_{n=1}^{\infty}\frac{6}{\delta_n^5}\Bigg[-\left(\frac{\mu_{A+B}}{\mu_A}\right)(\delta_n r\xi_2+1)\exp\{-\delta_n r\xi_1\} - \left(\frac{\mu_B}{\mu_A}\right)\frac{\sin\left(\theta_S(r,\theta_{(i+1)})\right)}{DI_{1,(i+1)}\sin(\theta_H)}(\delta_n r\xi_2-1)\exp\{\delta_n r\xi_2\}\Bigg] \tag{6.33h}$$

$$P3_{2N+1}(r,\theta,z)=\sum_{n=1}^{\infty}\frac{6}{\delta_n^5}\Bigg[\left(\frac{\mu_A}{\mu_B}\right)\frac{\sin\left(\theta_S(r,\theta_i)\right)}{DI_{2,i}\sin(\theta_H)}(\delta_n r\xi_{2N}+1)\exp\{-\delta_n r\xi_{2N}\} - \left(\frac{\mu_{A+B}}{\mu_B}\right)\left(\delta_n r\xi_{(2N+1)}-1\right)\exp\left\{\delta_n r\xi_{(2N+1)}\right\}\Bigg] \tag{6.33i}$$

$$P4_i(r,\theta,z)=\left(\frac{\mu_{(i-1)}}{\mu_i}\right)\sum_{n=1}^{\infty}\Bigg\{\delta_n r\Bigg[\frac{\sin\left(\theta_S(r,\theta_i)\right)}{\sin(\theta_H)}\xi_i\exp\{-\delta_n r\xi_i\} + \frac{\sin\left(\theta_S(r,\theta_{(i+1)})\right)}{\sin(\theta_H)}\xi_{(i+1)}\exp\left\{\delta_n r\xi_{(i+1)}\right\}\Bigg]\left[\frac{E_n}{\delta_n}\sin(\delta_n z)-\frac{6}{\delta_n^4}\left(\frac{3z-z^3}{6}\right)\right]\Bigg\} \tag{6.33j}$$

for $2\le i\le 2\mathrm{N}-1$

$$P4_1(r,\theta,z)=\sum_{n=1}^{\infty}\Bigg\{\delta_n r\Bigg[-\left(\frac{\mu_{A+B}}{\mu_A}\right)\xi_1\exp\{-\delta_n r\xi_1\} + \left(\frac{\mu_B}{\mu_A}\right)\frac{\sin\left(\theta_S(r,\theta_2)\right)}{\sin(\theta_H)}\xi_2\exp\{\delta_n r\xi_2\}\Bigg]\left[\frac{E_n}{\delta_n}\sin(\delta_n z)-\frac{6}{\delta_n^4}\left(\frac{3z-z^3}{6}\right)\right]\Bigg\} \tag{6.33k}$$

$$P4_{(2N+1)}(r,\theta,z)=\sum_{n=1}^{\infty}\Bigg\{\delta_n r\Bigg[\left(\frac{\mu_A}{\mu_B}\right)\frac{\sin\left(\theta_S(r,\theta_{2N})\right)}{\sin(\theta_H)}\xi_{2N}\exp\{-\delta_n r\xi_1\} + \left(\frac{\mu_{A+B}}{\mu_B}\right)\xi_{(2N+1)}\exp\left\{\delta_n r\xi_{(2N+1)}\right\}\Bigg]\left[\frac{E_n}{\delta_n}\sin(\delta_n z)-\frac{6}{\delta_n^4}\left(\frac{3z-z^3}{6}\right)\right]\Bigg\} \tag{6.33l}$$

6.8 Locations of Fluid Interfaces

At this stage, the locations of fluid boundaries have yet to be determined. As stated in the introduction of this chapter, these boundary locations constitute both the central question and the central difficulty addressed by the present two-fluid perturbation analysis. Having determined the form of the velocity field to $\mathcal{O}(\alpha)$, the tools to complete this critical task are now available.

First, an implicit expression for θ_i for $2 \leq i \leq 2N$ is derived. With $\theta_2 \ldots \theta_{2N}$ known, the inner variables $\xi_2 \ldots \xi_{2N}$ can then be evaluated along r. Second, the composite velocity field developed in the preceding sections for two fluids can be evaluated at any point within the domain of interest defined in Section 6.3.

Substituting the definitions for A_0 and B_0 provided in Equations (6.29a) and (6.29b) into Equation (6.32a) and integrating across the channel cross-section yields the flow rate contribution for a given region bounded by $\theta_S(r, \theta_i)$ and $\theta_S\big(r, \theta_{(i+1)}\big)$. This result can be rearranged as the following implicit expressions for $\theta_S\big(r, \theta_{(i+1)}\big)$:

$$\theta_S(r,\theta_2) = -\theta_H + \frac{2\theta_H}{N}\left(\frac{\mu_A Q_A}{\mu_A Q_A + \mu_B Q_B}\right)$$
$$+\left(\frac{\alpha}{r}\right)\left\{2\left(\frac{\mu_B}{\mu_{A+B}} + \frac{1}{2}\frac{\mu_A}{\mu_{A+B}}\right)\right.$$
$$\left. - \left(\frac{2N+1}{1-A_{0,err}}\right)\left[\frac{\sin(\theta_{i+1}) - \sin(\theta_i)}{2\sin(\theta_H)}\right]\right\}\left(\sum_{n=1}^{\infty}\frac{6}{\delta_n^5}\right)$$
$$+\left(\frac{\alpha}{r}\right)^2\left(\frac{2N+1}{1-A_{0,err}}\right)\left[\left(\frac{\mu_B}{\mu_{A+B}}\right)\frac{\cos(\theta_i)+\cos(\theta_{i+1})}{2\sin(\theta_H)}\right.$$
$$\left. + \left(\frac{\mu_A}{\mu_{A+B}}\right)\frac{\cot(\theta_H)}{2}\right]\left(\sum_{n=1}^{\infty}\frac{6}{\delta_n^5}\right)^2 \quad (6.34a)$$

$$\theta_S(r,\theta_{i+1}) = \theta_S(r,\theta_i) + \frac{2\theta_H}{N}\left(\frac{\mu_B Q_B}{\mu_A Q_A + \mu_B Q_B}\right)$$
$$+\left(\frac{\alpha}{r}\right)\left\{2\left(\frac{\mu_A}{\mu_{A+B}}\right)\right.$$
$$\left. - \left(\frac{2N+1}{1-A_{0,err}}\right)\left[\frac{\sin\left(\theta_S(r,\theta_{i+1})\right) - \sin\left(\theta_S(r,\theta_i)\right)}{2\sin(\theta_H)}\right]\right\}\left(\sum_{n=1}^{\infty}\frac{6}{\delta_n^5}\right) \quad (6.34b)$$
$$+\left(\frac{\alpha}{r}\right)^2\left(\frac{2N+1}{1-A_{0,err}}\right)\left(\frac{\mu_A}{\mu_{A+B}}\right)\left[\frac{\cos\left(\theta_S(r,\theta_{i+1})\right) + \cos\left(\theta_S(r,\theta_i)\right)}{2\sin(\theta_H)}\right]\left(\sum_{n=1}^{\infty}\frac{6}{\delta_n^5}\right)^2$$

for even $2 \le i \le 2N$

$$\theta_S(r,\theta_{i+1}) = \theta_S(r,\theta_i) + \frac{2\theta_H}{N}\left(\frac{\mu_A Q_A}{\mu_A Q_A + \mu_B Q_B}\right)$$

$$+\left(\frac{\alpha}{r}\right)\left\{2\left(\frac{\mu_B}{\mu_{A+B}}\right)\right.$$

$$\left.-\left(\frac{2N+1}{1-A_{0,err}}\right)\left[\frac{\sin\left(\theta_S(r,\theta_{i+1})\right)-\sin\left(\theta_S(r,\theta_i)\right)}{2\sin(\theta_H)}\right]\right\}\left(\sum_{n=1}^{\infty}\frac{6}{\delta_n^5}\right) \qquad (6.34c)$$

$$+\left(\frac{\alpha}{r}\right)^2\left(\frac{2N+1}{1-A_{0,err}}\right)\left(\frac{\mu_B}{\mu_{A+B}}\right)\left[\frac{\cos\left(\theta_S(r,\theta_{i+1})\right)+\cos\left(\theta_S(r,\theta_i)\right)}{2\sin(\theta_H)}\right]\left(\sum_{n=1}^{\infty}\frac{6}{\delta_n^5}\right)^2$$

for odd $3 \le i \le 2N$

Above, $A_{0,err} \equiv \left(\frac{\alpha}{r}\right)\left(\sum_{n=1}^{\infty}\frac{6}{\delta_n^5}\right)\sum_{i=1}^{2N+1}\frac{\cos(\theta_i)}{2\sin(\theta_H)}$. Equations (6.34a)-(6.34c) can be evaluated iteratively, starting with Equation (6.34a), then alternating bewteen Equations (6.34b) and (6.34c) and progressing across the interior fluid boundaires from left to right. Intermediate steps leading to these results are provided in Appendix C3. While these implicit expressions seem complex, they lend themselves readily to physical interpretation. Terms containing $(2N+1)$ reflect the idea that boundary locations are displaced somewhat from the single-fluid streamline locations and that the displacement is more pronounced with a greater number of interior fluid boundaries. This is intuitively satisfying, since one expects effects in the vicinity of fluid boundaries – *i.e.*, the inner velocity terms – to have some bearing on the total flow through each stripe region.

As for the relative significance of these effects, the (α/r) and $(\alpha/r)^2$ coefficient terms provide a an understanding of precisely how much the order $\mathcal{O}(1)$ and order $\mathcal{O}(\alpha)$ velocity components displace fluid boundaries from a configuration that fully conforms to the channel wall geometry. In the limit that $(\alpha/r) \to 0$, the interior fluid boundaries approach precisely such a configuration, and Equations (6.34a)-(6.34c) reduce to the following:

$$\lim_{(\alpha/r)\to 0}\{\theta_S(r,\theta_i)\}$$
$$= \begin{cases} \left(\frac{2\theta_H}{N}\right)\frac{i\mu_A Q_A + (i-1)\mu_B Q_B}{\mu_A Q_A + \mu_B Q_B} - \theta_H & \text{for even } 2 \le i \le 2N \\ \left(\frac{2\theta_H}{N}\right)\frac{i(\mu_A Q_A + \mu_B Q_B)}{\mu_A Q_A + \mu_B Q_B} - \theta_H & \text{for odd } 3 \le i \le 2N+1 \end{cases} \tag{6.35}$$

Equation (6.35) expresses interior boundary locations explicitly to leading order, as a function of channel geometry, fluid viscosity, and flow rate. In this limit, it can also be shown that the angular displacement across fluid boundaries for each fluid species exhibits the following relationship:

$$\lim_{(\alpha/r)\to 0}\left\{\frac{\theta_S(r,\theta_i) - \theta_S(r,\theta_{i-1})}{\theta_S(r,\theta_{i+1}) - \theta_S(r,\theta_i)}\right\} = \left(\frac{\mu_A}{\mu_B}\right)\left(\frac{Q_A}{Q_B}\right) \tag{6.36}$$

for even $2 \le i \le 2N$

Equation (6.36) expresses apparent stripe widths for fluid species *A* and *B* as a ratio, which equates to the product of viscosity and flow rate ratios. This result can be verified by enforcing the flow-rate conditions for fluids *A* and *B*, assuming the same form of the order $\mathcal{O}(1)$ pressure field obtained in Equation (5.14b). The reuse of the same pressure field for both fluids reflects the assumption that pressure is continuous across interior fluid boundaries. Details for the alternate derivation are provided in Appendix C5.

While Equations (6.34)-(6.36) describe cases where the number of stripes for material *A* and material *B* are equal, it is also helpful to consider the case of an odd total number of stripes. Denoting the number of material *A* regions as M and the number of material *B* regions as $M-1$, the $\mathcal{O}(1)$ expressions for stripe width interfaces can be shown to be:

$$\lim_{(\alpha/r)\to 0}\{\theta_S(r,\theta_i)\} = \begin{cases} \left(\frac{2\theta_H}{M}\right)\frac{i\mu_A Q_A + (i-1)\mu_B Q_B}{\mu_A Q_A + \mu_B Q_B} - \theta_H & \text{for even } 2 \le i \le 2M \\ \left(\frac{2\theta_H}{M-1}\right)\frac{i(\mu_A Q_A + \mu_B Q_B)}{\mu_A Q_A + \mu_B Q_B} - \theta_H & \text{for odd } 3 \le i \le 2M-1 \end{cases} \tag{6.37}$$

From this expression, the stripe width ratio can be expressed as follows:

$$\lim_{(\alpha/r)\to 0}\left\{\frac{\theta_S(r,\theta_i) - \theta_S(r,\theta_{i-1})}{\theta_S(r,\theta_{i+1}) - \theta_S(r,\theta_i)}\right\} = \left(\frac{\mu_A}{\mu_B}\right)\left(\frac{Q_A}{Q_B}\right)\left(\frac{M-1}{M}\right) \tag{6.38}$$

for even $2 \leq i \leq 2M-1$

Intermediate steps in the derivation of these expressions, as well as expressions for the $\mathcal{O}(\alpha)$ estimates of stripe boundary locations for an odd total number of stirpes, are also provided in Appendix C3.

The locations of stripe interfaces as predicted by Equations (6.34)-(6.36) are illustrated in Figure 6.2 for case with 7 interior fluid boundaries and 8 stripe regions alternating between material *A* and material *B*. Spacing between interfaces is denoted as $\Delta\theta_i \equiv \theta_S(r,\theta_{i+1}) - \theta_S(r,\theta_i)$, or alternatively, as $\Delta\theta_A$ for fluid regions comprising fluid *A*, and as $\Delta\theta_B$ for fluid regions comprising fluid *B*, as shown in Figure 6.2(a). Figure 6.2(b) plots relationship between flow rate ratio, Q_A/Q_B, and stripe width ratio, $\Delta\theta_A/\Delta\theta_B$, for various slot geometry. It should be noted that α/r conveys the inverse aspect ratio across a particular cross section, whereas α alone corresponds to the aspect ratio at the outflow boundary of the domain. For this reason, it is more informative to consider α/r as the geometric representation of the slot aspect ratio. As expected from the form of Equations (6.34a)-(6.34c), the correlation between flow rate and stripe width approaches the leading-order approximation from Equation (6.36) as $\alpha/r \to 0$.

To understand the role of viscosity, Figure 6.2(c) repeats the analysis from Figure 6.2(b) for several values of μ_A/μ_B. As expected from Equations (6.34)-(6.36), the a change in flow rate ratio results in a proportional displacement of the correlation between stripe

width ratio. To interpret this result in physical terms, it is helpful first to recall from the mathematical analysis that the pressure field is continuous across the entire domain and inherited across fluid interfaces to order $\mathcal{O}(\alpha)$. To account for a mismatch in viscosity, a corresponding mismatch in average flow velocity must arise. Then, in order for continuity to be satisfied, there must also be an adjustment in the position of the stripe widths. This adjustment is proportional to the ratio μ_A/μ_B.

Finally, it is important also to consider the influence of the channel convergence angle, θ_H, in the widths of stripes. In Figure 6.2(d), which plots stripe width ratio across $\theta_H = \pi/3$, $\theta_H = \pi/6$, and $\theta_H = \pi/12$, this influence appears minimal. In fact, an examination of Equations (6.34a)-(6.34c) suggests that the ajustment of stripe width ratio due to a change in θ_H is on the order of $\mathcal{O}(\alpha/r)$. Therefore, it is unsurprising that the convergence angle of the channel has minimal effect on stripe width ratio, as shown in Figure 6.2(d). This observation agrees well with physical understanding obtained previously with the single-fluid analysis in Chapter 5, which showed that the domain of influence of wall boundaries was also on the order $\mathcal{O}(\alpha/r)$. Here, with co-laminar flow of two fluids, Equations (6.34a)-(6.34c) not only relfect the influence from channel sidewalls, but also demonstrate that the influence of the additional fluid interfaces is even smaller, on the order of $\mathcal{O}\left(\alpha^2/r^2\right)$.

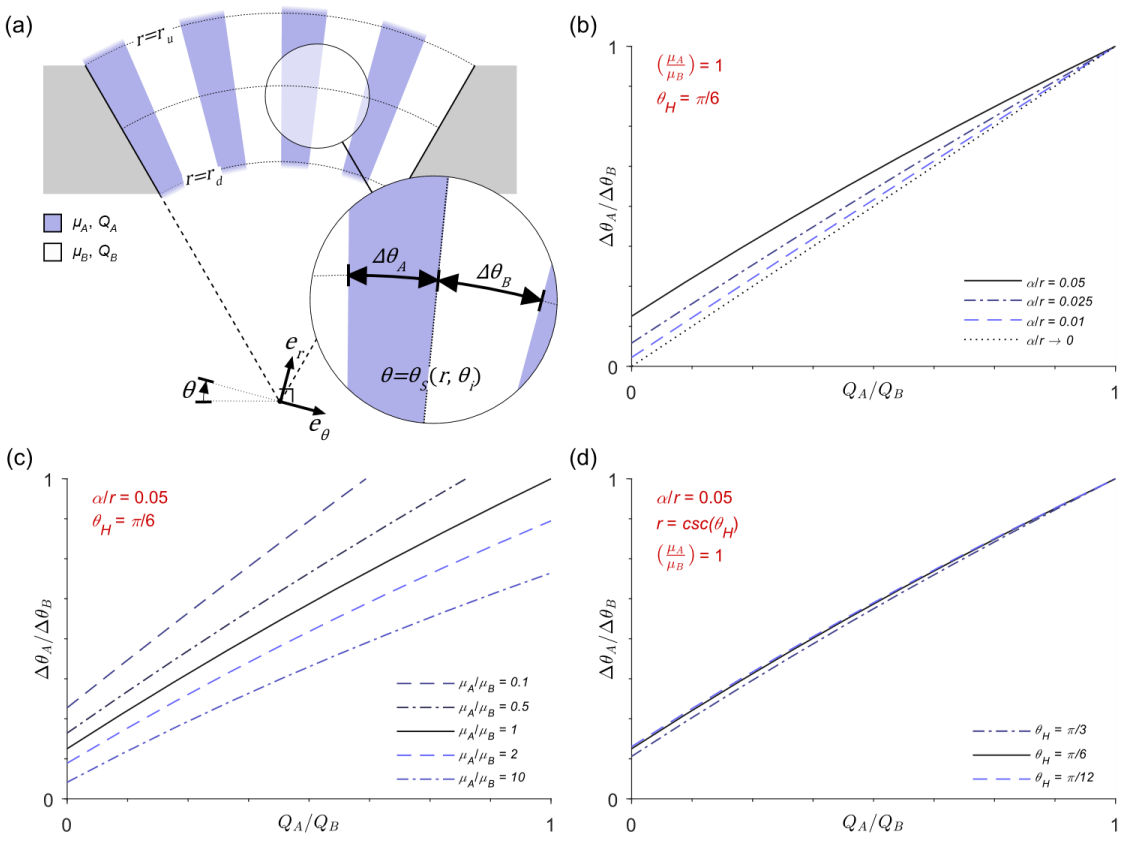

Figure 6.2 – (a) Schematic illustration of fluid interface locations for the case of 8 fluid stripes, with 4 stripes of each fluid material *A* and *B*. The ratio between stripe widths for *A* and *B* is plotted versus the flow rate ratio, for various (b) α/r, (c) viscosity ratios (μ_A/μ_B), and (d) convergence angle (θ_H). As a point of reference, the solid lines in plots (a)-(c) represent the same combination of α/r, μ_A/μ_B and θ_H.

In considering the combined parameter α/r, the results in Figure 6.2 have been able to consider pattern geometry across the entire domain. However, it is also illustrative to consider the evolution of the stripe pattern along the direction of flow. This analysis is shown in Figure 6.3(a) and (b) for various μ_A/μ_B and α, respectively. The results from both plots show distortion of the pattern along r which is most pronounced near the outflow boundary at $r = r_d$. From Figure 6.3(a), the severity of this distortion is most pronounced

for very large and very small μ_A/μ_B, while no distortion is predicted for $\mu_A = \mu_B$. The evolution of $\Delta\theta_A/\Delta\theta_B$ is also more significant with increasing α, as the slot geometry approaches a square cross-section and flow becomes less planar.

Here, again, key features of the plotted results can be connected directly with the form of the mathematical expressions in Equations (6.34a)-(6.34c). In the equations for stripe interface locations, terms containing (α/r) and $(\alpha/r)^2$ account for the deviation from the leading-order approximation. Based on this observation alone, it is sufficient to infer that any difference between the leading-order and $\mathcal{O}(\alpha)$ models will evolve along r proportional to r^{-1}. Furthermore, μ_A/μ_B appears in terms containing (α/r), which indicates that difference between stripe width ratio predicted by the order $\mathcal{O}(1)$ and $\mathcal{O}(\alpha)$ models due to viscosity ratio should also be order $\mathcal{O}(\alpha/r)$.

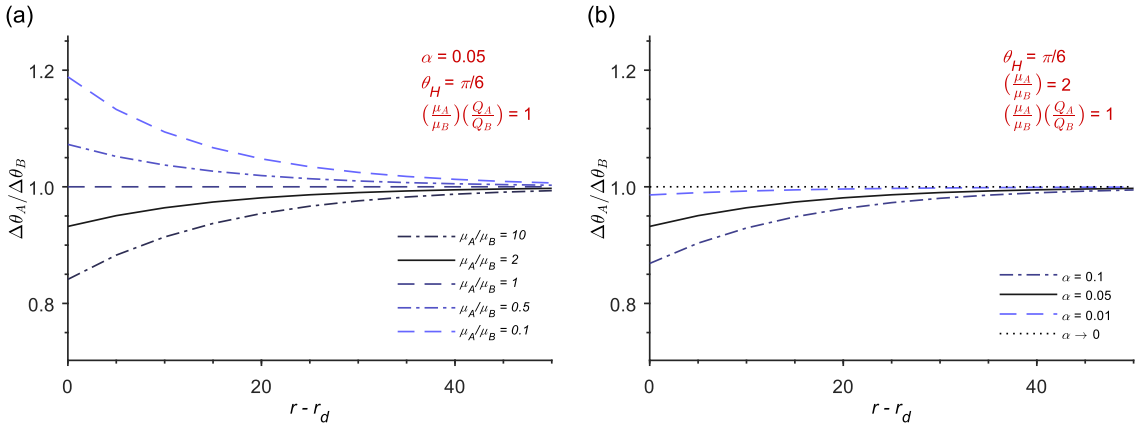

Figure 6.3 – Evolution of stripe width ratios with r as a function of (a) viscosity ratio and (b) inverse aspect ratio of the channel (α). In both (a) and (b), r_d takes its minimum possible value, $r_d = \csc(\theta_H)$. As a point of reference, the solid lines in plots (a)-(b) represent the same combination of α, μ_A/μ_B and θ_H.

In context of the HSSC process, the results in Figure 6.2 and Figure 6.3 provide insightful guidance to the design of tool geometry and process conditions required to achieve a desired patterned outflow. First, it has been shown that the combined influence of convergence angle (θ_H), inverse aspect ratio (α), flow rate ratio (Q_A/Q_B), and viscosity ratio (μ_A/μ_B) require an adjustment to the stripe widths predicted by the simple scaling in Equation (6.36). However, the relative importance of this adjustment is on the order of $\mathcal{O}(\alpha/r)$. Thus, the small parameter α/r constitutes a simple and effective metric to estimate not only whether the simple scaling applies, but roughly how accurate its estimate will be.

The results in Figure 6.2 and Figure 6.3 also illustrate how differences between the $\mathcal{O}(\alpha)$ and $\mathcal{O}(1)$ analytical results are exacerbated by extreme viscosity ratio. However, the results also suggest that the convergence angle (θ_H) is relatively insignificant for the accuracy of the $\mathcal{O}(1)$ model. While this may be true within the assumptions stated in Sections 6.3 and 6.4, a measure of practical caution is necessary. It should be noted that a key assumption in the model is a point-wise reference pressure, and thus, that inflow and outflow pressure profiles do not distort the shape of the velocity field. This is unlikely to be the case for large values of θ_H, unless measures are taken in the design of the HSSC geometry to contrive the same pressure field predicted Equations (6.11a) and (6.11b).

6.9 Experimental Validation of Fluid Interfaces Under Hydrodynamic Focusing Using HSSC

Two-fluid flow through the HSCC with hydrodynamic focusing can easily be implemented using the experimental setup described in Chapter 2 to provide a measure of validation for the leading-order model for stripe widths from Equation (6.36). Among the features of the flow discussed in previous sections, the locations of stripe interfaces are particularly convenient to visualize experimentally. In addition, for the applications motivating this work, where steady co-laminar flow is used to generate patterns, the boundaries between the two fluids are a primary flow characteristic of interest.

6.9.1 Materials

Aqueous polyvinyl alcohol (PVA) prepared in 7.5 wt.%, 10 wt.%, 15 wt.%, 17.5 wt.%, and 20 wt.%, concentrations was used as a model fluid for experimental investigations on internal flow. Two liquid phases were used for each experiment, with less than 3% dye added to one member of each pair for visualization purposes. These solutions were chosen to ensure to fulfill the assumptions for material selection from Section 6.3. Specifically, the two materials must exhibit nonzero but negligibly small cross-mixing, such that the interfaces between stripes are well-defined with an associated surface tension of zero. For small molecules in dilute PVA solutions, diffusivity values of less than 2.5×10^{-9} m^2s^{-1} are expected based on existing literature[253]. This is sufficient to ensure that the

Peclet number (*Pe*) is large for the flow rates and channel geometry used in experiments, such that diffusion mixing across fluid boundaries is negligibly small.

6.9.2 HSSC Hydrodynamic Focusing Setup

As in previous experiments, the planar geometry of the HHSC coating tool was defined by cutouts in a polyethylene terephthalate (PET) shim. To achieve co-laminar flow and hydrodynamic focusing of the two-fluid pattern, the internal channel was designed with an array of inlets that empty into a shared cavity, followed by a section with a converging width, before the tool outlet, as illustrated in Figure 6.4(a).

Imaging of internal flow was carried out on the setup illustrated schematically in Figure 6.4(b). Fluids *A* and *B* were injected into the microfluidic cavity via separate manifolds for each fluid species, and the total flow rate for each fluid across several stripes was regulated by two Chemyx Fusion 200 syringe pumps. The cavity was positioned between an LED illumination panel and Thorlabs DCC324 digital camera equipped with an Edmond Optics 59-871 25 mm fixed-focal length lens. The optical transparency of the two polymethyl methacrylate (PMMA) die blocks enabled visualization of the internal flow during each experiment. Outflow from the coating tool was collected by a small external reservoir rather than deposited on the substrate.

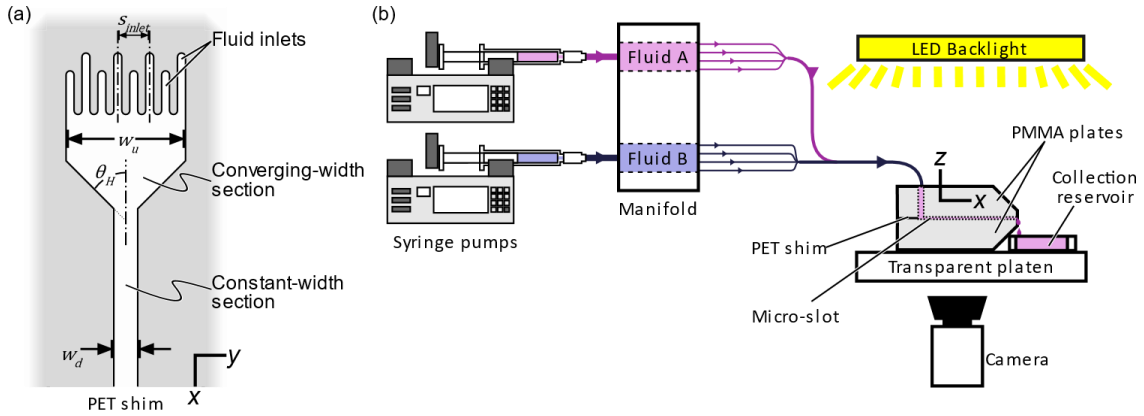

Figure 6.4 – (a) The microfluidic slot geometry defined by a cutout in a PET shim. (b) Physical apparatus, imaging setup, and fluid source used for experiments.

A summary of experimental runs carried out for various combinations and concentrations of aqueous PVA fluid, flow rate ratio (Q_A/Q_B), and channel geometry is organized in Table 6.2. For all trials, the total flow rate ($Q_A + Q_B$) was fixed at 10 μL/s. Trials 1-3, 6, and 7, where both fluids are of the same PVA concentration, provide an assessment of stripe width control due to flow rate alone, while trials 4 and 5, where the fluid concentrations are different, explore the role of an additional mismatch between fluid viscosities. It should be cautioned, however, that the presence of the visualization dye is expected to influence viscosity. For this reason, a differential viscosity calibration was carried out *in situ* across all image data collected for each trial, by the procedure described in Section 6.9.3. This also ensured that other sources of error related to viscosity, such as temperature change and solvent evaporation, were accounted for automatically over the course of experimental trials.

The depth of the shim, which defines the slot gap (G) was fixed at 76.2 μm and center-to-center spacing of inlets (s_{inlet}), was fixed at 3.35 mm. The minimum channel width, w_d, is also fixed at 5 mm for all experimental trials. Except where noted otherwise, the total flow rate through the channel is 10 μL/s, and the rate of width reduction for the channels is given by $\theta_H = \pi/4$.

Table 6.2 – Summary of fluid concentrations and geometry used for experimental trials.

Trial No.	Fluid *A*	Fluid *B*	θ_H (°)	r_d (mm)	Q_A/Q_B	No. of images
1	10% PVA	10% PVA + dye	45	5	1, 1.5, 2	19
2	15% PVA	15% PVA + dye	45	5	1, 1.5, 2	26
3	17.5% PVA	17.5% PVA + dye	45	5	1, 1.5, 2	17
4	10% PVA	15% PVA + dye	45	5	0.1, 0.5, 1	21
5	20% PVA	15% PVA + dye	45	5	0.5, 1	14
6	10% PVA	10% PVA + dye	63	5	0.1,0.5,1	11
7	10% PVA	10% PVA + dye	30	5, 1.5, 1	1	32

6.9.3 Image Processing of Internal Flow Visualizations

For investigations of internal flow, the process of identifying and measuring fluid boundaries was carried out in an automated fashion using the MATLAB image processing toolbox. This ensured that the criteria for locating fluid boundaries were applied

consistently across the high volume of image data under consideration. Visualizations of the image processing algorithms used for this work are summarized visually in Figure 6.5.

The first step for programmatic image characterization was edge detection, carried out using the Sobel operator[254] to produce a spatial map of the grayscale gradient magnitude, as illustrated in Figure 6.5(a)-(b). The image clarity and contrast afforded by the experimental setup precluded the need for any pre-processing or filtering of image data prior to this step. At each row of pixels across the width of the channel, the troughs and peaks in the gradient map were taken as the likely locations of interfaces between fluids. This provided a collection of coordinates, which were binned, compared, and assigned to fluid boundaries, with obvious outliers discarded. Figure 6.5(c) illustrates the final step in the process of modeling fluid boundaries from image data. Here, a polynomial regression fit was constructed for each collection of boundary-located points. Adjacent polynomial curves were then compared at various locations in the flow to extract the widths of fluid regions as the key parameter of interest.

For these experiments, flow was visualized across a channel geometry comprising both a converging-width feature, in addition to a constant-width portion. These locations are shown for a sample image in Figure 6.5(d). Measurements along the constant-width portion of the channel were collected across various flow rate ratios for each experimental trial, and used to estimate the viscosity ratio for the two fluids based on the model

predictions in Section 6.8. Finally, measurements at the converging portion of the channel were then compared to the analytical model results for individual images.

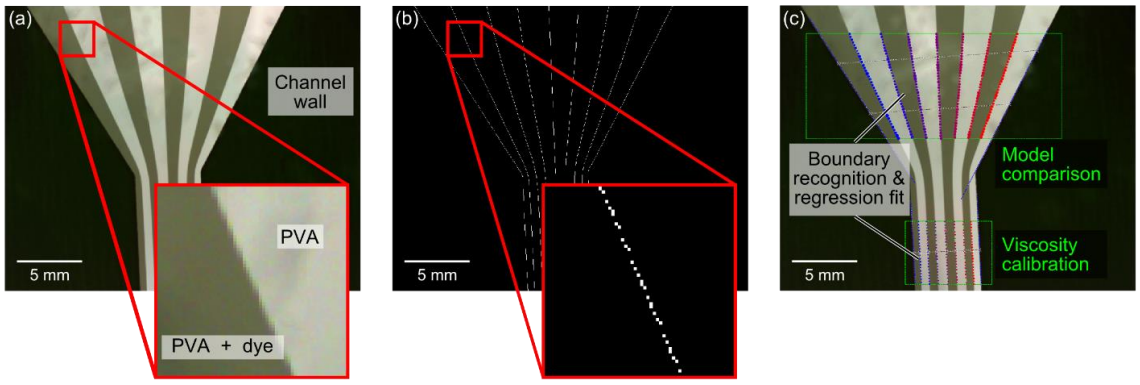

Figure 6.5 – Visualizations of image processing steps, comprising (a) the original image, (b) edge detection at fluid interfaces, and (c) regression fits across points assigned to each fluid boundary.

6.9.4 Validation of Leading-Order Analytical Model

Experimental stripe width measurements with predictions from the leading-order expression for stripe width Equation (6.36) are shown in Figure 6.6(a). In general, the agreement between the two is satisfactory. The most obvious disparity between experiment and model appears to be a set of measurements from experimental set 4, with co-flow between 15 wt.% and 10 wt.% at a flow rate ratio of 0.5. Although deviations from the model due to the presence of shear-dependent viscosity is a potential concern for higher PVA concentrations, experimental trials 3 and 5, which involve 17.5 wt.% and 20 wt.% PVA, respectively, exhibit reasonable agreement with the model predictions. Therefore, it is likely that the discrepancy between model and experiment for series 4 is attributable to

more mundane sources of experimental error. For example, the nominal flow rate delivered by the syringe pump may deviate from the actual rate through the microfluidic slot due to flexure of the tubing and the syringe used to deliver the model fluid.

In order to provide an intuitive interpretation of the model results, visualizations of two-fluid co-laminar flow through the converging slot are provided in Figure 6.6(b) and (c), across various Q_A/Q_B and μ_A/μ_B. The expected change in differential stripe width across changing flow rate, due to continuity, for two PVA solutions of the same concentration, is conformed in Figure 6.6(b1)-(b3). In a similar manner, the ratio between stripe widths for the two fluid species are proportional to μ_A/μ_B, as confirmed in Figure 6.6(c1)-(c3).

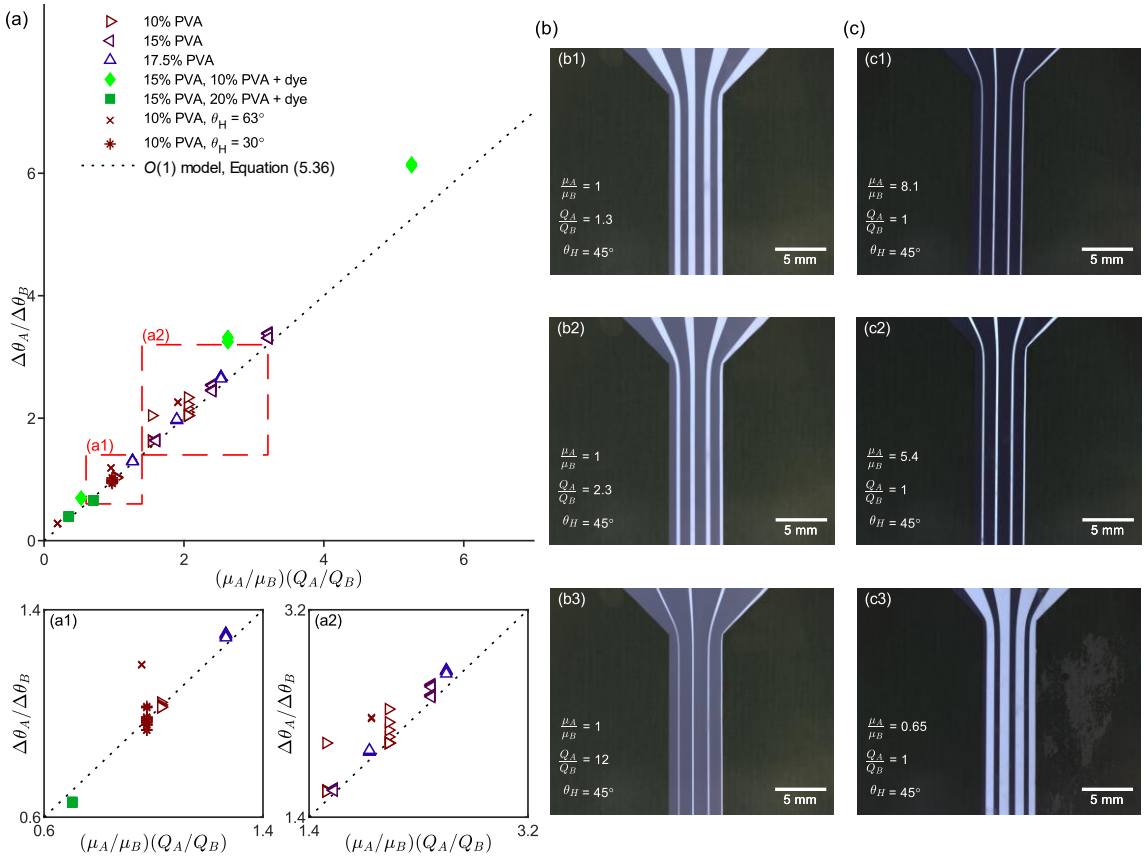

Figure 6.6 – (a) Comparison between experimental measurement and model predictions for fluid boundary spacing. To distinguish between closely spaced individual data points, insets (a1) and (a2) provide magnified views of the data in regions of high density of points. (b) Co-laminar flow of 17.5 wt.% PVA and 17.5 wt.% PVA + dye for various flow rate ratios. (c) Co-laminar flow of 15 wt.% PVA with dye added, and a second fluid phase consisting of (c1) 7.5 wt.%PVA, (c2) 10 wt.% PVA, and (c3) 20 wt.% PVA.

6.9.5 Validation Assumptions for Mixing

Several key assumptions and qualitative predictions from the analytical model are corroborated by the experimental flow visualizations. Following the discussion points in Sections 6.4 and 6.8, fluid boundaries are expected to correspond to streamlines in single-fluid flow, which are insensitive to viscosity. That appears to be the case here, even with

significant viscosity mismatch across the two fluid phases. The perturbation analysis in this chapter also assumes that diffusion mixing across the interface between the two solutions is sufficiently small that any chemical gradation across the fluid interfaces can be neglected. For the flow conditions considered here, this also appears to be the case. Within the resolution capabilities of the imaging setup, the apparent width of fluid boundaries is unvarying throughout the domain of interest, as illustrated in Figure 6.7(a) for a representative case. Here, the gradation between dark and light regions of the flow is more readily attributable to light diffraction than to chemical gradients.

With respect to mixing at the fluid boundaries, flow appears to be steady and laminar. Large-scale vortices can be contrived purposefully by means of air bubbles injected into the flow, or by sudden disruptions to the flow rate of one fluid. Under such conditions, the presence and growth of the vortices is easily detected with the imaging resolution provided by the experimental setup, as illustrated in Figure 6.7(b), before steady state is eventually recovered. This indicates that while transient vortex-driven mixing can exist at length scales detectable by the imaging setup available, it does not occur under steady flow rate conditions. However, vortices and advective mixing at length-scales below the camera resolution cannot be ruled out categorically.

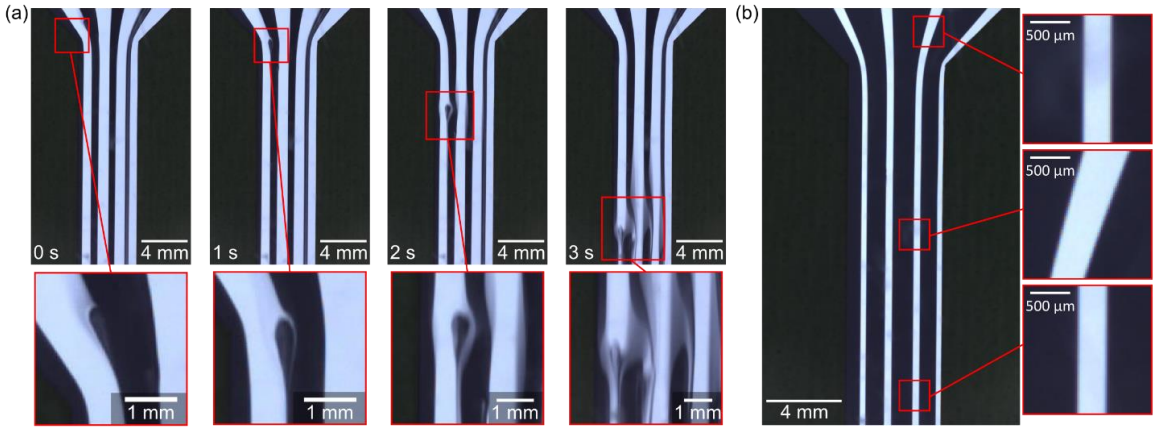

Figure 6.7 – (a) Development of a vortex at a boundary between 20 wt.% PVA (clear) and 15 wt.% PVA + dye (dark) due to a sudden flow rate disruption. (b) Magnified views of the fluid interfaces for co-laminar flow of 10 wt.% PVA (clear) and 15 wt.% PVA + dye (dark), at a total flow rate of 1 µL/s through the channel.

6.10 HSSC with Hydrodynamic Focusing of Ag-NP Stripes

The commercial pilot-scale R2R tool featured in this portion of the work provides an opportunity for demonstration of hydrodynamically focused HSSC in an industrial scale setting. The value of such a demonstration with is that it couples the manufacturing scale with commercially available Ag-NP ink. Therefore, the manufacturing readiness of the HSSC method can be substantiated, in context of achievable feature size performance beyond the laboratory scale.

It is important to note that the commercial-scale R2R system lacks the specialized process imaging capability from previous experimental work in this dissertation. Thus, the analysis in this section is carried out on measurements of the final pattern morphology of printed films, following outflow from the HSSC tool, deposition, and curing. In lieu of a

vision system, the derived mathematical models are used to obtain first approximation for the expected stripe widths at the coating tool outlet. The comparison between model and final stripe morphology provides a case study on the relative importance of flow phenomena, post-deposition wetting, and curing processes on the final size of hydrodynamically focused pattern features deposited with HSSC.

6.10.1 Materials for Pilot-Scale Testing

For devices and applications requiring high-conductivity structures, metallic nano-dispersions are a widely used option[60-62, 98, 139]. For demonstration of the heterogeneous stripe slot coating process with this category of materials, silver nanoparticle (Ag-NP) ink, Metalon® JS-102A from NCC Nano, LLC (d.b.a. NovaCentrix), was selected. A modified formulation of the ink, with proprietary surfactants removed, was provided by NovaCentrix for this investigation. Polyvinyl pyrrolidone (PVP), provided by NovaCentrix as a surfactant-doped 30 wt.% aqueous solution, was used as the support material to define the heterogeneous alternating-stripe pattern. Both materials were co-deposited on silica-coated PET substrate provided by NovaCentrix.

6.10.2 Pilot-Scale R2R Integration at NovaCentrix

Ag-NP ink and PVP support material were co-deposited in narrow stripe-patterned heterogeneous films using an HSSC coting tool with hydrodynamic focusing. The internal slot depth (G) was 50.2 μm, the width convergence angle (θ_H) was 60°, inflow width (w_u) was 28 mm, outflow width (w_d) was 5.4 mm, and center-to-center inlet spacing (s_{inlet}) was

6.35 mm. The tool was configured for nine total stripes, with five stripes of support PVP solution alternating with Ag-NP ink.

For these experiments, the HSSC tool was integrated onto a commercial pilot-scale R2R system hosted by NovaCentrix, illustrated schematically in Figure 6.8(a). For all deposition runs, the substrate velocity (U_{web}) was held constant at 35.5 mm/s, coating gap (H) was fixed at 50 μm, and the combined flow rate of both Ag-NP ink and support material was 10 μL/s. Following deposition, printed samples are subject to in-line thermal curing at 120°C followed by photonic sintering using a Pulseforge® 1200 tool. The photonic sintering step is standard for the selected ink to improve conductivity of printed features. This process flow is illustrated schematically in Figure 6.8(b).

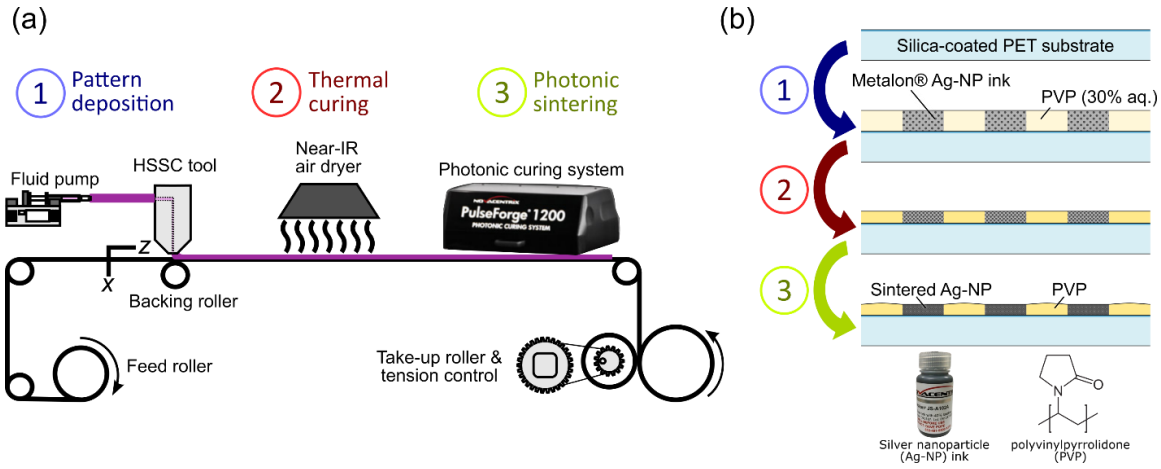

Figure 6.8 – (a) Schematic illustration of the pilot-scale R2R platform, with the inclusion of a photonic sintering step after thermal curing. (b) Illustration of the process flow for the manufacture of Ag-NP continuous-stripe patterns.

6.10.3 Microscopy of Cured Film Structures

Following deposition and photonic curing, composite Ag-NP/PVP films were treated with deionized water to remove the PVP. Removal of the PVP revealed the portions of the heterogeneous film where Ag-NP ink had successfully cured and adhered to the silica-coated PET substrate. Subsequently, optical images were obtained using a Keyence VK-X200 confocal laser microscope. The microscopy imaging setup provided a range of magnification up to 28,800x (<1 nm), well beyond the range required to distinguish edges of micro-scale pattern features.

6.10.4 HSSC with Hydrodynamic Focusing for Feature Size Verification using Ag-NP Stripes

Results for Ag-NP ink co-deposited with surfactant-doped aqueous PVP solution demonstrate exhibit the potential for process control over pattern morphology in HSSC. By varying the ratio between Ag-NP ink flow rate ($Q_{Ag\text{-}NP}$) and flow rate of aqueous PVP (Q_{PVP}) the range of pattern feature size shown in Figure 6.9 is achieved with a fixed tool geometry. While the converging-channel geometry and hydrodynamic focusing mechanism used for this process differs from the segmented slot geometry used for deposition of PEDOT:PSS in Section 4.4, the same essential principles for control over the widths (w) and spacing (s) of narrow stripes apply to both approaches. In both cases, it is the geometry of the slot that dictates the patterning of outflow from the tool. The fractional width of each fluid species in the heterogeneous coating bead follows from the geometry of the internal slot cavity, in addition to the flow rate ratio between the two fluids. Thus,

by varying value of $Q_{Ag\text{-}NP}/Q_{PVP}$, it is possible to achieve in-process control over feature size, without any change to the tool geometry.

Previous demonstrations of HSSC with PVA in Section 4.5.1, and with PEDOT:PSS in Section 4.5.2 have asserted that the width of the heterogeneous coating bead helps to ensure that the majority of the patterned flow is not distorted by spreading behavior at the lateral edges of the bead. To evaluate the validity of this point for HSSC with hydrodynamic focusing, it is necessary to state the expected center-to-center spacing of stripes as:

$$\{s\}_{expected} = s_{inlet}\frac{w_d}{w_u} \tag{6.39}$$

Equation (4.4) above describes the center-to-center spacing of stripes at the coating tool outlet, before they enter the coating bead and are deposited onto the substrate. Equation (4.4) assumes that the boundaries of coated stripes conform to the channel geometry along the entire length of the slot, without any deviation from the leading-order model in Equation (6.36). With this assumption, the expected center-to-center spacing is simply the spacing of inlets, scaled by the fractional reduction in total pattern width (w_d/w_u).

For the experimental setup used in the deposition of Ag-NP stripes, $s_{expected}$ can be calculated as 1.22 mm, which falls within the range of observed s shown in Figure 6.9(a). Nevertheless, the experimental data in Figure 6.9(a) do exhibit considerable variation, and

apparent spreading beyond the total width of the slot orifice (w_d). This variation is attributable primarily to the fact that the pilot-scale R2R system uses a backing roll, rather than a platen, to support the substrate as it passes beneath the coating tool. This facilitates a stretching and compression of the coating bead that is periodic with rotation of the backing roll. For example, a roller with an offset of ε between its axis of rotation and geometric center results in an error of $\pm\varepsilon/2$ in the slot gap (H). While it would be desirable to correct this limitation of the experimental setup for future studies, it does succeed in underscoring principles of patterned slot die coating highlighted previously in this work. First, the variation shows unequivocally that some amount of pattern distortion is possible with the coating tool used for this study. Furthermore, the likely cause of this distortion is variation in the slot gap (H), which has been shown in Sections 3.3.2 and 4.5.1 to strongly influence spreading behavior of narrow coating beads along the bottom of the coating tool. The observed severity of this spreading behavior is not entirely unexpected considering that the total width of the outlet is less than 6 mm. Because the outlet width is relatively narrow, at less than 3 times the total length of the slot die lip (L_u+L_d+G), the coating flow behaves as a narrow coating bead. This narrow coating bead exhibits the dependence between the width (w) of the coated region and H illustrated in Figure 4.6, and described by the empirical model developed in Section 3.3.

The range of stripe width (w) produced by varying $Q_{Ag\text{-}NP}/Q_{PVP}$, which is shown in Figure 6.9(b), also exhibits considerable variation across each flow rate ratio tested. A significant portion of this variation can also be attributed to the periodic fluctuation in H

caused by the backing roller, again, because it influences the spreading of coating flow within the narrow coating bead. In addition, another potential cause that must be considered is uneven distribution of ink among individual stripes, based on imperfections in the geometry of the fluid manifolds and tubing upstream from the coating tool inlets.

Based on the measured viscosity of both Ag-NP ink and PVP coating fluids (11 cP and 75 cP, respectively), the leading-order analytical model in Equation (6.36) predicts stripe width ratios, denoted here as $\{\theta_{Ag-NP}/\theta_{PVP}\}_{model}$ of 0.029, 0.059, and 0.073 across the three flow rate ratios in Figure 6.9(b). Using observed center-to-center spacing values, the leading order model can be used to predict the widths of Ag-NP stripes, denoted here as $\{w\}_{expected}$, according to the following relation:

$$\{w\}_{expected} = s\left\{\frac{\theta_{Ag-NP}}{\theta_{PVP}}\right\}_{model} \tag{6.40}$$

For the data in Figure 6.9(a), these expected stripe widths are 38.7 μm, 68.8 μm, and 87.3 μm, which are significantly lower than the observed values. This discrepancy could be explained by spreading and passive mixing effects within the heterogeneous coating bead, or following deposition and before thermal curing. It is important to note that the analytical model from Section 6.8 extends only as only far as the internal HSSC geometry. Therefore, while predictions provided by the model can be considered as a starting point or initial

guess for the final pattern morphology, future work is required to obtain complete modeling of the deposition flow in its entirety.

Images of the narrow stripe samples following removal of the PVP are shown in Figure 6.9 for two representative cases. Wide stripes near the high end of the feature size range are shown in Figure 6.8(c), and features in the range of 100 μm are shown in Figure 6.8(d). The features in Figure 6.8(c) exhibit sharp edges, which may be indicative of chipping during removal of the PVP. Near the bottom of the range of *w*, in Figure 6.8(d), stripe edges have a more diffuse appearance. The difference in morphology for these stripe boundaries can reasonably be expected to depend on energy transfer processes during the photonic sintering step. For the purposes of the present study, photonic sintering settings were fixed across all experiments, and were not optimized in any way for the expected morphology of the stripes. Therefore, the potential influence of curing and PVP removal steps on the stripe widths in Figure 6.8(b) cannot be eliminated, and constitute a potential avenue for future research.

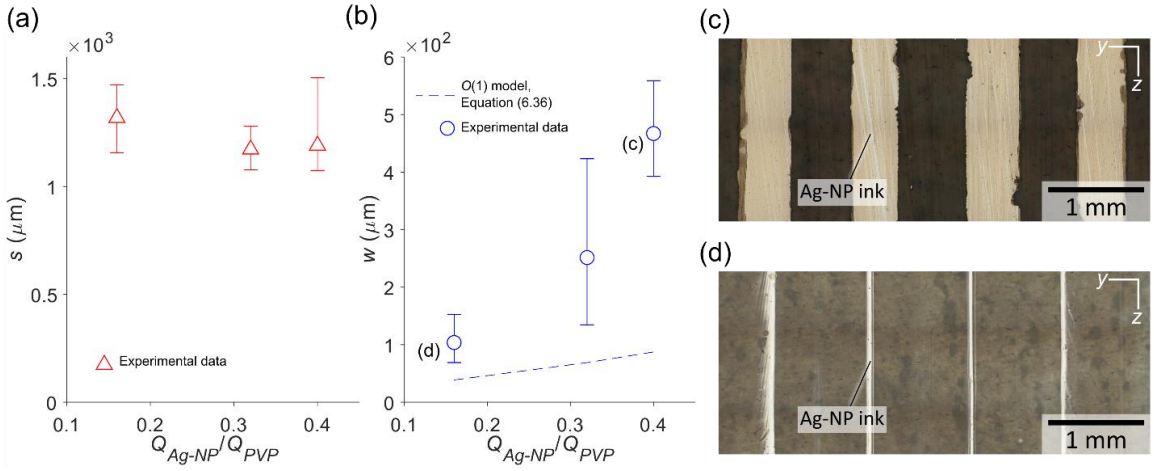

Figure 6.9 – (a) Stripe morphology, width (*w*) and center-to-center spacing (s), plotted against the flow rate ratio to demonstrate process control. (b) Microscope images of cured and sintered Ag-NP stripes.

While the results summarized in Figure 6.9 represent a feature size range of 70-550 μm, narrow stripes narrower than 50 microns, shown in Figure 6.10, were achieved using flow rate ratio of 0.07. The feature shown here exhibits a core region of sintered ink material roughly 20 μm in diameter, and a more diffuse boundary spanning roughly 40 μm. This can be compared to the stripe width of 12.8 μm predicted by Equation (6.36). A few observations are possible based on the morphology of this stripe. First, the width of the stripe relative to its length suggests that the feature size performance of the process does not benefit from dewetting. If that were true, instability and break-up of the deposited stripe would be expected based previous studies on rivulets and liquid stripes[255-257]. The straight and unbroken structure of stripe features deposited with HSSC, as represented in in Figure 6.9 (c), Figure 6.9 (d), and Figure 6.10, are not indicative of post-deposition dewetting. On the other hand, the diffuse and granular structure of the stripe boundary in Figure 6.10

could suggest post-deposition sedimentation of the silver dispersion. While the nanoparticles remain dispersed near ambient temperature, degradation of their surface chemistry during the thermal annealing and photonic sintering could allow sedimentation to occur.

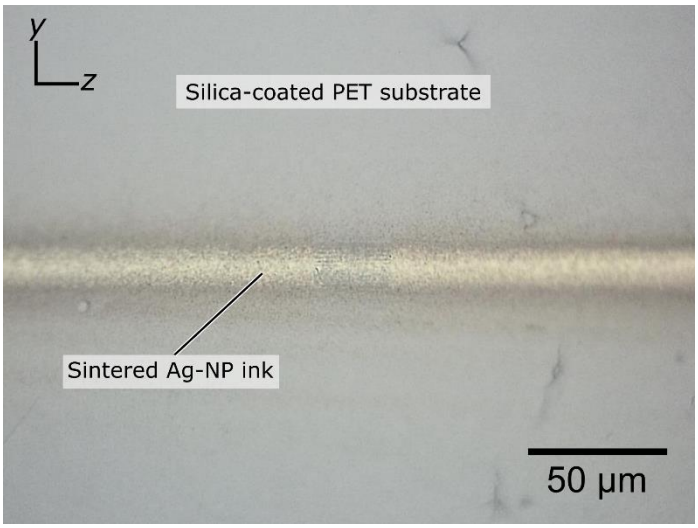

Figure 6.10 – Confocal microscope image of the final Ag-NP stripe structure at the minimum feature size produced.

6.11 Conclusions

The perturbation analysis from this chapter provides a simple relation to describe patterned outflow from an HSSC tool, along with fundamental insights relevant to the design and optimization of the internal tool geometry. One such insight, which has greatly facilitated extrapolation of previous mathematical results to the scenario considered in this chapter, is the inheritance of streamline shapes from the single-fluid case in Chapter 5. The key result from the analysis is a simple scaling relation between stripe width ratio, viscosity

ratio, and flow rate ratio, in conjunction with a small correction based on both channel geometry and the number of fluid boundaries. Here, the perturbation methodology is perhaps most helpful in providing clear limits on the importance of the correction, and in phrasing those limits in terms of physically meaningful parameters.

Sections 6.9 and 6.10 have provided experimental evidence for significant pattern resolution improvements that HSSC offers when combined with hydrodynamic focusing. The first experimental investigation has provided validation of the leading-order analytical model for outflow from an HSSC tool developed in Sections 6.3-6.8. At present, the experiments show that the model assumptions regarding diffusion and convection are reasonable for a simple ternary polymer-solvent system, and that cross-mixing can be neglected on a length scale conducive to patterned slot die coating. In future work, it will be important to design and execute new experiments that can evaluate the limits on model accuracy more thoroughly, including the $\mathcal{O}(\alpha)$ correction, and across additional materials and coating tool geometry.

In the larger context of pattern capability, the range of Ag-NP stripe widths achieved with hydrodynamically focused HSSC represents a significant improvement relative to the current state-of-the art for conventional slot die coating. The investigation of this chapter has demonstrated a range of feature sizes spanning an order of magnitude with fixed tooling by adjusting only one parameter, the flow rate ratio between functional ink and support material. More importantly, the resolution performance of less than 50 μm

demonstrated for HSSC with hydrodynamic focusing is excellent compared to the practical limit of 1 mm for conventional slot die coating. It should also be stressed that the tooling and apparatuses used in this investigation are only early implementations, and that much potential exists for optimization of the process in future work. Therefore, the true feature size capability of HSSC is likely to be much better than 50 μm.

CHAPTER 7. CONCLUSIONS

The work of this dissertation has pursued a novel slot die-inspired coating capability for printing features in the range of 50 μm, which incorporates novel patterning capabilities offered by internal flow patterning and liquid bridge phenomena. To achieve this objective, the investigations in this work have sought to address several fundamental questions related to two slot die coating-inspired approaches, coating/extrusion-on-demand (C/EOD) and heterogeneous stripe slot coating (HSSC).

The first of these fundamental questions relates to the **physical mechanisms** that mediate pattern generation. Experimental visualizations of coating flows have been carried out using the roll-to-roll imaging system (R2RIS) to identify and study these mechanisms for C/EOD and HSSC. These studies have highlighted the relationship between geometry of the coating bead contact line and the shape of the printed pattern. This relationship has been shown to depend significantly on spreading and confinement behavior along the bottom of the slot die coating tool, and to couple process inputs to the printed feature size. Development, coalescence and breakup of an array of liquid bridges have been tied to complex patterning capabilities of C/EOD. Finally, the spatial composition of heterogeneous coating beads has been identified as the physical aspect of HSSC that determines the width and center-to-center spacing of continuous printed stripes.

Second, this dissertation has identified **restrictions on pattern capability** that are implied by the physical mechanisms identified above. Using experimental visualizations obtained using the R2RIS, narrow coated stripes have been considered as a representative pattern feature for resolution performance of slot die coating-inspired techniques. Drawing on insights from existing literature, the observed geometry of a narrow coating bead has been compared to analogous characteristics in isolated liquid bridges. In particular, the width of a narrow coating bead, and thus the feature size achievable with slot coating of narrow stripes, has been compared to the contact radius of an axisymmetric liquid bridge. To address limitations on the minimum achievable liquid bridge size, a heterogeneous flow field has been introduced as a novel patterning mechanism for HSSC. The feature sizes produced using the HSSC approach have been shown to correspond to the widths of co-laminar stripe-patterned regions at the coating tool outlet. In addition, hydrodynamic focusing of heterogeneous co-laminar flow inside the coating tool has also been demonstrated as a means to scale a deposited pattern well below the width of the coating tool outlet. Passive mixing that limits the hydrodynamically focused HSSC approach has been addressed through a perturbation analysis of internal flow through the converging internal slot geometry of the tool. This analysis has quantified limits on the severity and domain of influence for secondary flows located at the slot sidewalls that induce unwanted mixing.

This dissertation has also explored the coupling between **process inputs and pattern output** for slot die coating-inspired approaches. For C/EOD and conventional

narrow stripe slot coating, an empirical model has been developed that predicts the widths of narrow stripes as a function of process parameters flow rate (Q), substrate velocity (U_{web}), and coating gap (H). The form of the empirical model draws inspiration from experimental observations on spreading and wetting of the coating flow along the bottom of the slot die coating tool. For HSSC, significantly reduced process dependence on Q, U_{web}, and H has been observed for co-deposition of two aqueous polyvinyl alcohol (PVA) solutions, as well as co-deposition of poly(3,4-ethylenedioxythiophene):polystyrene sulfonate (PEDOT:PSS) ink. Independent control over film thickness and pattern morphology has also been demonstrated with HSSC, in contrast to conventional narrow stripe slot coating and C/EOD. Based on in-process imaging from the R2RIS, these desirable attributes of HSSC derive in part from the large width of the coating bead through which narrow features are deposited. The width of the HSSC coating bead negates the importance of spreading of the lateral edges of the contact line, which is responsible for the coupling between pattern output and Q, U_{web}, and H in C/EOD.

Considerations for **material formulation** that are specific to the slot die coating-inspired approach have also been addressed in this work. For C/EOD, rheological and wetting requirements are largely unchanged versus conventional slot die coating. For HSSC, however, the co-deposited support material has been found to help ensure wetting stability in the final patterned film, even when the other co-deposited fluid exhibits poor wettability when deposited alone. Thus, HSSC has been shown to afford significant flexibility in material formulation for wetting stability of printed patterns. In the context of

material selection, these formulation requirements can be satisfied by the co-deposited support material, thereby reducing the burden of formulation for the functional material. Additionally, a static equilibrium analysis has been carried out for the contact lines formed by interaction of two immiscible materials deposited in an alternating-stripe pattern by HSSC. This analysis has predicted unwanted spreading of the pattern due to the formation the liquid-liquid interface. Thus, it has been shown that miscible materials are preferable for HSSC of continuous narrow stripe patterns.

Finally, initial demonstrations with functional materials have been carried out in order to **compare added complexity and potential challenges against the novel capabilities** offered by patterned slot die coating-inspired techniques. A solution-processible conductive polymer, PEDOT:PSS, has been deposited in narrow stripes using HSSC to assess the influence of the process on the functional performance of the final patterned film. Here, passive mixing at the interface between the two co-deposited materials was identified as the most significant limitation on functional performance. Despite this limitation, electrical conductivity (σ) of around 1.5 S cm^{-1} was measured for the PEDOT:PSS film without additional post-treatment. This performance compares favorably with previously reported values. To assess the feature size capability of the slot die coating-inspired approach, a commercially available silver nanoparticle (Ag-NP) ink was deposited by HSSC with hydrodynamic focusing in continuous stripes narrower than 50 μm. In these investigations, modulation of stripe width independently from wet film thickness has also been demonstrated. In summary, the work of this dissertation has shown clear advantages

to patterning resolution and material selection for C/EOD and HSSC, while maintaining the wide-area capability that helps distinguish slot die coating as a highly scalable approach.

CHAPTER 8. CONTRIBUTIONS AND OUTLOOK

8.1 Key Contributions

The work of this dissertation has been carried out with the aim of elevating the viability of wide-area patterned coating at high resolution through novel slot die coating-inspired techniques. The manufacturing strategies considered in this work have been evaluated on the basis of patterning complexity and feature size performance, considerations and restrictions on material formulation, and suitability for process scale-up. Investigations on the physical mechanisms inherent to these techniques that generate printed patterns have provided fundamental knowledge to inform continued development of the technique and practical implementation. The fundamental and applied contributions from this work are summarized as follows:

8.1.1 Fundamental Contributions

- **Wetting and spreading behaviors** of the narrow coating bead have been identified as the physical mechanisms mediating pattern output during continuous coating of small features ranging from 0.9 to 11 mm, as illustrated using a coating/extrusion-on-demand (C/EOD) process. Compared to key findings from previous literature:
    - **Steady-state coating bead width** has been found to depend on its previous spreading state as well as conventional process parameters in slot die coating.

- Experimentally observed wetting and spreading behaviors have been successfully incorporated into an **empirical model** of narrow stripe width as a function of slot die coating process parameters, which corroborates many of the process-pattern trends observed in previous studies of narrow stripe slot coating by other authors.
- Regimes of **contact line confinement** were observed to influence the correlation between process parameters and pattern output via the coating bead width.
- **Attachment, development, and separation** have been highlighted as the mechanisms mediating feature size performance of intermittent stripes and patches, and the coating bead response to flow actuation has been conceptually tied to residual coating fluid volume.
- **Coalescence of adjacent coating beads** has been illustrated both as a mechanism to generate complex patterns, and as a defect mode that limits the range of operability for C/EOD and conventional narrow stripe slot coating.

- Mathematical analysis of **internal co-laminar flow** within a converging channel such as that used in the heterogeneous stripe slot coating (HSSC) tool has provided physical insights regarding flow behavior in a planar converging slot:

- It has been shown that sufficiently far from the sidewalls, the shapes of **fluid interfaces conform to streamlines**, such that a narrow stripe pattern can be established and scaled to the overall width of a converging slot.
- **Secondary flows** near the slot sidewalls have been conceptually separated into a conformal or squeezing effect which scales the pattern, and a boundary layer effect which facilitates mixing.
- The **3D velocity field** for flow through a converging planar channel has been derived for moderate to large convergence angles, whereas previous literature has so far considered only gradually varying channel cross-sections.
- A simple scaling relationship between the **locations of fluid interfaces** which define the pattern, and the viscosity and flow rate ratios of two co-laminar fluids, has been developed.
- By virtue of the perturbation approach chosen for the analysis, the **model accuracy** is clearly understood in terms of the aspect ratio and overall width of the slot.

8.1.2 Applied Contributions

- **Complex patterning capabilities** have been demonstrated using a coating/extrusion-on-demand (C/EOD) approach. Independent actuation of multiple coating beads on a single coating tool has been used as a generative

mechanism for diagonal stripes and intermittent patches which cannot be manufacturing using the conventional approach.

- **Continuous stripe widths below 50 μm** have been demonstrated with heterogeneous stripe slot coating (HSSC), which represents an order-of-magnitude improvement in feature size over conventional slot die coating. Based on the observations of this work, it is reasonable to expect patterning at even higher resolution to be achievable using the same approach.
- Modeling efforts have yielded practical correlations between process inputs and feature size:
    - A procedure for correlating **steady-state coating bead width** with process conditions has been developed and demonstrated with a sample material system. The empirical model formulation, which can be replicated on a standard roll-to-roll (R2R) setup without additional specialized infrastructure, accounts for observed spreading behaviors which strongly influence the geometry of the coating bead.
    - A perturbation analysis of internal flow within an HSSC tool provides a predictive capability for the outflow that defines the deposited pattern. The analytical model describes the **locations of fluid interfaces that define the pattern**, as well as the **size of boundary layers** that induce mixing at the edges of the pattern.
- Clear benefits have been demonstrated for HSSC with respect to **process control**:

    - De-coupling of film thickness and feature size for continuous stripes significantly reduces the burden of empirical process modeling for HSSC relative to C/EOD and conventional slot die coating of narrow stripes.
    - **Wetting requirements** for post-deposition pattern stability have been transferred from a functional material to a non-functional support material, in order to achieve stable deposition of inks formulated without wettability-enhancing additives.
- C/EOD and HSSC have both been demonstrated with **commercially available ink materials** widely used to deposit electrically conductive films. These demonstrations help to build a case for slot die-inspired pattern coating as a viable manufacturing approach for functional devices.

In summary, this thesis has developed a novel manufacturing capability in terms of pressing initial questions related to patterning, material compatibility, and process control. The applied contributions of this work offer a favorable balance of novel process capabilities against the complexity and unique considerations of the new slot die coating-inspired techniques. The fundamental contributions of this work provide meaningful physical interpretation of the observed process behavior, as well as expectations for process capabilities in other contexts.

8.2 Outlook for Future Work

The continuation of research efforts related to C/EOD and HSSC slot die coating of narrow stripes will benefit greatly from additional **fundamental research on liquid bridge phenomena**. The empirical correlations developed for steady-state coating bead width, while of practical value for the materials considered, lack the physical underpinning that a numerical or analytical model would provide. This task will not be trivial, since it must account for dynamic behavior of contact lines on at least two solid phases, confined by a complex geometry, and subject to ambient humidity and temperature conditions. Furthermore, the characterizations of contact angle and contact line geometry along the lateral edges of the coating bead have not yet been addressed in related previous literature, to the best knowledge of the author. Nevertheless, a simplified model is likely to provide insights relevant to the appropriate empirical model form and its constituent dimensionless groups. It is conceivable that the results of such an effort will produce a relationship between process inputs and steady-state stripe width that is more intricate than the simple logarithmic correlation assumed in this work. It will also be important to study the physical origin of observed wetting-receding configurations of the steady-state bridge.

The utility of C/EOD for deposition of functional applications will also benefit from additional **applied research on manipulation of the narrow coating bead geometry**. Innovative tool designs and novel mechanisms for forcing separation of the coating bead, and for achieving rapid coupling between flow actuation and pattern response, will

contribute significantly towards a practical capability for manufacturing complex patterns at large-scale. This is especially important considering the underdeveloped performance of the specific implementations of MIF and PAF control strategies evaluated in this work.

There remain several avenues for future fundamental study of **co-laminar internal flow** through the HSSC geometry, beyond the scope of this dissertation. Previous modeling efforts on hydrodynamic focusing have noted, and occasionally highlighted, the difficultly in locating fluid boundaries in variable-width channel geometries. On the other hand, the numerical modeling strategies demonstrated in previous work have addressed diffusion transport in high-*Pe* sheath flows. Provided a suitable motivating application can be identified, it would be interesting to combine the modeling results of this work with a numerical treatment of diffusion transport across the fluid interfaces. It may also be of interest to consider the case of two fluids with nonzero interfacial tension, or time-varying flow rates and stripe widths for the purpose of potential complex patterning capabilities. With sufficient care, it may be possible to extend the existing analysis in order to address some of these points. On the other hand, a numerical treatment of the problem may be more expedient, as well as helpful for verifying the accuracy of the perturbation analysis. One topic that previous computational work has addressed successfully for other problems is chemical transport across fluid interfaces at length-scales where diffusion becomes significant. It would likely be feasible to follow a similar approach for the case of hydrodynamically focused HSSC.

Another area of future fundamental study for HSSC is phenomena of **mixing in the heterogeneous coating flow** emanating from the tool outlet. While the work in this dissertation has provided useful guidance for patterned outflow from an HSSC tool, the experimental work has also demonstrated that the effects of spreading and mixing can be significant in the fluid domain that follows outflow. The results from this work could be used to establish appropriate upstream boundary conditions for the heterogeneous coating bead in future modeling efforts.

For both C/EOD and HSSC, further studies that consider **additional materials** will be critical for verifying this work's fundamental observations and for expanding the impact of its applied contributions. In particular, it would be interesting to consider materials formulated for to minimize post-deposition mixing across interfaces, or applications where a diffuse interface constitutes a functional pattern feature. Furthermore, it should be noted that the functional ink materials deposited by HSSC in this work are colloid dispersions, and that extending the experimental efforts to simpler polymer solutions constitutes an easily achievable next step. It will also be important in the future to demonstrate both C/EOD and HSSC methods for the manufacture of functional devices. While the feasibility of both methods has been established to a reasonable degree, efforts with functional devices are ubiquitous in manufacturing research and likely to further elevate the practical impact of this work.

APPENDIX A. EMPIRICAL MODEL DETAILS

A1 Determination of Dimensionless Groups for Empirical Model

This section provides a brief validation and discussion of the empirical dimensionless groups Π_a and Π_r used in the empirical model for narrow stripes, which are developed in Section 3.3. Π_a and Π_r are selected on the basis of goodness-of-fit and physical significance. Figure A1.1 presents R^2 values for various linear combinations of Q, U_{web} and H used in place of Π_a and Π_r in the analysis from Section 3.3. Vertical bars denote R^2 for the full data set, and the error bars denote the range of R^2 across individual data subsets defined by fixed H.

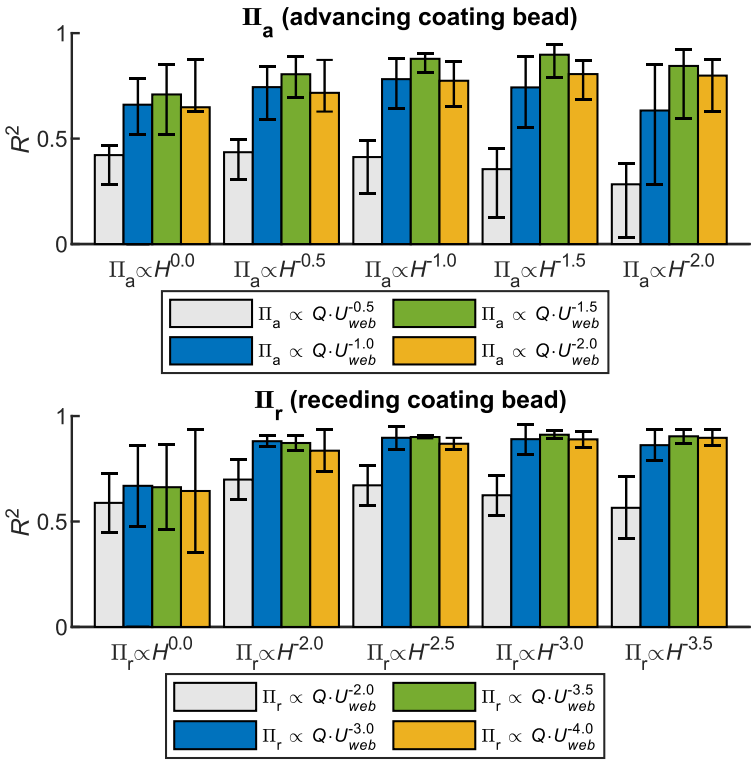

Figure A1.1 Sensitivity analysis of empirical model fit for 10% wt. PVA across linear combinations of *Q*, U_{web}, and *H*. Adapted from [198].

The appropriate choice of Π_a and Π_r should produce the strongest correlations which are consistent across data sets. Examining the results presented in Figure A1.1, $\Pi_r \propto QU_{web}^{-3.5}H^{-2.5}$ meets this criterion. The appropriate choice for Π_a, is less clear, however. $\Pi_a \propto QU_{web}^{-1.5}H^{-1.5}$ results in the highest R^2 value while $\Pi_a \propto QU_{web}^{-1.5}H^{-1}$ produces the smallest range of R^2. A comparison of the residuals for each of these two cases, shown in Figure A1.2, suggests that $\Pi_a \propto QU_{web}^{-1.5}H^{-1.5}$ is the better choice, since the sums of the residuals across each constant-*H* data subset are more uniform for this case. Dimensionless groups should be selected to satisfy the following proportionality:

$$\Pi_a \propto QU_{web}^{-1.5}H^{-1.5} \tag{A1.1}$$

$$\Pi_r \propto QU_{web}^{-3.5}H^{-2.5} \tag{A1.2}$$

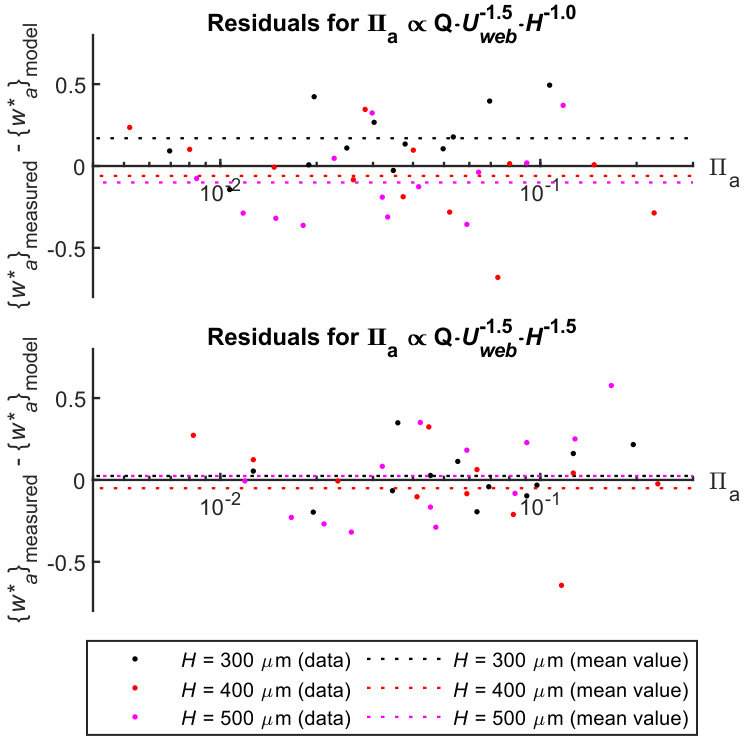

Figure A1.2 Residual values for the empirical model for advancing coating bead width, using (a) $\Pi_a \propto QU_{web}^{-1.5}H^{-1}$ and (b) $\Pi_a \propto QU_{web}^{-1.5}H^{-1.5}$ Adapted from [198].

Next, the physical significance of dimensionless groups must be assessed. The groups selected to satisfy Eqns. (A1.1) and (A1.2) are as follows:

$$\Pi_a \equiv Re^{0.5} Ca^{-1} H^{*-2} \tag{A1.3}$$

$$\Pi_r \equiv Re^{0.5} Ca^{-3} H^{*-3} \tag{A1.4}$$

Previous work has shown that narrow stripe width correlates negatively with viscosity, and that coating bead width increases as inertial forces become dominant over viscous and interfacial forces[154, 197]. These observations are reflected in the positive correlation with *Re* for both Π_a and Π_r. Similarly, the negative correlation between *H** and *w** parallels the observed relationship between height and contact radius in a fixed-volume liquid bridge[186, 188]. Finally, Π_a and Π_r correlate negatively with *Ca*, which reflects the balance between surface tension forces that maintain the liquid bridge against the viscous shear imposed by the motion of the substrate relative to the slot die.

APPENDIX B. MATHEMATICAL DERIVATIONS FOR SINGLE-FLUID INTERNAL FLOW ANALYSIS

The purpose of this section is to provide mathematical derivations and clarifying intermediate steps for the perturbation analysis of single-fluid flow through a converging rectangular slot in Chapter 5. The content of the following sections has been provided for the benefit and scrutiny of interested readers. The notation here is consistent with the main manuscript.

B1 Derivation of Fourier Series Solution for Single-Fluid Outer Velocity

This section provides intermediate steps for derivation of the form of the solution to Equations (5.10a)- (5.10d) in Section 5.5.

Integrating Equations (5.10b) and (5.10c) twice gives, respectively:

$$U_{r,0} = \frac{1}{2}\frac{\partial p_0}{\partial r} z^2 + f_1(r,\theta)z + f_2(r,\theta) \tag{B1.1}$$

$$U_{\theta,0} = \frac{1}{2r}\frac{\partial p_0}{\partial \theta} z^2 + f_3(r,\theta)z + f_4(r,\theta) \tag{B1.2}$$

where f_1 ... f_4 are undetermined functions of integration. Enforcing the symmetry condition about $z = 0$ gives $f_1 = f_3 = 0$, and enforcing the no-slip condition at $z = 1$ gives $f_2 = -\frac{1}{2}\frac{\partial p_0}{\partial r}$, $f_4 = -\frac{1}{2r}\frac{\partial p_0}{\partial \theta}$. This leaves us with $U_{r,0} = -\frac{\partial p_0}{\partial r}\left(\frac{1-z^2}{2}\right)$ and $U_{\theta,0} = -\frac{1}{r}\frac{\partial p_0}{\partial \theta}\left(\frac{1-z^2}{2}\right)$,

and substituting this result into Equation (5.10a) to satisfy continuity provides the following result:

$$-\left[\frac{1}{r}\frac{\partial}{\partial r}\left(r\frac{\partial p_0}{\partial r}\right)+\frac{1}{r}\frac{\partial}{\partial \theta}\left(\frac{1}{r}\frac{\partial p_0}{\partial \theta}\right)\right]\left(\frac{1-z^2}{2}\right)+\frac{\partial}{\partial z}\left(U_{z,0}\right)=0 \tag{B1.3}$$

This expression can be integrated again with respect to z to yield:

$$U_{z,0}=\left[\frac{1}{r}\frac{\partial}{\partial r}\left(r\frac{\partial p_0}{\partial r}\right)+\frac{1}{r}\frac{\partial}{\partial \theta}\left(\frac{1}{r}\frac{\partial p_0}{\partial \theta}\right)\right]\left(\frac{3z-z^3}{6}\right)+f_5(r,\theta) \tag{B1.4}$$

Symmetry about $z=0$ implies that the function of integration above, $f_5(r,\theta)$, is zero. Then, the no-slip boundary condition requires that $U_{z,0}=0$ at $z=1$. Therefore the $\mathcal{O}(1)$ outer velocity field planar. This implies that the expression in brackets above is equal to zero, or equivalently, pressure to leading order is governed by Laplace's equation in 2D cylindrical coordinates:

$$\frac{1}{r}\frac{\partial}{\partial r}\left(r\frac{\partial p_0}{\partial r}\right)+\frac{1}{r^2}\frac{\partial^2 p_0}{\partial \theta^2}=0 \tag{B1.5}$$

Together with the symmetry condition about $\theta=0$, as well as the pressure condition at $(r,\theta)=(r_d,0)$, Equation (B1.5) permits a series of solutions of the following form:

$$p_0 - p_d = C_0 \ln\left(\frac{r}{r_d}\right) + \sum_{n=1}^{\infty}\left(-C_{n,1}r^{-n} + C_{n,2}r^{n}\right)\cos(n\theta) - \sum_{n=1}^{\infty}\left(-C_{n,1}{r_d}^{-n} + C_{n,2}{r_d}^{n}\right) \tag{B1.6}$$

where C_0, $C_{n,1}$, and $C_{n,2}$ are constants that will be determined based on boundary conditions and by matching with the inner solution. It may be noted that while non-integer values of n will also produce solutions to Equation (B1.5), it will be confirmed later that the necessity of matching with the inner solutions imply that the coefficients of such terms must be zero.

Through an analogous process, the $\mathcal{O}(\alpha)$ pressure field correction can be expressed as follows:

$$p_1 = D_0 \ln\left(\frac{r}{r_d}\right) + \sum_{n=1}^{\infty}\left(-D_{n,1}r^{-n} + D_{n,2}r^{n}\right)\cos(n\theta) - \sum_{n=1}^{\infty}\left(-D_{n,1}{r_d}^{-n} + D_{n,2}{r_d}^{n}\right) \tag{B1.7}$$

Taking partial derivatives of Equation (B1.6) gives the form of the $\mathcal{O}(1)$ velocity components as follows:

$$U_{r,0} = -\frac{1}{r}\left\{C_0 + \sum_{n=1}^{\infty} n\left(C_{n,1}r^{-n} + C_{n,2}r^{n}\right)\cos(n\theta)\right\}\left(\frac{1-z^2}{2}\right) \tag{B1.8}$$

$$U_{\theta,0} = \frac{1}{r}\left\{\sum_{n=1}^{\infty} n\left(-C_{n,1}r^{-n} + C_{n,2}r^{n}\right)\sin(n\theta)\right\}\left(\frac{1-z^2}{2}\right) \tag{B1.9}$$

$$U_{z,0} = 0 \tag{B1.10}$$

Similarly, by taking partial derivatives of Equation (B1.7), the $\mathcal{O}(\alpha)$ velocity field correction can be expressed as follows:

$$U_{r,1} = -\frac{1}{r}\left\{D_0 + \sum_{n=1}^{\infty} n\left(D_{n,1}r^{-n} + D_{n,2}r^{n}\right)\cos(n\theta)\right\}\left(\frac{1-z^2}{2}\right) \tag{B1.11}$$

$$U_{\theta,1} = \frac{1}{r}\left\{\sum_{n=1}^{\infty} n\left(-D_{n,1}r^{-n} + D_{n,2}r^{n}\right)\sin(n\theta)\right\}\left(\frac{1-z^2}{2}\right) \tag{B1.12}$$

$$U_{z,1} = 0 \tag{B1.13}$$

B2 Derivation of a Fourier Series Solution for Single-Fluid Inner r-Velocity

An expression for $V_{r,0}$ is sought which satisfies the following governing equation:

$$\frac{C_0}{r} = \frac{1}{r^2}\frac{\partial^2 V_{r,0}}{\partial {\xi_r}^2} + \frac{\partial^2 V_{r,0}}{\partial z^2} \tag{B2.1}$$

where r, ξ_r, and z are spatial coordinates, and C_0 is a constant coefficeint. Taking a separation of variables approach, solutions of the following form are sought:

$$V_{r,0} = \frac{1}{r}\Xi_{r,0}(r\xi_r)Z_{r,0}(z) - \frac{C_0}{r}\left(\frac{1-z^2}{2}\right) \tag{B2.2}$$

Here, $\Xi_{r,0}(r\xi_r)$ and $Z_{r,0}(z)$ are functions that must be selected to satisfy the boundary conditions. The factor $\frac{1}{r}$ has been included in the first term in the right-hand side of the equation to ensure that no-slip at $\theta = \pm\theta_H$ is satisfied for all r. Alternatively, a generic function of r could have been used in its place, and found to be $\frac{1}{r}$ during by enforcing the no-slip boundary condition afterward. Substituting the assumed form of $V_{r,0}$ into Equation (B2.1) gives:

$$\frac{{\Xi_{r,0}}''}{\Xi_{r,0}} + \frac{{Z_{r,0}}''}{Z_{r,0}} = 0 \tag{B2.3}$$

In order to satisfy the symmetry boundary condition at $z = 0$ as well as the no-slip boundary condition at $z = 1$ along with this expression, it is expected that $Z_{r,0} \propto \cos(\delta_n z)$ such that $\cos(\delta_n) = 0$, where $\delta_n \equiv \frac{2n-1}{2}\pi$ for positive integers n. In order to ensure the possibility of matching with the outer solution, where $\xi_r \to -\infty$, it is also expected that

$\Xi_{r,0} \propto \exp\{\delta_n r \xi_r\}$ for positive n. The superposition of all possible solutions of this type gives the general expression for $V_{r,0}$:

$$V_{r,0} = \frac{C_0}{r} \sum_{n=1}^{\infty} E_n \exp\{\delta_n r \xi_r\} \cos(\delta_n z) - \frac{C_0}{r}\left(\frac{1-z^2}{2}\right) \tag{B2.4}$$

Here, the coefficient C_0 has been added to the second term in the right-hand side of Equation (B2.4) for convenience in later calculations. E_n are constant coefficients that must be chosen to satisfy the inhomogeneous no-slip boundary condition at $\xi_r = 0$, such that:

$$\sum_{n=1}^{\infty} E_n \cos(\delta_n z) = \frac{(1-z^2)}{2} \tag{B2.5}$$

To proceed, it is convenient to consider the orthogonality of the cosine function, which implies the following:

$$2\int_0^1 \cos(\delta_n z)\cos(\delta_m z)\, dz = \begin{cases} 1 & \text{for} \quad n = m \\ 0 & \text{for} \quad n \neq m \end{cases} \tag{B2.6}$$

This property can be exploited by multiplying both sides of Equation (B2.5) by $\cos(\delta_m z)$ and integrating with respect to z from $z = 0$ to $z = 1$, as follows:

$$\int_0^1 \left\{\frac{(1-z^2)}{2}\right\} \cos(\delta_m z)\, dz = \int_0^1 \left\{\sum_{n=1}^{\infty} E_n \cos(\delta_n z)\right\} \cos(\delta_m z)\, dz \tag{B2.7}$$

This expression can be evaluated as follows:

$$\frac{1}{2}\left[\frac{(1-z^2)}{\delta_m}\sin(\delta_m z) - 2z\frac{\cos(\delta_m z)}{(\delta_m)^2} + 2\frac{\sin(\delta_m z)}{(\delta_m)^3}\right]_{z=0}^{z=1} = \frac{1}{2}E_m$$

$$\rightarrow 2\left[-\frac{\cos(\delta_m)}{(\delta_m)^2} + \frac{\sin(\delta_m)}{(\delta_m)^3}\right] = E_m \tag{B2.8}$$

Finally, upon observation that $\cos(\delta_m) = (-1)^{m-1}$, the following definition for the coefficients $E_1, E_2, \ldots$ is obtained:

$$E_n = 2\frac{(-1)^{n-1}}{(\delta_n)^3} \tag{B2.9}$$

B3 Derivation of Single-Fluid θ- and z-Velocity Components

This section provides intermediate steps for derivation of the form of the solution to Equations (5.23a), (5.23c) and (5.23d) that appear in Section 5.6. Briefly, the partial derivatives that appear in Equations (5.23a)- (5.23d) are computed as follows:

$$\frac{1}{r}\frac{\partial}{\partial r}\left(rV_{r,0}\right) = \frac{C_0}{r^2}\left\{\sum_{n=1}^{\infty}\delta_n r\xi_r \exp\{\delta_n r\xi_r\}\left[E_n \cos(\delta_n z)\right]\right\} \tag{B3.1}$$

$$\frac{\partial^2 V_{\theta,0}}{\partial {\xi_r}^2} = 0 \tag{B3.2}$$

$$\frac{\partial^2 V_{\theta,0}}{\partial z^2} = 0 \tag{B3.3}$$

Substituting these intermediate results into Equations (5.23a)- (5.23d) gives the following:

$$\frac{C_0}{r^2}\sum_{n=1}^{\infty}\delta_n r\xi_r \exp\{\delta_n r\xi_r\}\left[E_n \cos(\delta_n z)\right] + \frac{1}{r}\frac{\partial}{\partial \xi_r}\left(V_{\theta,1}\right) + \frac{\partial}{\partial z}\left(V_{z,0}\right) = 0 \tag{B3.4}$$

$$\frac{\partial p_1}{\partial r} = \frac{1}{r^2}\frac{\partial^2 V_{r,1}}{\partial {\xi_r}^2} + \frac{\partial^2 V_{r,1}}{\partial z^2} \tag{B3.5}$$

$$\frac{\partial p_1}{\partial \xi_r} = 0 \tag{B3.6}$$

$$\frac{\partial p_1}{\partial z} = 0 \tag{B3.7}$$

Equation (B3.6) implies that to $\mathcal{O}(\alpha)$, the pressure from the outer region is again imposed on the inner region. Thus, again, $\frac{\partial p_1}{\partial r}$ in Equation (B3.8) can be obtained from its value in the outer region near the boundary at $\theta = \theta_H$. To determine the velocity components $V_{\theta,1}$

and $V_{z,0}$ in Equation (B3.4), each will be expressed as a superposition of particular and homogenous components, $(V_{\theta,1P}, V_{z,0P})$ and $(V_{\theta,1H}, V_{z,0H})$, respectively. The $\mathcal{O}(\alpha)$ continuity correction is then given by the following:

$$\frac{C_0}{r^2}\sum_{n=1}^{\infty}\delta_n r\xi_r \exp\{\delta_n r\xi_r\}\left[E_n \cos(\delta_n z)\right] + \frac{1}{r}\frac{\partial}{\partial \xi_r}\left(V_{\theta,1P}\right) + \frac{\partial}{\partial z}\left(V_{z,0P}\right) = 0 \tag{B3.9}$$

$$\frac{1}{r}\frac{\partial}{\partial \xi_r}\left(V_{\theta,1H}\right) + \frac{\partial}{\partial z}\left(V_{z,0H}\right) = 0 \tag{B3.10}$$

The right-hand side of Equation (B3.9) implies an $\mathcal{O}(\alpha)$ net flux from the outer region to the inner region along either of the z- or θ-axes. $V_{z,0}$ must match with $U_{z,0} = 0$ in the outer region, and is on the order of one $\mathcal{O}(1)$. Together, these points suggest that in the outer region, $V_{\theta,1}$ approaches a nonzero value and $V_{z,0}$ decays to zero. Both inferences are satisfied by a particular solution of the following form:

$$V_{\theta,1P} = -\frac{C_0}{r^2}\sum_{n=1}^{\infty}\left[\frac{1}{\delta_n}(\delta_n r\xi_r - 1)\exp\{\delta_n r\xi_r\} + \frac{1}{\delta_n}\right]\left[E_n \cos(\delta_n z)\right] \tag{B3.11}$$

$$V_{z,0P} = 0 \tag{B3.12}$$

As written above, this solution satisfies no-slip and no-flux at $\xi_r = 0$, as well as at $z = -1,1$. In the limit that $\xi_r \to -\infty$, however, $V_{\theta,1P}$ approaches a function of r and z which is not parabolic along the z-axis, as required for matching with the outer solution. The

homogenous component will provide the necessary correction to rectify this issue. To determine $V_{\theta,1H}$, a separation of variables approach is again assumed in order to satisfy Equation (B3.10):

$$V_{\theta,1H} = \frac{C_0}{r^2}\Xi_{\theta,1}(r\xi)Z'_{\theta,1}(z) \tag{B3.13}$$

$$V_{z,0H} = -\frac{C_0}{r^2}\Xi'_{\theta,1}(r\xi)Z_{\theta,1}(z) \tag{B3.14}$$

Here, the factor C_0 has been included for convenience in later calculations. The term $\frac{1}{r^2}$ has been used to permit matching with the outer solution, in the same fashion as with $V_{r,0}$. Alternatively, a generic function of r could have been used in its place, and found to be $\frac{1}{r^2}$ during the matching procedure.

To satisfy no-slip z-axis boundaries and enable matching with a velocity profile that is parabolic along the z-axis, the following definition of $Z_{\theta,1}$ is used:

$$Z_{\theta,1}(z) \equiv \frac{1}{\delta_n}\sin(\delta_n z) - F_n\left(\frac{3z - z^3}{6}\right) \tag{B3.15}$$

$$Z'_{\theta,1}(z) \equiv \cos(\delta_n z) - F_n\left(\frac{1 - z^2}{2}\right) \tag{B3.16}$$

where δ_n is defined as above, and $F_n = (-1)^{n-1}\frac{3}{\delta_n}$, for positive integers n. This specific definition of F_n ensures that $Z_{\theta,1}(z)\big|_{z=1} = Z_{\theta,1}(z)\big|_{z=-1} = 0$, such that no-flux at the z-axis boundaries is satisfied. Next, in order to satisfy no-slip and no-flux the θ-axis boundary, and to ensure that matching with the outer solution is possible, the following definition of $\Xi_{\theta,1}$ is used:

$$\Xi_{\theta,1}(r\xi) \equiv H_n(\delta_n r\xi_r - 1)\exp\{\delta_n r\xi_r\} + H_n \tag{B3.17}$$

$$\Xi'_{\theta,1}(r\xi) \equiv H_n\delta_n^2 r\xi_r \exp\{\delta_n r\xi_r\} \tag{B3.18}$$

It should be noted that as $\xi_r \to -\infty$, $\Xi'_{\theta,1}$ decays to zero, while $\Xi_{\theta,1}$ approaches a constant value, H_n, which must be determined for all n such that the superposition of $V_{\theta,1P}$ and $V_{\theta,1H}$ is parabolic along the z-axis as $\xi_r \to -\infty$.

$$\begin{aligned}\lim_{\xi_r\to-\infty}\{V_{\theta,1P} + V_{\theta,1H}\} &= \lim_{\xi_r\to-\infty}\{V_{\theta,1P}\} + \lim_{\xi_r\to-\infty}\{V_{\theta,1H}\} \\ &= \frac{C_0}{r^2}\sum_{n=1}^{\infty}\left(-\frac{E_n}{\delta_n} + H_n\right)\cos(\delta_n z) - \frac{C_0}{r^2}\sum_{n=1}^{\infty} H_n F_n\left(\frac{1-z^2}{2}\right)\end{aligned} \tag{B3.19}$$

Above, the term $\sum_{n=1}^{\infty}\left(-\frac{E_n}{\delta_n} + H_n\right)\cos(\delta_n z)$ will be parabolic along the z-axis provided $H_n = \frac{E_n}{\delta_n}$. After substituting the expressions for F_n and H_n into the definitions for

$\Xi_{\theta,1}$ and $Z_{\theta,1}$ given above, the particular and homogenous components of $V_{\theta,1}$ are superposed, as follows:

$$V_{\theta,1P} + V_{\theta,1H} = \frac{C_0}{r^2}\left\{-\sum_{n=1}^{\infty}[(\delta_n r\xi_r - 1)\exp\{\delta_n r\xi_r\} + 1]\left[\frac{6}{\delta_n^5}\left(\frac{1-z^2}{2}\right)\right]\right\} \tag{B3.20}$$

The above steps have made use of the straightforward substitution $E_n F_n = \left[(-1)^{n-1}\frac{2}{\delta_n^3}\right]\left[(-1)^{n-1}\frac{3}{\delta_n}\right] = \frac{6}{\delta_n^4}$, and the identity $\sum_{n=1}^{\infty} E_n F_n = 1$. Brief derivations of these identities are given in Appendix B4.

The velocity components with terms collected and simplified are expressed below:

$$V_{\theta,1} = -\frac{C_0}{r^2}\sum_{n=1}^{\infty}\frac{6}{\delta_n^5}[(\delta_n r\xi_r - 1)\exp\{\delta_n r\xi_r\} + 1]\left(\frac{1-z^2}{2}\right) \tag{B3.21}$$

$$V_{z,0} = -\frac{C_0}{r^2}\sum_{n=1}^{\infty}\delta_n r\xi_r \exp\{\delta_n r\xi_r\}\left[\frac{E_n}{\delta_n}\sin(\delta_n z) - \frac{6}{\delta_n^4}\left(\frac{3z - z^3}{6}\right)\right] \tag{B3.22}$$

It should be noted that $V_{z,1}$ does not appear in the $\mathcal{O}(\alpha)$ equations, suggesting that $V_{z,1}$ is smaller than $\mathcal{O}(\alpha)$. If the analysis was extended to higher-order corrections, it would be found that the $\mathcal{O}(\alpha^2)$ equations must be considered to determine $V_{z,1}$.

B4 A Useful Infinite Summation Identity Involving Odd Multiples of π/2

Here, the summation of $E_n F_n = \frac{6}{\delta_n^4}$ for all positive integers n will be evaluated, where $E_n = 2\frac{(-1)^{n-1}}{(\delta_n)^3}$, and $F_n = 3\frac{(-1)^{n-1}}{\delta_n}$, and $\delta_n = \frac{2n-1}{2}\pi$. First, the following identity is considered, were z is real:

$$\int_{-1}^{1}\left\{E_n \cos(\delta_n z) - \frac{6}{\delta_n^4}\left(\frac{1-z^2}{2}\right)\right\}dz = 0 \tag{B4.3}$$

Next, the summation of $\int_{-1}^{1}\left\{E_n \cos(\delta_n z) - \frac{6}{\delta_n^4}\left(\frac{1-z^2}{2}\right)\right\}dz$ over all positive integers n can be rearranged as follows:

$$\sum_{n=1}^{\infty}\int_{-1}^{1}\left\{E_n \cos(\delta_n z) - \frac{6}{\delta_n^4}\left(\frac{1-z^2}{2}\right)\right\}dz$$

$$= \int_{-1}^{1}\left\{\sum_{n=1}^{\infty} E_n \cos(\delta_n z)\right\}dz - \int_{-1}^{1}\left\{\sum_{n=1}^{\infty}\left(\frac{6}{\delta_n^4}\right)\right\}\left(\frac{1-z^2}{2}\right)dz \tag{B4.4}$$

$$= \left\{\int_{-1}^{1}\left(\frac{1-z^2}{2}\right)dz\right\}\cdot\left\{1 - \sum_{n=1}^{\infty}\left(\frac{6}{\delta_n^4}\right)\right\}$$

$$= \frac{2}{3}\left(1 - \sum_{n=1}^{\infty}\left(\frac{6}{\delta_n^4}\right)\right)$$

From Equation (B4.1), this quantity is known to be zero. Thus, the following may be inferred.

$$\sum_{n=1}^{\infty}\frac{6}{\delta_n^4} = 1 \tag{B4.5}$$

B5 Matching of Inner and Outer Velocities for Single-Fluid Case

In this section, intermediate steps for the matching procedure in Section 5.7 are provided, with numbering and naming conventions preserved from that section. Additionally, the formality of matching for the pressure field has been forgone, since the governing equations in Section 5.4 imply that the outer pressure is imposed upon the inner region.

First, it is helpful to define an intermediate variable $\zeta_r \equiv (\theta - \theta_r)/\psi(\alpha)$, where $\lim_{\alpha\to 0}\big(\psi(\alpha)\big) = 0$ and $\lim_{\alpha\to 0}(\alpha/\psi(\alpha)) = 0$. For moderate ζ_r, both $\vec{U}$ and $\vec{V}$ are valid. This can be formalized as follows:

$$\lim_{\alpha\to 0}\left\{\vec{U}(\theta = \psi(\alpha)\zeta_r + \theta_H)\right\} = \lim_{\alpha\to 0}\left\{\vec{V}(\xi_r = \alpha^{-1}\psi(\alpha)\zeta_r)\right\} \tag{B5.1}$$

The expression above must be satisfied for each set of terms that are of the same order. The standard matching procedure consists of the following three steps. First, components of $\vec{U}$ and $\vec{V}$ are expressed in terms of the intermediate variable, ζ_r. Next, terms in $\vec{U}$ that are of the same order with respect to α (for example, all $\mathcal{O}(1)$ terms or all $\mathcal{O}(\alpha)$ terms) are set equal to the sum of terms that appear in $\vec{V}$ that are of the same order. This produces a series of equations that must be satisfied as $\alpha \to 0$. Finally, unknown constants are determined such that each equation developed in step 2 is satisfied in the limit that $\alpha \to 0$. The results for each of these steps are presented below for each component in the velocity field.

B5.1 Matching of $\boldsymbol{r}$-velocity Terms

The r-velocity components are expressed in terms of intermediate variables as follows:

$$\begin{aligned} U_r(\theta = \psi(\alpha)\zeta_r + \theta_H) \\ &= -\frac{C_0}{r}\left(\frac{1-z^2}{2}\right) \\ &-\frac{\alpha}{r}\left\{D_0 + \sum_{n=1}^{\infty} n\left(D_{n,1}r^{-n} + D_{n,2}r^{n}\right)\cos(n\psi(\alpha)\zeta_r + n\theta_H)\right\}\left(\frac{1-z^2}{2}\right) \\ &+ \mathcal{O}(\alpha^2) \end{aligned} \tag{B5.2}$$

$$
\begin{aligned}
&V_r(\xi_r = \alpha^{-1}\psi(\alpha)\zeta_r) \\
&\quad = -\frac{C_0}{r}\left(\frac{1-z^2}{2}\right) + \frac{C_0}{r}\sum_{n=1}^{\infty} E_n \exp\{\delta_n r\psi(\alpha)\alpha^{-1}\zeta_r\}\cos(\delta_n z) \\
&\quad -\frac{\alpha}{r}\left\{D_0 - \sum_{n=1}^{\infty} n\left(D_{n,1}r^{-n} + D_{n,2}r^{n}\right)\cos(n\theta_H)\right\} \\
&\quad \cdot\left\{\sum_{n=1}^{\infty} E_n \exp\{\delta_n r\alpha^{-1}\psi(\alpha)\}\cos(\delta_n z) - \frac{(1-z^2)}{2}\right\} + \mathcal{O}(\alpha^2)
\end{aligned}
\tag{B5.3}
$$

In the limit that $\alpha \to 0$, and with $\zeta_r < 0$, setting the order $\mathcal{O}(1)$ terms of the inner velocity equal to order $\mathcal{O}(1)$ terms of the outer velocity gives:

$$
-\frac{C_0}{r}\left(\frac{1-z^2}{2}\right) = -\frac{C_0}{r}\left(\frac{1-z^2}{2}\right) + \frac{C_0}{r}\sum_{n=1}^{\infty} E_n \exp\{-\infty\}\cos(\delta_n z) \tag{B5.4}
$$

Thus, matching for $\mathcal{O}(1)$ has already been satisfied. Next, repeating the steps above for $\mathcal{O}(\alpha)$ terms gives the following:

$$-\frac{\alpha}{r}\left\{D_0-\sum_{n=1}^{\infty}n\left(D_{n,1}r^{-n}+D_{n,2}r^{n}\right)\cos(0+n\theta_H)\right\}\left(\frac{1-z^2}{2}\right)$$

$$=-\frac{\alpha}{r}\left\{D_0-\sum_{n=1}^{\infty}n\left(D_{n,1}r^{-n}+D_{n,2}r^{n}\right)\cos(n\theta_H)\right\} \tag{B5.5}$$

$$\cdot\left\{\sum_{n=1}^{\infty}E_n\exp\{-\infty\}\cos(\delta_n z)-\left(\frac{1-z^2}{2}\right)\right\}$$

Thus, matching for $\mathcal{O}(\alpha)$ terms has also already been satisfied. The values of D_0, $D_{n,1}$ and $D_{n,2}$ are still undetermined.

B5.2 Matching of $\boldsymbol{\theta}$-velocity Terms

The θ-velocity components are expressed in terms of intermediate variables as follows:

$$U_\theta(\theta=\psi(\alpha)\zeta_r+\theta_H)$$

$$=\frac{\alpha}{r}\left\{\sum_{n=1}^{\infty}n\left(-D_{n,1}r^{-n}+D_{n,2}r^{n}\right)\sin(n\psi(\alpha)\zeta_r+n\theta_H)\right\}\left(\frac{1-z^2}{2}\right) \tag{B5.6}$$

$$V_\theta(\xi_r = \alpha^{-1}\psi(\alpha)\zeta_r)$$

$$= -\alpha\frac{C_0}{r^2}\left(\frac{1-z^2}{2}\right)\sum_{n=1}^{\infty}\frac{6}{\delta_n^5}[(\delta_n r\psi(\alpha)\alpha^{-1}\zeta_r$$

$$-1)\exp\{\delta_n r\psi(\alpha)\alpha^{-1}\zeta_r\}+1] \tag{B5.7}$$

$$= -\frac{C_0}{r^2}\left(\frac{1-z^2}{2}\right)\sum_{n=1}^{\infty}\frac{6}{\delta_n^5}[(\delta_n r\psi(\alpha)\zeta_r-\alpha)\exp\{\delta_n r\psi(\alpha)\alpha^{-1}\zeta_r\}$$

$$+\alpha]$$

There are no $\mathcal{O}(1)$ terms that need matching. In the limit that $\alpha \to 0$, and with $\zeta_r < 0$, setting the order $\mathcal{O}(1)$ terms of the inner velocity equal to order $\mathcal{O}\big(\psi(\alpha)\big)$ terms of the outer velocity gives:

$$0 = -\frac{C_0}{r^2}\left(\frac{1-z^2}{2}\right)\sum_{n=1}^{\infty}\frac{6}{\delta_n^5}(\delta_n r\zeta_r)\exp\{-\infty\} \tag{B5.8}$$

Matching is already satisfied for $\mathcal{O}\big(\psi(\alpha)\big)$ due to the presence of $\exp\{-\infty\}$ terms. Next, for $\mathcal{O}(\alpha)$, matching follows the following equivalence:

$$\frac{1}{r}\left\{\sum_{n=1}^{\infty}n\big(-D_{n,1}r^{-n}+D_{n,2}r^{n}\big)\sin(0+n\theta_H)\right\}\frac{(1-z^2)}{2}$$

$$= -\frac{C_0}{r^2}\left(\frac{1-z^2}{2}\right)\sum_{n=1}^{\infty}\frac{6}{\delta_n^5}[1-\exp\{-\infty\}] \tag{B5.9}$$

This implies that $D_{n,2} = 0$ for all $n \neq 1$, and that $D_{n,2} = 0$ for all n. It is now possible to determine the value of $D_{1,1}$ as follows:

$$-\frac{D_{1,1}}{r^2}\sin(\theta_H)\frac{(1-z^2)}{2} = -\frac{C_0}{r^2}\left(\frac{1-z^2}{2}\right)\sum_{n=1}^{\infty}\frac{6}{\delta_n^5} \tag{B5.10}$$

Thus, $D_{1,1} = \frac{C_0}{\sin(\theta_H)}\sum_{n=1}^{\infty}\frac{6}{\delta_n^5}$.

B5.3 Matching of $\boldsymbol{z}$-velocity Terms

The z-velocity components are expressed in terms of intermediate variables as follows:

$$U_z(\theta = \psi(\alpha)\zeta_r + \theta_H) = 0 + \mathcal{O}(\alpha^2) \tag{B5.11}$$

$$\begin{aligned} V_z(\xi_r = \alpha^{-1}\psi(\alpha)\zeta_r) \\ &= -\frac{C_0}{r^2}\sum_{n=1}^{\infty}\Bigg(H_3 \\ &+ \frac{1}{\delta_n}\Bigg)\delta_n^2 r\alpha^{-1}\psi(\alpha)\zeta_r \exp\{\delta_n r\alpha^{-1}\psi(\alpha)\zeta_r\}\left[\frac{E_n}{\delta_n}\sin(\delta_n z)\right. \\ &\left. -\frac{6}{\delta_n^4}\left(\frac{3z-z^3}{6}\right)\right] + \mathcal{O}(\alpha^2) \end{aligned} \tag{B5.12}$$

Interestingly, there are $\mathcal{O}\left(\alpha^{-1}\psi(\alpha)\right)$ terms in the inner solution. However, due to the presence of the $\exp\{\delta_n r\alpha^{-1}\psi(\alpha)\zeta_r\}$ terms, these decay to zero in the outer region:

$$\lim_{\alpha\to 0}\{V_z(\xi_r = \alpha^{-1}\psi(\alpha)\zeta_r)\}$$

$$= -\frac{C_0}{r^2}\sum_{n=1}^{\infty}(H_3\delta_n^2 + \delta_n)r\zeta_r \exp\{-\infty\}\left[\frac{E_n}{\delta_n}\sin(\delta_n z)\right.$$

$$\left. -\frac{6}{\delta_n^4}\left(\frac{3z - z^3}{6}\right)\right] \tag{B5.13}$$

$$= -\frac{C_0}{r^2}\sum_{n=1}^{\infty}(H_3\delta_n^2 + \delta_n)r\zeta_r\{0\}\left[\frac{E_n}{\delta_n}\sin(\delta_n z) - \frac{6}{\delta_n^4}\left(\frac{3z - z^3}{6}\right)\right]$$

Thus, matching for the z-velocity components has already been satisfied.

B6 Subtraction of Overlap for Single-Fluid Case

This section provides some intermediate steps for the subtraction of overlap mentioned in Section 5.7. Subsequently, the composite solution is expressed in terms of θ and simplified to a reasonable degree. The numbering and naming conventions here are the same as in Section 5.7.

B4.1. r-Velocity Terms

$$u_{r,0} = U_{r,0} + V_{r,0} + W_{r,0} - \lim_{\alpha\to 0}\{U_{r,0}(\theta = \psi(\alpha)\zeta_r + \theta_H)\} - \lim_{\alpha\to 0}\{U_{r,0}(\theta = \psi(\alpha)\zeta_r - \theta_H)\} \tag{B6.1}$$

$$= \frac{C_0}{r}\sum_{n=1}^{\infty} E_n \exp\{\delta_n r\xi_r\}\cos(\delta_n z) + \frac{C_0}{r}\sum_{n=1}^{\infty} E_n \exp\{-\delta_n r\xi_l\}\cos(\delta_n z) - \frac{C_0}{r}\left(\frac{1-z^2}{2}\right)$$

$$= \frac{C_0}{r}\sum_{n=1}^{\infty} E_n \exp\left\{\delta_n r\frac{\theta}{\alpha}\right\}\exp\left\{-\delta_n r\frac{\theta_H}{\alpha}\right\}\cos(\delta_n z) + \frac{C_0}{r}\sum_{n=1}^{\infty} E_n \exp\left\{-\delta_n r\frac{\theta}{\alpha}\right\}\exp\left\{-\delta_n r\frac{\theta_H}{\alpha}\right\}\cos(\delta_n z) - \frac{C_0}{r}\left(\frac{1-z^2}{2}\right)$$

$$= 2\frac{C_0}{r}\sum_{n=1}^{\infty} E_n \exp\left\{-\delta_n r\frac{\theta_H}{\alpha}\right\}\cosh\left\{\delta_n r\frac{\theta}{\alpha}\right\}\cos(\delta_n z) - \frac{C_0}{r}\left(\frac{1-z^2}{2}\right)$$

$$u_{r,1} = U_{r,1} + V_{r,1} + W_{r,1} - \lim_{\alpha\to 0}\{U_{r,1}(\theta = \psi(\alpha)\zeta_r + \theta_H)\} - \lim_{\alpha\to 0}\{U_{r,1}(\theta = \psi(\alpha)\zeta_r - \theta_H)\}$$

$$\begin{aligned} &= -\left\{\frac{D_0}{r} + \frac{D_{1,1}}{r^2}\cos(\theta)\right\}\left(\frac{1-z^2}{2}\right) + \left\{\frac{D_0}{r} + \frac{D_{1,1}}{r^2}\cos(\theta_H)\right\}\cdot \\ &\quad \left\{\sum_{n=1}^{\infty} E_n \exp\{\delta_n r\xi_r\}\cos(\delta_n z) - \left(\frac{1-z^2}{2}\right)\right\} + \left\{\frac{D_0}{r} + \frac{D_{1,1}}{r^2}\cos(-\theta_H)\right\}\cdot \\ &\quad \left\{\sum_{n=1}^{\infty} E_n \exp\{-\delta_n r\xi_l\}\cos(\delta_n z) - \left(\frac{1-z^2}{2}\right)\right\} + \left\{\frac{D_0}{r} + \right. \\ &\quad \left.\frac{D_{1,1}}{r^2}\cos(\theta_H)\right\}\left(\frac{1-z^2}{2}\right) + \left\{\frac{D_0}{r} + \frac{D_{1,1}}{r^2}\cos(-\theta_H)\right\}\left(\frac{1-z^2}{2}\right) \end{aligned} \quad \text{(B6.2)}$$

$$= -\left\{\frac{D_0}{r} + \frac{D_{1,1}}{r^2}\cos(\theta)\right\}\left(\frac{1-z^2}{2}\right) + \left\{\frac{D_0}{r} + \frac{D_{1,1}}{r^2}\cos(\theta_H)\right\} \cdot$$

$$\{\sum_{n=1}^{\infty} E_n \exp\{\delta_n r\xi_r\}\cos(\delta_n z)\} + \left\{\frac{D_0}{r} + \frac{D_{1,1}}{r^2}\cos(-\theta_H)\right\} \cdot$$

$$\{\sum_{n=1}^{\infty} E_n \exp\{-\delta_n r\xi_l\}\cos(\delta_n z)\}$$

$$= -\left\{\frac{D_0}{r} + \frac{D_{1,1}}{r^2}\cos(\theta)\right\}\left(\frac{1-z^2}{2}\right) + \left\{\frac{D_0}{r} + \frac{D_{1,1}}{r^2}\cos(\theta_H)\right\} \cdot$$

$$\left\{2\sum_{n=1}^{\infty} E_n \exp\left\{-\delta_n r\frac{\theta_H}{\alpha}\right\}\cosh\left\{\delta_n r\frac{\theta}{\alpha}\right\}\cos(\delta_n z)\right\}$$

$$u_{r,0} + \alpha u_{r,1} = \left(\frac{C_0}{r} + \alpha\frac{D_0}{r}\right) \cdot \left\{2\sum_{n=1}^{\infty} E_n \exp\left\{-\delta_n r\frac{\theta_H}{\alpha}\right\}\cosh\left\{\delta_n r\frac{\theta}{\alpha}\right\}\cos(\delta_n z) - \left(\frac{1-z^2}{2}\right)\right\} + \left(\alpha\frac{C_0}{r^2}\cot(\theta_H)\sum_{n=1}^{\infty}\frac{6}{\delta_n^5}\right) \cdot \left\{2\sum_{n=1}^{\infty} E_n \exp\left\{-\delta_n r\frac{\theta_H}{\alpha}\right\}\cosh\left\{\delta_n r\frac{\theta}{\alpha}\right\}\cos(\delta_n z) - \left(\frac{\cos(\theta)}{\cos(\theta_H)}\right)\left(\frac{1-z^2}{2}\right)\right\} \quad \text{(B6.3)}$$

B4.2. θ-Velocity Terms

$$u_{\theta,1} = U_{\theta,1} + V_{\theta,1} + W_{\theta,1} - \lim_{\alpha\to 0}\{U_{\theta,1}(\theta = \psi(\alpha)\zeta_r + \theta_H)\} - \lim_{\alpha\to 0}\{U_{\theta,1}(\theta = \psi(\alpha)\zeta_r - \theta_H)\} \quad \text{(B6.4)}$$

$$= -\frac{D_{1,1}}{r^2}\sin(\theta)\left(\frac{1-z^2}{2}\right) - \frac{C_0}{r^2}\left(\frac{1-z^2}{2}\right)\sum_{n=1}^{\infty}\frac{6}{\delta_n^5}\left[(\delta_n r\xi_r - 1)\exp\{\delta_n r\xi_r\} + 1\right] -$$

$$\frac{C_0}{r^2}\left(\frac{1-z^2}{2}\right)\sum_{n=1}^{\infty}\frac{6}{\delta_n^5}\left[(\delta_n r\xi_l + 1)\exp\{-\delta_n r\xi_l\} - 1\right] +$$

$$\frac{D_{1,1}}{r^2}\sin(\theta_H)\left(\frac{1-z^2}{2}\right) + \frac{D_{1,1}}{r^2}\sin(-\theta_H)\left(\frac{1-z^2}{2}\right)$$

$$= -\frac{C_0}{r^2}\frac{\sin(\theta)}{\sin(\theta_H)}\left(\frac{1-z^2}{2}\right)\sum_{n=1}^{\infty}\frac{6}{\delta_n^5} - \frac{C_0}{r^2}\left(\frac{1-z^2}{2}\right)\sum_{n=1}^{\infty}\frac{6}{\delta_n^5}\left[(\delta_n r\xi_r - 1)\exp\{\delta_n r\xi_r\}\right] -$$

$$\frac{C_0}{r^2}\left(\frac{1-z^2}{2}\right)\sum_{n=1}^{\infty}\frac{6}{\delta_n^5}\left[(\delta_n r\xi_l + 1)\exp\{-\delta_n r\xi_l\}\right]$$

$$= -\frac{C_0}{r^2}\left(\frac{1-z^2}{2}\right)\sum_{n=1}^{\infty}\frac{6}{\delta_n^5}\left\{\frac{\sin(\theta)}{\sin(\theta_H)} + (\delta_n r\xi_r - 1)\exp\{\delta_n r\xi_r\} + (\delta_n r\xi_l +\right.$$

$$\left. 1)\exp\{-\delta_n r\xi_l\}\right\}$$

$$= -\frac{C_0}{r^2}\left(\frac{1-z^2}{2}\right)\sum_{n=1}^{\infty}\frac{6}{\delta_n^5}\left\{\frac{\sin(\theta)}{\sin(\theta_H)} + \left[\delta_n\frac{r(\theta-\theta_H)}{\alpha} - 1\right]\exp\{\delta_n r\xi_r\} + \left[\delta_n\frac{r(\theta+\theta_H)}{\alpha} +\right.\right.$$

$$\left.\left. 1\right]\exp\{-\delta_n r\xi_l\}\right\}$$

$$= -\frac{C_0}{r^2}\left(\frac{1-z^2}{2}\right)\sum_{n=1}^{\infty}\frac{6}{\delta_n^5}\left\{\frac{\sin(\theta)}{\sin(\theta_H)} + \exp\left\{-\delta_n\frac{r\theta_H}{\alpha}\right\}\left[2\left(\delta_n\frac{r\theta}{\alpha}\right)\cosh\left\{\delta_n\frac{r\theta}{\alpha}\right\} -\right.\right.$$

$$\left.\left.2\left(1 + \delta_n\frac{r\theta_H}{\alpha}\right)\sinh\left\{\delta_n\frac{r\theta}{\alpha}\right\}\right]\right\}$$

B4.3. z-Velocity Terms

$$u_{z,0} = U_{z,0} + V_{z,0} + W_{z,0} - \lim_{\alpha\to 0}\{U_{z,0}(\theta = \psi(\alpha)\zeta_r + \theta_H)\} - \lim_{\alpha\to 0}\{U_{z,0}(\theta = \psi(\alpha)\zeta_r - \theta_H)\}$$

$$= 0 - \frac{C_0}{r^2}\sum_{n=1}^{\infty}\delta_n r\xi_r \exp\{\delta_n r\xi_r\}\left[\frac{E_n}{\delta_n}\sin(\delta_n z) - \frac{6}{\delta_n^4}\left(\frac{3z-z^3}{6}\right)\right] + \frac{C_0}{r^2}\sum_{n=1}^{\infty}\delta_n r\xi_l \exp\{-\delta_n r\xi_l\}\left[\frac{E_n}{\delta_n}\sin(\delta_n z) - \frac{6}{\delta_n^4}\left(\frac{3z-z^3}{6}\right)\right]$$

$$= \frac{C_0}{r^2}\sum_{n=1}^{\infty}\delta_n r[\xi_l \exp\{-\delta_n r\xi_l\} - \xi_r \exp\{\delta_n r\xi_r\}]\left[\frac{E_n}{\delta_n}\sin(\delta_n z) - \frac{6}{\delta_n^4}\left(\frac{3z-z^3}{6}\right)\right]$$

$$= \frac{C_0}{r^2}\sum_{n=1}^{\infty}\delta_n r\left[\left(\frac{\theta+\theta_H}{\alpha}\right)\exp\left\{-\delta_n r\left(\frac{\theta+\theta_H}{\alpha}\right)\right\} - \left(\frac{\theta-\theta_H}{\alpha}\right)\exp\left\{\delta_n r\left(\frac{\theta-\theta_H}{\alpha}\right)\right\}\right]\left[\frac{E_n}{\delta_n}\sin(\delta_n z) - \frac{6}{\delta_n^4}\left(\frac{3z-z^3}{6}\right)\right] \quad \text{(B6.5)}$$

$$= \frac{C_0}{\alpha r}\sum_{n=1}^{\infty}\exp\left\{-\delta_n r\frac{\theta_H}{\alpha}\right\}\left[(\theta+\theta_H)\exp\left\{-\delta_n\frac{r\theta}{\alpha}\right\} - (\theta - \theta_H)\exp\left\{\delta_n r\frac{r\theta}{\alpha}\right\}\right]\left[E_n\sin(\delta_n z) - \frac{6}{\delta_n^3}\left(\frac{3z-z^3}{6}\right)\right]$$

$$= 2\frac{C_0}{\alpha r}\sum_{n=1}^{\infty}\exp\left\{-\delta_n\frac{r\theta_H}{\alpha}\right\}\left[\theta_H\cosh\left\{\delta_n\frac{r\theta}{\alpha}\right\} - \theta\sinh\left\{\delta_n\frac{r\theta}{\alpha}\right\}\right]\left[E_n\sin(\delta_n z) - \frac{6}{\delta_n^3}\left(\frac{3z-z^3}{6}\right)\right]$$

B7 Application of Flow Rate Condition for Single-Fluid Case

This section provides some intermediate steps for the application of the flow rate condition for the single-fluid case, whose results are presented in Section 5.7. Subsequently, the composite solution is expressed in terms of θ and simplified to a reasonable degree. The numbering and naming conventions here are the same as in Section 5.7.

The flow rate condition can be expressed as follows:

$$-1 = \int_{-1}^{1}\int_{-\theta_H}^{\theta_H} u_r \, r d\theta dz = 4\int_{0}^{1}\int_{0}^{\theta_H} \left(u_{r,0} + \alpha u_{r,1}\right) r d\theta dz + \mathcal{O}(\alpha^2) \tag{B7.1}$$

Above, the term $\mathcal{O}(\alpha^2)$ denotes flow rate contributions from higher-order terms in the asymptotic expansion of u_r. Neglecting these contributions and substituting expressions for $u_{r,0}$ and $u_{r,1}$ in terms of constant coefficients C_0 and D_0 gives the following:

$$\begin{aligned} -1 = -4\int_{0}^{\theta_H}\int_{0}^{1} &\left[C_0 + \alpha D_0 + \alpha\frac{C_0}{r}\left(\sum_{n=1}^{\infty}\frac{6}{\delta_n^5}\right)\frac{\cos(\theta)}{\sin(\theta_H)}\right]\left(\frac{1-z^2}{2}\right) dz\, d\theta \\ &+ 8\int_{0}^{\theta_H}\int_{0}^{1}\left[C_0 + \alpha D_0 + \alpha\frac{C_0}{r}\left(\sum_{n=1}^{\infty}\frac{6}{\delta_n^5}\right)\cot(\theta_H)\right] \\ &\cdot \sum_{n=1}^{\infty} E_n \exp\left\{-\delta_n\frac{r\theta_H}{\alpha}\right\}\cosh\left\{\delta_n\frac{r\theta}{\alpha}\right\}\cos(\delta_n z)\, dz\, d\theta \end{aligned} \tag{B7.2}$$

Integrating and simplifying the above integral gives:

$$-1 = -\frac{4}{3}\left[(C_0 + \alpha D_0)\theta_H + \alpha\frac{C_0}{r}\sum_{n=1}^{\infty}\frac{6}{\delta_n^5}\right] + \frac{4}{3}\left[C_0 + \alpha D_0 + \alpha\frac{C_0}{r}\sum_{n=1}^{\infty}\frac{6}{\delta_n^5}\cot(\theta_H)\right] \cdot 2\left(\frac{\alpha}{r}\right)\sum_{n=1}^{\infty}\frac{6}{{\delta_n}^5}\exp\left\{-\delta_n\frac{r\theta_H}{\alpha}\right\}\sinh\left\{\delta_n\frac{r\theta_H}{\alpha}\right\} \tag{B7.3}$$

Above, the product of exponential and hyperbolic sine functions under the summation symbol can be simplified as follows:

$$\sum_{n=1}^{\infty}\frac{6}{{\delta_n}^5}\exp\left\{-\delta_n\frac{r\theta_H}{\alpha}\right\}\sinh\left\{\delta_n\frac{r\theta_H}{\alpha}\right\} = \frac{1}{2}\sum_{n=1}^{\infty}\frac{6}{{\delta_n}^5}\left(1-\exp\left\{-2\delta_n\frac{r\theta_H}{\alpha}\right\}\right) \tag{B7.4}$$

For $\alpha \ll 1$, this expression approximates to $\frac{1}{2}\sum_{n=1}^{\infty}\frac{6}{{\delta_n}^5}\left(1-\exp\left\{-2\delta_n\frac{r\theta_H}{\alpha}\right\}\right) \approx \frac{1}{2}\sum_{n=1}^{\infty}\frac{6}{{\delta_n}^5}$. After making this substitution and simplifying, Equation (B7.3) can be expressed as follows:

$$0 = \left[1-\frac{4}{3}(C_0 + \alpha D_0)\theta_H\right] + \frac{4}{3}\left(\frac{\alpha^2}{r^2}\right)\left[rD_0 + C_0\cot(\theta_H)\left(\sum_{n=1}^{\infty}\frac{6}{{\delta_n}^5}\right)\right]\left(\sum_{n=1}^{\infty}\frac{6}{{\delta_n}^5}\right) \tag{B7.5}$$

At first glance, it appears that no choice of C_0 and D_0 will satisfy Equation (B7.5) for all r. To resolve this issue, it should be noted that only the first term in Equation (B7.5) is greater than $\mathcal{O}(\alpha^2)$. Any C_0 and D_0 that satisfy the following relation are sufficient to enforce the flow rate condition to order $\mathcal{O}(\alpha)$:

$$C_0 + \alpha D_0 = \frac{4}{3\theta_H} \tag{B7.6}$$

Next, the second term in Equation (B7.5) can be examined. In physical terms, this represents an $\mathcal{O}(\alpha^2)$ flow rate contribution balanced by higher-order terms in the asymptotic expansion. To enforce the flow rate condition exactly without knowledge of these higher-order terms, it is permissible to temporarily relax the constraint that C_0 and D_0 are constants. This provides the following relation:

$$0 = rD_0 + C_0 \cot(\theta_H)\left(\sum_{n=1}^{\infty} \frac{6}{{\delta_n}^5}\right) \tag{B7.7}$$

Together, Equation (B7.6) and Equation (B7.7) provides the following definition for C_0:

$$C_0 = \frac{4}{3\theta_H}\left[1 - \frac{\alpha}{r}\cot(\theta_H)\left(\sum_{n=1}^{\infty} \frac{6}{{\delta_n}^5}\right)\right]^{-1} \tag{B7.8}$$

This form implies that C_0 does, in fact, approximate to a constant value for $\frac{\alpha}{r} \ll 1$. However, near the outflow boundary for sufficiently large α, the influence of the walls at $\theta = \pm\theta_H$ are sufficiently great to require an $\mathcal{O}\left(\frac{\alpha}{r}\right)$ correction to velocity terms involving the coefficient C_0. It is also notable that D_0 does not appear alone in any of the $\mathcal{O}(1)$ or $\mathcal{O}(\alpha)$ velocity components. Rather, it appears in the term $C_0 + \alpha D_0$, which has previously been shown to be constant.

APPENDIX C. MATHEMATICAL DERIVATIONS FOR TWO-FLUID INTERNAL FLOW ANALYSIS

The purpose of this appendix is to provide mathematical derivations and clarifying intermediate steps for the perturbation analysis of co-laminar flow through a converging rectangular slot in Chapter 6. The content of the following sections has been provided for the benefit and scrutiny of interested readers. The notation here is consistent with the main manuscript.

C1 Determination of Constant Coefficients that Appear in θ-Axis Inner Velocity Components for Two-material Case

This section provides intermediate calculations for the determination of constant coefficients appearing in the expressions for inner velocity θ-components in Section 6.6. The naming and numbering conventions, as well as the definitions of coefficient terms, are retained from the end of Section 6.6.

The θ-components of inner velocity at an interior fluid boundary defined by $\theta = \theta_S(r, \theta_i)$ are expressed as follows:

$$V_{\theta i} = -\alpha \frac{A_0}{r^2} CI_{1,i} \sum_{n=1}^{\infty} \frac{6}{\delta_n^5} \left[(\delta_n r \xi_i - 1) \exp\{\delta_n r \xi_i\} + DI_{1,i} \right] \left(\frac{1 - z^2}{2} \right) + \mathcal{O}(\alpha^2) \qquad \text{(C1.1)}$$

$$W_{\theta i} = -\alpha \frac{A_0}{r^2} CI_{2,i} \sum_{n=1}^{\infty} \frac{6}{\delta_n^5} \left[(\delta_n r \xi_i + 1) \exp\{-\delta_n r \xi_i\} - DI_{2,i} \right] \left(\frac{1 - z^2}{2} \right) + \mathcal{O}(\alpha^2) \quad \text{(C1.2)}$$

Above, $CI_{1,i}$, $CI_{2,i}$, $DI_{1,i}$, and $DI_{2,i}$ are constant coefficients that will be determined here. First, continuity of velocity across the interface requires that $V_{ri}|_{\theta=\theta_S(r,\theta_i)} = W_{ri}|_{\theta=\theta_S(r,\theta_i)}$. Evaluating both velocity components at the interface, with order $\mathcal{O}(\alpha^2)$ terms neglected, elucidates the following relationship between the two constants:

$$CI_{1,i}\left(DI_{1,i} - 1\right) = CI_{2,i}\left(1 - DI_{2,i}\right) \quad \text{(C1.3)}$$

For $2 \leq i \leq 2N$

Additionally, the no-flux condition at $\theta = \pm\theta_H$ imposes the following:

$$DI_{1,2N+1} = DI_{2,1} = 1 \quad \text{(C1.4)}$$

Next, the necessity of matching between the inner and outer expansions must be addressed. The θ-component of outer velocity in the region bounded by $\theta = \theta_S(r, \theta_i)$ and $\theta = \theta_S(r, \theta_{i+1})$ are expressed as follows:

$$U_{\theta i} = -\left(\frac{\mu_{A+B}}{\mu_i}\right) \left(\alpha \frac{A_0}{r^2} \frac{\sin(\theta)}{\sin(\theta_H)} \sum_{n=1}^{\infty} \frac{6}{\delta_n^5} \right) \left(\frac{1 - z^2}{2r} \right) + \mathcal{O}(\alpha^2) \quad \text{(C1.5)}$$

Equating inner and outer velocities near interior boundaries at $\theta = \theta_S(r, \theta_i)$ gives the following:

$$CI_{1,i} = \left(\frac{\mu_{A+B}}{\mu_i}\right)\left(\frac{\sin\left(\theta_S(r,\theta_i)\right)}{DI_{1,i}\sin(\theta_H)}\right) \tag{C1.6}$$

$$CI_{2,i} = -\left(\frac{\mu_{A+B}}{\mu_{(i-1)}}\right)\left(\frac{\sin\left(\theta_S(r,\theta_i)\right)}{DI_{2,i}\sin(\theta_H)}\right) \tag{C1.7}$$

One additional relation is required to determine precise definitions for $DI_{1,i}$ and $DI_{2,i}$. Following the discussion in Section 6.4, the shapes of the streamlines defining the fluid boundary at $\theta = \theta_S(r, \theta_i)$ can be expressed in terms of inner velocity components, as follows:

$$\frac{\partial}{\partial r}\{\theta_S(r,\theta_i)\} = \frac{V_{\theta i}|_{\theta=\theta_S(r,\theta_i)}}{V_{ri}|_{\theta=\theta_S(r,\theta_i)}} = \frac{W_{\theta i}|_{\theta=\theta_S(r,\theta_i)}}{W_{ri}|_{\theta=\theta_S(r,\theta_i)}} \tag{C1.8}$$

To exploit this knowledge, the inner velocity components must first be evaluated at the interior fluid boundary and subsequently substituted into Equation (C1.8). The r-velocity components are reiterated below:

$$V_{ri}|_{\theta=\theta_S(r,\theta_i)} = -\left[\left(\frac{A_0}{r} + \alpha\frac{B_0}{r}\right) + \left(\frac{\alpha}{r}\right)\frac{A_0\cos\left(\theta_S(r,\theta_i)\right)}{r\sin(\theta_H)}\sum_{n=1}^{\infty}\frac{6}{\delta_n^5}\right]\left(\frac{1-z^2}{2}\right) + \mathcal{O}(\alpha^2) \tag{C1.9}$$

$$W_{ri}|_{\theta=\theta_S(r,\theta_i)} = -\left[\left(\frac{A_0}{r}+\alpha\frac{B_0}{r}\right)+\left(\frac{\alpha}{r}\right)\frac{A_0\cos\left(\theta_S(r,\theta_i)\right)}{r\sin(\theta_H)}\sum_{n=1}^{\infty}\frac{6}{\delta_n^5}\right]\left(\frac{1-z^2}{2}\right) + \mathcal{O}(\alpha^2) \tag{C1.10}$$

Here, it should be noted that $(A_0+\alpha B_0)A_0^{-1} = \frac{2}{(2N+1)}\left[1-\left(\frac{\alpha}{r}\right)\left(\sum_{n=1}^{\infty}\frac{6}{\delta_n^5}\right)\sum_{i=1}^{2N+1}\frac{\cos(\theta_i)}{2\sin(\theta_H)}\right]$. Next, substituting the velocity components into Equation (C1.8) provides the following:

$$\frac{V_{\theta i}|_{\theta=\theta_S(r,\theta_i)}}{V_{ri}|_{\theta=\theta_S(r,\theta_i)}} = \frac{\frac{\alpha}{r}CI_{1,i}\left(\sum_{n=1}^{\infty}\frac{6}{\delta_n^5}\right)\left(DI_{1,i}-1\right)}{\frac{2\left(1-A_{0,err}\right)}{(2N+1)}+\frac{\alpha}{r}\frac{\cos\left(\theta_S(r,\theta_i)\right)}{\sin(\theta_H)}\sum_{n=1}^{\infty}\frac{6}{\delta_n^5}} \tag{C1.11}$$

$$\frac{W_{\theta i}|_{\theta=\theta_S(r,\theta_i)}}{W_{ri}|_{\theta=\theta_S(r,\theta_i)}} = \frac{\frac{\alpha}{r}CI_{2,i}\left(\sum_{n=1}^{\infty}\frac{6}{\delta_n^5}\right)\left(1-DI_{2,i}\right)}{\frac{2\left(1-A_{0,err}\right)}{(2N+1)}+\frac{\alpha}{r}\frac{\cos\left(\theta_S(r,\theta_i)\right)}{\sin(\theta_H)}\sum_{n=1}^{\infty}\frac{6}{\delta_n^5}} \tag{C1.12}$$

Substituting previously determined relationships between $CI_{1,i}$, $CI_{2,i}$, $DI_{1,i}$, and $DI_{2,i}$ allows Equations (C1.11) and (C1.12) to be expressed in terms of just one of these constant coefficients:

$$\frac{\partial}{\partial r}\{\theta_S(r,\theta_i)\} = \frac{\frac{\alpha}{r}\left(\frac{\mu_{A+B}}{\mu_i}\right)\left(\frac{\sin\left(\theta_S(r,\theta_i)\right)}{\sin(\theta_H)}\right)\left(\sum_{n=1}^{\infty}\frac{6}{\delta_n^5}\right)\left(1-DI_{1,i}^{-1}\right)}{\frac{2\left(1-A_{0,err}\right)}{(2N+1)}+\frac{\alpha}{r}\frac{\cos\left(\theta_S(r,\theta_i)\right)}{\sin(\theta_H)}\sum_{n=1}^{\infty}\frac{6}{\delta_n^5}} \tag{C1.13}$$

Finally, to determine $\frac{\partial}{\partial r}\{\theta_S(r,\theta_i)\}$, one may refer to the previously determined expression for streamline shapes, reiterated below:

$$\begin{aligned}
&\theta_S(r,\theta_{i+1}) \\
&= \theta_S(r,\theta_i) + \frac{2\theta_H}{N}\left(\frac{\mu_i Q_i}{\mu_A Q_A + \mu_B Q_B}\right) \\
&+ \left(\frac{\alpha}{r}\right)\left\{2\left(\frac{\mu_{(i+1)}}{\mu_{A+B}}\right)\right. \\
&\left. - \left(\frac{2N+1}{1-A_{0,err}}\right)\left[\frac{\sin\left(\theta_S(r,\theta_{i+1})\right)-\sin\left(\theta_S(r,\theta_i)\right)}{2\sin(\theta_H)}\right]\right\}\left(\sum_{n=1}^{\infty}\frac{6}{\delta_n^5}\right) \\
&+ \left(\frac{\alpha}{r}\right)^2\left(\frac{2N+1}{1-A_{0,err}}\right)\left(\frac{\mu_{(i+1)}}{\mu_{A+B}}\right)\left[\frac{\cos\left(\theta_S(r,\theta_{i+1})\right)+\cos\left(\theta_S(r,\theta_i)\right)}{2\sin(\theta_H)}\right]\left(\sum_{n=1}^{\infty}\frac{6}{\delta_n^5}\right)^2
\end{aligned} \tag{C1.14}$$

for $2 \le i \le 2N$

$$\theta_S(r,\theta_2) = \theta_H + \frac{2\theta_H}{N}\left(\frac{\mu_A Q_A}{\mu_A Q_A + \mu_B Q_B}\right) + \left(\frac{\alpha}{r}\right)\left\{2\left(\frac{\mu_B}{\mu_{A+B}} + \frac{1}{2}\frac{\mu_A}{\mu_{A+B}}\right) - \left(\frac{2N+1}{1-A_{0,err}}\right)\left[\frac{\sin\left(\theta_S(r,\theta_2)\right)}{2\sin(\theta_H)} - \frac{1}{2}\right]\right\}\left(\sum_{n=1}^{\infty}\frac{6}{\delta_n^5}\right) + \left(\frac{\alpha}{r}\right)^2\left(\frac{2N+1}{1-A_{0,err}}\right)\left(\frac{\mu_B}{\mu_{A+B}}\right)\left[\frac{\cos\left(\theta_S(r,\theta_2)\right)}{2\sin(\theta_H)} + \cot(\theta_H)\right]\left(\sum_{n=1}^{\infty}\frac{6}{\delta_n^5}\right)^2 \quad \text{(C1.15)}$$

It is most expedient to solve for $\frac{\partial}{\partial r}\{\theta_S(r,\theta_i)\}$ numerically, iterating from left to right across the channel starting from $\theta_S(r,\theta_2)$. The results can be substituted into Equation (C1.13) to determine the constants $DI_{1,i}$ and $DI_{2,i}$. Subsequently, Equations (C1.6) and (C1.7) can be employed to determine $CI_{1,i}$ and $CI_{2,i}$.

C2 Interfacial Stress Condition for Two-fluid Case

This section provides intermediate calculations for the application of boundary conditions at fluid interfaces from Section 6.6. The naming and numbering conventions, as well as the definitions of coefficient terms, are retained from the end of Section 6.6. For reference, the stress tensor is expressed in terms of order $\mathcal{O}(1)$ and $\mathcal{O}(\alpha)$ terms as follows:

$$\boldsymbol{T}_i = \boldsymbol{T}_{i,0} + \alpha \boldsymbol{T}_{i,1} + \mathcal{O}(\alpha^2) \tag{C2.1}$$

Where:

$$\boldsymbol{T}_{i,0} \equiv \left(\frac{\mu_i}{\mu_{A+B}}\right)\begin{bmatrix} 0 & \frac{1}{r}\frac{\partial u_{ri,0}}{\partial \xi_i} & \frac{\partial u_{ri,0}}{\partial z} \\ \frac{1}{r}\frac{\partial u_{ri,0}}{\partial \xi_i} & 2\left(\frac{1}{r}\frac{\partial u_{\theta i,0}}{\partial \xi_i}\right) & \left(\frac{\partial u_{\theta i,0}}{\partial z} + \frac{1}{r}\frac{\partial u_{zi,0}}{\partial \xi_i}\right) \\ \frac{\partial u_{ri,0}}{\partial z} & \left(\frac{\partial u_{\theta i,0}}{\partial z} + \frac{1}{r}\frac{\partial u_{zi,0}}{\partial \xi_i}\right) & 2\frac{\partial u_{zi,0}}{\partial z} \end{bmatrix} \tag{C2.2}$$

$$\begin{aligned} &\boldsymbol{T}_{i,1} \\ &\equiv -\begin{bmatrix} p_i & 0 & 0 \\ 0 & p_i & 0 \\ 0 & 0 & p_i \end{bmatrix} \\ &+\left(\frac{\mu_i}{\mu_{A+B}}\right)\begin{bmatrix} 2\frac{\partial u_{ri,0}}{\partial r} & \left[r\frac{\partial}{\partial r}\left(\frac{u_{\theta i,0}}{r}\right) + \frac{1}{r}\frac{\partial u_{ri,1}}{\partial \xi_i}\right] & \left(\frac{\partial u_{ri,1}}{\partial z} + \frac{\partial u_{zi,0}}{\partial r}\right) \\ \left[r\frac{\partial}{\partial r}\left(\frac{u_{\theta i,0}}{r}\right) + \frac{1}{r}\frac{\partial u_{ri,1}}{\partial \xi_i}\right] & 2\left(\frac{1}{r}\frac{\partial u_{\theta i,1}}{\partial \xi_i} + \frac{u_{ri,0}}{r}\right) & \left(\frac{\partial u_{\theta i,1}}{\partial z} + \frac{1}{r}\frac{\partial u_{zi,1}}{\partial \xi_i}\right) \\ \left(\frac{\partial u_{ri,1}}{\partial z} + \frac{\partial u_{zi,0}}{\partial r}\right) & \left(\frac{\partial u_{\theta i,1}}{\partial z} + \frac{1}{r}\frac{\partial u_{zi,1}}{\partial \xi_i}\right) & 2\frac{\partial u_{zi,1}}{\partial z} \end{bmatrix} \end{aligned} \tag{C2.3}$$

C2.1 Partial Integrals that Appear in Stress Tensor

Partial integrals of the velocity terms given in (6.18a) and (6.18b), (6.24a) and (6.24b), and (6.26a)-(6.26d), evaluated at the interface located at $\xi_i = 0$, are given below:

$$\left.\frac{\partial V_{ri,0}}{\partial r}\right|_{\xi_i=0} = \left(\frac{\mu_{A+B}}{\mu_{(i-1)}}\right)\frac{A_{0,(i-1)}}{r^2}\left(\frac{1-z^2}{2}\right) - \left[\left(\frac{\mu_{A+B}}{\mu_{(i-1)}}\right)\frac{A_{0,(i-1)}}{r^2} - \frac{AI_i}{r^2}\right]\sum_{n=1}^{\infty} E_n(1)\cos(\delta_n z) = \frac{AI_i}{r^2}\left(\frac{1-z^2}{2}\right) \tag{C2.4}$$

$$\left.\frac{\partial W_{ri,0}}{\partial r}\right|_{\xi_i=0} = \left(\frac{\mu_{A+B}}{\mu_i}\right)\frac{A_{0,i}}{r^2}\left(\frac{1-z^2}{2}\right) - \left[\left(\frac{\mu_{A+B}}{\mu_i}\right)\frac{A_{0,i}}{r^2} - \frac{AI_i}{r^2}\right]\sum_{n=1}^{\infty} E_n(1)\cos(\delta_n z) = \frac{AI_i}{r^2}\left(\frac{1-z^2}{2}\right) \quad \text{(C2.5)}$$

$$\left.\frac{\partial V_{ri,1}}{\partial r}\right|_{\xi_i=0} = \frac{\partial BI_i}{\partial r}\left(\frac{1-z^2}{2}\right) \quad \text{(C2.6)}$$

$$\left.\frac{\partial W_{ri,1}}{\partial r}\right|_{\xi_i=0} = \frac{\partial BI_i}{\partial r}\left(\frac{1-z^2}{2}\right) \quad \text{(C2.7)}$$

$$\left.\frac{\partial V_{\theta i,1}}{\partial \theta}\right|_{\xi_i=0} = \frac{1}{\alpha}\left.\frac{\partial V_{\theta i,1}}{\partial \xi_r}\right|_{\xi_i=0} = -\frac{1}{\alpha r^2}\left[\left(\frac{\mu_{A+B}}{\mu_{(i-1)}}\right)A_{0,(i-1)} - AI_i\right]\sum_{n=1}^{\infty}\frac{6}{\delta_n^3}r(0)^2(1)\left(\frac{1-z^2}{2}\right) = 0 \quad \text{(C2.8)}$$

$$\left.\frac{\partial W_{\theta i,1}}{\partial \theta}\right|_{\xi_i=0} = 0 \quad \text{(C2.9)}$$

$$\left.\left(\frac{V_{ri,0}}{r}\right)\right|_{\xi_i=0} = -\left(\frac{\mu_{A+B}}{\mu_{(i-1)}}\right)\frac{A_{0,(i-1)}}{r^2}\left(\frac{1-z^2}{2}\right) + \left[\left(\frac{\mu_{A+B}}{\mu_{(i-1)}}\right)\frac{A_{0,(i-1)}}{r^2} - \frac{AI_i}{r^2}\right]\sum_{n=1}^{\infty} E_n(1)\cos(\delta_n z) = -\frac{AI_i}{r^2}\left(\frac{1-z^2}{2}\right) \quad \text{(C2.10)}$$

$$\left(\frac{W_{ri,0}}{r}\right)\Big|_{\xi_i=0} = -\left(\frac{\mu_{A+B}}{\mu_i}\right)\frac{A_{0,i}}{r^2}\left(\frac{1-z^2}{2}\right) + \left[\left(\frac{\mu_{A+B}}{\mu_i}\right)\frac{A_{0,i}}{r^2} - \frac{AI_i}{r^2}\right]\sum_{n=1}^{\infty} E_n(1)\cos(\delta_n z) = -\frac{AI_i}{r^2}\left(\frac{1-z^2}{2}\right) \quad \text{(C2.11)}$$

$$\left(\frac{V_{ri,1}}{r}\right)\Big|_{\xi_i=0} = -\frac{\partial BI_i}{\partial r}\left(\frac{1-z^2}{2}\right) \quad \text{(C2.12)}$$

$$\left(\frac{W_{ri,1}}{r}\right)\Big|_{\xi_i=0} = -\frac{\partial BI_i}{\partial r}\left(\frac{1-z^2}{2}\right) \quad \text{(C2.13)}$$

$$\frac{\partial V_{zi,0}}{\partial z}\Big|_{\xi_i=0} = -\left[\left(\frac{\mu_{A+B}}{\mu_{(i-1)}}\right)A_{0,(i-1)} - AI_i\right]\sum_{n=1}^{\infty}\delta_n r(0)(1)\left[E_n\cos(\delta_n z) - \frac{6}{\delta_n^4}\left(\frac{1-z^2}{2}\right)\right] = 0 \quad \text{(C2.14)}$$

$$\frac{\partial W_{zi,0}}{\partial z}\Big|_{\xi_i=0} = 0 \quad \text{(C2.15)}$$

$$r\frac{\partial}{\partial r}\left(\frac{V_{\theta i,1}}{r}\right)\Big|_{\xi_i=0} = \frac{3}{r^3}\left[\left(\frac{\mu_{A+B}}{\mu_{(i-1)}}\right)A_{0,(i-1)} - AI_i\right]\sum_{n=1}^{\infty}\frac{6}{\delta_n^5}[(\delta_n r(0)-1)(1)+1]\left(\frac{1-z^2}{2}\right) - \frac{1}{r^2}\left[\left(\frac{\mu_{A+B}}{\mu_{(i-1)}}\right)A_{0,(i-1)} - AI_i\right]\sum_{n=1}^{\infty}\frac{6}{\delta_n^5}\delta_n^2 r(0)^2(1)\left(\frac{1-z^2}{2}\right) = 0 \quad \text{(C2.16)}$$

$$r\frac{\partial}{\partial r}\left(\frac{V_{\theta i,1}}{r}\right)\Big|_{\xi_i=0} = r\frac{\partial}{\partial r}\left(\frac{W_{\theta i,1}}{r}\right)\Big|_{\xi_i=0} = 0 \quad \text{(C2.17)}$$

$$\frac{1}{r}\frac{\partial V_{ri,0}}{\partial \theta}\Big|_{\xi_i=0} = \left[\left(\frac{\mu_{A+B}}{\mu_{(i-1)}}\right)\frac{A_{0,(i-1)}}{\alpha r} - \frac{AI_i}{\alpha r}\right]\sum_{n=1}^{\infty} E_n\delta_n(1)\cos(\delta_n z) = \frac{1}{\alpha}\left[\left(\frac{\mu_{A+B}}{\mu_{(i-1)}}\right)A_{0,(i-1)} - AI_i\right]\frac{1}{r}\sum_{n=1}^{\infty} E_n\delta_n\cos(\delta_n z) \tag{C2.18}$$

$$\frac{1}{r}\frac{\partial W_{ri,0}}{\partial \theta}\Big|_{\xi_i=0} = \left[\left(\frac{\mu_{A+B}}{\mu_i}\right)\frac{A_{0,i}}{\alpha r} - \frac{AI_i}{\alpha r}\right]\sum_{n=1}^{\infty} -E_n\delta_n(1)\cos(\delta_n z) = -\frac{1}{\alpha}\left[\left(\frac{\mu_{A+B}}{\mu_i}\right)A_{0,i} - AI_i\right]\frac{1}{r}\sum_{n=1}^{\infty} E_n\delta_n\cos(\delta_n z) \tag{C2.19}$$

$$\frac{1}{r}\frac{\partial V_{ri,1}}{\partial \theta}\Big|_{\xi_i=0} = \frac{1}{\alpha}\left[\left(\frac{\mu_{A+B}}{\mu_{(i-1)}}\right)\frac{\partial p_{(i-1),1}}{\partial r}\Big|_{\theta=\theta_S(r,\theta_i)} - BI_i(r)\right]\sum_{n=1}^{\infty}\delta_n E_n\cos(\delta_n z) \tag{C2.20}$$

$$\frac{1}{r}\frac{\partial W_{ri,1}}{\partial \theta}\Big|_{\xi_i=0} = -\frac{1}{\alpha}\left[\left(\frac{\mu_{A+B}}{\mu_i}\right)\frac{\partial p_{i,1}}{\partial r}\Big|_{\theta=\theta_S(r,\theta_i)} - BI_i(r)\right]\sum_{n=1}^{\infty}\delta_n E_n\cos(\delta_n z) \tag{C2.21}$$

$$\frac{\partial V_{\theta i,1}}{\partial z}\Big|_{\xi_i=0} = \frac{z}{r^2}\left[\left(\frac{\mu_{A+B}}{\mu_{(i-1)}}\right)A_{0,(i-1)} - AI_i\right]\sum_{n=1}^{\infty}\frac{6}{\delta_n^5}[(\delta_n r(0)-1)(1)+1] = 0 \tag{C2.22}$$

$$\frac{\partial V_{\theta i,1}}{\partial z}\Big|_{\xi_i=0} = \frac{\partial W_{\theta i,1}}{\partial z}\Big|_{\xi_i=0} = 0 \tag{C2.23}$$

$$\frac{1}{r}\frac{\partial V_{zi,0}}{\partial \theta}\Big|_{\xi_i=0} = -\frac{1}{\alpha r^3}\left[\left(\frac{\mu_{A+B}}{\mu_{(i-1)}}\right)A_{0,(i-1)} - AI_i\right]\sum_{n=1}^{\infty}[\delta_n^2 r^2(0)(1) + \delta_n r(1)]\left[\frac{E_n}{\delta_n}\sin(\delta_n z) - \frac{6}{\delta_n^4}\left(\frac{3z-z^3}{6}\right)\right] = -\frac{1}{\alpha r^2}\left[\left(\frac{\mu_{A+B}}{\mu_{(i-1)}}\right)A_{0,(i-1)} - AI_i\right]\sum_{n=1}^{\infty}\left[E_n\sin(\delta_n z) - \frac{6}{\delta_n^3}\left(\frac{3z-z^3}{6}\right)\right] \tag{C2.24}$$

$$\frac{1}{r}\frac{\partial W_{zi,0}}{\partial \theta}\Big|_{\xi_i=0} = \frac{1}{\alpha r^3}\left[\left(\frac{\mu_{A+B}}{\mu_i}\right)A_{0,i} - AI_i\right]\sum_{n=1}^{\infty}[\delta_n r - \delta_n^2 r^2(0)](1)\left[\frac{E_n}{\delta_n}\sin(\delta_n z) - \frac{6}{\delta_n^4}\left(\frac{3z-z^3}{6}\right)\right] = \frac{1}{\alpha r^2}\left[\left(\frac{\mu_{A+B}}{\mu_i}\right)A_{0,i} - AI_i\right]\sum_{n=1}^{\infty}\left[E_n\sin(\delta_n z) - \frac{6}{\delta_n^3}\left(\frac{3z-z^3}{6}\right)\right] \quad \text{(C2.25)}$$

$$\frac{\partial V_{ri,0}}{\partial z}\Big|_{\xi_i=0} = \left(\frac{\mu_{A+B}}{\mu_{(i-1)}}\right)\frac{A_{0,(i-1)}}{r}(z) - \left[\left(\frac{\mu_{A+B}}{\mu_{(i-1)}}\right)\frac{A_{0,(i-1)}}{r} - \frac{AI_i}{r}\right]\sum_{n=1}^{\infty}\delta_n E_n(1)\sin(\delta_n z) \quad \text{(C2.26)}$$

$$\frac{\partial W_{ri,0}}{\partial z}\Big|_{\xi_i=0} = \left(\frac{\mu_{A+B}}{\mu_i}\right)\frac{A_{0,(i-1)}}{r}(z) - \left[\left(\frac{\mu_{A+B}}{\mu_{(i-1)}}\right)\frac{A_{0,(i-1)}}{r} - \frac{AI_i}{r}\right]\sum_{n=1}^{\infty}\delta_n E_n(1)\sin(\delta_n z) \quad \text{(C2.27)}$$

$$\frac{\partial V_{zi,0}}{\partial r}\Big|_{\xi_i=0} = \frac{3}{r^4}\left[\left(\frac{\mu_{A+B}}{\mu_{(i-1)}}\right)A_{0,(i-1)} - AI_i\right]\sum_{n=1}^{\infty}\delta_n(0)(1)\left[\frac{E_n}{\delta_n}\sin(\delta_n z) - \frac{6}{\delta_n^4}\left(\frac{3z-z^3}{6}\right)\right] - \frac{1}{r^3}\left[\left(\frac{\mu_{A+B}}{\mu_{(i-1)}}\right)A_{0,(i-1)} - AI_i\right]\sum_{n=1}^{\infty}\delta_n^2(0)^2(1)\left[\frac{E_n}{\delta_n}\sin(\delta_n z) - \frac{6}{\delta_n^4}\left(\frac{3z-z^3}{6}\right)\right] = 0 \quad \text{(C2.28)}$$

$$\frac{\partial V_{zi,0}}{\partial r}\Big|_{\xi_i=0} = \frac{\partial W_{zi,0}}{\partial r}\Big|_{\xi_i=0} = 0 \quad \text{(C2.29)}$$

C2.2 Application of Normal Stress Condition at Interfaces

To circumvent the difficulty of orienting the stress tensor against the interface, it is helpful to use the first stress invariant, $I_1 \equiv \tau_{rr} + \tau_{\theta\theta} + \tau_{zz} = tr\{\boldsymbol{T}\}$, where the components τ_{rr}, $\tau_{\theta\theta}$, and τ_{zz} are given by Equation (6.7), and $tr\{\boldsymbol{T}\} = \tau_{rr} + \tau_{\theta\theta} + \tau_{zz}$

denotes the sum of the diagonal components of $\boldsymbol{T}$. Thus, the normal stress condition becomes:

$$tr\{\boldsymbol{T}_{(\boldsymbol{i-1})}\} = tr\{\boldsymbol{T}_i\} \text{ at } \theta_S(r,\theta_i) \text{ for } 2 \le i \le 2N \qquad \text{(Normal stress condition at interfaces)} \tag{C2.30}$$

where the diagonal components τ_{rr}, $\tau_{\theta\theta}$, and τ_{zz} are given by Equation (6.7).

Next, using the evaluated partial integrals from the previous section, I_1 can be evaluated on either side of the interface as follows:

$$\begin{aligned} tr\{\boldsymbol{T}_{(i-1)}\} &= -3\alpha p_{(i-1)} \\ &\quad + 2\frac{\mu_{(i-1)}}{\mu_{A+B}}\left(\alpha\frac{\partial V_{ri}}{\partial r}\bigg|_{\xi_i=0} + \frac{\partial V_{\theta i}}{\partial \xi_i}\bigg|_{\xi_i=0} + \alpha\frac{V_{ri}}{r}\bigg|_{\xi_i=0} + \frac{\partial V_{zi}}{\partial z}\bigg|_{\xi_i=0}\right) \\ &\quad = \left\{2\frac{\mu_{(i-1)}}{\mu_{A+B}}(0+0)\right\} \\ &\quad + \alpha\left\{-3p_{i,0} + 2\frac{\mu_{(i-1)}}{\mu_{A+B}}\left(\frac{AI_i}{r^2} - \frac{AI_i}{r^2}\right)\left(\frac{1-z^2}{2}\right)\right\} + \mathcal{O}(\alpha^2) \end{aligned} \tag{C2.31}$$

$$
\begin{aligned}
tr\{\boldsymbol{T}_i\} = -3\alpha p_i \\
&+ 2\frac{\mu_i}{\mu_{A+B}}\left(\alpha\frac{\partial W_{ri}}{\partial r}\bigg|_{\xi_i=0} + \frac{\partial W_{\theta i}}{\partial \xi_i}\bigg|_{\xi_i=0} + \alpha\frac{W_{ri}}{r}\bigg|_{\xi_i=0}\right. \\
&\left. + \frac{\partial W_{zi}}{\partial z}\bigg|_{\xi_i=0}\right) \qquad \text{(C2.32)} \\
&= \left\{2\frac{\mu_i}{\mu_{A+B}}(0+0)\right\} \\
&+ \alpha\left\{-3p_{i,0} + 2\frac{\mu_i}{\mu_{A+B}}\left(\frac{AI_i}{r^2} - \frac{AI_i}{r^2}\right)\left(\frac{1-z^2}{2}\right)\right\} + \mathcal{O}(\alpha^2)
\end{aligned}
$$

All normal stress components are of order $\mathcal{O}(\alpha)$ or smaller. Equating the $\mathcal{O}(\alpha)$ terms of $tr\{\boldsymbol{T}_{(i-1)}\}$ and $tr\{\boldsymbol{T}_i\}$ verifies the expected lack of pressure drop across fluid boundaries to leading order:

$$p_{(i-1),0} - p_{i,0} = 0 \qquad \text{(C2.33)}$$

Further consideration of the $\mathcal{O}(\alpha^2)$ components would require evaluation of the partial derivatives of $\mathcal{O}(\alpha^2)$ velocity terms, $\frac{\partial V_{\theta(i-1),2}}{\partial \xi_i}$, $\frac{\partial W_{\theta i,2}}{\partial \xi_i}$, $\frac{\partial V_{z(i-1),2}}{\partial z}$ and $\frac{\partial W_{zi,2}}{\partial z}$.

C2.3 Application of Shear Stress Condition at Interfaces

The shear stress condition will be enforced by equating off-diagonal components of $\boldsymbol{T}_{(i-1)}$ and $\boldsymbol{T}_i$, starting with $\mathcal{O}(\alpha^{-1})$ terms and proceeding to $\mathcal{O}(1)$ terms. In this case, we will find it least onerous to equate individual components, and then verify that the shear

boundary condition is satisfied for the components that remain. In the steps below, $A_{0,(i-1)} = A_{0,i} = A_0$ for $2 \leq i \leq 2N$, based on application of the normal stress condition across interfaces.

In the inner region, the partial derivatives $\frac{1}{r}\frac{\partial V_{r,0}}{\partial \xi_i}$, $\left(\frac{\partial V_{\theta,0}}{\partial z} + \frac{1}{r}\frac{\partial V_{z,0}}{\partial \xi_i}\right)$, and $\frac{\partial V_{r,0}}{\partial z}$ are potentially of order $\mathcal{O}(1)$. We first equate the leading order terms of shear for both fluids as follows:

$$\tau_{r\theta} = \frac{\mu_{(i-1)}}{\mu_{A+B}}\left(\frac{1}{r}\frac{\partial V_{r,0}}{\partial \xi_i}\right) + \mathcal{O}(\alpha) = \frac{\mu_i}{\mu_{A+B}}\left(\frac{1}{r}\frac{\partial W_{r,0}}{\partial \xi_i}\right) + \mathcal{O}(\alpha) \tag{C2.34}$$

$$\tau_{r\theta} = \frac{\mu_{(i-1)}}{\mu_{A+B}}\left(\frac{1}{r}\frac{\partial V_{r,0}}{\partial \xi_i}\right) + \mathcal{O}(\alpha) = \frac{\mu_i}{\mu_{A+B}}\left(\frac{1}{r}\frac{\partial W_{r,0}}{\partial \xi_i}\right) + \mathcal{O}(\alpha)$$

$$\rightarrow \mu_{(i-1)}\frac{\partial V_{ri,0}}{\xi_i} = \mu_i\frac{\partial W_{ri,0}}{\xi_i}$$

$$\rightarrow \mu_{(i-1)}\left[\left(\frac{\mu_{A+B}}{\mu_{(i-1)}}\right)A_0 - AI_i\right]\frac{1}{r}\sum_{n=1}^{\infty} E_n\delta_n\cos(\delta_n z) \tag{C2.35}$$

$$= -\mu_i\left[\left(\frac{\mu_{A+B}}{\mu_i}\right)A_0 - AI_i\right]\frac{1}{r}\sum_{n=1}^{\infty} E_n\delta_n\cos(\delta_n z)$$

$$\rightarrow \mu_{(i-1)}\left[\left(\frac{\mu_{A+B}}{\mu_{(i-1)}}\right)A_0 - AI_i\right] = -\mu_i\left[\left(\frac{\mu_{A+B}}{\mu_i}\right)A_0 - AI_i\right]$$

$$\rightarrow \left[\mu_{(i-1)} + \mu_i\right]AI_i = \mu_{A+B}A_0$$

Thus, an expression has been found for the constant coefficient AI_i, which describes velocity at fluid interfaces, in terms of A_0, which corresponds to pressure field impressed upon the inner regions from the outer regions.

$$AI_i = A_0 \tag{C2.36}$$

This expression must be verified for the remaining $\mathcal{O}(1)$ shear components. For $\tau_{\theta z}$, this can be expressed as follows:

$$\tau_{\theta z} = \frac{\mu_{(i-1)}}{\mu_{A+B}}\left(\frac{\partial V_{\theta i,0}}{\partial z} + \frac{1}{r}\frac{\partial V_{zi,0}}{\partial \xi_i}\right) + \mathcal{O}(\alpha) = \frac{\mu_i}{\mu_{A+B}}\left(\frac{\partial W_{\theta i,0}}{\partial z} + \frac{1}{r}\frac{\partial W_{zi,0}}{\partial \xi_i}\right) + \mathcal{O}(\alpha) \tag{C2.37}$$

$$\rightarrow \frac{\mu_{(i-1)}}{\mu_i}\left\{0 - \frac{1}{r^2}\left[\left(\frac{\mu_{A+B}}{\mu_{(i-1)}}\right)A_0 - AI_i\right]\sum_{n=1}^{\infty}\left[E_n \sin(\delta_n z) - \frac{6}{\delta_n^3}\left(\frac{3z - z^3}{6}\right)\right]\right\}$$

$$= \left\{0 + \frac{1}{r^2}\left[\left(\frac{\mu_{A+B}}{\mu_i}\right)A_0 - AI_i\right]\sum_{n=1}^{\infty}\left[E_n \sin(\delta_n z) - \frac{6}{\delta_n^3}\left(\frac{3z - z^3}{6}\right)\right]\right\} \tag{C2.38}$$

$$\rightarrow \mu_{(i-1)}\left[\left(\frac{\mu_{A+B}}{\mu_{(i-1)}}\right)A_0 - AI_i\right] = -\mu_i\left[\left(\frac{\mu_{A+B}}{\mu_i}\right)A_0 - AI_i\right]$$

$$\rightarrow AI_i = A_0$$

It should be noted that τ_{rz} need not be continous across the interfaces to ensure that the assumed shape is preserved (where fluid interfaces are functions of r and θ only). However, equating $\mathcal{O}(1)$ terms for τ_{rz} gives the following:

$$\tau_{rz} = \frac{\mu_{(i-1)}}{\mu_{A+B}}\frac{\partial V_{ri,0}}{\partial z} + \mathcal{O}(\alpha) = \frac{\mu_i}{\mu_{A+B}}\frac{\partial W_{r1,0}}{\partial z} + \mathcal{O}(\alpha) \tag{C2.39}$$

$$\rightarrow \frac{\mu_{(i-1)}}{\mu_{A+B}} AI_i \frac{z}{r} = \frac{\mu_i}{\mu_{A+B}} AI_i \frac{z}{r}$$

$$\rightarrow A_0\left(\frac{\mu_{A+B}}{\mu_i}\right) = A_0\left(\frac{\mu_{A+B}}{\mu_{(i-1)}}\right) = \tag{C2.40}$$

$$\rightarrow \left(\frac{\mu_{(i-1)}}{\mu_i}\right) = 1$$

This suggests that τ_{rz} will be continuous across the interface only when $\mu_A = \mu_B$. The above steps can now be repeated for $\tau_{r\theta}$, the $\mathcal{O}(\alpha)$ terms involving $BI_i(r)$:

$$\begin{aligned}\tau_{r\theta} - \left[\left(\frac{\mu_{A+B}}{\mu_{(i-1)}}\right)\frac{1}{\alpha r}\frac{\partial V_{ri}}{\xi_i}\right] \\ = \alpha\mu_{(i-1)}\left[\left(\frac{\mu_{A+B}}{\mu_{(i-1)}}\right)\frac{\partial p_{(i-1),1}}{\partial r}\bigg|_{\theta=\theta_S(r,\theta_i)}\right. \\ \left. - BI_i(r)\right]\sum_{n=1}^{\infty}\delta_n E_n \cos(\delta_n z) + \mathcal{O}(\alpha^2)\end{aligned} \tag{C2.41}$$

$$\begin{aligned}\tau_{r\theta}|_{\xi_i=0} - \left[\left(\frac{\mu_{A+B}}{\mu_i}\right)\frac{1}{\alpha r}\frac{\partial W_{ri}}{\xi_i}\right] \\ = -\alpha\mu_i\left[\left(\frac{\mu_{A+B}}{\mu_i}\right)\frac{\partial p_{i,1}}{\partial r}\bigg|_{\theta=\theta_S(r,\theta_i)} - BI_i(r)\right]\sum_{n=1}^{\infty}\delta_n E_n \cos(\delta_n z) \\ + \mathcal{O}(\alpha^2)\end{aligned} \tag{C2.42}$$

Equating the $\mathcal{O}(\alpha)$ terms in the expression above gives:

$$\mu_{(i-1)}\left[\left(\frac{\mu_{A+B}}{\mu_{(i-1)}}\right)\frac{\partial p_{(i-1),1}}{\partial r}\bigg|_{\theta=\theta_S(r,\theta_i)} - BI_i(r)\right]\sum_{n=1}^{\infty}\delta_n E_n\cos(\delta_n z) \tag{C2.43}$$

$$= -\mu_i\left[\left(\frac{\mu_{A+B}}{\mu_i}\right)\frac{\partial p_{i,1}}{\partial r}\bigg|_{\theta=\theta_S(r,\theta_i)} - BI_i(r)\right]\sum_{n=1}^{\infty}\delta_n E_n\cos(\delta_n z)$$

$$\begin{aligned}\rightarrow \mu_{(i-1)}\left[\left(\frac{\mu_{A+B}}{\mu_{(i-1)}}\right)\frac{\partial p_{(i-1),1}}{\partial r}\bigg|_{\theta=\theta_S(r,\theta_i)} - BI_i(r)\right] \\ = -\mu_i\left[\left(\frac{\mu_{A+B}}{\mu_i}\right)\frac{\partial p_{i,1}}{\partial r}\bigg|_{\theta=\theta_S(r,\theta_i)} - BI_i(r)\right]\end{aligned} \tag{C2.44}$$

$$\rightarrow \mu_{A+B}BI_i(r) = \mu_{A+B}\left(\frac{\partial p_{(i-1),1}}{\partial r}\right)\bigg|_{\theta=\theta_S(r,\theta_i)}$$

Finally, since the pressure drop across interfaces is zero, $\frac{\partial p_{(i-1),1}}{\partial r} = \frac{\partial p_{i,1}}{\partial r}$ and $BI_i(r)$ can be expressed in terms of the outer pressure gradients and viscosity as follows:

$$BI_i(r) = \left(\frac{\partial p_{(i-1),1}}{\partial r}\right)\bigg|_{\theta=\theta_S(r,\theta_i)} \tag{C2.45}$$

This result can be verified for the $\mathcal{O}(\alpha)$ terms in $\tau_{\theta z}$.

C3 Application of Flow Rate Condition for Two-Fluid Case

This section provides some intermediate steps for the application of the flow rate condition for the two-fluid case, whose results are presented in Section 6.8. For brevity, fluid boundaries located at $\theta = \theta_S(r, \theta_i)$ will be denoted simply as θ_i. All other numbering and naming conventions here are the preserved from the end of Section 6.7.

The radial component of flow velocity for the two-material case can be expressed as the following asymptotic expansion about powers of the small parameter α as follows:

$$\begin{aligned} u_{ri} = &\left(\frac{A_0}{r} + \alpha\frac{B_0}{r}\right)\left[P1_i(r,\theta,z) - \left(\frac{\mu_{A+B}}{\mu_i}\right)\left(\frac{1-z^2}{2}\right)\right] \\ &+ \left(\frac{\alpha}{r}\right)\left(\frac{A_0}{r}\sum_{n=1}^{\infty}\frac{6}{\delta_n^5}\right)\left[P2_i(r,\theta,z) - \left(\frac{\mu_{A+B}}{\mu_i}\right)\frac{\cos(\theta)}{\sin(\theta_H)}\left(\frac{1-z^2}{2}\right)\right] \\ &+ \mathcal{O}(\alpha^2) \end{aligned} \tag{C3.1}$$

Above, A_0 and B_0 are as-of-yet unknown constant coefficients, $\mu_i = \mu_A$ for odd i and $\mu_i = \mu_B$ for even i, and $P1_i$ and $P2_i$ retain their definitions from Appendix C4. Next, the total flow rate across the region bounded by streamlines at θ_i and θ_{i+1} can be expressed as follows:

$$Q_i = \int_{-1}^{1}\int_{\theta_i}^{\theta_{i+1}} u_{ri}\, r\, d\theta dz \tag{C3.2}$$

The calculations required evaluate this integral for u_{ri} in Equation (C3.1) are lengthy. To manage the process, Equation (C3.2) is expressed as the sum of four constituent terms, which are defined as follows:

$$Q_{i,U0} = \int_{-1}^{1}\int_{\theta_i}^{\theta_{i+1}} \left(\frac{A_0}{r} + \alpha\frac{B_0}{r}\right)\left[-\left(\frac{\mu_{A+B}}{\mu_i}\right)\left(\frac{1-z^2}{2}\right)\right] r d\theta dz \tag{C3.3}$$

$$Q_{i,U1} = \int_{-1}^{1}\int_{\theta_i}^{\theta_{i+1}} \left(\frac{\alpha}{r}\right)\left(\frac{A_0}{r}\sum_{n=1}^{\infty}\frac{6}{\delta_n^5}\right)\left[-\left(\frac{\mu_{A+B}}{\mu_i}\right)\frac{\cos(\theta)}{\sin(\theta_H)}\left(\frac{1-z^2}{2}\right)\right] r d\theta dz \tag{C3.4}$$

$$Q_{i,V0} = \int_{-1}^{1}\int_{\theta_i}^{\theta_{i+1}} \left(\frac{A_0}{r} + \alpha\frac{B_0}{r}\right) P1_i(r,\theta,z) r d\theta dz \tag{C3.5}$$

$$Q_{i,V1} = \int_{-1}^{1}\int_{\theta_i}^{\theta_{i+1}} \left(\frac{A_0}{r} + \alpha\frac{B_0}{r}\right) P2_i(r,\theta,z) r d\theta dz \tag{C3.6}$$

Here, $Q_{i,U0} + Q_{i,U1}$ constitutes the flow rate contribution from the outer velocity field. The remaining terms, which involve $P1_i$ and $P2_i$, reflect additional flow rate contributions due to channel walls and interior fluid boundaries.

The integrals in Equations (C3.3)-(C3.6) can be evaluated as follows:

$$Q_{i,U0} = -\frac{2}{3}(A_0 + \alpha B_0)\left(\frac{\mu_{A+B}}{\mu_i}\right)(\theta_{i+1} - \theta_i) \tag{C3.7}$$

$$Q_{i,U1} = -\frac{2}{3}\left(\frac{\alpha}{r}\right) A_0 \left(\sum_{n=1}^{\infty} \frac{6}{\delta_n^5}\right)\left(\frac{\mu_{A+B}}{\mu_i}\right)\left[\frac{\sin(\theta_{i+1}) - \sin(\theta_i)}{\sin(\theta_H)}\right] \tag{C3.8}$$

$$Q_{i,V0} = \begin{cases} \frac{4}{3}(A_0 + \alpha B_0)\left(\frac{\alpha}{r}\right)\left(\frac{\mu_{(i-1)}}{\mu_i}\right)\sum_{n=1}^{\infty}\frac{6}{\delta_n^5} & 2 \le i \le 2N \\ \frac{4}{3}(A_0 + \alpha B_0)\left(\frac{\alpha}{r}\right)\left(\frac{\mu_{(i-1)}}{\mu_i} + \frac{1}{2}\right)\sum_{n=1}^{\infty}\frac{6}{\delta_n^5} & i = 1,2N+1 \end{cases} \tag{C3.9}$$

$$Q_{i,V1}$$

$$= \begin{cases} \frac{2}{3}\left(\frac{\alpha}{r}\right)^2 \left(A_0 \sum_{n=1}^{\infty}\frac{6}{\delta_n^5}\right)\left(\frac{\mu_{(i-1)}}{\mu_i}\right)\sum_{n=1}^{\infty}\frac{6}{\delta_n^5}\left[\frac{\cos(\theta_i) + \cos(\theta_{i+1})}{\sin(\theta_H)}\right] & 2 \le i \le 2N \\ \frac{2}{3}\left(\frac{\alpha}{r}\right)^2 \left(A_0 \sum_{n=1}^{\infty}\frac{6}{\delta_n^5}\right)\sum_{n=1}^{\infty}\frac{6}{\delta_n^5}\left[\left(\frac{\mu_{(i-1)}}{\mu_i}\right)\frac{\cos(\theta_i) + \cos(\theta_{i+1})}{\sin(\theta_H)} + \cot(\theta_H)\right] & i = 1,2N+1 \end{cases} \tag{C3.10}$$

It should be noted that these expressions for $Q_{i,V0}$ and $Q_{i,V1}$ make use of the approximation $\left(\frac{\alpha}{r}\right)\exp\left\{\delta_n \frac{r(\theta_i - \theta_{i+1})}{\alpha}\right\} \approx 0$, which is acceptable for the $\mathcal{O}(\alpha)$ expansion.

Summing each of these terms across all regions containing material *A* gives the following:

$$\sum_{i=1}^{N} Q_{(2i-1),U0} = -\frac{2}{3}(A_0 + \alpha B_0)\left(\frac{\mu_{A+B}}{\mu_A}\right)\sum_{i=1}^{N}(\theta_{2i} - \theta_{2i-1}) \tag{C3.11}$$

$$\sum_{i=1}^{N} Q_{(2i-1),U1} = -\frac{2}{3}\left(\frac{\alpha}{r}\right)\left(A_0 \sum_{n=1}^{\infty} \frac{6}{\delta_n^5}\right)\left(\frac{\mu_{A+B}}{\mu_A}\right)\sum_{i=1}^{N}\left[\frac{\sin(\theta_{2i}) - \sin(\theta_{2i-1})}{\sin(\theta_H)}\right] \tag{C3.12}$$

$$\sum_{i=1}^{N} Q_{(2i-1),V0} = \frac{4}{3}(A_0 + \alpha B_0)\left(\frac{\alpha}{r}\right)\left[N\left(\frac{\mu_B}{\mu_A}\right) + \frac{1}{2}\right]\sum_{n=1}^{\infty} \frac{6}{\delta_n^5} \tag{C3.13}$$

$$\sum_{i=1}^{N} Q_{(2i-1),V1} = \frac{2}{3}\left(\frac{\alpha}{r}\right)^2 A_0 \left(\sum_{n=1}^{\infty} \frac{6}{\delta_n^5}\right)^2 \left\{\cot(\theta_H) + \left(\frac{\mu_B}{\mu_A}\right)\sum_{i=1}^{N}\left[\frac{\cos(\theta_{2i}) + \cos(\theta_{2i-1})}{\sin(\theta_H)}\right]\right\} \tag{C3.14}$$

Repeating the above process for material *B* gives the following:

$$\sum_{i=1}^{N} Q_{2i,U0} = -\frac{2}{3}(A_0 + \alpha B_0)\sum_{i=1}^{N}\left[\left(\frac{\mu_{A+B}}{\mu_B}\right)(\theta_{2i+1} - \theta_{2i})\right] \tag{C3.15}$$

$$\sum_{i=1}^{N} Q_{2i,U1} = -\frac{2}{3}\left(\frac{\alpha}{r}\right) A_0 \left(\sum_{n=1}^{\infty} \frac{6}{\delta_n^5}\right)\sum_{i=1}^{N}\left[\left(\frac{\mu_{A+B}}{\mu_B}\right)\frac{\sin(\theta_{2i+1}) - \sin(\theta_{2i})}{\sin(\theta_H)}\right] \tag{C3.16}$$

$$\sum_{i=1}^{N} Q_{2i,V0} = \sum_{i=1}^{N}\{Q_{2i,V0}\} = \frac{4}{3}(A_0 + \alpha B_0)\left(\frac{\alpha}{r}\right)\left[N\left(\frac{\mu_A}{\mu_B}\right) + \frac{1}{2}\right]\sum_{n=1}^{\infty} \frac{6}{\delta_n^5} \tag{C3.17}$$

$$\sum_{i=1}^{N} Q_{2i,V1} = \frac{2}{3}\left(\frac{\alpha}{r}\right)^2 A_0 \left(\sum_{n=1}^{\infty} \frac{6}{\delta_n^5}\right)^2 \left\{\cot(\theta_H) + \left(\frac{\mu_A}{\mu_B}\right)\sum_{i=1}^{N}\left[\frac{\cos(\theta_{2i+1}) + \cos(\theta_{2i})}{\sin(\theta_H)}\right]\right\} \tag{C3.18}$$

With these intermediate results, the flow rate condition for each material can now be expressed as follows:

$$\begin{aligned} -\frac{Q_A}{Q_{A+B}} = &-\frac{2}{3}(A_0 + \alpha B_0)\left(\frac{\mu_{A+B}}{\mu_A}\right)\sum_{i=1}^{N}[(\theta_{2i} - \theta_{2i-1})] \\ &+ \frac{2}{3}\left(\frac{\alpha}{r}\right)\left\{(A_0 + \alpha B_0)\left[2N\left(\frac{\mu_B}{\mu_A}\right) + 1\right]\right. \\ &\left. - A_0\left(\frac{\mu_{A+B}}{\mu_A}\right)\sum_{i=1}^{N}\left[\frac{\sin(\theta_{2i}) - \sin(\theta_{2i-1})}{\sin(\theta_H)}\right]\right\}\left(\sum_{n=1}^{\infty}\frac{6}{\delta_n^5}\right) \\ &+ \frac{2}{3}\left(\frac{\alpha}{r}\right)^2 A_0\left(\sum_{n=1}^{\infty}\frac{6}{\delta_n^5}\right)^2\left\{\cot(\theta_H)\right. \\ &\left. + \left(\frac{\mu_B}{\mu_A}\right)\sum_{i=1}^{N}\left[\frac{\cos(\theta_{2i}) + \cos(\theta_{2i-1})}{\sin(\theta_H)}\right]\right\} \end{aligned} \tag{C3.19}$$

$$-\frac{Q_B}{Q_{A+B}} = -\frac{2}{3}(A_0 + \alpha B_0)\left(\frac{\mu_{A+B}}{\mu_B}\right)\sum_{i=1}^{N}[(\theta_{2i+1} - \theta_{2i})]$$

$$+\frac{2}{3}\left(\frac{\alpha}{r}\right)\Bigg\{(A_0 + \alpha B_0)\left[2N\left(\frac{\mu_A}{\mu_B}\right) + 1\right]$$

$$- A_0\left(\frac{\mu_{A+B}}{\mu_B}\right)\sum_{i=1}^{N}\left[\frac{\sin(\theta_{2i+1}) - \sin(\theta_{2i})}{\sin(\theta_H)}\right]\Bigg\}\left(\sum_{n=1}^{\infty}\frac{6}{\delta_n^5}\right) \qquad \text{(C3.20)}$$

$$+\frac{2}{3}\left(\frac{\alpha}{r}\right)^2 A_0\left(\sum_{n=1}^{\infty}\frac{6}{\delta_n^5}\right)^2\Bigg\{\cot(\theta_H)$$

$$+\left(\frac{\mu_A}{\mu_B}\right)\sum_{i=1}^{N}\left[\frac{\cos(\theta_{2i+1}) + \cos(\theta_{2i})}{\sin(\theta_H)}\right]\Bigg\}$$

The sum of these expressions can be rearranged as follows:

$$0 = \left(\frac{\mu_A Q_A + \mu_B Q_B}{\mu_{A+B} Q_{A+B}}\right) - \frac{4\theta_H}{3}(A_0 + \alpha B_0)$$

$$+\frac{2}{3}\left(\frac{\alpha}{r}\right)\Bigg[(A_0 + \alpha B_0)(2N + 1) - 2A_0 \qquad \text{(C3.21)}$$

$$+\left(\frac{\alpha}{r}\right)A_0\left(\sum_{n=1}^{\infty}\frac{6}{\delta_n^5}\right)\sum_{i=1}^{2N+1}\left[\frac{\cos(\theta_i)}{\sin(\theta_H)}\right]\Bigg]\left(\sum_{n=1}^{\infty}\frac{6}{\delta_n^5}\right)$$

The above expression comprises terms which are constant, as well as terms of order $\mathcal{O}(\alpha)$ or higher which also depend on r. In order to satisfy the flow rate condition, each set of terms must equate to zero. This can be expressed as follows:

$$A_0 + \alpha B_0 = \frac{3}{4\theta_H}\left(\frac{\mu_A Q_A + \mu_B Q_B}{\mu_{A+B} Q_{A+B}}\right) \tag{C3.22}$$

$$A_0 = (A_0 + \alpha B_0)\left(\frac{2N+1}{2}\right) + \left(\frac{\alpha}{r}\right) A_0 \left(\sum_{n=1}^{\infty} \frac{6}{\delta_n^5}\right) \sum_{i=1}^{2N+1} \left[\frac{\cos(\theta_i)}{2\sin(\theta_H)}\right] \tag{C3.23}$$

Noting that the coefficient term $(A_0 + \alpha B_0)$ appears several times throughout the expressions for the velocity field, Equation (C3.23) constitutes a convenient definition required to express the velocity field explicitly in terms of fluid properties and channel geometry. The other coefficient term that appears throughout the velocity field components is A_0. An expression for this parameter can be obtained from Equation (C3.24):

$$A_0 = \frac{3}{4\theta_H}\left(\frac{\mu_A Q_A + \mu_B Q_B}{\mu_{A+B} Q_{A+B}}\right)\left(\frac{2N+1}{2}\right)\left\{1 - \left(\frac{\alpha}{r}\right)\left(\sum_{n=1}^{\infty} \frac{6}{\delta_n^5}\right) \sum_{i=1}^{2N+1} \frac{\cos(\theta_i)}{2\sin(\theta_H)}\right\}^{-1} \tag{C3.24}$$

The proportionality of A_0 to $(2N+1)$ is perhaps the most interesting aspect of this result. This reflects the fact that the $\mathcal{O}(\alpha)$ terms in the velocity field scale with the number of fluid interfaces, even in the outer regions. Briefly, it should also be noted that as with the single-fluid case, the constant coefficients in the two-fluid velocity field require a

correction factor corresponding to flow rate contributions from higher-order terms in the asymptotic expansion.

Finally, it is also possible now to express the total flow rate through a region bounded by $\theta = \theta_i$ on the left and by $\theta = \theta_{i+1}$ on the right. Where $Q_i = Q_A$ for odd i and $Q_i = Q_B$ for even i, the flow rate is as follows:

$$
\begin{aligned}
-\frac{Q_i}{NQ_{A+B}} = &-\frac{2}{3}(A_0 + \alpha B_0)\left(\frac{\mu_{A+B}}{\mu_i}\right)(\theta_{i+1} - \theta_i) \\
&-\frac{2}{3}\left(\frac{\alpha}{r}\right)A_0\left(\sum_{n=1}^{\infty}\frac{6}{\delta_n^5}\right)\left(\frac{\mu_{A+B}}{\mu_i}\right)\left[\frac{\sin(\theta_{i+1}) - \sin(\theta_i)}{\sin(\theta_H)}\right] \\
&+\frac{4}{3}(A_0 + \alpha B_0)\left(\frac{\alpha}{r}\right)\left(\frac{\mu_{(i-1)}}{\mu_i}\right)\sum_{n=1}^{\infty}\frac{6}{\delta_n^5} \\
&+\frac{2}{3}\left(\frac{\alpha}{r}\right)^2 A_0\left(\sum_{n=1}^{\infty}\frac{6}{\delta_n^5}\right)^2\left(\frac{\mu_{(i-1)}}{\mu_i}\right)\left[\frac{\cos(\theta_i) + \cos(\theta_{i+1})}{\sin(\theta_H)}\right]
\end{aligned}
\qquad \text{(C3.25)}
$$

for $2 \leq i \leq 2N$

$$
\begin{aligned}
-\frac{Q_i}{NQ_{A+B}} = &-\frac{2}{3}(A_0 + \alpha B_0)\left(\frac{\mu_{A+B}}{\mu_i}\right)(\theta_{i+1} - \theta_i) \\
&-\frac{2}{3}\left(\frac{\alpha}{r}\right)A_0\left(\sum_{n=1}^{\infty}\frac{6}{\delta_n^5}\right)\left(\frac{\mu_{A+B}}{\mu_i}\right)\left[\frac{\sin(\theta_{i+1}) - \sin(\theta_i)}{\sin(\theta_H)}\right] \\
&+\frac{4}{3}(A_0 + \alpha B_0)\left(\frac{\alpha}{r}\right)\left(\frac{\mu_{(i-1)}}{\mu_i} + \frac{1}{2}\right)\sum_{n=1}^{\infty}\frac{6}{\delta_n^5} \\
&+\frac{2}{3}\left(\frac{\alpha}{r}\right)^2 A_0\left(\sum_{n=1}^{\infty}\frac{6}{\delta_n^5}\right)^2\left[\left(\frac{\mu_{(i-1)}}{\mu_i}\right)\frac{\cos(\theta_i) + \cos(\theta_{i+1})}{\sin(\theta_H)}\right. \\
&\left.+\cot(\theta_H)\right]
\end{aligned}
\qquad \text{(C3.26)}
$$

for $i = 1$

These expressions can be rearranged to a more convenient form as follows:

$$
\begin{aligned}
&-\frac{Q_i}{NQ_{A+B}}\left(\frac{3}{2}\right)(A_0+\alpha B_0)^{-1}\left(\frac{\mu_i}{\mu_{A+B}}\right) \\
&\qquad = -(\theta_{i+1}-\theta_i) \\
&\qquad -\left(\frac{\alpha}{r}\right)\left(\frac{A_0}{A_0+\alpha B_0}\right)\left(\sum_{n=1}^{\infty}\frac{6}{\delta_n^5}\right)\left[\frac{\sin(\theta_{i+1})-\sin(\theta_i)}{\sin(\theta_H)}\right] \\
&\qquad +2\left(\frac{\alpha}{r}\right)\left(\frac{\mu_{(i-1)}}{\mu_{A+B}}\right)\sum_{n=1}^{\infty}\frac{6}{\delta_n^5} \\
&\qquad +\left(\frac{\alpha}{r}\right)^2\left(\frac{A_0}{A_0+\alpha B_0}\right)\left(\sum_{n=1}^{\infty}\frac{6}{\delta_n^5}\right)^2\left(\frac{\mu_{(i-1)}}{\mu_{A+B}}\right)\left[\frac{\cos(\theta_i)+\cos(\theta_{i+1})}{\sin(\theta_H)}\right]
\end{aligned}
\qquad \text{(C3.27)}
$$

for $2 \le i \le 2N$

$$
\begin{aligned}
&-\frac{Q_i}{NQ_{A+B}}\left(\frac{3}{2}\right)(A_0+\alpha B_0)^{-1}\left(\frac{\mu_i}{\mu_{A+B}}\right)\\
&\qquad=-(\theta_{i+1}-\theta_i)\\
&\qquad-\left(\frac{\alpha}{r}\right)\left(\frac{A_0}{A_0+\alpha B_0}\right)\left(\sum_{n=1}^{\infty}\frac{6}{\delta_n^5}\right)\left[\frac{\sin(\theta_{i+1})-\sin(\theta_i)}{\sin(\theta_H)}\right]\\
&\qquad+2\left(\frac{\alpha}{r}\right)\left(\frac{\mu_{(i-1)}}{\mu_{A+B}}+\frac{1}{2}\frac{\mu_i}{\mu_{A+B}}\right)\sum_{n=1}^{\infty}\frac{6}{\delta_n^5}\\
&\qquad+\left(\frac{\alpha}{r}\right)^2\left(\frac{A_0}{A_0+\alpha B_0}\right)\left(\sum_{n=1}^{\infty}\frac{6}{\delta_n^5}\right)^2\left[\left(\frac{\mu_{(i-1)}}{\mu_{A+B}}\right)\frac{\cos(\theta_i)+\cos(\theta_{i+1})}{\sin(\theta_H)}\right.\\
&\qquad\left.+\left(\frac{\mu_i}{\mu_{A+B}}\right)\cot(\theta_H)\right]
\end{aligned}
\tag{C3.28}
$$

for $i=1$

Finally, substituting the known expressions for constant coefficients A_0 and B_0 gives an implicit expression for the locations of interior fluid boundaries:

$$\theta_{i+1} = \theta_i + \frac{2\theta_H}{N}\left(\frac{\mu_i Q_i}{\mu_A Q_A + \mu_B Q_B}\right) + \left(\frac{\alpha}{r}\right)\left\{2\left(\frac{\mu_{(i+1)}}{\mu_{A+B}}\right) - \left(\frac{2N+1}{1-A_{0,err}}\right)\left[\frac{\sin(\theta_{i+1}) - \sin(\theta_i)}{2\sin(\theta_H)}\right]\right\}\left(\sum_{n=1}^{\infty}\frac{6}{\delta_n^5}\right) + \left(\frac{\alpha}{r}\right)^2\left(\frac{2N+1}{1-A_{0,err}}\right)\left[\left(\frac{\mu_{(i+1)}}{\mu_{A+B}}\right)\frac{\cos(\theta_i) + \cos(\theta_{i+1})}{2\sin(\theta_H)}\right]\left(\sum_{n=1}^{\infty}\frac{6}{\delta_n^5}\right)^2 \quad \text{(C3.29)}$$

for $2 \leq i \leq 2N$

$$\theta_{i+1} = \theta_i + \frac{2\theta_H}{N}\left(\frac{\mu_i Q_i}{\mu_A Q_A + \mu_B Q_B}\right) + \left(\frac{\alpha}{r}\right)\left\{2\left(\frac{\mu_{(i+1)}}{\mu_{A+B}} + \frac{1}{2}\frac{\mu_i}{\mu_{A+B}}\right) - \left(\frac{2N+1}{1-A_{0,err}}\right)\left[\frac{\sin(\theta_{i+1}) - \sin(\theta_i)}{2\sin(\theta_H)}\right]\right\}\left(\sum_{n=1}^{\infty}\frac{6}{\delta_n^5}\right) + \left(\frac{\alpha}{r}\right)^2\left(\frac{2N+1}{1-A_{0,err}}\right)\left[\left(\frac{\mu_{(i+1)}}{\mu_{A+B}}\right)\frac{\cos(\theta_i) + \cos(\theta_{i+1})}{2\sin(\theta_H)} + \left(\frac{\mu_i}{\mu_{A+B}}\right)\frac{\cot(\theta_H)}{2}\right]\left(\sum_{n=1}^{\infty}\frac{6}{\delta_n^5}\right)^2 \quad \text{(C3.30)}$$

for $i = 1$

Above, $A_{0,err} \equiv \left(\frac{\alpha}{r}\right)\left(\sum_{n=1}^{\infty}\frac{6}{\delta_n^5}\right)\sum_{i=1}^{2N+1}\frac{\cos(\theta_i)}{2\sin(\theta_H)}$. Equations (C3.29) and (C3.30) constitute implicit expressions for fluid boundaries. They can be solved explicitly to leading order, while higher-order evaluations are possible using numerical tools. However, even without solving, there are some interesting aspects of the flow evident from these equations alone. In particular, the no-slip condition at the channel walls imposes an additional $\mathcal{O}(\alpha^2/r^2)$ displacement of the nearest interior fluid boundary.

Briefly, it is possible also to consider the case of an odd number of stripes, where M regions of material *A* alternate with $M-1$ regions of material *B*. The mathematical steps are similar to those given above, with the following results summarized below. First, the flow-rate condition expressed for $2N$ stripes in Equation (C3.21) becomes the following:

$$\begin{aligned} 0 = \left(\frac{\mu_A Q_A + \mu_B Q_B}{\mu_{A+B} Q_{A+B}}\right) - \frac{4\theta_H}{3}(A_0 + \alpha B_0) \\ + \frac{2}{3}\left(\frac{\alpha}{r}\right)\Bigg[(A_0 + \alpha B_0)\left(2M - 1 + \frac{\mu_A}{\mu_{A+B}}\right) - 2A_0 \\ + \left(\frac{\alpha}{r}\right)A_0\left(\sum_{n=1}^{\infty}\frac{6}{\delta_n^5}\right)\sum_{i=1}^{2M}\left[\frac{\cos(\theta_i)}{\sin(\theta_H)}\right]\Bigg]\left(\sum_{n=1}^{\infty}\frac{6}{\delta_n^5}\right) \end{aligned} \tag{C3.31}$$

The definitions for constant coefficients then become the following:

$$A_0 + \alpha B_0 = \frac{3}{4\theta_H}\left(\frac{\mu_A Q_A + \mu_B Q_B}{\mu_{A+B} Q_{A+B}}\right) \tag{C3.32}$$

$$A_0 = \frac{3}{4\theta_H}\left(\frac{\mu_A Q_A + \mu_B Q_B}{\mu_{A+B} Q_{A+B}}\right)\left(\frac{2M - 1 + \mu_A/\mu_{A+B}}{2}\right)\Bigg\{1 - \left(\frac{\alpha}{r}\right)\left(\sum_{n=1}^{\infty}\frac{6}{\delta_n^5}\right)\sum_{i=1}^{2N+1}\frac{\cos(\theta_i)}{2\sin(\theta_H)}\Bigg\}^{-1} \tag{C3.33}$$

Finally, substituting the known expressions for constant coefficients A_0 and B_0 gives an implicit expression for the locations of interior fluid boundaries, in the case of an odd number of stripe-patterned fluid regions:

$$\begin{aligned}\theta_2 = -\theta_H &+ \frac{2\theta_H}{M}\left(\frac{\mu_A Q_A}{\mu_A Q_A + \mu_B Q_B}\right) \\ &+ \left(\frac{\alpha}{r}\right)\Bigg\{2\left(\frac{\mu_B}{\mu_{A+B}} + \frac{1}{2}\frac{\mu_A}{\mu_{A+B}}\right) \\ &- \left(\frac{2M - 1 + \mu_A/\mu_{A+B}}{1 - A_{0,err}}\right)\left[\frac{\sin(\theta_{i+1}) - \sin(\theta_i)}{2\sin(\theta_H)}\right]\Bigg\}\left(\sum_{n=1}^{\infty}\frac{6}{\delta_n^5}\right) \\ &+ \left(\frac{\alpha}{r}\right)^2\left(\frac{2M - 1 + \mu_A/\mu_{A+B}}{1 - A_{0,err}}\right)\left[\left(\frac{\mu_B}{\mu_{A+B}}\right)\frac{\cos(\theta_2)}{2\sin(\theta_H)} \\ &+ \frac{\cot(\theta_H)}{2}\right]\left(\sum_{n=1}^{\infty}\frac{6}{\delta_n^5}\right)^2\end{aligned} \tag{C3.34}$$

for $i = 1$

$$\theta_{i+1} = \theta_i + \frac{2\theta_H}{M-1}\left(\frac{\mu_B Q_B}{\mu_A Q_A + \mu_B Q_B}\right) + \left(\frac{\alpha}{r}\right)\left\{2\left(\frac{\mu_A}{\mu_{A+B}}\right) - \left(\frac{2M-1+\mu_A/\mu_{A+B}}{1-A_{0,err}}\right)\left[\frac{\sin(\theta_{i+1})-\sin(\theta_i)}{2\sin(\theta_H)}\right]\right\}\left(\sum_{n=1}^{\infty}\frac{6}{\delta_n^5}\right) + \left(\frac{\alpha}{r}\right)^2\left(\frac{2M-1+\mu_A/\mu_{A+B}}{1-A_{0,err}}\right)\left[\left(\frac{\mu_A}{\mu_{A+B}}\right)\frac{\cos(\theta_i)+\cos(\theta_{i+1})}{2\sin(\theta_H)}\right]\left(\sum_{n=1}^{\infty}\frac{6}{\delta_n^5}\right)^2 \quad \text{(C3.35)}$$

for even $2 \leq i \leq 2M$

$$\theta_{i+1} = \theta_i + \frac{2\theta_H}{M}\left(\frac{\mu_A Q_A}{\mu_A Q_A + \mu_B Q_B}\right) + \left(\frac{\alpha}{r}\right)\left\{2\left(\frac{\mu_B}{\mu_{A+B}}\right) - \left(\frac{2M-1+\mu_A/\mu_{A+B}}{1-A_{0,err}}\right)\left[\frac{\sin(\theta_{i+1})-\sin(\theta_i)}{2\sin(\theta_H)}\right]\right\}\left(\sum_{n=1}^{\infty}\frac{6}{\delta_n^5}\right) + \left(\frac{\alpha}{r}\right)^2\left(\frac{2M-1+\mu_A/\mu_{A+B}}{1-A_{0,err}}\right)\left[\left(\frac{\mu_B}{\mu_{A+B}}\right)\frac{\cos(\theta_i)+\cos(\theta_{i+1})}{2\sin(\theta_H)}\right]\left(\sum_{n=1}^{\infty}\frac{6}{\delta_n^5}\right)^2 \quad \text{(C3.36)}$$

for odd $3 \leq i \leq 2M-1$

where $A_{0,err} \equiv \left(\frac{\alpha}{r}\right)\left(\sum_{n=1}^{\infty}\frac{6}{\delta_n^5}\right)\sum_{i=1}^{2M}\frac{\cos(\theta_i)}{2\sin(\theta_H)}$

C4 Subtraction of Overlap for Two-fluid Case

This section provides some intermediate steps for the subtraction of overlap in Section 6.7. Here, the numbering and naming conventions here are the same as in Section 6.7. The overlap between $\vec{U}_{(i-1)}$ and $\vec{V}_i$ and the overlap between $\vec{U}_i$ and $\vec{W}_i$, denoted as OR_i and OL_i, respectively, are defined as follows:

$$OR_i = \lim_{\alpha \to 0}\left\{\vec{U}_{(i-1)}\left(\theta = \psi(\alpha)\zeta_i - \theta_S(r,\theta_i)\right)\right\} = \lim_{\alpha \to 0}\left\{\vec{V}_i(\xi_i = \alpha^{-1}\psi(\alpha)\zeta_i)\right\} \tag{C4.1}$$

$$OL_i = \lim_{\alpha \to 0}\left\{\vec{U}_i\left(\theta = \psi(\alpha)\zeta_i - \theta_S(r,\theta_i)\right)\right\} = \lim_{\alpha \to 0}\left\{\vec{W}_i(\xi_i = \alpha^{-1}\psi(\alpha)\zeta_i)\right\} \tag{C4.2}$$

Following the evaluation of overlap terms, the composite velocity field is assembled according to the following definition:

$$\vec{u}_i = \vec{U}_i + \vec{W}_i + \vec{V}_{(i+1)} - OL_i - OR_{(i+1)} + \mathcal{O}(\alpha^2) \tag{C4.3}$$

Here, $\vec{u}_i$ denotes a region of the flow bounded by $\theta_S(r,\theta_i)$ and $\theta_S\left(r,\theta_{(i+1)}\right)$. The composite solutions are expressed in terms of r, θ, and z, as well as inner coordinates ξ_i.

C4.1 Evaluation of Overlap

Overlap near fluid interfaces can be evaluated as follows, neglecting order $\mathcal{O}(\alpha^2)$ terms:

$$OR_{(i+1)} = -\left(\frac{\mu_{A+B}}{\mu_i}\right)\left[\frac{A_0}{r} + \alpha\frac{B_0}{r} + \alpha\frac{A_0}{r^2}\frac{\cos\left(\theta_S\left(r,\theta_{(i+1)}\right)\right)}{\sin(\theta_H)}\sum_{n=1}^{\infty}\frac{6}{\delta_n^5}\right]\left(\frac{1-z^2}{2}\right)\boldsymbol{e}_r$$
$$-\alpha\frac{A_0}{r^2}\left(\frac{\mu_{A+B}}{\mu_i}\right)\left(\frac{\sin\left(\theta_S\left(r,\theta_{(i+1)}\right)\right)}{\sin(\theta_H)}\sum_{n=1}^{\infty}\frac{6}{\delta_n^5}\right)\left(\frac{1-z^2}{2}\right)\boldsymbol{e}_\theta \tag{C4.4}$$

$$OL_i = -\left(\frac{\mu_{A+B}}{\mu_i}\right)\left[\frac{A_0}{r} + \alpha\frac{B_0}{r} + \alpha\frac{A_0}{r^2}\frac{\cos\left(\theta_S(r,\theta_i)\right)}{\sin(\theta_H)}\sum_{n=1}^{\infty}\frac{6}{\delta_n^5}\right]\left(\frac{1-z^2}{2}\right)\boldsymbol{e}_r$$
$$-\alpha\frac{A_0}{r^2}\left(\frac{\mu_{A+B}}{\mu_i}\right)\left(\frac{\sin\left(\theta_S(r,\theta_i)\right)}{\sin(\theta_H)}\sum_{n=1}^{\infty}\frac{6}{\delta_n^5}\right)\left(\frac{1-z^2}{2}\right)\boldsymbol{e}_\theta \tag{C4.5}$$

At channel boundaries, the overlap is given by:

$$OR_{(2N+1)} = -\left(\frac{\mu_{A+B}}{\mu_B}\right)\left[\frac{A_0}{r} + \alpha\frac{B_0}{r} + \alpha\frac{A_0}{r^2}\cot(\theta_H)\sum_{n=1}^{\infty}\frac{6}{\delta_n^5}\right]\left(\frac{1-z^2}{2}\right)\boldsymbol{e}_r$$
$$-\alpha\frac{A_0}{r^2}\left(\frac{\mu_{A+B}}{\mu_B}\right)\sum_{n=1}^{\infty}\frac{6}{\delta_n^5}\left(\frac{1-z^2}{2}\right)\boldsymbol{e}_\theta \tag{C4.6}$$

$$OL_1 = -\left(\frac{\mu_{A+B}}{\mu_A}\right)\left[\frac{A_0}{r} + \alpha\frac{B_0}{r} + \alpha\frac{A_0}{r^2}\cot(\theta_H)\sum_{n=1}^{\infty}\frac{6}{\delta_n^5}\right]\left(\frac{1-z^2}{2}\right)\boldsymbol{e}_r + \alpha\frac{A_0}{r^2}\left(\frac{\mu_{A+B}}{\mu_A}\right)\sum_{n=1}^{\infty}\frac{6}{\delta_n^5}\left(\frac{1-z^2}{2}\right)\boldsymbol{e}_\theta \tag{C4.7}$$

Where $\boldsymbol{e}_r$ and $\boldsymbol{e}_\theta$ are the unit vectors for the r-axis and θ-axis, respectively. The overlap along $\boldsymbol{e}_z$ is zero.

C4.2 $\boldsymbol{r}$-Velocity Components

Partial derivatives of the pressure field, which appear in the definitions of $U_{r,0}$ and $U_{r,1}$ in Section 6.5, and $V_{r,0}, V_{r,1}$, $W_{r,0}$, and $W_{r,1}$ in Section 6.6, are evaluated following matching between inner and outer solutions:

$$\frac{\partial p_{i,0}}{\partial r} = \frac{A_0}{r} \tag{C4.8}$$

$$\left.\frac{\partial p_{i,0}}{\partial r}\right|_{\theta=\theta_S(r,\theta_i)} = \frac{A_0}{r} \tag{C4.9}$$

$$\frac{\partial p_{i,1}}{\partial r} = \frac{B_0}{r} + \frac{A_0}{r^2}\frac{\cos(\theta)}{\sin(\theta_H)}\sum_{n=1}^{\infty}\frac{6}{\delta_n^5} \tag{C4.10}$$

$$\left.\frac{\partial p_{i,1}}{\partial r}\right|_{\theta=\theta_S(r,\theta_i)} = \frac{B_0}{r} + \frac{A_0}{r^2}\frac{\cos\left(\theta_S(r,\theta_i)\right)}{\sin(\theta_H)}\sum_{n=1}^{\infty}\frac{6}{\delta_n^5} \tag{C4.11}$$

Radial velocity components of the composite velocity field in the region bounded by interfaces at $\theta = \theta_S(r, \theta_i)$ and $\theta = \theta_S\left(r, \theta_{(i+1)}\right)$ can then be evaluated as follows:

$u_{ri,0} =$

$$\begin{aligned} & U_{ri,0} + W_{ri,0} + V_{r(i+1),0} - \lim_{\alpha \to 0}\left\{U_{ri,0}\left(\theta = \psi(\alpha)\zeta_i - \theta_S(r, \theta_i)\right)\right\} \\ & \quad - \lim_{\alpha \to 0}\left\{U_{ri,0}\left(\theta = \psi(\alpha)\zeta_{(i+1)} - \theta_S\left(r, \theta_{(i+1)}\right)\right)\right\} \\ & \quad = \frac{A_0}{r}\left[P1_i(r, \theta, z) - \left(\frac{\mu_{A+B}}{\mu_i}\right)\left(\frac{1 - z^2}{2}\right)\right] \end{aligned} \tag{C4.12}$$

$u_{ri,1} =$

$$\begin{aligned} & U_{ri,1} + W_{ri,1} + V_{r(i+1),1} - \lim_{\alpha \to 0}\left\{U_{ri,1}\left(\theta = \psi(\alpha)\zeta_i - \theta_S(r, \theta_i)\right)\right\} \\ & \quad - \lim_{\alpha \to 0}\left\{U_{ri,1}\left(\theta = \psi(\alpha)\zeta_{(i+1)} - \theta_S\left(r, \theta_{(i+1)}\right)\right)\right\} \\ & \quad = \frac{B_0}{r}\left[P1_i(r, \theta, z) - \left(\frac{\mu_{A+B}}{\mu_i}\right)\left(\frac{1 - z^2}{2}\right)\right] \\ & \quad + \left(\frac{A_0}{r^2}\sum_{n=1}^{\infty}\frac{6}{\delta_n^5}\right)\left[P2_i(r, \theta, z) - \left(\frac{\mu_{A+B}}{\mu_i}\right)\frac{\cos(\theta)}{\sin(\theta_H)}\left(\frac{1 - z^2}{2}\right)\right] \end{aligned} \tag{C4.13}$$

$u_{ri,0} + \alpha u_{ri,1} =$ (C4.14)

$$\left(\frac{A_0}{r}+\alpha\frac{B_0}{r}\right)\left[P1_i(r,\theta,z)-\left(\frac{\mu_{A+B}}{\mu_i}\right)\left(\frac{1-z^2}{2}\right)\right]$$

$$+\left(\frac{\alpha}{r}\right)\left(\frac{A_0}{r}\sum_{n=1}^{\infty}\frac{6}{\delta_n^5}\right)\left[P2_i(r,\theta,z)-\left(\frac{\mu_{A+B}}{\mu_i}\right)\frac{\cos(\theta)}{\sin(\theta_H)}\left(\frac{1-z^2}{2}\right)\right]$$

where:

$$P1_i(r,\theta,z)=\left(\frac{\mu_{(i-1)}}{\mu_i}\right)\sum_{n=1}^{\infty}E_n\left(\exp\{-\delta_n r\xi_i\}+\exp\{\delta_n r\xi_{(i+1)}\}\right)\cos(\delta_n z) \tag{C4.15}$$

for $2 \le i \le 2N-1$

$$P1_1(r,\theta,z)=\left(\frac{\mu_{A+B}}{\mu_A}\right)\sum_{n=1}^{\infty}E_n\exp\{-\delta_n r\xi_1\}\cos(\delta_n z)+\left(\frac{\mu_B}{\mu_A}\right)\sum_{n=1}^{\infty}E_n\exp\{\delta_n r\xi_2\}\cos(\delta_n z) \tag{C4.16}$$

$$P1_{2N}(r,\theta,z)=\left(\frac{\mu_A}{\mu_B}\right)\sum_{n=1}^{\infty}E_n\exp\{\delta_n r\xi_{(2N+1)}\}\cos(\delta_n z)$$
$$+\left(\frac{\mu_{A+B}}{\mu_B}\right)\sum_{n=1}^{\infty}E_n\exp\{-\delta_n r\xi_{2N}\}\cos(\delta_n z) \tag{C4.17}$$

$$P2_i(r,\theta,z)=\left(\frac{\mu_{(i-1)}}{\mu_i}\right)\sum_{n=1}^{\infty}E_n\left[\frac{\cos\left(\theta_S(r,\theta_i)\right)}{\sin(\theta_H)}\exp\{-\delta_n r\xi_i\}\right.$$
$$\left.+\frac{\cos\left(\theta_S(r,\theta_{i+1})\right)}{\sin(\theta_H)}\exp\{\delta_n r\xi_{i+1}\}\right]\cos(\delta_n z) \tag{C4.18}$$

for $2 \le i \le 2N-1$

$$P2_1(r,\theta,z) = \left(\frac{\mu_{A+B}}{\mu_A}\right)\sum_{n=1}^{\infty} E_n \cot(\theta_H)\exp\{-\delta_n r\xi_1\}\cos(\delta_n z) + \left(\frac{\mu_B}{\mu_A}\right)\sum_{n=1}^{\infty} E_n \frac{\cos\left(\theta_S(r,\theta_2)\right)}{\sin(\theta_H)}\exp\{\delta_n r\xi_2\}\cos(\delta_n z) \tag{C4.19}$$

$$P2_{(2N)}(r,\theta,z) = \left(\frac{\mu_A}{\mu_B}\right)\sum_{n=1}^{\infty} E_n \frac{\cos\left(\theta_S(r,\theta_{2N})\right)}{\sin(\theta_H)}\exp\{-\delta_n r\xi_N\}\cos(\delta_n z) + \left(\frac{\mu_{A+B}}{\mu_B}\right)\sum_{n=1}^{\infty} E_n \cot(\theta_H)\ \exp\{\delta_n r\xi_{(2N+1)}\}\cos(\delta_n z) \tag{C4.20}$$

C4.3 $\boldsymbol{\theta}$-Velocity Components

The θ-axis components of the inner and outer velocity fields in the region bounded by interfaces at $\theta = \theta_S(r,\theta_i)$ and $\theta = \theta_S\left(r,\theta_{(i+1)}\right)$ are reiterated below:

$$\alpha U_{\theta i,1} = -\alpha\left(\frac{\mu_{A+B}}{\mu_i}\right)\left(\frac{A_0}{r^2}\frac{\sin(\theta)}{\sin(\theta_H)}\sum_{n=1}^{\infty}\frac{6}{\delta_n^5}\right)\left(\frac{1-z^2}{2}\right) \tag{C4.21}$$

$$\alpha V_{\theta(i+1),1} = -\alpha\frac{A_0}{r^2}CI_{1,(i+1)}\sum_{n=1}^{\infty}\frac{6}{\delta_n^5}\left[\left(\delta_n r\xi_{(i+1)}-1\right)\exp\left\{\delta_n r\xi_{(i+1)}\right\} + DI_{1,(i+1)}\right]\left(\frac{1-z^2}{2}\right) \tag{C4.22}$$

$$\alpha W_{\theta i,1} = -\alpha\frac{A_0}{r^2}CI_{2,i}\sum_{n=1}^{\infty}\frac{6}{\delta_n^5}\left[\left(\delta_n r\xi_i+1\right)\exp\{-\delta_n r\xi_i\} - DI_{2,i}\right]\left(\frac{1-z^2}{2}\right) \tag{C4.23}$$

Matching between the inner and outer solutions necessitates the following relationship between the unknown constants $CI_{1,i}$, $CI_{2,i}$, $DI_{1,i}$, and $DI_{2,i}$:

$$\left(\frac{\mu_{A+B}}{\mu_i}\right)\left(\frac{\sin\left(\theta_S(r,\theta_i)\right)}{\sin(\theta_H)}\right) = CI_{1,i}\left(DI_{1,i}\right) \tag{C4.24}$$

$$\left(\frac{\mu_{A+B}}{\mu_{(i-1)}}\right)\left(\frac{\sin\left(\theta_S(r,\theta_i)\right)}{\sin(\theta_H)}\right) = -CI_{2,i}\left(DI_{2,i}\right) \tag{C4.25}$$

Thus, Equations (C4.21)-(C4.23) above can be expressed as follows:

$$\alpha U_{\theta i,1} = -\alpha\left(\frac{\mu_{A+B}}{\mu_i}\right)\left(\frac{A_0}{r^2}\frac{\sin(\theta)}{\sin(\theta_H)}\sum_{n=1}^{\infty}\frac{6}{\delta_n^5}\right)\left(\frac{1-z^2}{2}\right) \tag{C4.26}$$

$$\begin{aligned}\alpha V_{\theta(i+1),1} = -\alpha\frac{A_0}{r^2}\left(\frac{\mu_{(i-1)}}{\mu_i}\right)\frac{\sin\left(\theta_S\left(r,\theta_{(i+1)}\right)\right)}{DI_{1,(i+1)}\sin(\theta_H)}\sum_{n=1}^{\infty}\frac{6}{\delta_n^5}\left[\left(\delta_n r\xi_{(i+1)}\right.\right.\\ \left.\left.-1\right)\exp\left\{\delta_n r\xi_{(i+1)}\right\}+DI_{1,(i+1)}\right]\left(\frac{1-z^2}{2}\right)\end{aligned} \tag{C4.27}$$

$$\begin{aligned}\alpha W_{\theta i,1} = \alpha\frac{A_0}{r^2}\left(\frac{\mu_{(i-1)}}{\mu_i}\right)\frac{\sin\left(\theta_S(r,\theta_i)\right)}{DI_{2,i}\sin(\theta_H)}\sum_{n=1}^{\infty}\frac{6}{\delta_n^5}\left[\left(\delta_n r\xi_i+1\right)\exp\{-\delta_n r\xi_i\}\right.\\ \left.-DI_{2,i}\right]\left(\frac{1-z^2}{2}\right)\end{aligned} \tag{C4.28}$$

The sum of these components minus the θ-axis components of overlap constitute the composite velocity field, which can be evaluated and simplified with order $\mathcal{O}(\alpha^2)$ terms omitted as follows:

$$\begin{aligned} u_{\theta i,0} + \alpha u_{\theta i,1} &= 0 + \alpha U_{\theta i,1} + \alpha W_{\theta i,1} + \alpha V_{\theta(i+1),1} \\ &\quad - \alpha \lim_{\alpha \to 0}\{U_{\theta i,1}(\theta = \psi(\alpha)\zeta_i - \theta_S(r,\theta_i))\} \\ &\quad - \alpha \lim_{\alpha \to 0}\left\{U_{\theta i,1}\left(\theta = \psi(\alpha)\zeta_{(i+1)} - \theta_S\left(r,\theta_{(i+1)}\right)\right)\right\} \end{aligned} \tag{C4.29}$$

$$\begin{aligned} = &-\left(\frac{\mu_{A+B}}{\mu_i}\right)\alpha\left(\frac{A_0}{r^2}\frac{\sin(\theta) - \sin\left(\theta_S(r,\theta_i)\right) - \sin\left(\theta_S\left(r,\theta_{(i+1)}\right)\right)}{\sin(\theta_H)}\sum_{n=1}^{\infty}\frac{6}{\delta_n^5}\right)\left(\frac{1-z^2}{2}\right) \\ &- \alpha\frac{A_0}{r^2}\left(\frac{\mu_{(i-1)}}{\mu_i}\right)\frac{\sin\left(\theta_S\left(r,\theta_{(i+1)}\right)\right)}{DI_{1,(i+1)}\sin(\theta_H)}\sum_{n=1}^{\infty}\frac{6}{\delta_n^5}\left[\left(\delta_n r\xi_{(i+1)}\right.\right. \\ &\left.\left. - 1\right)\exp\{\delta_n r\xi_{(i+1)}\} + DI_{1,(i+1)}\right]\left(\frac{1-z^2}{2}\right) \\ &+ \alpha\frac{A_0}{r^2}\left(\frac{\mu_{(i-1)}}{\mu_i}\right)\frac{\sin\left(\theta_S(r,\theta_i)\right)}{DI_{2,i}\sin(\theta_H)}\sum_{n=1}^{\infty}\frac{6}{\delta_n^5}\left[(\delta_n r\xi_i + 1)\exp\{-\delta_n r\xi_i\}\right. \\ &\left. - DI_{2,i}\right]\left(\frac{1-z^2}{2}\right) \end{aligned} \tag{C4.30}$$

$$= \alpha \frac{A_0}{r^2}\Bigg\{\left(\frac{\mu_{(i-1)}}{\mu_i}\right)\frac{\sin\left(\theta_S(r,\theta_i)\right)}{DI_{2,i}\sin(\theta_H)}\sum_{n=1}^{\infty}\frac{6}{\delta_n^5}\left[(\delta_n r\xi_i + 1)\exp\{-\delta_n r\xi_i\}\right]$$

$$-\left(\frac{\mu_{(i-1)}}{\mu_i}\right)\frac{\sin\left(\theta_S\left(r,\theta_{(i+1)}\right)\right)}{DI_{1,(i+1)}\sin(\theta_H)}\sum_{n=1}^{\infty}\frac{6}{\delta_n^5}\Big[\left(\delta_n r\xi_{(i+1)}\right. \tag{C4.31}$$

$$\left.-1\right)\exp\left\{\delta_n r\xi_{(i+1)}\right\}\Big] - \left(\frac{\mu_{A+B}}{\mu_i}\right)\frac{\sin(\theta)}{\sin(\theta_H)}\sum_{n=1}^{\infty}\frac{6}{\delta_n^5}\Bigg\}\left(\frac{1-z^2}{2}\right)$$

The composite θ-velocity can be expressed more succinctly as follows:

$$u_{\theta i} = \alpha\frac{A_0}{r^2}\left\{P3_1(r,\theta,z) - \left(\frac{\mu_{A+B}}{\mu_i}\right)\frac{\sin(\theta)}{\sin(\theta_H)}\sum_{n=1}^{\infty}\frac{6}{\delta_n^5}\right\}\left(\frac{1-z^2}{2}\right) + \mathcal{O}(\alpha^2) \tag{C4.32}$$

Where:

$$P3_i(r,\theta,z) = \left(\frac{\mu_{(i-1)}}{\mu_i}\right)\sum_{n=1}^{\infty}\frac{6}{\delta_n^5}\left[\frac{\sin\left(\theta_S(r,\theta_i)\right)}{DI_{2,i}\sin(\theta_H)}(\delta_n r\xi_i + 1)\exp\{-\delta_n r\xi_i\}\right.$$

$$\left.-\frac{\sin\left(\theta_S\left(r,\theta_{(i+1)}\right)\right)}{DI_{1,(i+1)}\sin(\theta_H)}\left(\delta_n r\xi_{(i+1)} - 1\right)\exp\left\{\delta_n r\xi_{(i+1)}\right\}\right] \tag{C4.33}$$

for $2 \leq \mathrm{i} \leq 2\mathrm{N}-1$

$$P3_1(r,\theta,z) = \sum_{n=1}^{\infty} \frac{6}{\delta_n^5}\left[-\left(\frac{\mu_{A+B}}{\mu_A}\right)(\delta_n r\xi_2 + 1)\exp\{-\delta_n r\xi_1\}\right.$$
$$\left. -\left(\frac{\mu_B}{\mu_A}\right)\frac{\sin\left(\theta_S\left(r,\theta_{(i+1)}\right)\right)}{DI_{1,(i+1)}\sin(\theta_H)}(\delta_n r\xi_2 - 1)\exp\{\delta_n r\xi_2\}\right] \quad \text{(C4.34)}$$

$$P3_{2N+1}(r,\theta,z) = \sum_{n=1}^{\infty} \frac{6}{\delta_n^5}\left[\left(\frac{\mu_A}{\mu_B}\right)\frac{\sin\left(\theta_S(r,\theta_i)\right)}{DI_{2,i}\sin(\theta_H)}(\delta_n r\xi_{2N} + 1)\exp\{-\delta_n r\xi_{2N}\}\right.$$
$$\left. -\left(\frac{\mu_{A+B}}{\mu_B}\right)\left(\delta_n r\xi_{(2N+1)} - 1\right)\exp\left\{\delta_n r\xi_{(2N+1)}\right\}\right] \quad \text{(C4.35)}$$

Above, constant coefficients $DI_{1,i}$ and $DI_{2,i}$ remain unknown, and can be determined by the procedure detailed in Appendix C1.

C4.4 $\boldsymbol{z}$-Velocity Components

The z-axis components of the inner velocity fields in the region bounded by interfaces at $\theta = \theta_S(r,\theta_i)$ and $\theta = \theta_S\left(r,\theta_{(i+1)}\right)$ are reiterated below:

$$V_{z(i+1),0}$$

$$= -\frac{A_0}{r^2}\left(\frac{\mu_{(i-1)}}{\mu_i}\right)\frac{\sin\left(\theta_S\left(r,\theta_{(i+1)}\right)\right)}{\sin(\theta_H)}\sum_{n=1}^{\infty}\delta_n r\xi_{(i+1)}\exp\{\delta_n r\xi_{(i+1)}\}\left[\frac{E_n}{\delta_n}\sin(\delta_n z)\right. \quad \text{(C4.36)}$$

$$\left. -\frac{6}{\delta_n^4}\left(\frac{3z-z^3}{6}\right)\right]$$

$$W_{zi,0} = -\frac{A_0}{r^2}\left(\frac{\mu_{(i-1)}}{\mu_i}\right)\frac{\sin\left(\theta_S(r,\theta_i)\right)}{\sin(\theta_H)}\sum_{n=1}^{\infty}\delta_n r\xi_i\exp\{-\delta_n r\xi_i\}\left[\frac{E_n}{\delta_n}\sin(\delta_n z)\right. \quad \text{(C4.37)}$$

$$\left. -\frac{6}{\delta_n^4}\left(\frac{3z-z^3}{6}\right)\right]$$

The sum of these components minus the z-axis components of overlap constitute the composite velocity field, which can be evaluated and simplified with order $\mathcal{O}(\alpha^2)$ terms omitted as follows:

$$u_{zi,0} = U_{zi,0} + W_{zi,0} + V_{z(i+1),0} - \lim_{\alpha\to 0}\left\{U_{\theta i,1}\left(\theta = \psi(\alpha)\zeta_i - \theta_S(r,\theta_i)\right)\right\} \quad \text{(C4.38)}$$

$$- \lim_{\alpha\to 0}\left\{U_{\theta i,1}\left(\theta = \psi(\alpha)\zeta_{(i+1)} - \theta_S\left(r,\theta_{(i+1)}\right)\right)\right\}$$

$$
\begin{aligned}
&= 0 \\
&-\frac{A_0}{r^2}\sum_{n=1}^{\infty}\delta_n r\left[\left(\frac{\mu_{(i-1)}}{\mu_i}\right)\frac{\sin\left(\theta_S(r,\theta_i)\right)}{\sin(\theta_H)}\xi_i\exp\{-\delta_n r\xi_i\}\right. \\
&\left.+\left(\frac{\mu_{(i-1)}}{\mu_i}\right)\frac{\sin\left(\theta_S\left(r,\theta_{(i+1)}\right)\right)}{\sin(\theta_H)}\xi_{(i+1)}\exp\left\{\delta_n r\xi_{(i+1)}\right\}\right]\left[\frac{E_n}{\delta_n}\sin(\delta_n z)\right. \\
&\left.-\frac{6}{\delta_n^4}\left(\frac{3z-z^3}{6}\right)\right]
\end{aligned}
\tag{C4.39}
$$

It should be noted that the contributions from the outer region and overlap are both zero, and that $V_{zi,1}$ and $W_{zi,1}$ are both of order $\mathcal{O}(\alpha^2)$. Finally, the composite z-velocity can be expressed more succinctly as follows:

$$u_{zi} = -\frac{A_0}{r^2}P4_i(r,\theta,z) \tag{C4.40}$$

Where:

$$P4_i(r,\theta,z) = \left(\frac{\mu_{(i-1)}}{\mu_i}\right)\sum_{n=1}^{\infty}\left\{\delta_n r\left[\frac{\sin\left(\theta_S(r,\theta_i)\right)}{\sin(\theta_H)}\xi_i \exp\{-\delta_n r\xi_i\}\right.\right.$$
$$\left.\left. + \frac{\sin\left(\theta_S(r,\theta_{(i+1)})\right)}{\sin(\theta_H)}\xi_{(i+1)} \exp\{\delta_n r\xi_{(i+1)}\}\right]\left[\frac{E_n}{\delta_n}\sin(\delta_n z) - \frac{6}{\delta_n^4}\left(\frac{3z-z^3}{6}\right)\right]\right\} \quad \text{(C4.41)}$$

for $2 \le i \le 2N-1$

$$P4_1(r,\theta,z) = \sum_{n=1}^{\infty}\left\{\delta_n r\left[-\left(\frac{\mu_{A+B}}{\mu_A}\right)\xi_1 \exp\{-\delta_n r\xi_1\}\right.\right.$$
$$\left.\left. + \left(\frac{\mu_B}{\mu_A}\right)\frac{\sin\left(\theta_S(r,\theta_2)\right)}{\sin(\theta_H)}\xi_2 \exp\{\delta_n r\xi_2\}\right]\left[\frac{E_n}{\delta_n}\sin(\delta_n z) - \frac{6}{\delta_n^4}\left(\frac{3z-z^3}{6}\right)\right]\right\} \quad \text{(C4.42)}$$

$$P4_{(2N+1)}(r,\theta,z)$$
$$= \sum_{n=1}^{\infty}\left\{\delta_n r\left[\left(\frac{\mu_A}{\mu_B}\right)\frac{\sin\left(\theta_S(r,\theta_{2N})\right)}{\sin(\theta_H)}\xi_{2N} \exp\{-\delta_n r\xi_1\}\right.\right.$$
$$\left.\left. + \left(\frac{\mu_{A+B}}{\mu_B}\right)\xi_{(2N+1)} \exp\{\delta_n r\xi_{(2N+1)}\}\right]\left[\frac{E_n}{\delta_n}\sin(\delta_n z) - \frac{6}{\delta_n^4}\left(\frac{3z-z^3}{6}\right)\right]\right\} \quad \text{(C4.43)}$$

C5 Alternate Derivation of $\mathcal{O}(1)$ Stripe Width Relation

This section provides a simple and direct derivation for Equations (6.36) and (6.38), which express stripe width ratio to order $\mathcal{O}(1)$ as a function of viscosity ratio (μ_A/μ_B) and flow-rate ratio (Q_A/Q_B) for two fluids *A* and *B*. Rather than deriving the full velocity field

for the two fluid case, the approach here is to proceed from the single-fluid outer pressure field given in Equation (5.14a), with the assumption that pressure is continuous across fluid interfaces. Expressing Equation (5.14a) in terms of dimensionless variables as defined in Section 6.3, then taking the partial derivative with respect to r, gives the following expressions:

$$\left(\frac{\mu_{A+B}}{\mu_A}\right)\frac{\partial p_0}{\partial r} = \left(\frac{C_{0,A}}{r}\right) \tag{C5.1}$$

$$\left(\frac{\mu_{A+B}}{\mu_B}\right)\frac{\partial p_0}{\partial r} = \left(\frac{C_{0,B}}{r}\right) \tag{C5.2}$$

where $C_{0,A}$ and $C_{0,B}$ are two constant coefficients for materials *A* and *B*, respectively, which correspond to C_0 in Equation (5.14a). In order for the pressure field to be continuous across fluid interfaces, these two coefficients must be related as follows:

$$\mu_A C_{0,A} = \mu_B C_{0,B} \tag{C5.3}$$

Next, by the steps given in Section 6.5, the order $\mathcal{O}(1)$ outer r-velocity for the two-fluid case has the following form:

$$U_{ri,0} = -\left(\frac{\mu_{A+B}}{\mu_i}\right)\left(\frac{1-z^2}{2}\right)\frac{\partial p_0}{\partial r} \tag{C5.4}$$

where $U_{ri,0}$ denotes the order $\mathcal{O}(1)$ outer velocity in regions bounded by fluid interfaces at $\theta_S(r,\theta_{i-1})$ and $\theta_S(r,\theta_i)$, and μ_i denotes the viscosity of the fluid species within that region. Substituting this expression into Equations (C5.1) and (C5.2) gives the following:

$$U_{ri,0} = \left(\frac{C_{0,i}}{r}\right)\left(\frac{1-z^2}{2}\right) \tag{C5.5}$$

The flow-rate contribution of the order $\mathcal{O}(1)$ outer r-velocity component within the region bounded by streamlines at $\theta_S(r,\theta_{i-1})$ and $\theta_S(r,\theta_i)$ can now be computed as follows:

$$\int_{-1}^{1}\int_{\theta_S(r,\theta_{i-1})}^{\theta_S(r,\theta_i)} U_{ri,0}\, r d\theta dz = \frac{2}{3} C_{0,i}[\theta_S(r,\theta_i) - \theta_S(r,\theta_{i-1})] \tag{C5.6}$$

For N stripes of fluid *A* alternating with N stripes of fluid *B*, the flow rate through each stripe region can be expressed as follows:

$$\frac{Q_A}{N} = \frac{2}{3} C_{0,A}[\theta_S(r,\theta_i) - \theta_S(r,\theta_{i-1})] \tag{C5.7}$$

$$\frac{Q_B}{N} = \frac{2}{3} C_{0,B}[\theta_S(r,\theta_{i+1}) - \theta_S(r,\theta_i)] \tag{C5.8}$$

where $2 \le i \le 2N$ is an even integer. The stripe width ratio can then be expressed to order $\mathcal{O}(1)$ in terms of flow rate ratio and viscosity ratio:

$$\frac{\theta_S(r,\theta_i)-\theta_S(r,\theta_{i-1})}{\theta_S(r,\theta_{i+1})-\theta_S(r,\theta_{i-1})}=\frac{Q_A}{Q_B}\frac{C_{0,B}}{C_{0,A}}=\left(\frac{Q_A}{Q_B}\right)\left(\frac{\mu_A}{\mu_B}\right) \tag{C5.9}$$

for even $2 \leq i \leq 2N$

Similarly, for the case where M stripes of fluid *A* alternate with $M-1$ stripes of fluid *B*, the flow rate condition gives the following stripe width ratio:

$$\frac{\theta_S(r,\theta_i)-\theta_S(r,\theta_{i-1})}{\theta_S(r,\theta_{i+1})-\theta_S(r,\theta_{i-1})}=\frac{Q_A}{Q_B}\frac{C_{0,B}}{C_{0,A}}=\left(\frac{M-1}{M}\right)\left(\frac{Q_A}{Q_B}\right)\left(\frac{\mu_A}{\mu_B}\right) \tag{C5.10}$$

for even $2 \leq i \leq 2M-1$

Equations (C5.9) and (C5.10) are equivalent to the results in Equations (6.36) and (6.38) for the order $\mathcal{O}(\alpha)$ solution.

REFERENCES

1. G. Gustafsson, Y. Cao, G. M. Treacy, F. Klavetter, N. Colaneri and A. J. Heeger, Nature **357** (6378), 477-479 (1992).

2. J. Bharathan and Y. Yang, Appl. Phys. Lett. **72** (21), 2660-2662 (1998).

3. T. R. Hebner, C. C. Wu, D. Marcy, M. H. Lu and J. C. Sturm, Appl. Phys. Lett. **72** (5), 519-521 (1998).

4. S. E. Shaheen, R. Radspinner, N. Peyghambarian and G. E. Jabbour, Appl. Phys. Lett. **79** (18), 2996-2998 (2001).

5. C. J. Brabec and J. R. Durrant, MRS Bull. **33** (7), 670-675 (2008).

6. L. Blankenburg, K. Schultheis, H. Schache, S. Sensfuss and M. Schrödner, Sol. Energy Mater. Sol. Cells **93** (4), 476-483 (2009).

7. C. M. Amb, M. R. Craig, U. Koldemir, J. Subbiah, K. R. Choudhury, S. A. Gevorgyan, M. Jørgensen, F. C. Krebs, F. So and J. R. Reynolds, ACS Appl. Mater. Interfaces **4** (3), 1847-1853 (2012).

8. A. Sandström, H. F. Dam, F. C. Krebs and L. Edman, Nat. Commun. **3**, 1002 (2012).

9. J. Zhang, Y. Zhao, J. Fang, L. Yuan, B. Xia, G. Wang, Z. Wang, Y. Zhang, W. Ma, W. Yan, W. Su and Z. Wei, Small **13** (21), 1700388-n/a (2017).

10. G. H. Gelinck, H. E. A. Huitema, E. van Veenendaal, E. Cantatore, L. Schrijnemakers, J. B. P. H. van der Putten, T. C. T. Geuns, M. Beenhakkers, J. B. Giesbers, B.-H. Huisman, E. J. Meijer, E. M. Benito, F. J. Touwslager, A. W. Marsman, B. J. E. van Rens and D. M. de Leeuw, Nat. Mater. **3** (2), 106-110 (2004).

11. J. D. Newman, A. P. F. Turner and G. Marrazza, Anal. Chim. Acta **262** (1), 13-17 (1992).

12. M. Albareda-Sirvent, A. Merkoçi and S. Alegret, Sens. Actuators, B **69** (1), 153-163 (2000).

13. D. Nilsson, T. Kugler, P.-O. Svensson and M. Berggren, Sens. Actuators, B **86** (2), 193-197 (2002).

14. K. Abe, K. Suzuki and D. Citterio, Anal. Chem. **80** (18), 6928-6934 (2008).

15. A. Pecora, E. Zampetti, S. Pantalei, A. Valletta, A. Minotti, L. Maiolo, D. Simeone, M. Cuscuna, A. Bearzotti, A. Macagnano, L. Mariucci and G. Fortunato, Proc. IEEE Int. Conf. Sens., 7th, 21-24 (2008).

16. S. Ali, A. Hassan, G. Hassan, J. Bae and C. H. Lee, Carbon **105**, 23-32 (2016).

17. G. Azzellino, A. Grimoldi, M. Binda, M. Caironi, D. Natali and M. Sampietro, Adv. Mater. **25** (47), 6829-6833 (2013).

18. M. T. Rahman, A. Rahimi, S. Gupta and R. Panat, Sens. Actuators, A **248**, 94-103 (2016).

19. Z. Bao, Y. Feng, A. Dodabalapur, V. R. Raju and A. J. Lovinger, Chem. Mater. **9** (6), 1299-1301 (1997).

20. A. R. Brown, C. P. Jarrett, D. M. de Leeuw and M. Matters, Synth. Met. **88** (1), 37-55 (1997).

21. H. Sirringhaus, T. Kawase, R. H. Friend, T. Shimoda, M. Inbasekaran, W. Wu and E. P. Woo, Science **290** (5499), 2123-2126 (2000).

22. A. C. Arias, S. E. Ready, R. Lujan, W. S. Wong, K. E. Paul, A. Salleo, M. L. Chabinyc, R. Apte, R. A. Street, Y. Wu, P. Liu and B. Ong, Appl. Phys. Lett. **85** (15), 3304-3306 (2004).

23. W. Clemens, W. Fix, J. Ficker, A. Knobloch and A. Ullmann, J. Mater. Res. **19** (7), 1963-1973 (2004).

24. A. Dodabalapur, Materials Today **9** (4), 24-30 (2006).

25. K. Chen, W. Gao, S. Emaminejad, D. Kiriya, H. Ota, H. Y. Y. Nyein, K. Takei and A. Javey, Adv. Mater. **28** (22), 4397-4414 (2016).

26. M. Halik, H. Klauk, U. Zschieschang, T. Kriem, G. Schmid, W. Radlik and K. Wussow, Appl. Phys. Lett. **81** (2), 289-291 (2002).

27. J. Vaillancourt, H. Zhang, P. Vasinajindakaw, H. Xia, X. Lu, X. Han, D. C. Janzen, W.-S. Shih, C. S. Jones, M. Stroder, M. Y. Chen, H. Subbaraman, R. T. Chen, U. Berger and M. Renn, Appl. Phys. Lett. **93** (24), 243301 (2008).

28. M. Watanabe, Sens. Actuators, B **122** (1), 141-147 (2007).

29. M. J. Swickrath, S. Shenoy, J. A. Mann, J. Belcher, R. Kovar and G. E. Wnek, Microfluid. Nanofluid. **4** (6), 601-611 (2008).

30. A. Naderi, N. Bhattacharjee and A. Folch, Annual Review of Biomedical Engineering **21** (1), 325-364 (2019).

31. N. M. White, P. Glynne-Jones and S. P. Beeby, Smart Mater. Struct. **10** (4), 850 (2001).

32. J. Weber, K. Potje-Kamloth, F. Haase, P. Detemple, F. Völklein and T. Doll, Sens. Actuators, A **132** (1), 325-330 (2006).

33. Y. Qi, N. T. Jafferis, K. Lyons, C. M. Lee, H. Ahmad and M. C. McAlpine, Nano Lett. **10** (2), 524-528 (2010).

34. G. Zhou, L. Li, D.-W. Wang, X.-y. Shan, S. Pei, F. Li and H.-M. Cheng, Adv. Mater. **27** (4), 641-647 (2015).

35. R. F. Service, Science **278** (5337), 383-384 (1997).

36. S. R. Forrest, Nature **428** (6986), 911-918 (2004).

37. F. C. Krebs, Sol. Energy Mater. Sol. Cells **93** (4), 394-412 (2009).

38. J. Park, K. Shin and C. Lee, Int. J. Precis. Eng. Manuf. **17** (4), 537-550 (2016).

39. R. Abbel, Y. Galagan and P. Groen, Adv. Eng. Mater. **20** (8), 1701190 (2018).

40. G. Wang, M. A. Adil, J. Zhang and Z. Wei, Adv. Mater., 1805089 (2018).

41. Y. M. Lee, J. H. Kim, J. S. Kang and S. Y. Ha, Macromolecules **33** (20), 7431-7439 (2000).

42. R. W. T. Higgins, N. A. Zaidi and A. P. Monkman, Adv. Funct. Mater. **11** (6), 407-412 (2001).

43. X. Crispin, F. L. E. Jakobsson, A. Crispin, P. C. M. Grim, P. Andersson, A. Volodin, C. van Haesendonck, M. Van der Auweraer, W. R. Salaneck and M. Berggren, Chem. Mater. **18** (18), 4354-4360 (2006).

44. J. Jensen, M. Hösel, A. L. Dyer and F. C. Krebs, Adv. Funct. Mater. **25** (14), 2073-2090 (2015).

45. J. Chang, C. Chi, J. Zhang and J. Wu, Adv. Mater. **25** (44), 6442-6447 (2013).

46. H. Gorter, M. J. J. Coenen, M. W. L. Slaats, M. Ren, W. Lu, C. J. Kuijpers and W. A. Groen, Thin Solid Films **532**, 11-15 (2013).

47. K. Peters, L. Wengeler, P. Scharfer and W. Schabel, J. Coat. Technol. Res. **11** (1), 75-81 (2014).

48. H. Liu, W. Xu, W. Tan, X. Zhu, J. Wang, J. Peng and Y. Cao, J. Colloid Interface Sci. **465**, 106-111 (2016).

49. G. Yu, J. Gao, J. C. Hummelen, F. Wudl and A. J. Heeger, Science **270** (5243), 1789-1791 (1995).

50. G. Yu, J. Wang, J. McElvain and A. J. Heeger, Adv. Mater. **10** (17), 1431-1434 (1998).

51. G. Dennler, M. C. Scharber and C. J. Brabec, Adv. Mater. **21** (13), 1323-1338 (2009).

52. Y. Horii, M. Ikawa, M. Chikamatsu, R. Azumi, M. Kitagawa, H. Konishi and K. Yase, ACS Appl. Mater. Interfaces **3** (3), 836-841 (2011).

53. M. A. Meitl, Y. Zhou, A. Gaur, S. Jeon, M. L. Usrey, M. S. Strano and J. A. Rogers, Nano Lett. **4** (9), 1643-1647 (2004).

54. J. Mehlich, Y. Miyata, H. Shinohara and B. J. Ravoo, Small **8** (14), 2258-2263 (2012).

55. J. Huang, Y. Zhu, W. Jiang and Q. Tang, Composites, Part A **69**, 240-246 (2015).

56. Y. Zhou, L. Hu and G. Grüner, Appl. Phys. Lett. **88** (12), 123109 (2006).

57. G. Eda, G. Fanchini and M. Chhowalla, Nature Nanotechnology **3** (5), 270-274 (2008).

58. C. Mao, J. Huang, Y. Zhu, W. Jiang, Q. Tang and X. Ma, J. Phys. Chem. Lett. **4** (1), 43-47 (2013).

59. G. Ibáñez-Redín, D. Wilson, D. Gonçalves and O. N. Oliveira, J. Colloid Interface Sci. **515**, 101-108 (2018).

60. A. Kamyshny, M. Ben-Moshe, S. Aviezer and S. Magdassi, Macromol. Rapid Commun. **26** (4), 281-288 (2005).

61. H.-H. Lee, K.-S. Chou and K.-C. Huang, Nanotechnology **16** (10), 2436 (2005).

62. B. K. Park, D. Kim, S. Jeong, J. Moon and J. S. Kim, Thin Solid Films **515** (19), 7706-7711 (2007).

63. B. Radha, A. A. Sagade and G. U. Kulkarni, ACS Appl. Mater. Interfaces **3** (7), 2173-2178 (2011).

64. W. Tang, L. Feng, J. Zhao, Q. Cui, S. Chen and X. Guo, J. Mater. Chem. C **2** (11), 1995-2000 (2014).

65. J. Liang, K. Tong and Q. Pei, Adv. Mater. **28** (28), 5986-5996 (2016).

66. J. H. Song, M. J. Edirisinghe and J. R. G. Evans, J. Am. Ceram. Soc. **82** (12), 3374-3380 (1999).

67. B. Derby, Engineering **1** (1), 113-123 (2015).

68. F. Paglia, D. Vak, J. van Embden, A. S. R. Chesman, A. Martucci, J. J. Jasieniak and E. Della Gaspera, ACS Appl. Mater. Interfaces **7** (45), 25473-25478 (2015).

69. Z. Pan, Y. Wang, H. Huang, Z. Ling, Y. Dai and S. Ke, Ceram. Int. **41** (10, Part A), 12515-12528 (2015).

70. R. Koncki and M. Mascini, Anal. Chim. Acta **351** (1), 143-149 (1997).

71. Y. Li, L. Lan, P. Xiao, S. Sun, Z. Lin, W. Song, E. Song, P. Gao, W. Wu and J. Peng, ACS Appl. Mater. Interfaces **8** (30), 19643-19648 (2016).

72. F. Shao and Q. Wan, J. Phys. D: Appl. Phys. **52** (14), 143002 (2019).

73. N. Marinova, S. Valero and J. L. Delgado, J. Colloid Interface Sci. **488**, 373-389 (2017).

74. D. Lee, Y.-S. Jung, Y.-J. Heo, S. Lee, K. Hwang, Y.-J. Jeon, J.-E. Kim, J. Park, G. Y. Jung and D.-Y. Kim, ACS Appl. Mater. Interfaces **10** (18), 16133-16139 (2018).

75. F. Wang, Y. Cao, C. Chen, Q. Chen, X. Wu, X. Li, T. Qin and W. Huang, Adv. Funct. Mater. **28** (52), 1803753 (2018).

76. T. M. Schmidt, T. T. Larsen-Olsen, J. E. Carlé, D. Angmo and F. C. Krebs, Adv. Energy Mater. **5** (15), 1500569-n/a (2015).

77. H. Benkreira, R. Patel, M. F. Edwards and W. L. Wilkinson, J. Non-Newtonian Fluid Mech. **54**, 437-447 (1994).

78. J. O. Marston, M. J. H. Simmons, S. P. Decent and S. P. Kirk, Phys. Fluids **18** (11), 112102 (2006).

79. L. Friedrich and M. Begley, J. Colloid Interface Sci. **529**, 599-609 (2018).

80. C. Girotto, B. P. Rand, J. Genoe and P. Heremans, Sol. Energy Mater. Sol. Cells **93** (4), 454-458 (2009).

81. C. N. Hoth, R. Steim, P. Schilinsky, S. A. Choulis, S. F. Tedde, O. Hayden and C. J. Brabec, Org. Electron. **10** (4), 587-593 (2009).

82. S. Moon, I. L. Fritz, Z. S. Singer and T. Danino, 3D Printing and Additive Manufacturing **3** (4), 194-203 (2016).

83. L. S. Pali, R. Jindal and A. Garg, J. Mater. Sci.: Mater. Electron. **29** (13), 11030-11038 (2018).

84. W. J. Hyun, E. B. Secor, M. C. Hersam, C. D. Frisbie and L. F. Francis, Adv. Mater. **27** (1), 109-115 (2015).

85. V. Shanmugam, J. Wong, I. M. Peters, J. Cunnusamy, M. Zahn, A. Zhou, R. Yang, X. Chen, A. G. Aberle and T. Mueller, IEEE Journal of Photovoltaics **5** (2), 525-533 (2015).

86. N. Kapur, S. J. Abbott, E. D. Dolden and P. H. Gaskell, IEEE Transactions on Components, Packaging and Manufacturing Technology **3** (3), 508-515 (2013).

87. S. Leppävuori, J. Väänänen, M. Lahti, J. Remes and A. Uusimäki, Sens. Actuators, A **42** (1), 593-596 (1994).

88. P. Kopola, T. Aernouts, S. Guillerez, H. Jin, M. Tuomikoski, A. Maaninen and J. Hast, Sol. Energy Mater. Sol. Cells **94** (10), 1673-1680 (2010).

89. J. Yang, D. Vak, N. Clark, J. Subbiah, W. W. H. Wong, D. J. Jones, S. E. Watkins and G. Wilson, Sol. Energy Mater. Sol. Cells **109**, 47-55 (2013).

90. M. K. Kwak, K. H. Shin, E. Y. Yoon and K. Y. Suh, J. Colloid Interface Sci. **343** (1), 301-305 (2010).

91. G. Iannaccone, M. Välimäki, E. Jansson, A. Sunnari, G. Corso, A. Bernardi, M. Levi, S. Turri, J. Hast and G. Griffini, Sol. Energy Mater. Sol. Cells **143**, 227-235 (2015).

92. T. R. Andersen, N. A. Cooling, F. Almyahi, A. S. Hart, N. C. Nicolaidis, K. Feron, M. Noori, B. Vaughan, M. J. Griffith, W. J. Belcher and P. C. Dastoor, Sol. Energy Mater. Sol. Cells **149**, 103-109 (2016).

93. P. Calvert, Chem. Mater. **13** (10), 3299-3305 (2001).

94. B. J. de Gans, P. C. Duineveld and U. S. Schubert, Adv. Mater. **16** (3), 203-213 (2004).

95. B. Derby, Annu. Rev. Mater. Res. **40**, 395-414 (2010).

96. M. Singh, H. M. Haverinen, P. Dhagat and G. E. Jabbour, Adv. Mater. **22** (6), 673-685 (2010).

97. R. Haas, S. Lohse, C. E. Düllmann, K. Eberhardt, C. Mokry and J. Runke, Nuclear Instruments and Methods in Physics Research Section A: Accelerators, Spectrometers, Detectors and Associated Equipment **874**, 43-49 (2017).

98. T. Seifert, E. Sowade, F. Roscher, M. Wiemer, T. Gessner and R. R. Baumann, Ind. Eng. Chem. Res. **54** (2), 769-779 (2015).

99. J.-U. Park, M. Hardy, S. J. Kang, K. Barton, K. Adair, D. k. Mukhopadhyay, C. Y. Lee, M. S. Strano, A. G. Alleyne, J. G. Georgiadis, P. M. Ferreira and J. A. Rogers, Nat. Mater. **6** (10), 782-789 (2007).

100. D.-Y. Lee, J.-H. Yu, Y.-S. Shin, D. Park, T.-U. Yu and J. Hwang, Japanese Journal of Applied Physics **47** (3), 1723-1725 (2008).

101. K. Kim, G. Kim, B. R. Lee, S. Ji, S.-Y. Kim, B. W. An, M. H. Song and J.-U. Park, Nanoscale **7** (32), 13410-13415 (2015).

102. A. Lee, H. Jin, H.-W. Dang, K.-H. Choi and K. H. Ahn, Langmuir **29** (44), 13630-13639 (2013).

103. E. J. Choinski, US Patent No. 4 938 994 (July 3, 1990 1990).

104. W.-J. Yu, T.-J. Liu and T.-A. Yu, Chem. Eng. Sci. **50** (6), 917-920 (1995).

105. R. R. Søndergaard, M. Hösel and F. C. Krebs, J. Polym. Sci., Part B: Polym. Phys. **51** (1), 16-34 (2013).

106. O. J. Romero, L. E. Scriven and M. S. Carvalho, J. Non-Newtonian Fluid Mech. **138** (2), 63-75 (2006).

107. Y.-R. Chang, H.-M. Chang, C.-F. Lin, T.-J. Liu and P.-Y. Wu, J. Colloid Interface Sci. **308** (1), 222-230 (2007).

108. K. L. Bhamidipati, S. Didari and T. A. L. Harris, J. Power Sources **239**, 382-392 (2013).

109. B. G. Higgins and L. E. Scriven, Chem. Eng. Sci. **35** (3), 673-682 (1980).

110. S. H. Lee, H. J. Koh, B. K. Ryu, S. J. Kim, H. W. Jung and J. C. Hyun, Chem. Eng. Sci. **66** (21), 4953-4959 (2011).

111. X. Ding, J. Liu and T. A. L. Harris, AlChE J. **62** (7), 2508-2524 (2016).

112. K. J. Ruschak, Chem. Eng. Sci. **31** (11), 1057-1060 (1976).

113. K. L. Bhamidipati, S. Didari, P. Bedell and T. A. L. Harris, J. Non-Newtonian Fluid Mech. **166** (12), 723-733 (2011).

114. Y. Diao, L. Shaw, Z. Bao and S. C. B. Mannsfeld, Energy Environ. Sci. **7** (7), 2145-2159 (2014).

115. P. Tehrani, N. D. Robinson, T. Kugler, T. Remonen, L.-O. Hennerdal, J. Häll, A. Malmström, L. Leenders and M. Berggren, Smart Mater. Struct. **14** (4), N21 (2005).

116. C. L. Bower, E. A. Simister, E. Bonnist, K. Paul, N. Pightling and T. D. Blake, AlChE J. **53** (7), 1644-1657 (2007).

117. J. West, A. Michels, S. Kittel, P. Jacob and J. Franzke, Lab Chip **7** (8), 981-983 (2007).

118. B. J. Brasjen, A. W. van Cuijk and A. A. Darhuber, Chem. Eng. Process. **50** (5), 565-568 (2011).

119. T. Huiskamp, W. J. M. Brok, A. A. E. Stevens, E. J. M. v. Heesch and A. J. M. Pemen, IEEE Trans. Plasma Sci. **40** (7), 1913-1925 (2012).

120. A. N. Efremov, M. Grunze and P. A. Levkin, Adv. Mater. Interfaces **1** (2), 1300075-n/a (2014).

121. J. H. Brannon, J. R. Lankard, A. I. Baise, F. Burns and J. Kaufman, J. Appl. Phys. **58** (5), 2036-2043 (1985).

122. S. Röttinger, B. Schwarz, S. Schäfer, R. Gauch, B. Zimmermann and U. Würfel, Sol. Energy Mater. Sol. Cells **154**, 35-41 (2016).

123. W. Feng, J. N. Tey, Y. C. Wan, X. Shan and H. Zheng, Journal of Manufacturing Processes **38**, 445-452 (2019).

124. M. Friedrich and G. Gibson, in *18th International Coating Science and Technology Symposium* (Pittsburgh, PA, 2016).

125. K. Fukuda and T. Someya, Adv. Mater. **29** (25), 1602736 (2017).

126. J. G. Tait, E. Witkowska, M. Hirade, T.-H. Ke, P. E. Malinowski, S. Steudel, C. Adachi and P. Heremans, Org. Electron. **22**, 40-43 (2015).

127. A. M. Gaikwad, A. C. Arias and D. A. Steingart, Energy Technol. **3** (4), 305-328 (2015).

128. T. Mao, D. C. S. Kuhn and H. Tran, AlChE J. **43** (9), 2169-2179 (1997).

129. M. Ikegawa and H. Azuma, JSME Int J., Ser. B **47** (3), 490-496 (2004).

130. A. Lee, K. Sudau, K. H. Ahn, S. J. Lee and N. Willenbacher, Ind. Eng. Chem. Res. **51** (40), 13195-13204 (2012).

131. O. A. Basaran, H. Gao and P. P. Bhat, Annu. Rev. Fluid Mech. **45** (1), 85-113 (2013).

132. M. Hösel, R. R. Søndergaard, M. Jørgensen and F. C. Krebs, Energy Technol. **1** (1), 102-107 (2013).

133. M. Schmitt, P. Scharfer and W. Schabel, J. Coat. Technol. Res. **11** (1), 57-63 (2014).

134. D. I. Kutsarov, E. New, F. Bausi, A. Zoladek-Lemanczyk, F. A. Castro and S. R. P. Silva, Sol. Energy Mater. Sol. Cells **161**, 388-396 (2017).

135. S. M. Raupp, M. Schmitt, A.-L. Walz, R. Diehm, H. Hummel, P. Scharfer and W. Schabel, J. Coat. Technol. Res. **15** (5), 899-911 (2018).

136. T. Nuanes, B. Dieckman, T. New, B. S. Cook and E. Wheeler, presented at the 2016 46th European Microwave Conference (EuMC), 2016 (unpublished).

137. M. H. Overgaard, M. Kühnel, R. Hvidsten, S. V. Petersen, T. Vosch, K. Nørgaard and B. W. Laursen, Adv. Mater. Technol. **2** (7), 1700011 (2017).

138. J. Ho, T.-C. Wu, J.-J. Ho, C.-H. Hung, S.-Y. Chen, J.-S. Ho, S.-Y. Tsai, C.-C. Chou and C.-H. Yeh, Materials Science in Semiconductor Processing **83**, 22-26 (2018).

139. K. Park, K. Woo, J. Kim, D. Lee, Y. Ahn, D. Song, H. Kim, D. Oh, S. Kwon and Y. Lee, ACS Appl. Mater. Interfaces **11** (16), 14882-14891 (2019).

140. H. A. D. Nguyen, K.-H. Shin and D. Lee, Japanese Journal of Applied Physics **53** (5S3), 05HC04 (2014).

141. S. Thibert, J. Jourdan, B. Bechevet, S. Mialon, D. Chaussy, N. Reverdy-Bruas and D. Beneventi, Progress in Photovoltaics: Research and Applications **24** (2), 240-252 (2016).

142. D. Deganello, J. A. Cherry, D. T. Gethin and T. C. Claypole, Thin Solid Films **518** (21), 6113-6116 (2010).

143. L. Mo, J. Ran, L. Yang, Y. Fang, Q. Zhai and L. Li, Nanotechnology **27** (6), 065202 (2016).

144. M. Wegener, D. Spiehl, H. M. Sauer, F. Mikschl, X. Liu, N. Kölpin, M. Schmidt, M. P. M. Jank, E. Dörsam and A. Roosen, Journal of Materials Science **51** (9), 4588-4600 (2016).

145. T. Cheng, Y.-Z. Zhang, J.-P. Yi, L. Yang, J.-D. Zhang, W.-Y. Lai and W. Huang, J. Mater. Chem. A **4** (36), 13754-13763 (2016).

146. A. Mahajan, C. D. Frisbie and L. F. Francis, ACS Appl. Mater. Interfaces **5** (11), 4856-4864 (2013).

147. R. Eckstein, G. Hernandez-Sosa, U. Lemmer and N. Mechau, Org. Electron. **15** (9), 2135-2140 (2014).

148. S. Y. Kim, K. Kim, Y. H. Hwang, J. Park, J. Jang, Y. Nam, Y. Kang, M. Kim, H. J. Park, Z. Lee, J. Choi, Y. Kim, S. Jeong, B. S. Bae and J. U. Park, Nanoscale **8** (39), 17113-17121 (2016).

149. J. Stringer and B. Derby, Langmuir **26** (12), 10365-10372 (2010).

150. H. S. Kim, C. H. Lee, P. K. Sudeep, T. Emrick and A. J. Crosby, Adv. Mater. **22** (41), 4600-4604 (2010).

151. J. Tanwar, M. Vinjamur and L. E. Scriven, AlChE J. **53** (3), 572-578 (2007).

152. S.-H. Wen and T.-J. Liu, Polym. Eng. Sci. **35** (9), 759-767 (1995).

153. G. H. Han, S. H. Lee, W.-G. Ahn, J. Nam and H. W. Jung, J. Coat. Technol. Res. **11** (1), 19-29 (2014).

154. C.-F. Lin, B.-K. Wang, S.-H. Lo, D. S.-H. Wong, T.-J. Liu and C. Tiu, Asia-Pac. J. Chem. Eng. **9** (1), 134-145 (2014).

155. T. M. Milbourn and J. J. Barth, US Patent No. 5 360 629 (Nov. 1, 1994 1994).

156. Y. Iwashita, S. Endo and K. Morimoto, US Patent No. 5 989 622 (Nov. 23, 1999 1999).

157. D. Vak, K. Hwang, A. Faulks, Y.-S. Jung, N. Clark, D.-Y. Kim, G. J. Wilson and S. E. Watkins, Adv. Energy Mater. **5** (4), 1401539 (2015).

158. G.-E. Kim, D.-K. Shin, J.-Y. Lee and J. Park, Org. Electron. **66**, 116-125 (2019).

159. G. Kim, J. Lee, D. Shin and J. Park, IEEE Transactions on Electron Devices **66** (2), 1041-1049 (2019).

160. J. B. Knight, A. Vishwanath, J. P. Brody and R. H. Austin, Phys. Rev. Lett. **80** (17), 3863-3866 (1998).

161. G.-B. Lee, C.-I. Hung, B.-J. Ke, G.-R. Huang, B.-H. Hwei and H.-F. Lai, J. Fluids Eng. **123** (3), 672-679 (2001).

162. Z. Wu and N.-T. Nguyen, Sens. Actuators, B **107** (2), 965-974 (2005).

163. T. Cubaud and T. G. Mason, Phys. Rev. E **78** (5), 056308 (2008).

164. Y. Liu, Y. Shen, L. Duan and L. Yobas, Appl. Phys. Lett. **109** (14), 144101 (2016).

165. C. L. Cobb, US Patent No. 9,855,578 B2 (Jan 2, 2018 2018).

166. S. Onogi, T. Kobayashi, Y. Kojima and Y. Taniguchi, J. Appl. Polym. Sci. **7** (3), 847-859 (1963).

167. C. GmbH, Report No. Technical Report, 1999.

168. J. Drelich, J. D. Miller and R. J. Good, J. Colloid Interface Sci. **179** (1), 37-50 (1996).

169. H. Y. Erbil, G. McHale, S. M. Rowan and M. I. Newton, Langmuir **15** (21), 7378-7385 (1999).

170. B. He, J. Lee and N. A. Patankar, Colloids Surf., A **248** (1), 101-104 (2004).

171. P. C. Duineveld, J. Fluid Mech. **477**, 175-200 (2003).

172. Y. V. Kalinin, V. Berejnov and R. E. Thorne, Langmuir **25** (9), 5391-5397 (2009).

173. F. Restagno, C. Poulard, C. Cohen, L. Vagharchakian and L. Léger, Langmuir **25** (18), 11188-11196 (2009).

174. D. Soltman, B. Smith, H. Kang, S. J. S. Morris and V. Subramanian, Langmuir **26** (19), 15686-15693 (2010).

175. B. A. Johnson, J. Kreuter and G. Zografi, Colloids and Surfaces **17** (4), 325-342 (1986).

176. C. Ishino and K. Okumura, The European Physical Journal E **25** (4), 415-424 (2008).

177. P. S. H. Forsberg, C. Priest, M. Brinkmann, R. Sedev and J. Ralston, Langmuir **26** (2), 860-865 (2010).

178. M. E. R. Shanahan, Langmuir **11** (3), 1041-1043 (1995).

179. A. G. Lee, E. S. G. Shaqfeh and B. Khomami, J. Non-Newtonian Fluid Mech. **108** (1), 327-362 (2002).

180. J. Eggers and H. A. Stone, J. Fluid Mech. **505**, 309-321 (2004).

181. D. J. Broesch, F. Dutka and J. Frechette, Langmuir **29** (50), 15558-15564 (2013).

182. S. Dodds, M. d. S. Carvalho and S. Kumar, Phys. Fluids **21** (9), 092103 (2009).

183. S. Dodds, M. S. Carvalho and S. Kumar, J. Fluid Mech. **707**, 521-540 (2012).

184. K. Tanaka and K. Iwamoto, Tribology Letters **64** (1), 9 (2016).

185. P. V. Petkov and B. P. Radoev, Colloids Surf., A **460**, 18-27 (2014).

186. H. Chen, A. Amirfazli and T. Tang, Langmuir **29** (10), 3310-3319 (2013).

187. H. Chen, T. Tang and A. Amirfazli, Soft Matter **10** (15), 2503-2507 (2014).

188. H. Chen, T. Tang, H. Zhao, K. Y. Law and A. Amirfazli, Soft Matter **12** (7), 1998-2008 (2016).

189. S. Gaudet, G. H. McKinley and H. A. Stone, Phys. Fluids **8** (10), 2568-2579 (1996).

190. M. A. Verges, M. C. Larson and R. Bacou, Experimental Mechanics **41** (4), 351-357 (2001).

191. E. J. De Souza, L. Gao, T. J. McCarthy, E. Arzt and A. J. Crosby, Langmuir **24** (4), 1391-1396 (2008).

192. T. I. Vogel, SIAM J. Appl. Math. **47** (3), 516-525 (1987).

193. J. Eggers, Phys. Rev. Lett. **71** (21), 3458-3460 (1993).

194. M. P. Brenner, J. R. Lister and H. A. Stone, Phys. Fluids **8** (11), 2827-2836 (1996).

195. B. Qian and K. S. Breuer, J. Fluid Mech. **666**, 554-572 (2011).

196. S. Kumar, Annu. Rev. Fluid Mech. **47**, 67-94 (2015).

197. A. W. Parsekian and T. A. L. Harris, Chem. Eng. Process. **109**, 20-31 (2016).

198. A. W. Parsekian, T.-J. Jeong and T. A. L. Harris, J. Coat. Technol. Res. (2019).

199. N. Kim, B. H. Lee, D. Choi, G. Kim, H. Kim, J.-R. Kim, J. Lee, Y. H. Kahng and K. Lee, Phys. Rev. Lett. **109** (10), 106405 (2012).

200. T. J. Faircloth, J. G. Innocenzo and C. D. Lang, SID Symposium Digest of Technical Papers **39** (1), 645-647 (2008).

201. Y.-R. Chang, C.-F. Lin and T.-J. Liu, Polym. Eng. Sci. **49** (6), 1158-1167 (2009).

202. P. A. Levermore, L. Chen, X. Wang, R. Das and D. D. C. Bradley, Adv. Mater. **19** (17), 2379-2385 (2007).

203. K. Tvingstedt and O. Inganäs, Adv. Mater. **19** (19), 2893-2897 (2007).

204. K. Sun, S. Zhang, P. Li, Y. Xia, X. Zhang, D. Du, F. H. Isikgor and J. Ouyang, J. Mater. Sci.: Mater. Electron. **26** (7), 4438-4462 (2015).

205. P. Andersson, R. Forchheimer, P. Tehrani and M. Berggren, Adv. Funct. Mater. **17** (16), 3074-3082 (2007).

206. J. Jensen, M. Hösel, I. Kim, J.-S. Yu, J. Jo and F. C. Krebs, Adv. Funct. Mater. **24** (9), 1228-1233 (2014).

207. D. Eric Shen, A. M. Österholm and J. R. Reynolds, J. Mater. Chem. C **3** (37), 9715-9725 (2015).

208. B. Friedel, P. E. Keivanidis, T. J. K. Brenner, A. Abrusci, C. R. McNeill, R. H. Friend and N. C. Greenham, Macromolecules **42** (17), 6741-6747 (2009).

209. Z. Xiong and C. Liu, Org. Electron. **13** (9), 1532-1540 (2012).

210. Y. Seki, M. Takahashi and M. Takashiri, Org. Electron. **55**, 112-116 (2018).

211. J. S. Rowlinson and B. Widom, in *Molecular Theory of Capillarity* (Dover Publications, Mineloa, NY, 2002), pp. 209-212.

212. A. W. Parsekian and T. A. L. Harris, ACS Appl. Mater. Interfaces **12** (3), 3736-3745 (2020).

213. H. Shi, C. Liu, Q. Jiang and J. Xu, Adv. Electron. Mater. **1** (4), 1500017 (2015).

214. M. De Keersmaecker, A. W. Lang, A. M. Österholm and J. R. Reynolds, ACS Appl. Mater. Interfaces **10** (37), 31568-31579 (2018).

215. M. M. Voigt, R. C. I. Mackenzie, C. P. Yau, P. Atienzar, J. Dane, P. E. Keivanidis, D. D. C. Bradley and J. Nelson, Sol. Energy Mater. Sol. Cells **95** (2), 731-734 (2011).

216. A. H. Nayfeh, *Perturbation Methods*. (Wiley & Sons, New York, 1973).

217. E. J. Hinch, *Perturbation Methods*. (Cambridge University Press, Cambridge, 1991).

218. H. A. Stone and S. Kim, AlChE J. **47** (6), 1250-1254 (2001).

219. G. M. Whitesides and A. D. Stroock, Phys. Today **54** (6), 42-48 (2001).

220. G. M. Whitesides, Nature **442** (7101), 368-373 (2006).

221. K. Wang, L. Li, P. Xie and G. Luo, Reaction Chemistry & Engineering **2** (5), 611-627 (2017).

222. M. Hashimoto, R. Langer and D. S. Kohane, Lab Chip **13** (2), 252-259 (2013).

223. T. F. Balsa, J. Fluid Mech. **372**, 25-44 (1998).

224. H. Lamb, *Hydrodynamics*, 6th ed. (Dover Publications, 1932).

225. E. Lauga, A. D. Stroock and H. A. Stone, Phys. Fluids **16** (8), 3051-3062 (2004).

226. A. Groisman and V. Steinberg, Nature **410**, 905 (2001).

227. A. D. Stroock, S. K. W. Dertinger, A. Ajdari, I. Mezić, H. A. Stone and G. M. Whitesides, Science **295** (5555), 647-651 (2002).

228. P. Watts and S. J. Haswell, Chemical Engineering & Technology **28** (3), 290-301 (2005).

229. K. Ward and Z. H. Fan, J. Micromech. Microeng. **25** (9), 094001 (2015).

230. J. O. Hardin, T. J. Ober, A. D. Valentine and J. A. Lewis, Adv. Mater. **27** (21), 3279-3284 (2015).

231. M. Akbari, D. Sinton and M. Bahrami, Int. J. Heat Mass Transfer **54** (17), 3970-3978 (2011).

232. V. S. Duryodhan, S. G. Singh and A. Agrawal, Microfluid. Nanofluid. **14** (1), 53-67 (2013).

233. V. S. Duryodhan, S. G. Singh and A. Agrawal, J. Micromech. Microeng. **24** (12), 125002 (2014).

234. V. S. Duryodhan, S. G. Singh and A. Agrawal, J. Fluids Eng. **139** (6) (2017).

235. R. Tao, Y. Jin, X. Gao and Z. Li, Phys. Fluids **30** (11), 112004 (2018).

236. S. Goli, S. K. Saha and A. Agrawal, SN Applied Sciences **1** (11), 1353 (2019).

237. N. L. Jeon, S. K. W. Dertinger, D. T. Chiu, I. S. Choi, A. D. Stroock and G. M. Whitesides, Langmuir **16** (22), 8311-8316 (2000).

238. X. Mao, J. R. Waldeisen and T. J. Huang, Lab Chip **7** (10), 1260-1262 (2007).

239. W. Lan, S. Li, Y. Lu, J. Xu and G. Luo, Lab Chip **9** (22), 3282-3288 (2009).

240. J. Atencia, G. A. Cooksey and L. E. Locascio, Lab Chip **12** (2), 309-316 (2012).

241. S. Hong, P.-H. Tsou, C.-K. Chou, H. Yamaguchi, C. B. Su, M.-C. Hung and J. Kameoka, Biomicrofluidics **6** (2), 024132 (2012).

242. F. Sharifi, Z. Bai, R. Montazami and N. Hashemi, RSC Advances **6** (60), 55343-55353 (2016).

243. E. André, N. Pannacci, C. Dalmazzone and A. Colin, Soft Matter **15** (3), 504-514 (2019).

244. H. Hong, J. M. Song and E. Yeom, Biomicrofluidics **13** (1), 014104 (2019).

245. S. L. Anna, N. Bontoux and H. A. Stone, Appl. Phys. Lett. **82** (3), 364-366 (2003).

246. I.-L. Ngo, S. Woo Joo and C. Byon, J. Fluids Eng. **138** (5) (2016).

247. J. Buckmaster, J. Fluid Mech. **61** (3), 449-463 (1973).

248. N. M. Ribe, M. Habibi and D. Bonn, Annu. Rev. Fluid Mech. **44** (1), 249-266 (2012).

249. T. Cubaud and T. G. Mason, Soft Matter **8** (41), 10573-10582 (2012).

250. P. J. Stiles and D. F. Fletcher, Lab Chip **4** (2), 121-124 (2004).

251. S. Tripathi, P. Chakravarty and A. Agrawal, Current Science **107** (8), 1260-1274 (2014).

252. A. Sadeghi, J. Fluid Mech. **862**, 517-551 (2019).

253. J. M. Petit, X. X. Zhu and P. M. Macdonald, Macromolecules **29** (1), 70-76 (1996).

254. I. Sobel and G. Feldman, a talk at the Stanford Artificial Project in, 271-272 (1968).

255. S. H. Davis, J. Fluid Mech. **98** (2), 225-242 (1980).

256. F. Brochard-Wyart and C. Redon, Langmuir **8** (9), 2324-2329 (1992).

257. M. S. McCallum, P. W. Voorhees, M. J. Miksis, S. H. Davis and H. Wong, J. Appl. Phys. **79** (10), 7604-7611 (1996).